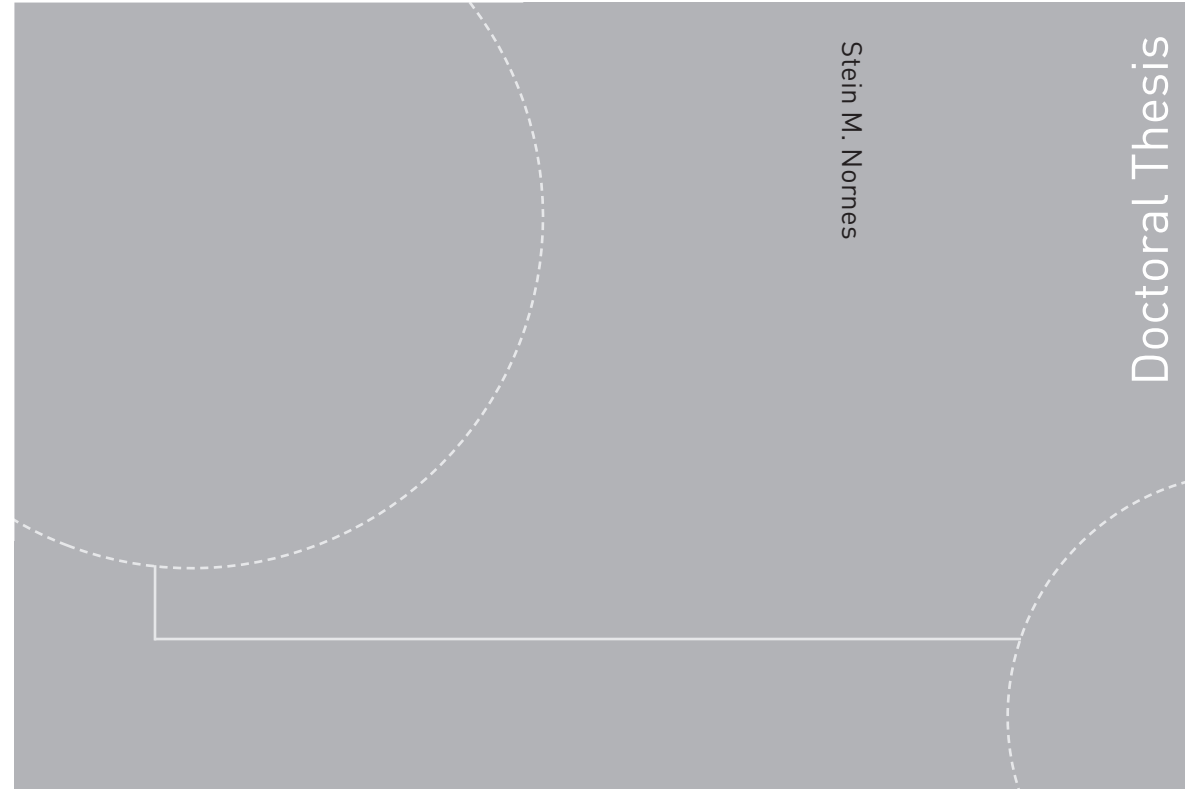


ISBN 978-82-326-3194-0 (printed version)  
ISBN 978-82-326-3195-7 (electronic version)  
ISSN 1503-8181



Doctoral theses at NTNU, 2018:202

Stein M. Nornes

# Guidance and Control of Marine Robotics for Ocean Mapping and Monitoring

Doctoral theses at NTNU, 2018:202

**NTNU**  
Norwegian University of  
Science and Technology  
Faculty of Engineering  
Department of Marine Technology

 **NTNU**  
Norwegian University of  
Science and Technology

 **NTNU**

 **NTNU**  
Norwegian University of  
Science and Technology

Stein M. Nornes

# Guidance and Control of Marine Robotics for Ocean Mapping and Monitoring

Thesis for the degree of Philosophiae Doctor

Trondheim, June 2018

Norwegian University of Science and Technology  
Faculty of Engineering  
Department of Marine Technology



Norwegian University of  
Science and Technology

**NTNU**

Norwegian University of Science and Technology

Thesis for the degree of Philosophiae Doctor

Faculty of Engineering  
Department of Marine Technology

© Stein M. Nornes

ISBN 978-82-326-3194-0 (printed version)

ISBN 978-82-326-3195-7 (electronic version)

ISSN 1503-8181

Doctoral theses at NTNU, 2018:202



Printed by Skipnes Kommunikasjon as

*“It doesn't stop being magic just because you know how it works.”*  
- Terry Pratchett

*“The stuff you see beneath the water often seems like a wild  
parody of the stuff you see above it.[...] If I were not an atheist  
I think I would have to be a Catholic because if it wasn't the forces  
of natural selection that designed fish, it must have been an Italian.”*  
- Douglas Adams



# Abstract

The ocean is an integral part of life on Earth, both as a source of food and oxygen, a medium of transportation and a major influence on weather and climate. Unfortunately, proper management and preservation of the ocean depend on knowledge we do not necessarily possess, due to what oceanographers refer to as a “century of undersampling”.

Autonomous marine robotic platforms are showing promising steps towards increasing the quantity and quality of ocean mapping and monitoring. This thesis concerns development of methods for motion control and mapping systems for marine robotic platforms with varying levels of autonomy. The main motivation of the work has been to increase the level of autonomy of the systems, in order to reduce costs and the need for human interaction, while simultaneously increasing recording efficiency and data quality. The research questions guiding the work are focused on how marine robotic platforms with increasing levels of autonomy can improve the quality, quantity and efficiency of ocean mapping and monitoring, both in terms of data collection and interpretation. The thesis presents contributions to different modules of an overarching autonomy architecture.

The primary task of a marine robotic platform during a mapping mission is to bring one or more payload sensors to the appropriate locations in time and space. The motion of the platform must be efficient in order to record the desired quantity of data, and accurate in order to achieve the desired quality of data. Sensors such as underwater optical cameras, benefit from a methodical motion pattern and a constant distance to the area of interest (AOI), both for data quality and area coverage. This work presents an automated relative motion control strategy for mapping steep underwater structures using a Remotely Operated Vehicle (ROV). The strategy employs a Doppler Velocity Logger (DVL) oriented in the viewing direction of the cameras to maintain a stable distance to the AOI, ensuring high image quality. Through several full-scale experiments, the strategy is demonstrated to efficiently record high quality datasets of challenging structures.

A major benefit of autonomous platforms is the ability to operate in scenarios that are deemed too dull, distant or dangerous for human operators. This work presents the results from several mapping missions performed with marine robotic platforms on multiple scientific cruises. Photogrammetry surveys that require highly accurate control over prolonged periods of time demonstrate situations where operator fatigue would have led to a gradual decrease in performance of a manual system. Arctic operations in the polar night that require measurements that are not polluted by artificial light exemplify scenarios which would have been

impossible to perform within safety regulations for crewed vessels.

In order to approach a truly autonomous system, the system must be able to acquire and analyze the information necessary to make informed decisions. In this work, underwater hyperspectral imaging (UHI) is demonstrated to be a promising tool for high-resolution seafloor exploration and classification. The increased spectral information present in UHI-data compared to regular RGB-imagery is well suited for computer analysis and online classification of objects of interest.

Autonomous inspection of seafloor structures or other AOIs poses interesting opportunities for both industry and marine science. This work presents experimental results from an ROV implementation of a behavior- and reactive based autonomy architecture. The architecture is able to conduct a realistic mission from surface launch to target area with obstacle avoidance.

The work is motivated by the needs of the end-users in the marine sciences, and involves interdisciplinary collaboration, in particular between the fields of marine control systems, marine biology and marine archaeology. The developed methods are applied to real world cases on a variety of scientific cruises, primarily in the Trondheimsfjord from the NTNU-owned and operated R/V *Gunnerus*, but also in the Arctic on the UiT R/V *Helmer Hanssen* and in the Pacific on the Geomar R/V *Sonne*.

The thesis is edited as a collection of papers.

# Preface

This thesis is submitted in partial fulfillment of the requirements for the degree of philosophiae doctor (PhD) at the Norwegian University of Science and Technology (NTNU). The work is a part of the Norwegian Centre of Excellence (SFF), Centre for Autonomous Marine Operations and Systems (NTNU AMOS), Project 2: Marine robotic platforms. It is a part of the Research Council of Norway (RCN) funding scheme, project number 223254.

I have done this work at NTNU AMOS at the Department of Marine Technology (IMT) at NTNU. My main supervisor has been Professor Asgeir J. Sørensen at IMT NTNU, and my co-supervisors have been Professor Geir Johnsen at the Department of Biology NTNU, Professor Martin Ludvigsen and Professor Ingrid Schjølberg at IMT NTNU, and Dr. Kjetil Bergh Ånonsen at the Norwegian Defence Research Establishment (FFI).

## Acknowledgments

### *Collaboration related to Chapter 3*

Thank you to fellow PhD candidate Øyvind Ødegård and Dr. Ines Dumke for their valuable input to this chapter, particularly in providing the marine science perspectives in Sections 3.5 and 3.6.

### *Collaboration related to Chapter 4*

The framework for an autonomous marine archaeological survey introduced in Section 4.2.1 was developed together with Øyvind Ødegård in a short writing break that quickly escalated into a full whiteboard of ideas.

### *Personal Acknowledgments*

I would like to thank my supervisor Asgeir J. Sørensen for his continuous support, motivation and feedback during my PhD studies. One of the first lessons he taught me was “The topic of your thesis should be so specific that you know what you’re doing, and so vague that you can do whatever you want.” At times I’ve certainly thought that we were more successful with the latter than the former, and whenever I felt like it was impossible to see which direction I was going, it was a huge relief to have Asgeir help me take a step back and see the bigger picture and the path forward.

I’ve been fortunate to have four great co-supervisors as well. Thank you to Martin Ludvigsen for the many fruitful discussions, pushing me to achieve my full

potential, and for giving me the unique opportunity to participate in so many research cruises ranging all the way from the high Arctic to the Pacific and Caribbean Oceans. Thank you to Geir Johnsen for helping me to think from the end-user perspective, learning how to explain my work without relying on equations, and for simply being an endless supply of enthusiasm. Ingrid Schjølberg deserves thanks, both as the person who first planted the idea of doing a PhD in my head while I was working on my Master's thesis, and for always emphasizing the importance of structured, continuous work to me. And thank you to Kjetil Bergh Ånonsen for welcoming me to FFI and helping me with algorithm implementations and software that would not have been available to me without him.

Both my research and my teaching assistant duty has involved a lot of work at AUR-Lab, with many long days preparing for and carrying out cruises. While sometimes exhausting, thanks to my co-workers Petter, Øystein, Frode, Pedro and Kay, this work has been the highlight of my PhD time. A special thanks goes to Fredrik and Mauro, who had the main responsibility for the ROV control system implementation before I inherited it. You guys were the giants whose shoulders I could stand on to see further.

A significant part of my time as a PhD candidate has been spent on research cruises, during which I have met a lot of friendly and helpful people that were instrumental in making the experiences rewarding both on a scientific and personal level. In particular, I need to thank the crew of R/V Gunnerus for all their help during the many cruises in the Trondheimsfjord, the crew of R/V Helmer Hanssen for the unforgettable arctic cruises, and the crews of R/V Sonne and ROV KIEL for managing to calm down a slightly panicked lone Norwegian (far from home) enough to get the necessary measurements from the bottom of the Pacific Ocean.

To all of my fellow PhD candidates and postdocs at AMOS: Thank you for the wonderful discussions over lunch or coffee, both the professional ones and the absurdly hilarious ones that only a group of engineering students can come up with. Extra thanks to my office mate Øyvind for the many brainstorming sessions and collaborations we've had, and for making the effort to fill in the gaps in my sci-fi education.

And finally, a huge thanks to my family who have always supported me. No matter how deep into the PhD-bubble I sank, unable to think beyond the nearest deadline, I could always count on a phone call of encouragement from home.

Sogndal, April 5th 2018

*Stein M. Nornes*

# Contents

<b>Abstract</b>	<b>iii</b>
<b>Preface</b>	<b>v</b>
<b>Contents</b>	<b>vii</b>
<b>List of Acronyms</b>	<b>ix</b>
<b>List of Figures</b>	<b>xi</b>
<b>List of Tables</b>	<b>xiii</b>
<b>I Thesis Overview</b>	<b>1</b>
<b>1 Introduction</b>	<b>3</b>
1.1 Motivation and Background . . . . .	3
1.2 Research Questions and Methodology . . . . .	5
1.3 List of Publications and Scientific Contributions . . . . .	6
1.4 Thesis Structure and Outline . . . . .	9
<b>2 Marine Robotic Platforms</b>	<b>11</b>
2.1 Platform Types . . . . .	11
2.2 Control System Architecture . . . . .	18
2.3 Relative Motion Control and Guidance . . . . .	19
<b>3 Ocean Mapping</b>	<b>23</b>
3.1 Mapping Sensors . . . . .	23
3.2 Underwater Image Color Correction . . . . .	27
3.3 Photogrammetry Post-Processing Procedure . . . . .	34
3.4 Image-Aided Post-Processing of Navigation Data . . . . .	36
3.5 Photogrammetry Examples in the Marine Sciences . . . . .	37
3.6 Mapping, Monitoring and Management . . . . .	44
<b>4 Towards Autonomy</b>	<b>47</b>
4.1 Levels of Autonomy . . . . .	47
4.2 Planning and Replanning . . . . .	48
	vii

4.3	Robotic Intervention . . . . .	50
<b>5</b>	<b>Conclusions and Recommendations for Further Work</b>	<b>51</b>
5.1	Conclusions . . . . .	51
5.2	Recommendations for Further Work . . . . .	52
	<b>References</b>	<b>55</b>
	<b>Appendices</b>	<b>63</b>
<b>A</b>	<b>ROV Specifications</b>	<b>63</b>
A.1	ROV Minerva . . . . .	63
A.2	ROV 30K . . . . .	64
A.3	ROV Kiel 6000 . . . . .	65
<b>B</b>	<b>Python Scripts</b>	<b>67</b>
B.1	Photoscan Distance Export . . . . .	67
B.2	Blender Navigation Data Import . . . . .	68
<b>II</b>	<b>Articles</b>	<b>69</b>
<b>Article A</b>	<b>- Automatic Relative Motion Control and Photogrammetry Mapping on Steep Underwater Walls using ROV</b>	<b>71</b>
<b>Article B</b>	<b>- Motion Control of ROVs for Mapping of Steep Underwater Walls</b>	<b>79</b>
<b>Article C</b>	<b>- Underwater Photogrammetric Mapping of an Intact Standing Steel Wreck with ROV</b>	<b>101</b>
<b>Article D</b>	<b>- Underwater Vehicles for Environmental Management in Coastal Areas</b>	<b>109</b>
<b>Article E</b>	<b>- Use of an Autonomous Surface Vehicle Reveals Small-scale Diel Vertical Migrations of Zooplankton and Susceptibility to Light Pollution under Low Solar Irradiance</b>	<b>117</b>
<b>Article F</b>	<b>- First Hyperspectral Imaging Survey of the Deep Seafloor: High-Resolution Mapping of Manganese Nodules</b>	<b>127</b>
<b>Article G</b>	<b>- Autonomy in Marine Archaeology</b>	<b>141</b>
<b>Article H</b>	<b>- Autonomous Robotic Intervention using ROV: An Experimental Approach</b>	<b>153</b>
<b>Article I</b>	<b>- Vision Based Obstacle Avoidance and Motion Tracking for Autonomous Behaviors in Underwater Vehicles</b>	<b>161</b>

# List of Acronyms

AMOS	Centre for Autonomous Marine Operations and Systems
AOI	Area Of Interest
ASV	Autonomous Surface Vehicle
AUV	Autonomous Underwater Vehicle
AUR-Lab	Applied Underwater Robotics Laboratory
CLAHE	Contrast Limited Adaptive Histogram Equalization
DAGW	Distance Adjusted Gray-World
DISCOL	DISturbance and reCOLonisation experiment
DP	Dynamic Positioning
DVL	Doppler Velocity Logger
FFI	Norwegian Defence Research Establishment
GNSS	Global Navigation Satellite System
GPS	Global Positioning System
GW	Gray-World
HE	Histogram Equalization
HISAS	High resolution Interferometric Synthetic Aperture Sonar
IMT	Department of Marine Technology
INS	Inertial Navigation System
JPIO	Joint Programming Initiative healthy and productive seas and Oceans
MBES	Multi-Beam EchoSounder
NED	North-East-Down reference frame
NOAA	National Oceanic and Atmospheric Administration
NTNU	Norwegian University of Science and Technology
OOI	Object Of Interest
RGB	Red, Green and Blue imagery
ROV	Remotely Operated Vehicle
R/V	Research Vessel
SAS	Synthetic Aperture Sonar
SfM	Structure from Motion
SLaM	Simultaneous Localization and Mapping
SSS	SideScan Sonar

*List of Acronyms*

---

UAV	Unmanned Aerial Vehicle
UHI	Underwater Hyperspectral Imager
UiT	University of Tromsø
UNESCO	United Nations Educational, Scientific and Cultural Organization
USBL	Ultra Short BaseLine acoustic positioning
UUV	Unmanned Underwater Vehicle

# List of Figures

1.1	Autonomy framework as presented in [41]	4
1.2	Overview of the papers in the thesis	9
2.1	Spatial and temporal platform capabilities	12
2.2	NTNU JetYak ASV	14
2.3	Three examples of ROVs	16
2.4	Hugin AUV being deployed from RV Gunnerus	16
2.5	The ROV motion control system architecture	18
2.6	Expanded view of the relative motion control architecture	20
3.1	The NTNU stereo camera rig with a horizontal DVL mounted on 30K	24
3.2	The camera setup of ROV Kiel 6000	25
3.3	The operating principle of a hyperspectral camera.	26
3.4	Ship wreck in SAS data from Paper D.	27
3.5	Illustration of the difference in optical path length in a two lamp setup	28
3.6	Image of bubblegum coral demonstrating the difference between color correction techniques	29
3.7	Illustration of the variables used in the Gray-World algorithms	31
3.8	Flowchart of the photogrammetry processing chain to create mosaics or 3D models and to improve navigation data	35
3.9	3D model of MS Herkules, seen from the starboard side	38
3.10	3D model of a 9 m x 12 m section of the wall at Stokkberghneset	39
3.11	Two 3.5 m x 1.8 m boxes of the 2D photomosaic presented in Fig. 3.10	40
3.12	HD-video frame showing manganese nodules in the Peru Basin	42
3.13	Demonstration of photogrammetry-based geocorrection of UHI	43
4.1	Concept flowchart for autonomous planning/replanning in a marine archaeological survey	49



# List of Tables

2.1	Pros and cons of ASVs . . . . .	13
2.2	Pros and cons of ROVs . . . . .	15
2.3	Pros and cons of AUVs . . . . .	17
3.1	Comparison of color correction algorithms . . . . .	33
3.2	Mapping efficiency of the Stokkberneset wall . . . . .	39



## Part I

# Thesis Overview



# Chapter 1

## Introduction

In this chapter, the motivation and the background for the thesis, the research questions and methodology, list of papers and scientific contributions are introduced. The structure of the thesis and the relations between the papers included in Part II of the thesis are presented at the end of the chapter.

### 1.1 Motivation and Background

According to the National Oceanic and Atmospheric Administration (NOAA), over 95% of the Earth's oceans remain unexplored [47]. The most detailed map covering the entire ocean floor currently only allows resolution of structures as small as 6 kilometers [60]. Oceanographers have referred to the 20th century as a “century of undersampling”, and stress the importance of adequate sampling in coming to the correct conclusions for climate processes with large scales in time and space [46]. Despite the steady development and improvement of marine robotics and sensor technology, increasing the spatial coverage and resolution of ocean mapping remains a challenge [48].

Wide varieties of marine robotic platforms are now available for both industry and research, both in the air, on the surface and underwater. While most in-situ oceanographic data traditionally has been gathered from crewed vessels [37], Autonomous Surface Vehicles (ASVs) are becoming an increasingly valid alternative or complement to a crewed vessel. An ASV relies on a computer controlled system and positioning from global navigation satellite system (GNSS), rather than a human operator that is susceptible to fatigue and needs to be kept safe. This means the ASV can operate in areas and conditions that would be deemed too dangerous for a manned platform, while maintaining consistent performance over extended periods of time. Being restricted to the surface does limit the types of measurements that can be made in contrast to underwater platforms, but in return allows for constant access to both GNSS and long range communication with relatively high bandwidth.

Unmanned Underwater Vehicles (UUVs) consist of both tethered Remotely Operated Vehicles (ROVs) that are piloted manually from the surface and untethered Autonomous Underwater Vehicles (AUVs) that can operate independent of human

intervention. If the AUV is within an acoustic network or surfacing for e.g. position fix from GNSS, the AUV may also communicate high level mission commands with a supervisor. Additionally, some hybrid vehicles combine strategies from both ROVs and AUVs for increased flexibility [7]. AUVs have become a highly reliable platform for seafloor mapping over the past decades [61]. While ROVs have lower capability in spatial coverage compared to AUVs, the ROV umbilical allows real-time transfer of video data to the pilot, and the traditional video and sampling surveys using a manually operated ROV are often preferred for seafloor mapping in both research and industry. These video surveys can be compared to looking at a huge picture through a tiny little tube [53]. While it is possible to study any part in great detail, it is also easy to lose the overview of the larger area.

If the platform carrying out the survey is not systematically navigated and motion controlled, the dataset may contain gaps that may not be detected until the post-processing stage after the survey. Even if the survey is not intended to fully cover a certain area, but rather provide a representative sample of the area, the limited overview can generate misleading results. For example, during acquisition along a manually piloted video transect, the pilot-scientist team may be prone to focus on any interesting features encountered along the transect. While this may yield a highly interesting dataset, it may also result in an overabundance of Objects of Interest (OOI), and hence the dataset will not constitute a representative sample of the Area of Interest (AOI).

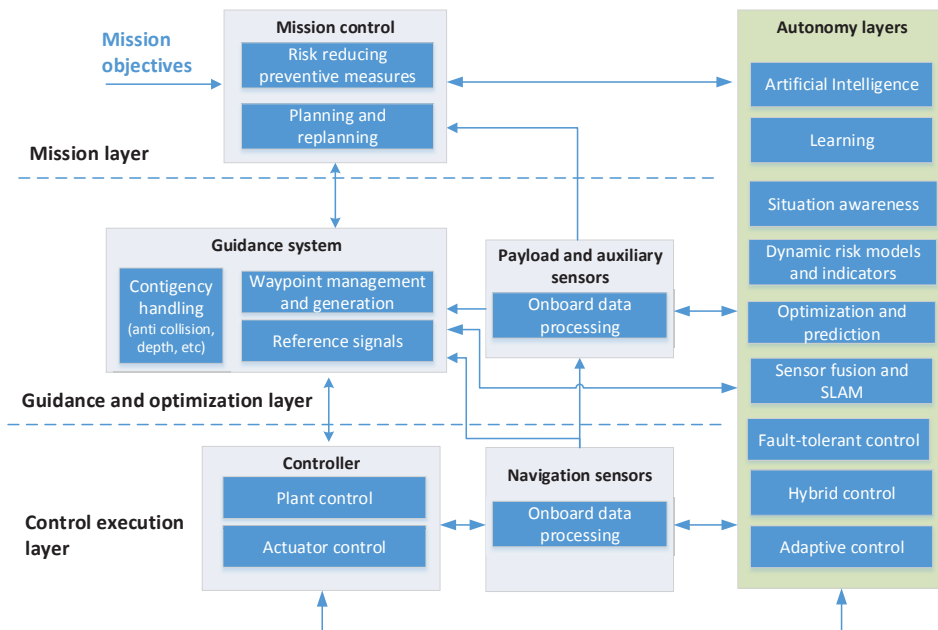


Figure 1.1: Autonomy framework as presented in [41]

Many of these issues are addressed in an autonomous system. However, there are many modules that are required to work in unison. Fig. 1.1 presents a framework for

an autonomous marine robotic platform introduced in [41]. This adopts a bottom-up approach to autonomy, where every improvement added to the lower levels increases the performance and capabilities of the higher levels and incrementally builds toward a higher degree of autonomy. The modules of the architecture are grouped into three main layers:

- The **Mission Layer**. Plans the mission based on the supplied mission objectives. Inputs from payload sensors and autonomy layers are used to evaluate the execution of the mission and replan if necessary.
- The **Guidance and Optimization Layer**. Handles waypoints and supplies the desired reference signals to the controllers. Analyses the payload sensor data that are able to be processed during the mission.
- The **Control Execution Layer**. Lower level plant control and actuator control is performed, and data from the navigation sensors is analyzed.

In times of growing awareness of climate changes, it is important to manage and make decisions regarding marine ecosystems based on knowledge. It is equally important to eliminate gaps in this knowledge, perhaps most so in the remote and as of yet inaccessible areas of the Arctic and Antarctic. If we are to cover these knowledge gaps in any reasonable amount of time, fully autonomous marine robotic platforms and automated post-processing procedures will be an integral part of the solution.

## 1.2 Research Questions and Methodology

This thesis is working towards fully autonomous marine robotic mapping systems and their application in the real world. Since this is a task that is far too large and comprehensive to tackle in a single PhD thesis, this main objective is broken down into smaller parts and limited to the following main research questions:

1. How can the quality of data collected by marine robotic platforms be improved through increased focus on proper positioning of payload sensors in space and time?
2. How can the data interpretation, both manually and automatically, be streamlined by improved mosaicing and georeferencing of the collected data.
3. How can the mapping and monitoring efficiency of marine robotic platforms be increased by autonomy to combat the undersampling of the oceans?

The research methodology includes theoretical analysis, numerical simulations and full-scale experiments. In order to address the research questions properly, they need to be examined both from the technological and the end-user perspective. This means the research relies on interdisciplinary collaboration, in particular between the fields of marine control systems, marine biology and marine archaeology. The needs of the different end users inspires the design of new technological approaches. Simulations are used to verify the behavior of experimental designs before full-scale experiments. Most of the simulations were conducted using the NTNU Verdandi Labview simulator developed in parallel with the NTNU ROV Control System [12, 16, 63]. Full-scale testing was performed on a variety of scientific cruises, primarily in the Trondheimsfjord from the NTNU-owned and operated R/V Gunnerus, but

also in the Arctic on the UiT R/V Helmer Hanssen and in the Pacific on the Geomar R/V Sonne.

### 1.3 List of Publications and Scientific Contributions

This thesis summarizes and complements a number of publications. Included in the thesis are three authored and six co-authored papers, of which four are journal papers/book chapters and five are conference papers. The papers are listed in the same order as they appear in part II, which is firstly according to topics and secondly according to publication order within the topics. Due to the interconnect- edness of the topics, the papers will in many cases span more than one topic. For the sake of structure they are grouped according to the topic that is the main focus of the paper. The scientific contribution of each paper is stated below the reference to the paper. Papers A-B are on ROV motion control and guidance, papers C-F are on ocean mapping, and papers G-I are on autonomy.

**A:** Conference paper

Stein M. Nornes, Martin Ludvigsen and Asgeir J. Sørensen. **Automatic Relative Motion Control and Photogrammetry Mapping on Steep Underwater Walls using ROV.** *MTS/IEEE OCEANS 2016*, Monterey, CA, USA, 19-22 September 2016.

Scientific contribution: A motion control strategy for automated visual mapping of steep underwater walls using an ROV is developed. The strategy utilizes a forward facing Doppler Velocity Logger (DVL) to provide relative velocity and distance measurements to the wall, enabling the vehicle to maintain a constant distance to the scene.

**B:** Peer-reviewed book chapter

Stein M. Nornes, Asgeir J. Sørensen and Martin Ludvigsen. **Motion Control of ROVs for Mapping of Steep Underwater Walls.** T.I. Fossen, K.Y. Pettersen, H. Nijmeijer editors, *Sensing and Control for Autonomous Vehicles*, Chapter 1.3, pages 51–69, Lecture Notes in Control and Information Sciences 474, Springer International Publishing AG, 2017.

Scientific contribution: The motion control strategy introduced in paper A is further generalized to allow for arbitrary vehicle and sensor orientations. The strategy also introduces the ability to autonomously adapt the vehicle/sensor orientation for optimal data collection.

**C:** Peer-reviewed conference paper

Stein M. Nornes, Martin Ludvigsen, Øyvind Ødegård and Asgeir J. Sørensen. **Underwater Photogrammetric Mapping of an Intact Standing Steel Wreck with ROV.** *4th IFAC Workshop on Navigation, Guidance and Control of Underwater Vehicles (NGCUV)*, IFAC-PapersOnLine, Volume 48 (2), pages 206-211. Girona, Spain, 28-30 April 2015.

Scientific contribution: An intact standing steel wreck with a complex 3D profile was mapped using stereo photography and processed into a complete

3D model, demonstrating how the emergence of commercially available photogrammetric software has reduced the required resources for creating high-resolution 3D-models of archaeological sites from photographs.

**D:** Conference paper

Martin Ludvigsen, Terje Thorsnes, Roy E. Hansen, Asgeir J. Sørensen, Geir Johnsen, Petter A. Lågstad, Øyvind Ødegård, Mauro Candeloro, Stein M. Nornes, and Christian Malmquist. **Underwater Vehicles for Environmental Management in Coastal Areas.** *MTS/IEEE OCEANS 2015*. Genova, Italy, 18-21 May 2015.

Scientific contribution: Based on the experimental work presented in this paper, a proposal for use of underwater vehicles in environmental management of coastal areas is described.

**E:** Peer-reviewed journal paper

Martin Ludvigsen, Jørgen Berge, Maxime Geoffroy, Jonathan H. Cohen, Pedro R. de la Torre, Stein M. Nornes, Hanumant Singh, Asgeir J. Sørensen, Malin Daase and Geir Johnsen. **Use of an Autonomous Surface Vehicle Reveals Small-Scale Diel Vertical Migrations of Zooplankton and Susceptibility to Light Pollution under Low Solar Irradiance.** *Science Advances*, Volume 4, no. 1, 10 January 2018.

Scientific contribution: An Autonomous Surface Vehicle is fitted with a hyperspectral irradiance sensor and an acoustic profiler to detect and quantify the behavior of zooplankton in an unpolluted light environment in the high Arctic polar night. Comparing the results with that from a light-polluted environment close to larger research vessels, this study underscores the need to adjust sampling platforms, particularly in dim-light conditions, to capture relevant physical and biological data for ecological studies.

**F:** Peer-reviewed journal paper

Ines Dumke, Stein M. Nornes, Autun Purser, Yann Marcon, Martin Ludvigsen, Steinar L. Ellefmo, Geir Johnsen and Fredrik Søreide. **First Hyperspectral Imaging Survey of the Deep Seafloor: High-Resolution Mapping of Manganese Nodules.** *Remote Sensing of Environment*, Volume 209, pages 19-30, 2018.

Scientific contribution: An Underwater Hyperspectral Imager (UHI) is mounted on an ROV and used to record the first hyperspectral image data from the deep seafloor (4200 m). Two classification methods are applied to the results, and are demonstrated to represent a promising tool for detection and mapping of mineral deposits in potential deep-sea mining areas.

**G:** Peer-reviewed book chapter

Øyvind Ødegård, Stein M. Nornes, Martin Ludvigsen, Thijs J. Maarleveld and Asgeir J. Sørensen. **Autonomy in Marine Archaeology.** *43rd Annual Conference on Computer Applications and Quantitative Methods In Archaeology (CAA)*, Siena, Italy, 30 March-3 April, 2015.

Scientific contribution: A strategy to implement archaeological mission objectives as input to the design of autonomous control systems for AUVs is proposed. By dividing the missions into tasks that the AUV can perform with behaviors within given parameters, the abstract goals are moved from the higher deliberative layer to the middle coordination layer and finally can be executed in the lowest control layer with commands and direct reactions to sensor data determining actions.

**H:** Conference paper

Trygve O. Fossum, Martin Ludvigsen, Stein M. Nornes, Ida Rist-Christensen and Lars Brusletto. **Autonomous Robotic Intervention using ROV: An Experimental Approach.** *MTS/IEEE OCEANS 2016*. Monterey, CA, USA, 19-22 September 2016.

Scientific contribution: A semi-autonomous agent architecture for robotic intervention with an ROV is proposed. The system was tested both in simulations and in field experiments. The ROV agent was able to execute an inspection type mission, navigating to the SOI from surface, while avoiding obstacles. This demonstrates the architectures feasibility in an environment similar to an operational situation.

**I:** Conference paper

Marco Leonardi, Annette Stahl, Michele Gazzea, Martin Ludvigsen, Ida Rist-Christensen and Stein M. Nornes. **Vision Based Obstacle Avoidance and Motion Tracking for Autonomous Behaviors in Underwater Vehicles.** *MTS/IEEE OCEANS 2017*. Aberdeen, UK, 19-22 June 2017.

Scientific contribution: The autonomy architecture introduced in paper H is expanded with an improved stereo vision system for obstacle avoidance. Results from laboratory research work and from field experiments demonstrate that underwater obstacle avoidance with stereo cameras is possible and can increase the autonomous capabilities of ROVs by providing appropriate information for navigation, path planning, safer missions and environment awareness.

The following papers are not included in the thesis:

Conference paper

Stein M. Nornes, Mauro Candloro, Øyvind Ødegård, Geir Johnsen and Asgeir J. Sørensen. **Photomosaic Camera as Simultaneous Data Collector and Navigation Aid on Unmanned Underwater Vehicles.** *Ocean Optics XXII*, Portland, ME, USA, 26-31 October 2014.

Peer-reviewed journal paper

Ines Dumke, Autun Purser, Yann Marcon, Stein M. Nornes, Geir Johnsen, Martin Ludvigsen and Fredrik Søreide. **Underwater Hyperspectral Imaging as an *In-situ* Taxonomical Tool for Deep-sea Megafauna.** Submitted to *Scientific Reports* 21 February 2018.

## 1.4 Thesis Structure and Outline

The first part of the thesis presents an overview of the research with background information that helps to fit the individual papers into the broader context of the autonomy framework in Fig. 1.1. The second part contains the papers. Fig. 1.2 illustrates how the different papers and topics are parts of the building blocks needed to build towards true autonomy, and this section elaborates on this.

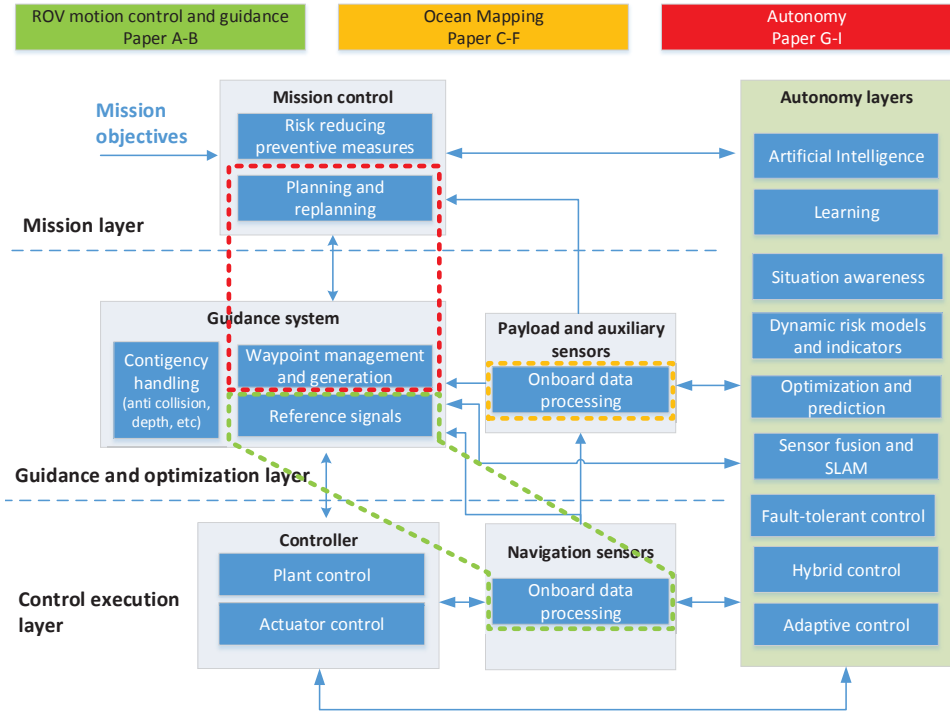


Figure 1.2: Overview of the papers in the thesis, and how they relate to the overall framework of autonomy.

### Part I

**Chapter 2** presents an overview of the marine robotic platforms that have been utilized in the papers, with focus on the strengths and limitations of each platform. Since the papers tend to focus on a confined part of the control system architecture, an introduction to the more overarching structure and common definitions is introduced here, using the NTNU ROV control system as an example.

**Chapter 3** gives an overview of some of the sensors used in the papers and discusses their applicability for different types of mapping. The main focus is on the use of underwater photogrammetry in the marine sciences and the necessary color

correction it requires.

**Chapter 4** introduces some basics of autonomy and elaborates on the autonomy framework presented in Fig. 1.1. The focus is on the bottom-up approach to autonomy, developing improved lower-level functions as a foundation building towards a fully autonomous system.

**Chapter 5** concludes the thesis and indicates the direction for future research.

**Appendix A** presents the specifications for the ROVs used in the thesis.

**Appendix B** presents some useful Python scripts for the photogrammetry procedure presented in Chapter 3.

## Part II

The papers contribute to different parts of a larger autonomous structure, and Fig. 1.2 indicates where the different topics fit into the larger picture.

**Papers A-B** present a DVL-based system for relative motion control of unmanned underwater vehicles. **Paper A** presents the initial development and verification of the validity of the system through experiments with a DVL mounted horizontally on an ROV. **Paper B** generalizes the motion control system to be valid for arbitrary orientations of the vehicle and sensor, and demonstrates the performance of the system in a larger biology survey. This low layer system contributes to improved measurements through better placement of the measuring instruments. In turn, this provides the higher layer systems with better foundation data for payload and decision making.

**Papers C-F** focus on the payload objectives of marine robotic platforms. **Paper C** presents the first implementation of the photogrammetry processing procedure in Section 3.3, as a proof-of-concept for archaeological applications. In **Paper D**, different underwater vehicles are applied for the purpose of environmental monitoring using a variety of sensors. **Paper E** employs an ASV in a biology survey to acquire unpolluted light measurements in the polar night paired with acoustic measurements of zooplankton migration. Finally, **Paper F** uses a UHI mounted on an ROV in a deep-sea geological survey of manganese nodules in potential mining areas.

**Papers G-I** approach the higher layers of the autonomy framework. **Paper G** explores the potential applications for autonomous vehicles in marine archaeology, and proposes a strategy design for an autonomous archaeological survey. **Paper H** and **I** present the gradual development of an autonomy layer for an ROV intended for autonomous robotic intervention.

## Chapter 2

# Marine Robotic Platforms

This chapter presents the main robotic platforms for ocean mapping, with focus on the platforms utilized in the papers in Part II. The NTNU ROV control system is presented and used as an example of a marine robotic guidance and control system for proper sensor positioning in time and space.

### 2.1 Platform Types

No single type of sensor platform is capable of covering all of the desired mapping and monitoring needs of the marine sciences and industries. The different demands for spatiotemporal resolution and coverage are simply too broad for this. On the spatial scale, biological studies of corals can require millimeter resolution or better, while ocean current measurements need to cover the entire globe. Likewise, on the temporal scale, animals may move in a matter of seconds, while the world's climate must be recorded over decades or centuries to fully comprehend its behavior. As a result, the selection of which platform(s) to use for mapping and monitoring must be tailored to the specific needs of each mission. Fig. 2.1 presents the spatiotemporal capabilities in terms of order of magnitude for the most relevant marine platforms for ocean mapping.

Remote sensing platforms like satellites are excellent for large coverage both in terms of time and space. This does however come at the expense of spatial resolution due to the altitude and temporal resolution due to a limited number of passes per day. Measurements are also limited to the ocean surface.

For closer range remote sensing, Unmanned Aerial Vehicles (UAV) are becoming an increasingly valid option [68]. While the sensor payload and flight time may be limited, the platforms are able to cover large areas with high resolution. In a network of marine robotic platforms, UAVs also show potential as a communication hub between sensor platforms [32].

Crewed vessels still remain the main in-situ data collector. They can stay at sea for considerable periods of time with a very large sensor payload, including smaller deployable robotic platforms. Limited mainly by the crew, supplies and fuel, the primary drawback of the crewed vessel is the large operating cost. As the capabilities of marine robotic platforms increases, the role of manned ships

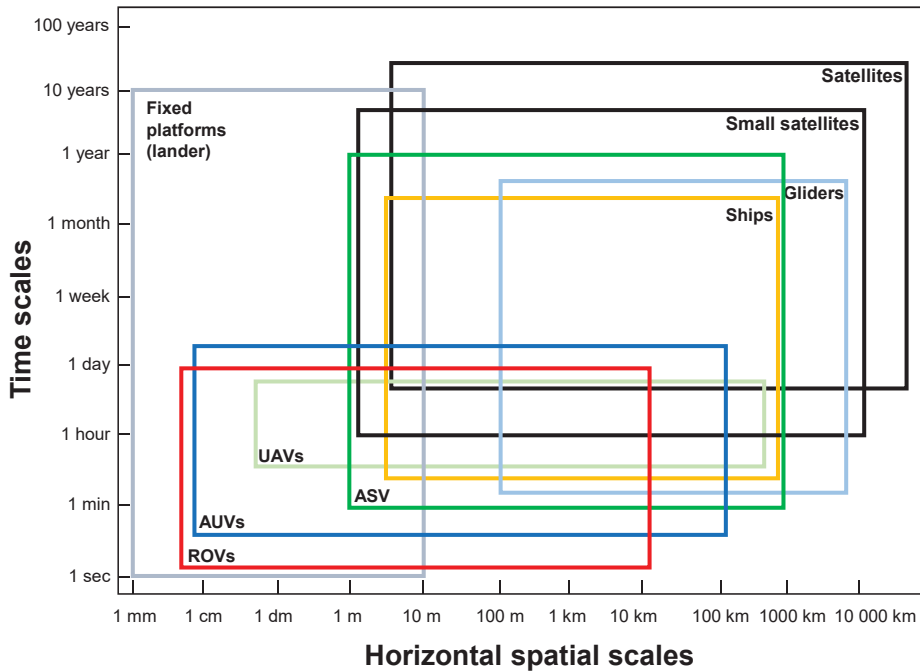


Figure 2.1: Spatial and temporal platform capabilities. The lower end of the axis represents resolution, while the upper end represents maximum coverage. ROV=Remotely Operated Vehicle, AUV=Autonomous Underwater Vehicle, ASV=Autonomous Surface Vehicle, UAV=Unmanned Aerial Vehicle [48].

gradually transition from primary sensor platform to more of a control center for an array of smaller robotic sensor platforms.

Landers, moorings and ocean observatories are stationary platforms that can facilitate continuous measurements with high temporal resolution over long time periods. Naturally, the fixed position results in the spatial coverage being limited to the range of the payload sensors.

Gliders are a special subcategory of AUVs, relying on buoyancy control and hydrodynamic shape for propulsion, rather than thrusters. This makes them very energy efficient and able to perform measurements over extended periods of time and considerable distances. It also gives the platform considerably lower control of its small scale movement, making them more suitable for large scale oceanographic measurements than for instance benthic mapping.

### 2.1.1 Autonomous Surface Vehicle

Development and refinement of ASVs have been the subject of much research over the past decade. Commercial vehicles are available in many shapes and sizes [4, 42]. The most common vehicles are gasoline powered vessels in the 15-30 foot

- 
- |  |   |
|--|---|
| <ul style="list-style-type: none"> <li>+ Unique 2D mapping capabilities</li> <li>+ Can operate well in shallow water</li> <li>+ High survey area coverage per time</li> <li>+ High spatial resolution data for large area providing detailed seafloor and water column mapping</li> <li>+ Less dependent on ship during operation</li> <li>+ Sensors: Wide payload capacity</li> <li>+ Perfect to aid AUV operations by serving as communication hub.</li> </ul> | <ul style="list-style-type: none"> <li>– Risk of operation – loss of data and vehicle</li> <li>– Weather window: Operation of ASV is sensitive to waves and current giving reduced availability</li> <li>– Vehicle motion can reduce data quality</li> <li>– Today: Relies on competent personnel for operation, troubleshooting. Autonomy may be improved</li> <li>– Possible limitations in operation due to ship traffic and risk for collision</li> </ul> |
|--|---|

Table 2.1: Pros and cons of ASVs

range [37]. With a wide speed range, these vessels are able to cover large distances, but also perform detailed high resolution measurements if the mission requires this. Smaller ASVs are also available, with very shallow drafts allowing the vessel to operate in shallow water areas that can not be reached with larger vessels. Energy-harvesting ASVs like wave gliders or solar powered vessels can perform long endurance missions of up to a year, though with some restrictions on top speed, mission complexity and payload capacity.

Table 2.1 summarizes some of the strengths and weaknesses of ASVs. Since an ASV operates on the surface, it generally has access to both GPS signals and long range communication. This makes the ASV less dependent on a mothership than AUVs, and also a prime candidate to aid in AUV operations as a navigation aid and communication hub [35, 62]. At the same time, being on the surface restricts the types of measurements that can be made, while also exposing the platform to waves, wind, currents and ship traffic.

The current lack of guidelines and legal framework for the handling of autonomous vessels in ship traffic is one of the main challenges for ASVs [59]. Fortunately, due to the potential that unmanned vessels represent for the transport and shipping industry, authorities are recognizing the need for regulations and are establishing test areas for autonomous ships. The world’s first test area for autonomous ships was established in the Trondheimsfjord in 2016 [40], and more test areas have been opened in both Norway, Finland and China [58]. Another important concern for long-term deployments is the reliability of the on-board mechanical and electronic systems. Without a crew to perform maintenance and repairs of critical components, the system needs to be highly reliable with redundancies preventing the loss of important data, or in the worst case the entire vessel.

As research continues, the capabilities of ASVs should be expected to significantly increase. Increased levels of autonomy combined with wind, wave and solar power can significantly increase mission duration and task complexity. With a high enough level of autonomy, ASVs may also be able to take on tasks currently covered by crewed vessels, for instance as the mothership of a fleet of AUVs.



Figure 2.2: NTNU JetYak ASV

The ASV used in Paper E is the NTNU Jetyak, shown in Fig. 2.2, an ASV developed by the Woods Hole Oceanographic Institution [37]. Based on a commercially available Mokai rotomolded polyethylene jet-powered kayak, the Jetyak is a low cost platform capable of operating in waters that are too shallow or dangerous for conventional manned surface vessels. Through the addition of an on-board computer and servos, the Jetyak can either be remotely controlled using a handheld radio transmitter, or be programmed to follow a series of predefined trajectories defined by latitude/longitude waypoints. A sea chest modification of the hull allows payload instruments to be mounted both under and on top of the vehicle. In Paper E, the platform was equipped with a downward looking Acoustic Doppler Fish Profiler (AZFP, Sec. 3.1.4) and an upward looking hyperspectral irradiance sensor (Sec. 3.1.3).

### 2.1.2 Remotely Operated Vehicle

For a long time, the ROV has been the default mobile underwater platform, both for research and industry. Table 2.2 summarizes some of the strengths and weaknesses of ROVs. They are deployed from a mothership with an umbilical cable

- 
- |  |   |
|--|---|
| <ul style="list-style-type: none"> <li>+ Sensors: high payload capacity</li> <li>+ High-resolution data for targeted area providing detailed seafloor mapping and sampling</li> <li>+ Umbilical gives unlimited electrical power and high bandwidth communication</li> <li>+ Manipulator arms for sampling and intervention</li> <li>+ Collection units (water masses and seafloor)</li> </ul> | <ul style="list-style-type: none"> <li>– Limited spatial range: usually <math>\leq 1</math>km transects lines. Spatial coverage/area usually lower than <math>\leq 1000</math> m<sup>2</sup></li> <li>– Umbilical limits spatial coverage and is exposed to current loads/drag forces</li> <li>– Expensive operation due to day rates of ships with DP systems and launch and recovery systems</li> <li>– Costly ROV operation involving pilots, technicians and supervisors. Possible to increase efficiency by improved automation/control and autonomy.</li> <li>– Weather window: Operation of ROV is sensitive to waves and current giving reduced availability</li> </ul> |
|--|---|

Table 2.2: Pros and cons of ROVs

providing near unlimited power and communication bandwidth, and this umbilical often represents both the greatest strength and the greatest weakness of the platform. The power and communication capabilities allow for a high sensor payload capacity with real-time data display to the operator and direct human interaction with the environment. At the same time, the umbilical severely limits the operating range of the ROV and makes it fully dependent on the mothership. The cable is exposed to significant loads and drag forces, in particular in environments with significant currents and waves. The dependence on the mothership results in high costs for operations, and given the limited spatial coverage, ROVs are better suited for detailed studies in defined areas than exploration missions. At the same time, they are an important test platform for experimental autonomy algorithms, since scientists can observe and evaluate the platform behavior in real-time.

The three different ROVs utilized in the papers are displayed in Fig. 2.3. ROV Minerva and ROV 30K are the two (light) workclass ROVs manufactured by Sperre AS and operated by the Applied Underwater Robotics Laboratory (AUR-Lab) at NTNU (Trondheim, Norway). Their depth rating of 700 m and 1000 m, respectively, enables full coverage of the seafloor of the Trondheimsfjord, Norway. They are usually deployed from the NTNU research vessel (RV) Gunnerus, and they are powered from and communicate with the surface vessel through an umbilical. All systems needed for operation such as power supply, navigation computers and monitors are fitted inside a control container. The motion control system is developed continuously expanded at NTNU. This system includes a DVL-based distance estimator and controller developed in [16] and Paper B, which allows the vehicle to maintain a constant distance to an arbitrarily oriented surface (see Section 2.3). ROV Minerva was used in Papers C and D, while ROV 30K was used in Papers

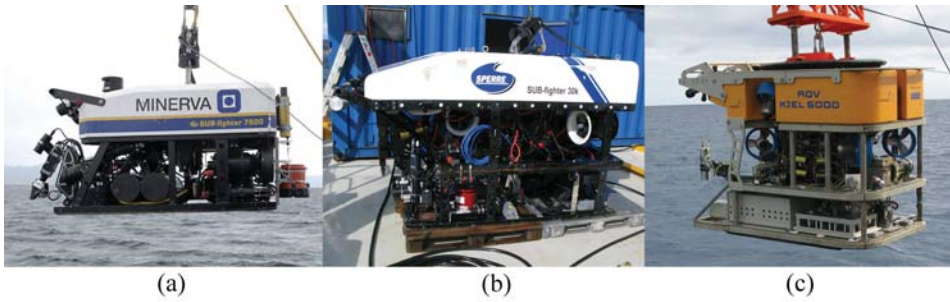


Figure 2.3: Three examples of ROVs: (a) Minerva (NTNU), (b) 30K (NTNU), (c) KIEL 6000 (GEOMAR)

A, B, D, H and I.

ROV KIEL 6000 is a work class vehicle manufactured by Schilling Robotics and operated by GEOMAR Helmholtz Centre for Ocean Research Kiel (Kiel, Germany). With a depth rating of 6000 m, the ROV is capable of reaching more than 90% of the seafloor. For the survey in Section 3.5.3 and Paper F, the ROV was deployed from the RV Sonne during cruise SO242-2 [6]. The vehicle motion is controlled using Schilling's 'Remote System Engine' RSE<sup>TM</sup>, and the primary payload sensor in this thesis was a UHI, described in more detail in Section 3.1.2

Further details on the ROVs are given in Appendix A.



Figure 2.4: Hugin AUV being deployed from RV Gunnerus

- 
- |  |  |
|--|--|
| <ul style="list-style-type: none"> <li>+ Unique 3D (longitude, latitude and depth) mapping capabilities</li> <li>+ High survey area coverage per time</li> <li>+ High spatial resolution data for large area providing detailed seafloor and water column mapping</li> <li>+ Avoid dependence on umbilical</li> <li>+ Less dependent on ship during operation</li> <li>+ Sensors: Wide payload capacity (less capacity compared to ROV).</li> <li>+ Potential to take advantage of autonomy for planning – re-planning handling of unexpected events for a smarter and more efficient operation</li> </ul> | <ul style="list-style-type: none"> <li>– Risk of operation – loss of data and vehicle</li> <li>– Weather window: Launch and recovery of AUV is sensitive to waves and current giving reduced availability</li> <li>– Limited power supply and energy storage capacity on-board</li> <li>– Limited navigation quality unless supported by a ship or seafloor infrastructure.</li> <li>– Today: Need for competence on personnel for launch and recovery, planning of operation, troubleshooting during different operational scenarios. Autonomy may be improved</li> <li>– Possible limitations in operation due to ship traffic and risk for collision</li> </ul> |
|--|--|

Table 2.3: Pros and cons of AUVs

### 2.1.3 Autonomous Underwater Vehicle

Survey AUVs are typically designed to be hydrodynamically streamlined and highly maneuverable, allowing them to cover large areas efficiently. Table 2.3 summarizes the strengths and weaknesses of AUVs. While some AUVs such as the Girona 500 are adding hovering and intervention capabilities, most AUVs are still limited to collecting sensor data to generate detailed maps of the water column and seafloor [54]. The lack of an umbilical makes an AUV less dependent on a mothership than an ROV, and the reduced drag allows for higher speeds and more efficient mapping. However, the corresponding drawback is that the AUV is limited to its on-board power supply, and communication is restricted acoustics with low bandwidth. Additionally, if high-precision positioning is important, the AUV will require position updates from either a surface vessel or seafloor installations. Research efforts are being made in terrain and feature-based navigation [1] and Simultaneous Localization and Mapping (SLaM) [17, 33] to reduce the dependence on external position updates, while concurrent ASV research is working to provide position updates from an unmanned vessel following the AUV [35, 49, 62].

In Paper D, the AUV Hugin HUS was deployed from RV Gunnerus (see Fig. 2.4). The AUV is operated by the Norwegian Defence Research Establishment (FFI), and with an operational time of 15 to 25 hours and a speed of 2-6 kn, it is

a highly efficient tool for underwater exploration. The Inertial Navigation System (INS), developed by a collaboration between FFI and Kongsberg Maritime [31], is aided by a DVL and acoustic Ultra-Short BaseLine (USBL) position updates from RV Gunnerus. For the operation in the Trondheimsfjord, the AUV was equipped with an optical camera and a Synthetic Aperture Sonar (see Section 3.1.5).

## 2.2 Control System Architecture

Since the majority of the work in this thesis has been related to ROVs, this section will specifically focus on the control system architecture of the NTNU ROV control system. Nevertheless, a similar architecture can also be applied to other marine robotic platforms.

The architecture of the ROV motion control system is shown in Fig. 2.5. The signal processing module receives all of the navigation measurements from the ROV and ship sensors and converts them to a common reference frame with timestamps. The validity of the measurements are checked in order to detect sensors with high variance, sensor freeze or dropout, and reject outliers and bad readings. Depending on the measurement type and quality, some filtering may also be applied.

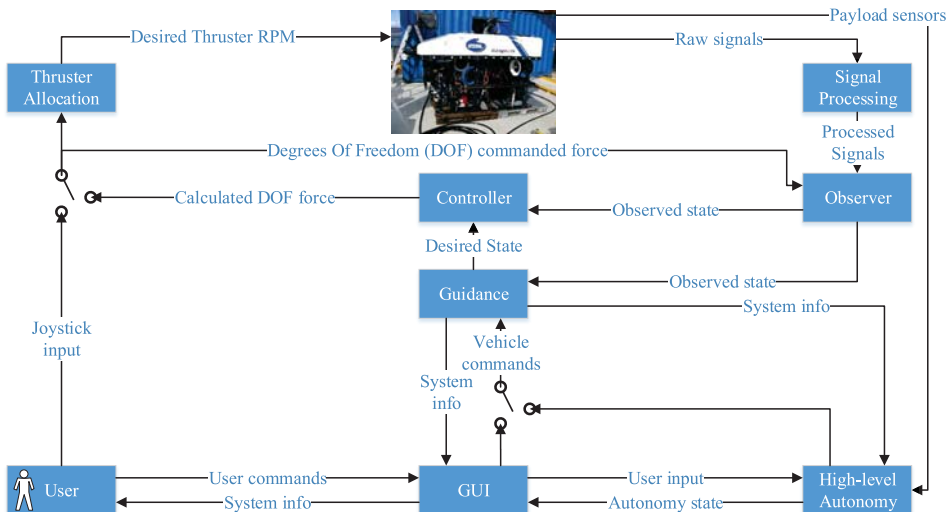


Figure 2.5: The ROV motion control system architecture. The user can either control the vehicle manually using the joystick, automatically using waypoints in the Graphical User Interface (GUI), or autonomously using inputs to the High-level Autonomy module.

The observer uses the processed measurements, the commanded thrust and models of the vehicle dynamics to provide smooth and accurate position and velocity state estimates. Some observers are also specifically developed to estimate the distance to the seafloor, more on this in Section 2.3. Even if the sensors have slow update rates, large noise and/or periods of time without measurements, the

observer must still be able to provide state estimates with sufficient accuracy and update rate required to control the vehicle dynamics [15]. These estimates can be acquired by using the concept of a corrector (deviation between estimated and measured state multiplied by an observer gain) and a predictor (using a mathematical model).

The guidance module generates the desired states for the system based on navigation waypoints received from either the user via the Graphical User Interface (GUI) or from an autonomy module. Guidance laws or reference models that consider the dynamic limitations of the vehicle are used to produce feasible and smooth desired trajectories for the vehicle to follow. A feedback from the observer ensures that the desired trajectories can be recalculated to maintain feasibility if the vehicle is not able to follow the original trajectory.

The controller computes the necessary forces in the Degrees Of Freedom (DOF) of the vehicle to follow the desired trajectory from the guidance module. These force outputs are calculated from the desired and estimated states.

The thruster allocation module translates the DOF forces from the controller to the rotation speed setpoints for each of the vehicles individual thrusters. Lower level controllers on the vehicle itself controls the actual rotation speeds of the thrusters and adjust them to the setpoints.

The user can control the system on three levels. Using a joystick to manually control the DOF forces of the thruster is the most direct control. The next level is via the GUI by setting waypoints that define a desired trajectory pattern, often a standard lawnmower pattern. Finally, the user interaction can be minimized by defining a broader mission that is given to an autonomy module. Using the control system input together with data collected from the payload sensors, this module plans a pattern of waypoints to achieve the mission criteria and replans if the input data indicates this is necessary (see also Section 3.6 or Paper H).

## 2.3 Relative Motion Control and Guidance

To properly map and monitor the ocean, scientists need an abundance of good measurements from the correct points in space and time. The control objective of a marine robotic platform therefore becomes “to efficiently position the desired payload sensor at the desired point in space and time”. Oceanographic measurements such as temperature, salinity and water quality are acquired directly where the platform is located, and often has limited demands for navigation accuracy. For remote sensing such as optical and acoustic imagery, the data is collected without making physical contact with the AOI, and there will typically be an ideal distance and direction from which the best possible measurement can be acquired. As is presented in Section 3.2, this is particularly true for optical imagery. To approach the ideal distance and direction, the marine platform needs a strategy for quality motion control that is defined relative to the AOI. In order to achieve the necessary quantity of measurements, this strategy must also be efficient.

The most common form of relative motion control is underwater vehicles maintaining a constant altitude above the seafloor, an important component in both visual and acoustic surveys of the seafloor. A bottom-following approaches based

on single altimeters and depth control are commonly implemented on many ROVs. A secondary altimeter was added in [11], one at the front and one at the rear of the Romeo ROV, in order to estimate the incline of the seafloor in the surge direction of the vehicle. Instead of dedicated altimeters, [16] relied on the four altitude measurements received from the DVL. This addition of two extra measurements allowed the incline of the seafloor to be estimated in both North and East coordinates following the surge and sway motions of the ROV.

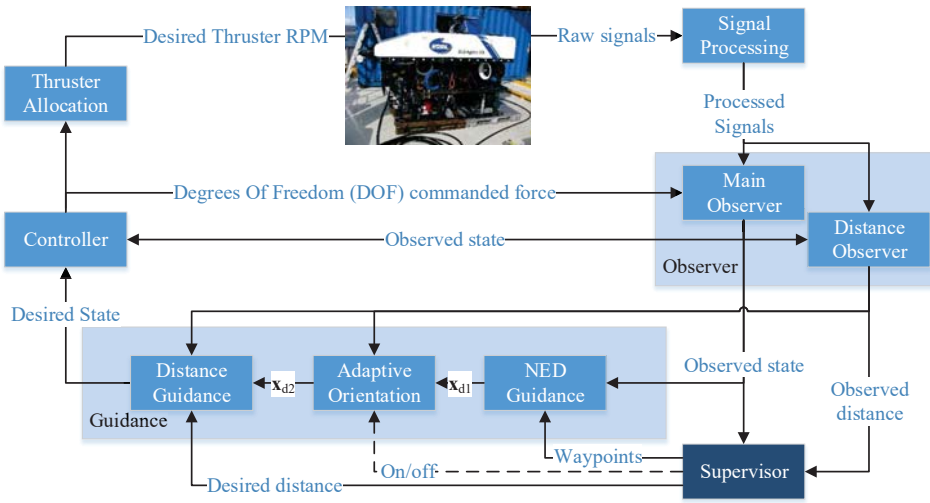


Figure 2.6: Expanded view of the ROV motion control system architecture focusing on the relative motion control system.

In Papers A and B, the vertical altitude controller from [16] is generalized to offer distance control in an arbitrary direction using a DVL tilted towards the AOI. Operating underwater vehicles close to high rock walls or other vertical environments often pose navigational challenges when limited to a DVL pointing downwards, and these locations are also prone to acoustical multi-path for position references. Simultaneously, such locations represent important of research and operation for a multitude of end-users within e.g. the marine science and oil and gas industry.

Fig. 2.6 shows an expanded view of the ROV control system architecture from Fig. 2.5, focusing on the relative motion control modules. The distance observer block uses the 4 range measurements from the DVL to compute a flat plane that is a least squares approximation of the seafloor at the measured location. After passing this through a Kalman filter, the resulting estimate of the distance to the seafloor and the seafloor gradient (rate of change) is sent to the supervisor and guidance modules.

The Supervisor provides the primary NED Guidance module with desired waypoints in North-East-Down (NED) coordinates, typically in a lawnmower pattern. The resulting smooth trajectory vector  $\mathbf{x}_{d1}$  is passed on to the adaptive orientation module, which is able to adjust the orientation of the platform to better match the

estimated gradient of the seafloor with the modified trajectory vector  $\mathbf{x}_{d2}$ . Finally, the distance guidance modifies the desired trajectory such that the resulting desired state (in NED coordinates) maintains the desired distance to the seafloor in the sensor direction. Paper B discusses the relative motion control system in further detail, while the example survey in Section 3.5.2 demonstrates both the quality and efficiency of the strategy.



## Chapter 3

# Ocean Mapping

This chapter presents the main optical and acoustic ocean mapping sensors and optical correction methods utilized in the papers in Part II. The main focus is on optical mapping of the seafloor, giving an overview of the color correction techniques and photogrammetry procedures employed in the papers. The results of papers B, C and F are expanded upon to demonstrate the different color correction techniques and the application of photogrammetry in different fields of marine science.

### 3.1 Mapping Sensors

A wide variety of in-situ and remote sensors are available for marine robotic platforms. The papers in Part II have focused primarily on remote sensors as the payload mapping sensors. This section presents the main optical and acoustic payload sensors used in the papers.

#### 3.1.1 RGB cameras

Regular optical RGB cameras are one of the most common sensors mounted on marine robotic platforms. They remain an important close range navigation sensor for manually piloted vehicles, but are also an important payload sensor. As seen in Papers H and I, they are now becoming important navigation sensors for autonomous platforms as well. One of the major drawbacks of optical mapping underwater is the limited distance range, requiring powerful illumination, good close range navigation and cameras with high light sensitivity.

The NTNU ROVs were equipped with a stereo camera rig, shown in Fig. 3.1. This rig features two Allied Vision GC1380C cameras [3] mounted in parallel with adjustable inter-axial distance. The cameras have a resolution of 1360x1024 pixels and are capable of recording at 20 frames per second (fps). Their high light sensitivity and signal to noise ratio make them suitable for underwater operation. The reduced resolution, combined with keeping the recording at 0.5 fps to reduce the number of redundant images, keeps the amount of data at a manageable level for

the post-processing stage. The lighting for the images was provided by two 400W HMI lamps mounted on the horizontal top bar at the front of the ROV.



Figure 3.1: The NTNU stereo camera (1) rig with a horizontal DVL (2) mounted on ROV 30K

The video cameras used on the KIEL 6000 were an ALPHA+ HD-camera from SubC Imaging and two OE14-366 MKII SD-cameras from Kongsberg Maritime, seen in Fig. 3.2.

#### 3.1.2 Underwater Hyperspectral Imager (UHI)

The Underwater Hyperspectral Imager is an optical sensor able to record/perceive the complete light spectrum from 350 nm to 850 nm. With a spectral resolution of up to 0.5 nm, it is possible to record the unique optical signatures of different materials or objects. This will allow algorithms to discriminate between materials, and assess (even possibly classify) features in situ and in near-real-time. Such non-invasive classification may prove useful for both archaeology, biology, geology and industry.

While the UHI provides a large quantity of useful data for analysis, classification and increased autonomy, it is also a very demanding in terms of quality of navigation and control. The UHI operates as a push-broom scanner, recording lines of  $1600 \times 1$  pixels while moving at constant speed over the area to be mapped, see Fig. 3.3. As a result, this mapping technique requires highly accurate navigation

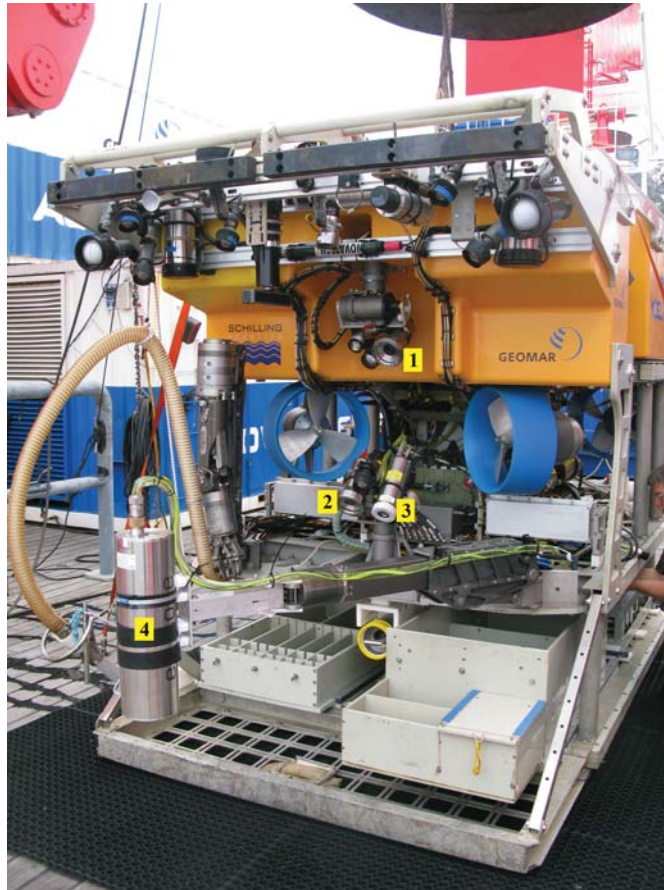


Figure 3.2: The camera setup of ROV Kiel 6000: Upper Pan & Tilt Unit with SD Camera (1), AQUOREA strobe and halogen light. Lower Pan & Tilt Unit with SD Camera (2), HD Camera (3) and halogen light. The Underwater Hyperspectral Imager (4) can be seen mounted on the extended manipulator arm.

data with high frequency in order to reconstruct a 2D mosaic of sufficient quality. Just like regular RGB imagery, the collected UHI data is also highly affected by the light travel distance in water. Uniformly illuminated and properly calibrated data is essential for the later analysis and classification of objects, and smooth and accurate control of the distance to the scene is necessary to achieve this.

Fig. 3.2 shows the Scientific Underwater Hyperspectral Imager (model UHI\_SCI.6000) from Ecotone A/S mounted on the manipulator arm of ROV Kiel 6000. This is the deep water model of the UHI, used in Section 3.5.3 and Paper F.

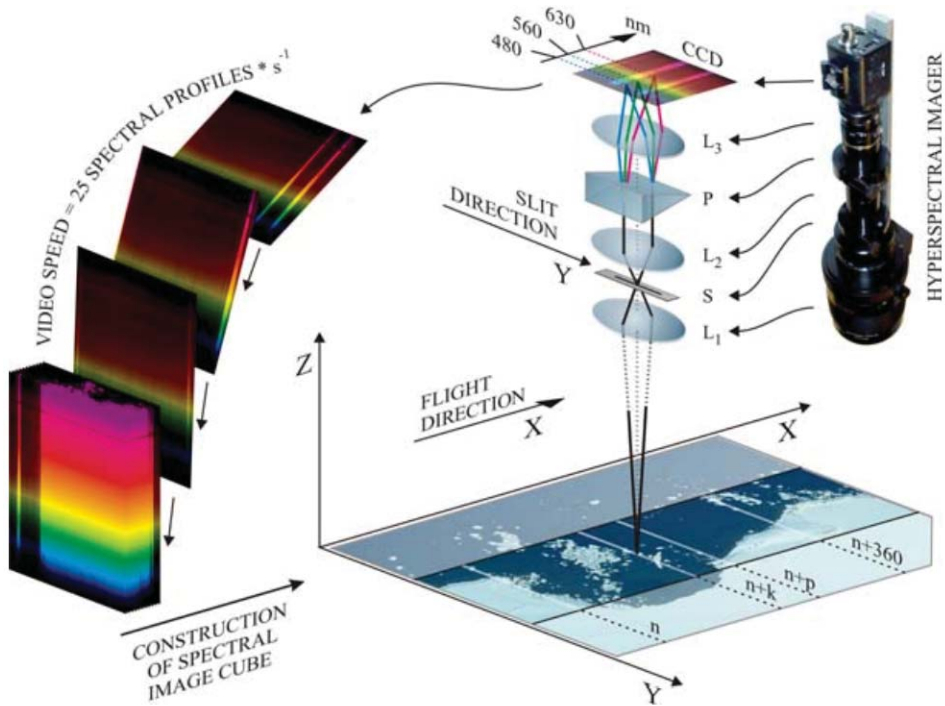


Figure 3.3: The operating principle of a hyperspectral camera [70].

### 3.1.3 Spectrometer

The QE Pro fiber optic spectrometer from Ocean Optics is a light sensor ideal for low light level applications. In Paper E, this sensor was set up to measure the diffuse sky spectral irradiance (the solar radiation reaching the Earth's surface). The spectrometer was mounted inside the Jetyak hull with an optical fiber leading out to a spectrally neutral reflectance standard plate facing upward collecting light. This allowed 99% of the diffuse skylight to be measured with 0.4 nm spectral resolution across the 350-730 nm range.

### 3.1.4 Acoustic Zooplankton and Fish Profiler (AZFP)

The AZFP is an advanced scientific echosounder designed to detect fish and zooplankton migration in the water column. By measuring acoustic backscatter returns at multiple ultrasonic frequencies (125, 200 and 455 kHz), the sensor is able to monitor the abundance of fish and zooplankton in the watercolumn at down to 11 mm vertical spatial resolution. In Paper E, the AZFP was mounted in the sea chest of the Jetyak looking downward. The sensor recorded acoustic backscatter with 1 m vertical resolution synchronously with the light measurements of the spectrometer in Section 3.1.3.

### 3.1.5 High resolution Interferometric Synthetic Aperture Sonar (HISAS)

The HISAS system is a Synthetic Aperture Sonar (SAS) system produced by Kongsberg Maritime [26]. By building a synthetic array of sensors using a moving platform equipped with a side facing sonar, the system is capable of producing acoustic images with much higher resolution than conventional SideScan Sonars (SSS). Also, while the resolution of regular SSS will typically decrease with increased range, the resolution of SAS imagery is range independent, allowing for resolutions of  $<5 \times 5$  cm over the full 200 m range of the sonar [39]. Depending on the bathymetry of the AOI, the HISAS system is able to cover up to  $730 \text{ m}^2/\text{s}$ , making it a highly efficient underwater mapping system. An example of SAS output data can be seen in Fig. 3.4.

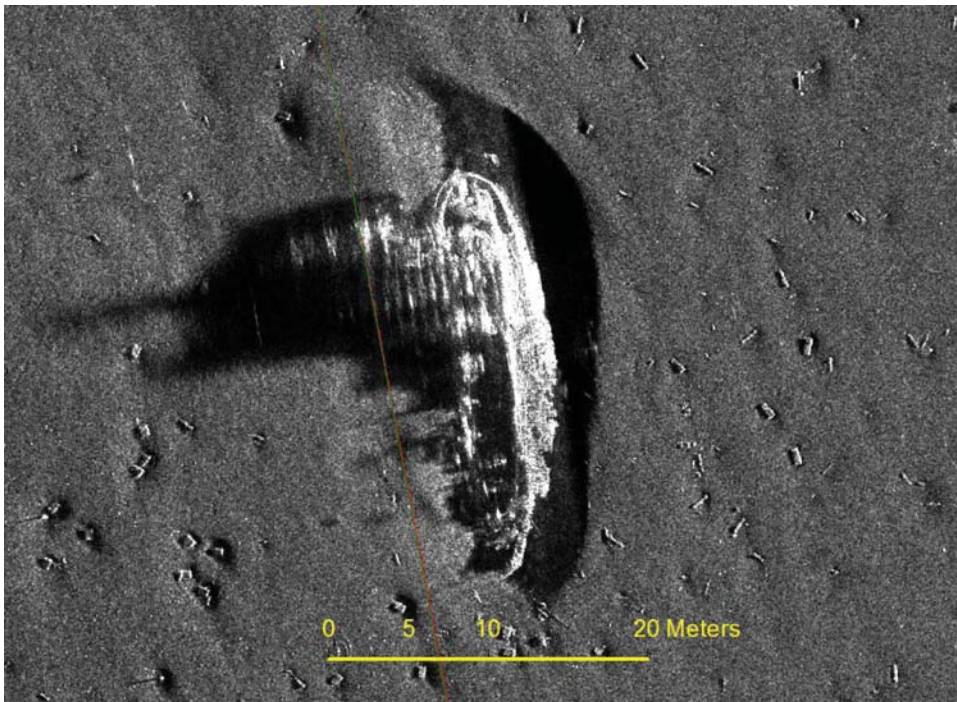


Figure 3.4: Ship wreck in SAS data from Paper D.

## 3.2 Underwater Image Color Correction

The quality of underwater images is heavily influenced by the light attenuation described by the Inherent Optical Properties (IOPs) of the water, in particular, absorption and scattering. IOPs characterize of the medium and depend on the concentrations of particulate and dissolved substances (phytoplankton, colored dissolved organic matter and total suspended matter), but not on the ambient light

field. That is, a volume of water has well defined absorption and scattering properties irrespective of the presence of light to be absorbed or scattered [45].

In addition to the IOPs of the water, the light attenuation depends on the optical pathlength, i.e., the distance the light travels through water. Fig. 3.5 illustrates how the topography of the scene causes variation in optical pathlength and hence light attenuation within a single image. Automated processing algorithms benefit from consistent and accurate color information, and therefore the images need to be color corrected first to counteract the effects of the water. Because a robotic survey can generate thousands of images, the color correction scheme also needs to be automated.

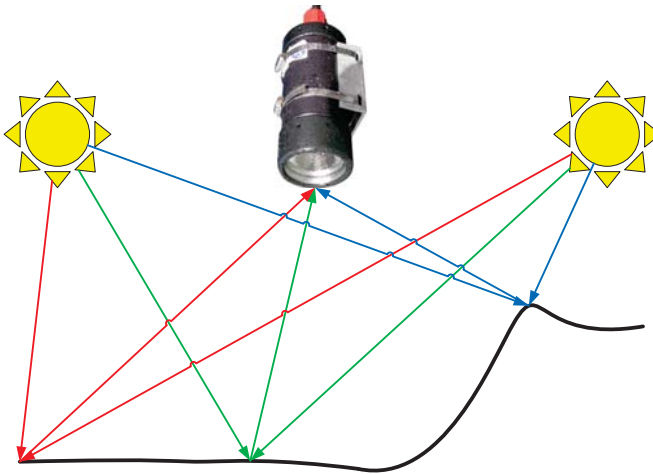


Figure 3.5: Illustration of the difference in travel distance for the light from lamp via the scene to the camera in a two lamp setup. The green lines represent a shorter combined distance than the red lines, leading to the vignetting effect characterized by a bright image center and dark image border. The blue lines cover an even shorter distance due to the vehicle being closer to the terrain, leading to higher illumination and potential overexposure that affects illumination evenness.

In this section, four different color correction techniques are presented and discussed in terms of implementation complexity, flexibility of use and quality of results. Fig. 3.6 demonstrates the different color correction techniques applied to an image from Stokkberneset, Norway (see Section 3.5.2). In the center of the image is a 1 m tall bubblegum coral (*Paragorgia arborea*), which appears brighter than the rest of the scene due to its closer proximity to the ROV camera and lights.

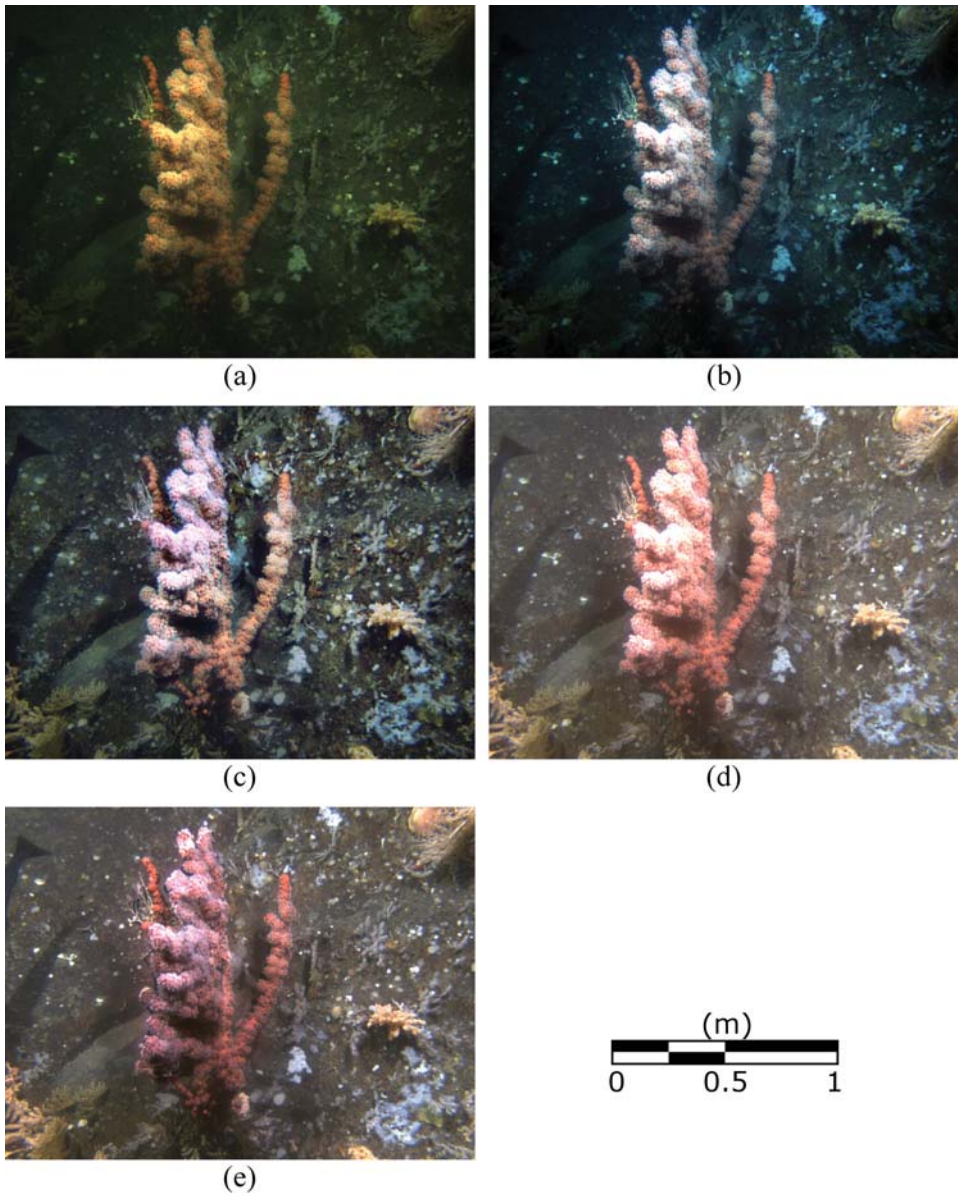


Figure 3.6: Image of bubblegum coral (*Paragorgia arborea*) demonstrating the difference between raw image and the four color correction techniques described in Section 3.2: (a) Raw image, (b) Histogram Equalization, (c) Contrast Limited Adaptive Histogram Equalization, (d) Gray-World, (e) Distance Adjusted Gray-World. The goal of the color correction is to obtain the natural color of the scene unaffected by light attenuation.

### 3.2.1 Histogram equalization (HE)

One of the simplest color correction techniques is the Histogram Equalization (HE). The histogram of an image describes the color tone distribution of the image by plotting the number of pixels for each color value. Processing each color channel separately, the algorithm stretches the histograms to get the largest possible range of color. In the image processing freeware GIMP 2.8, HE is implemented under the name "Auto white balance" [24]. Using a freeware batch plugin [23] for GIMP, this color correction can be applied automatically to the entire image set.

Because the top parts of the coral in Fig. 3.6a are very bright in the raw image, the rest of the HE-corrected image (Fig. 3.6b) becomes quite dark. The HE approach works better for images with less variation in optical path length, but will typically display the vignetting effect characterized by a brighter center and dark edges.

### 3.2.2 Contrast Limited Adaptive Histogram Equalization (CLAHE)

CLAHE was originally developed by [52] and [72] as a technique to improve low-contrast medical imaging, but is also highly useful for underwater images [21]. The technique improves the regular HE by dividing the image into blocks and running equalizations separately for each block. This approach is able to better account for varying distance/illumination, and thus reduces the vignetting effect (Fig. 3.6c). Imposing a limit on the contrast ensures that the algorithm does not excessively enhance noise in areas with little variation of color.

The CLAHE-algorithm is available in MATLAB through the function `adapthisteq`, but it may require some tuning of the block size and contrast limit to achieve satisfactory image quality. While the algorithm is flexible and easy to implement, it can lead to some halting and misrepresentation of the actual color [34].

### 3.2.3 Gray-World (GW)

The Gray-World (GW) transformation [10] operates on the assumption that the average of a large collection of images will be a uniform gray. For images taken in an underwater environment, this average will be heavily influenced by the IOPs of the water, the intensity and spectral characteristics of the lamps and the distance to the scene. By creating a transform that turns the average a uniform gray, we obtain a transform that can counteract the effects of the water for the individual images.

Each raw image  $x$  consists of an intensity value  $I_x(u, v, \lambda)$  for every row  $u$ , column  $v$  and color channel  $\lambda$ . The orthogonal distance from camera to scene for each pixel is denoted  $d = D_x(u, v)$ , where  $D_x$  is the depth map of the image (Fig. 3.7). If  $D_x \approx D \forall x$ , i.e., if the depth map is close to identical for the entire image set, the distance can be neglected and calculating the mean intensity  $\mu_x$  and variance  $\sigma_x^2$  of the raw images is straightforward. Otherwise, the more complex Distance Adjusted Gray-World (DAGW) approach (Section 3.2.4) is required. In

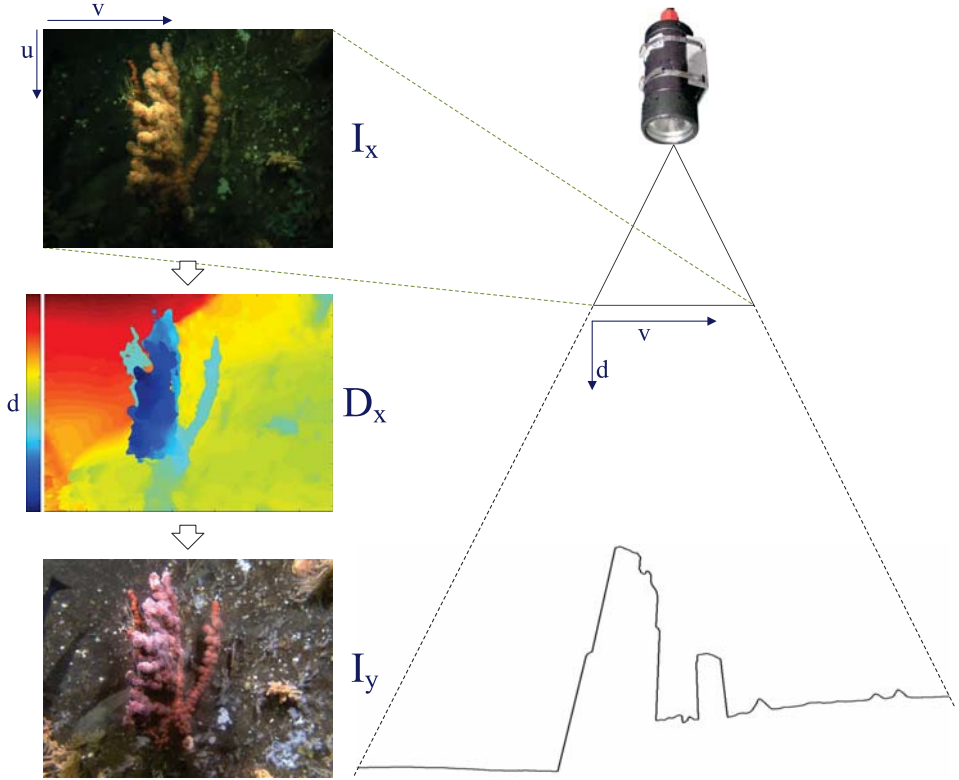


Figure 3.7: Illustration of the variables used in the Gray-World algorithms.  $u$  and  $v$  are the pixel positions in the image,  $d = D_x(u, v)$  is the orthogonal distance from the camera to the scene for the pixel at position  $[u, v]$ . The images on the left shows the flow from raw image  $I_x$  (top) through depth map  $D_x$  (middle) to the DAGW-corrected image  $I_y$  (bottom).

either case, the linear transform for each image is defined as

$$I_y(u, v, \lambda) = m(u, v, \lambda, d)I_x(u, v, \lambda) + n(u, v, \lambda, d) \quad (3.1)$$

where  $I_y$  is the intensity of the color corrected image  $y$ .

By selecting

$$m(u, v, \lambda, d) = \frac{\sigma_y(\lambda)}{\sigma_x(u, v, \lambda, d)} \quad (3.2)$$

$$n(u, v, \lambda, d) = \mu_y(\lambda) - m(u, v, \lambda, d)\mu_x(u, v, \lambda, d) \quad (3.3)$$

we are able to cancel out the effects of the lamps and water IOPs and produce an image with the desired mean intensity  $\mu_y$  and variance  $\sigma_y^2$ .

An alternate selection of

$$m_{alt}(u, v, \lambda, d) = \frac{\mu_y(\lambda)}{\mu_x(u, v, \lambda, d)}, n_{alt}(u, v, \lambda, d) = 0 \quad (3.4)$$

will also yield an image with the desired mean  $\mu_y$ , but no control over the variance. This can still be useful if the image set is too small to give a good estimate of the variance  $\sigma_x^2$ , or in order to save time on a preliminary onboard post-processing.

In order to function properly, this approach requires a relatively constant distance to the scene. The image set also needs to be both large enough and varied enough to get a proper estimate of  $\mu_x$  and  $\sigma_x$ . In Fig. 3.6d, the top parts of the coral clearly become overexposed due to the assumption of a constant distance across the image, indicating that GW is not the best color correction approach in this case.

### 3.2.4 Distance Adjusted Gray-World (DAGW)

Reference [8] introduced a new color correction technique (which we will refer to as Distance Adjusted Gray-world) that utilizes the same principles as the GW approach, but also takes into account variations in the depth map  $D_x$  from image to image (Fig. 3.7). A further developed version of this algorithm is presented in [9], requiring more detailed knowledge of the positioning, orientation and characteristics of the light sources. Since this background information was unavailable for the test cases in Section 3.5, this subsection will focus on the original algorithm from [8].

It is assumed that the intensity measured by the camera follows the camera model described by

$$I_x = A(u, v, \lambda)kC(u, v)R(\lambda)e^{b(\lambda)d} + c(u, v, \lambda) \quad (3.5)$$

where  $A$  and  $c$  are parameters in a linearized sensor response function,  $k$  is the exposure constant,  $C$  models the effect of the camera lens and lamps fixed to the vehicle,  $R$  is the surface reflectance and  $b$  is the light attenuation coefficient. If  $\mu_R$  is the mean reflectance of the surface, then the mean intensity measured by the camera is

$$\mu_x(u, v, \lambda, d) = \underbrace{A(u, v, \lambda)kC(u, v)\mu_R(\lambda)}_{a(u, v, \lambda)} e^{b(\lambda)d} + c(u, v, \lambda) \quad (3.6)$$

where  $a, b$  and  $c$  are parameters that can be estimated from the collected dataset using a nonlinear least squares solver like MATLABs `lsqcurvefit`.

The standard deviation of the measured intensity can be expressed as

$$\sigma_x(u, v, \lambda, d) = a(u, v, \lambda)e^{b(u, v, \lambda)d}\sigma_r(\lambda) \quad (3.7)$$

where  $\sigma_r = \sigma_R/\mu_R$  is the relative standard deviation of the surface reflectance while  $\sigma_R$  is the standard deviation of the surface reflectance.  $\sigma_r$  can be estimated using

$$\sigma_r^2(\lambda) = \frac{1}{nUV} \sum_{x, u, v \in S} \left( \frac{I_x(u, v, \lambda) - c(u, v, \lambda)}{a(u, v, \lambda)e^{b(u, v, \lambda)d}} - 1 \right)^2 \quad (3.8)$$

where  $n$  is the number of images in the dataset,  $[U, V]$  is the pixel resolution of the images, and

$$S = \{(x, u, v) : x \in [1, n], u \in [1, U], v \in [1, V]\} \quad (3.9)$$

#	Algorithm	Flexibility	Implementation Complexity	Quality
1	Histogram Equalization	Medium	None	Low
2	Contrast Limited Adaptive Histogram Equalization	High	Low	Medium
3	Gray-World	Low	Low	(High)
4	Distance Adjusted Gray-World	Medium	High	High

Table 3.1: Comparison of color correction algorithms to provide natural colors and enhance illumination evenness (see Section 3.2.#, #=1-4)

is the full set of pixels in the dataset.

When comparing the DAGW corrected image (Fig. 3.6e) with the GW corrected image (Fig. 3.6), the image color intensity is clearly more even when distance is taken into account with DAGW. It is important to be aware that a dataset that yields good results with the regular GW transformation, can give poor results with the DAGW approach. While the GW transformation requires a low variation in distance to the scene, the same lack of distance variation can be problematic when determining the parameters  $a$ ,  $b$  and  $c$  in (3.6).

### 3.2.5 Comparison of color correction algorithms

Each of the color correction algorithms presented in this section were tested in order to demonstrate the current range of quality and ease of use. A summary of this comparison is presented in Table 3.1.

The HE algorithm from Section 3.2.1 should only be viewed as a basic approach that does not require any implementation effort. While it will certainly be an improvement over working directly with raw images, comparing Fig. 3.9b to Fig. 3.9c clearly shows how much is gained by using the CLAHE algorithm from Section 3.2.2. Both coloring and intensity are more even when the CLAHE algorithm is used.

The GW algorithm from Section 3.2.3 gives a very even and high quality color correction, but only as long as the image depth maps remain near constant. This reduces its flexibility, though for datasets that fulfill the necessary assumptions, it has an excellent performance. When a dataset has minor variation in image depth maps, as seen in Fig 3.10, GW can still perform well enough to be a good choice for the color correction that precedes the aligning phase (Fig. 3.8). In Fig. 3.12b, a faint outline of the shadows from the ROV can still be detected (dark borders at the lower edge of the shadows and light borders at the upper edge of the shadows). These are caused by oscillations in the pitch motion of the ROV that induce variations in the depth maps, but have not been found to cause problems in the image aligning process. For datasets like the Herkules dataset in Section 3.5.1 with highly varied image depth maps, the algorithm fails.

The DAGW algorithm from Section 3.2.4 gives the best results in terms of evenness and quality for both the Herkules and Stokkberneset datasets (Figs.

3.9d, 3.10c). It was not applied to the Peru Basin dataset because the depth maps were near constant. Additionally, the improved navigation data was the primary end product for this dataset, so any extra color correction after the alignment was unnecessary.

The main drawbacks of the DAGW algorithm are the reliance on depth map input, implementation complexity and the computation time required for determining the parameters. In the color correction of the Herkules model, DAGW also resulted in amplification of image noise in frames with distant objects with low signal-to-noise ratio in the raw images, which gave parts of the initial model a red tint. In Fig. 3.9d, this was avoided by generating image masks based on the depth maps and instructing the software to only use the image parts that were closer than 4.7 m in the finished texture mosaic.

Low variation in distance can be problematic when determining the parameters  $a, b$  and  $c$  in (3.6) For instance, some initial tests on flat areas from Stokkbergneset yielded

$$a(u, v, \lambda)e^{b(u, v, \lambda)d} \approx 0 \implies \sigma_x(u, v, \lambda, d) \approx c(u, v, \lambda) \quad (3.10)$$

which leads to problems in (3.7) and (3.8). One potential way to deal with this is to assume that  $c$  is independent of water IOPs and lamp configuration, and can thus be obtained from other datasets using the same cameras. Since  $c$  is a constant in the sensor response function, this assumption seems reasonable. Alternatively, a smaller dataset could be recorded where the distance variation is increased specifically for determining the parameters.

Using a separate dataset to determine the DAGW parameters can also be appropriate in cases where the color of the scene is not evenly distributed with regards to elevation. An example would be an area with brightly colored corals rising up from a darker, flat seafloor. If data from this area is used to determine the DAGW parameters, the algorithm can overestimate the light attenuation coefficient  $b$ .

A potential addition that could reduce the need for a finished 3D model to generate depth maps for the DAGW algorithm would be to generate a simplified depth map based on altitude measurements from a DVL, similar to the approach presented in [34] and [61]. With precalculated parameters, this could allow for real-time color correction.

### 3.3 Photogrammetry Post-Processing Procedure

Once the entire area of interest has been sufficiently covered with still images, the photogrammetry processing can be initiated. Sufficiently covered typically means a minimum of 50% overlap between neighboring images, as every feature point needs to be present in at least two images in order to have its 3D position triangulated. An overview of the processing pipeline from captured 2D still images to finished 3D photogrammetry model is given in Fig. 3.8. The majority of the procedure is automated and can be run on an ordinary desktop computer or even a powerful laptop.

During the survey, online data (including images) from the ROV are collected using LabVIEW. Navigation data is post-processed (outlier removal, smoothing, etc.) and used to georeference the images using MATLAB. The images are color

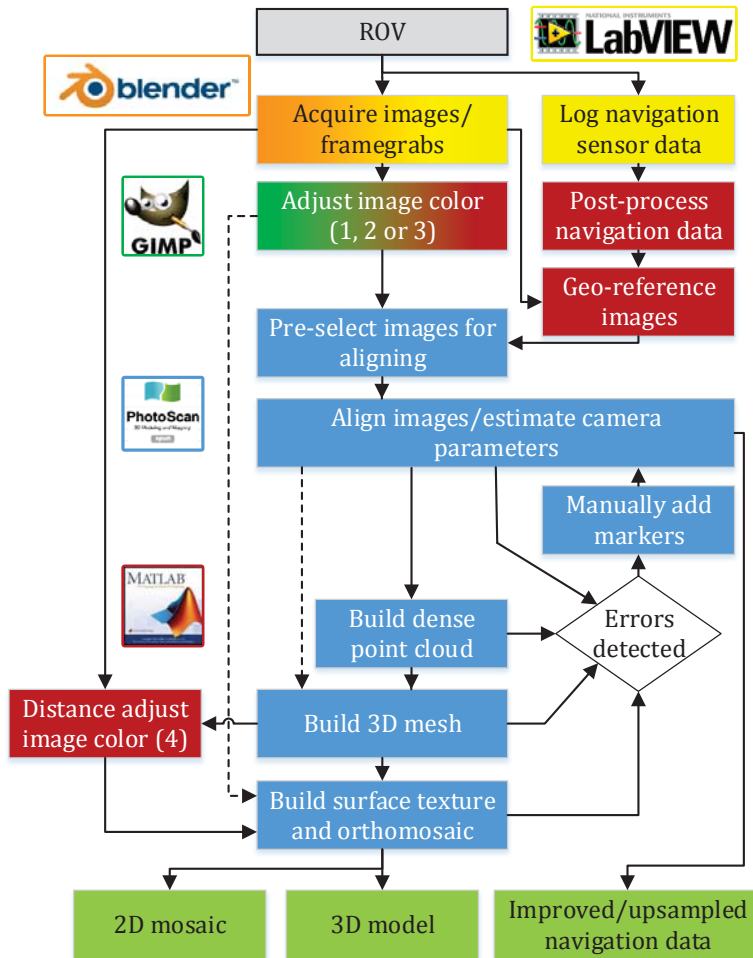


Figure 3.8: Flowchart of the processing chain to create mosaics or 3D models and to improve navigation data. The colors represent the software used for each step: Yellow=LabVIEW, orange=Blender, dark green=GIMP, red=MATLAB, blue=Photoscan. The dashed lines represent optional shortcuts that require less resources and time, which can be useful for on-site processing.

corrected using one of the algorithms in Section 3.2, where the appropriate algorithm selection is discussed in Section 3.2.5. The aligning of images and generation of the 3D-model is done using Agisoft Photoscan 1.2.

Georeferencing the images prior to alignment allows scaling and georeferencing of the final 3D model, and also greatly speeds up the processing since the software does not need to compare images that are too far apart to overlap. Aligning the images will produce a sparse point cloud. To obtain a higher quality model, the images will need to be reprocessed into a dense point cloud. This dense point

cloud is then used to generate a 3D mesh. Photoscan does not currently have a built in feature to export scaled depth maps for each image, but this can be accomplished by running a simple Python script in the built in “Run Script”-console (see Appendix B.1). These depth maps can then be used in the DAGW color correction before the images are projected onto the 3D mesh to create the finished 3D-model and/or a projected 2D orthomosaic. One of the possible uses for the 3D-model is to export it to the freeware Blender to create animations, using either a user defined camera path, or have the camera follow the vehicle track using the Python script in Appendix B.2 to import post-processed navigation data.

It should be noted that the dense cloud step and the calculation the parameters for the DAGW color correction are the most time- and memory-consuming steps in the processing chain. Therefore, in situations where time is more important than quality (such as on-site processing during a research cruise) both of these steps can be omitted to save time. Also, if there is little or no variation in distance to the scene (i.e., a flat seafloor) for the entire dataset, the benefit of using the DAGW correction over the GW correction is negligible and hence the faster GW correction should be applied instead.

## 3.4 Image-Aided Post-Processing of Navigation Data

In Section 3.3 we described the use of navigation data to speed up and improve the photogrammetry processing. The opposite approach of using photogrammetry to improve navigation data is also possible, as Photoscan is able to estimate its own positions and orientations based on the input navigation data and the supplied images.

While the procedure described in this section is an offline post-processing procedure based on commercially available software, methods for online processing of stereo imagery are a research topic of much interest. The process known as SLaM uses sensor data to build a map and at the same time uses this map to deduce the location of the sensor platform [17]. Systems relying on stereo imagery from an AUV and SLaM-based vehicle positions and orientations to deliver detailed 3D models of the seafloor have been shown to be robust [33].

Sensors that function as line scanners, such as multibeam echosounders, laser scanners and UHI pose high demands for both accuracy and sampling frequency of navigation data in their post-processing. The case in Section 3.5.3 is an example of a high-noise, low-frequency navigation dataset that initially does not meet the requirements for post-processing and georeferencing of UHI data (Paper F). However, the ROV HD video represents a high-frequency and high-resolution measurement that through the use of photogrammetry can be utilized to generate an improved, upsampled navigation data-set.

The processing pipeline for improving navigation data is shown in Fig. 3.8. Individual image frames are extracted from the video using Blender. The images are georeferenced using either a heavily filtered version of the position data, or a Dead Reckoning based approach to integrate DVL-measurements [22]. Alternatively, the images can be left unreferenced if instead a minimum of three georeferenced markers are added to the aligned model to provide scaling and georeferencing of the dataset.

The technique of using photogrammetry to improve navigation data is particularly useful for the georeferencing of image data such as UHI data, which require very high-resolution navigation data that may not always be provided by the survey platform used. Rather than upgrading the platform's navigation system to meet such demands, the photogrammetry-based approach represents a cost-effective alternative to obtain navigation data of sufficient quality and resolution. In this way, UHI surveys can also be carried out on platforms like the KIEL 6000 ROV, which was primarily designed for video and sampling surveys and not for carrying additional sensors requiring high-resolution navigation data.

The technique is also advantageous in deep-sea surveys, e.g. in the case in Section 3.5.3 with water depths of more than 4000 m. As the accuracy of standard USBL systems such as Posidonia is about 0.2% of the range, navigation data from deep-sea surveys may contain outliers and jumps of several meters or even tens of meters, which would consequently not allow accurate georeferencing of sensitive image data such as UHI data. As shown for the manganese nodule survey conducted in 4200 m water depth, the photogrammetry-based navigation data yielded a much improved geocorrected image (Fig. 3.13).

### **3.5 Photogrammetry Examples in the Marine Sciences**

This section expands on the results from three separate surveys described in some of the papers, showing some of the applications for the different marine sciences:

3.5.1 MS *Herkules*, a shipwreck with complex 3D structure (Paper C).

3.5.2 Stokkbergnaset, a vertical rock wall with many biological features (Paper B).

3.5.3 The Peru Basin, a deep ocean hyperspectral geological survey limited by navigation data with insufficient frequency and resolution for adequate processing of the hyperspectral data (Paper F).

#### **3.5.1 Archaeology: MS *Herkules***

The tugboat M/S *Herkules* sank on 16 September 1957, just outside Trondheim harbour, Norway [18]. Today the wreck rests on its keel at 60 m depth, reaching 10 m above the seafloor at its tallest. The bow creates an overhang as it is suspended over the seafloor, while the stern is buried in the sand (Fig. 3.9). The length of the visible section of the wreck is 20-25 m. Due to its low age the wreck remains quite intact, and while it does not hold particular archaeological significance in and of itself, it presents a useful training scenario for mapping of intact standing steel wrecks: Both the complex 3D structure, the high vertical profile and the entanglement risk posed by ropes and wires are common challenges for mapping and navigation that need to be resolved.

The wreck was surveyed using ROV *Minerva* in August 2014 in Paper C. The dataset consists of a total of 4715 images recorded with the stereo cameras over two sessions of approximately 40 minutes each. The images were captured at a pitch angle of 45° in order to map both horizontal and vertical surfaces.

As shown in Fig. 3.9a, the wreck presents a complex 3D structure that can be challenging to map. The ROV was piloted manually, further adding to varia-

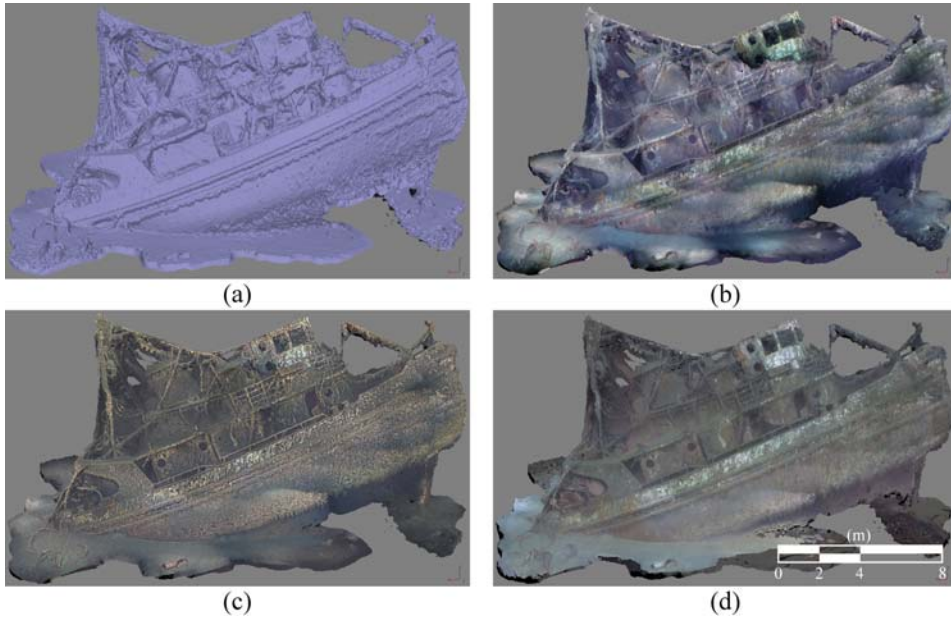


Figure 3.9: 3D model of MS Herkules, seen from the starboard side: (a) Shaded relief, (b) Textured with HE correction (Section 3.2.1), (c) Textured with CLAHE correction (Section 3.2.2), (d) Textured with DAGW correction (Section 3.2.4).

tions in scene distance, which again lead to large variations in image illumination. Consequently, the HE-corrected mosaic (Fig. 3.9b) displays significant variations in color intensity. Additionally, the image mosaic is characterized by a blue tint similar to what is observed in Fig. 3.6b. The CLAHE-corrected mosaic (Fig. 3.9c) displays a more consistent coloring, but partly shows stronger contrasts, whereas the DAGW-corrected mosaic (Fig. 3.9d) displays a smoother and more consistent coloring.

### 3.5.2 Biology: Stokkbergnset

This survey was conducted on a steep, close to vertical, rock wall near Stokkbergnset ( $63^{\circ}28'N$ ,  $9^{\circ}54'E$ ) in the Trondheimsfjord, Norway. The motion control aspects of the survey are discussed in detail in Paper B, while this section focuses more on the mapping itself.

The rock wall has a slope varying from  $50^{\circ}$  to  $100^{\circ}$  (i.e., overhang) starting from approximately 100 m depth and reaching the seafloor at approximately 530 m. The collected dataset is divided into eight boxes of approximately  $10 \times 10$  m, each consisting of 750-800 images collected over 13 minutes (see Table 3.2 for details). These boxes were recorded at 50 m depth intervals between 100 m and 450 m depth to provide representative areal coverage of biodiversity and patchiness as a function of depth. The images were collected by ROV 30k maneuvering in an automated lawn-mower pattern with constant scene distance.

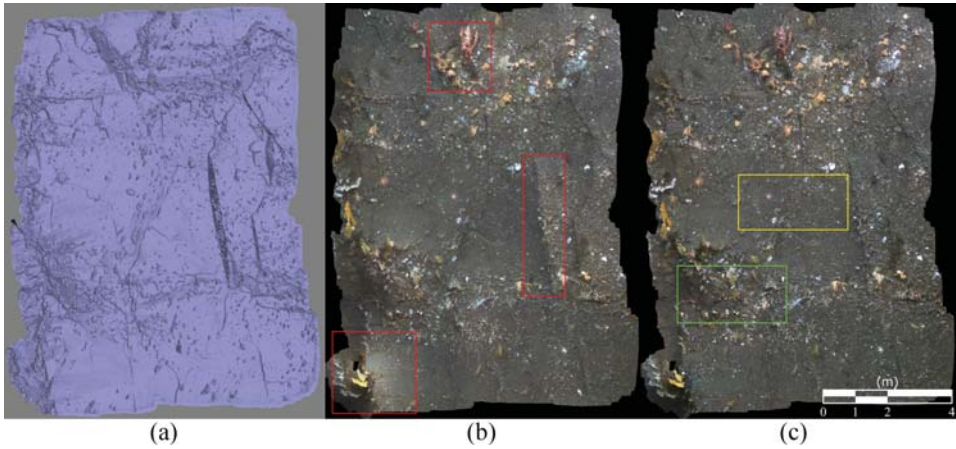


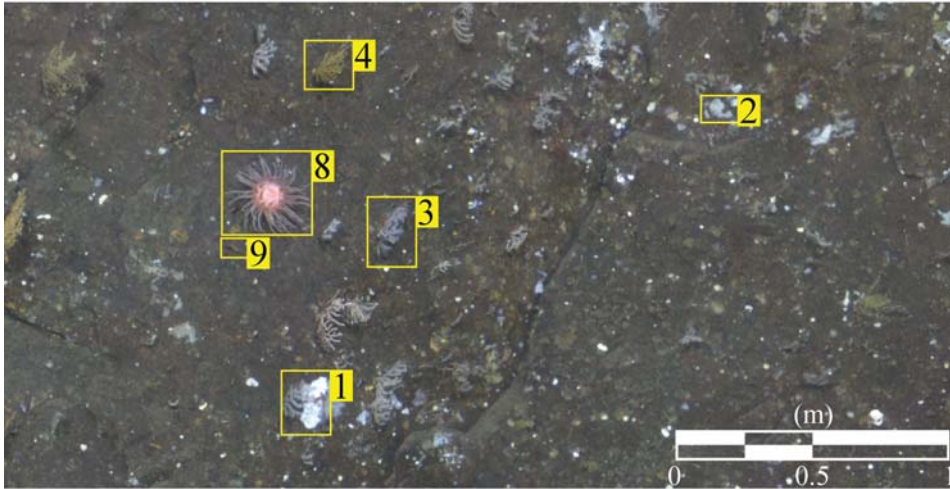
Figure 3.10: 3D model of a 9 m x 12 m section of the wall at Stokkbergnset at 200 m depth. Each mosaic is composed of 574 images. The full resolution mosaic is  $\sim 51$  megapixels with a pixelwidth/height of  $\sim 1.5$  mm. The coral from Fig. 3.6 can be seen in the top center part of the mosaics. (a) shows the shaded relief of the model. (b) shows the Gray-World corrected mosaic, with red boxes indicating some of the areas where the variation in distance causes over/under-exposure. (c) shows the Distance Adjusted Gray-World corrected mosaic, where the algorithm compensates for the variation in distance. The green box indicates a typical granulated area (detailed in Fig. 3.11a), while the yellow box indicates a typical smooth area (detailed in Fig. 3.11b).

Depth m	Time min	Images n	Width m	Height m	Area m <sup>2</sup>	Efficiency m <sup>2</sup> /min
100	12.7	770	13.4	14.0	188	14.7
150	12.7	766	11.3	12.7	144	11.3
200	9.5	574	8.6	12.0	103	10.9
250	13.0	784	13.1	13.0	170	13.1
300	13.0	780	12.3	13.3	164	12.6
350	12.9	774	12.1	12.4	150	11.7
400	13.0	784	11.2	12.0	134	10.3
450	13.2	796	11.3	11.8	133	10.1

Table 3.2: Mapping time, area coverage and mapping efficiency of the Stokkbergnset wall. The average mapping efficiency of the 8 boxes was  $11.8 \text{ m}^2/\text{min}$



(a)



(b)

Figure 3.11: Two 3.5 m x 1.8 m boxes of the 2D photomosaic presented in Fig. 3.10. The full resolution mosaic has a pixelwidth/height of 1.5 mm, making it possible to identify organisms or other OOI down to 3 mm in size. (a) Granulated surfaces are dominated by *Geodia*-like sponges (Porifera, 1), *Hymedesmia*-like sponges (Porifera, 2), *Swiftia pallida* (Cnidaria, 3), *Paragorgia arborea* (Cnidaria, not pictured), *Paramuricea placomus* (Cnidaria, 4), *Primnoa resedaeformis* (Cnidaria, 5), *Henricia* sp. (Echinodermata, 6), *Echinus* sp. (Echinodermata, not pictured) and *Acesta excavata* (Mollusca, 7). (b) Smooth bedrock surfaces are dominated by *Hymedesmia*-like sponges (Porifera, 2), *Swiftia pallida* (Cnidaria, 3) and *Bolocera tuedidae* (Anemone, 8), with occasional *Geodia*-like sponges (Porifera, 1) and *Atlantopandalus* sp. (Dekapoda, 9).

Due to the relatively constant distance to the scene, the image quality was high. The images were color corrected using both the GW approach (Section 3.2.3), and the DAGW approach (Section 3.2.4) for comparison. Fig. 3.10 shows the difference between these two approaches, specifically in terms of illumination evenness. Two areas representing two distinctly different biotopes are shown in greater detail (Fig. 3.11).

The relative motion control strategy presented in Section 2.3 not only facilitates high data quality for optical imagery, but is also efficient. Due to the limited swath width achieved by underwater cameras, optical mapping is significantly slower than acoustic methods, and an increase in efficiency can reduce costs and increase the viability of the mapping method.

For instance, [57] reports almost 3 hours of manually piloted ROV-video was necessary to cover an area of 500 m<sup>2</sup> of rock wall for photogrammetry purposes, which results in a mapping efficiency of  $\sim 2.8$  m<sup>2</sup>/min. The same survey also demonstrates the limitations of relying on a vertical DVL when operating on a near vertical wall [30, 57]. In comparison, the average mapping efficiency in the comparable survey of the wall at Stokkbergnset was 11.8 m<sup>2</sup>/min (see Table 3.2), which could have covered the same area in 42 minutes.

### 3.5.3 Geology: Peru Basin

In 1989, the DISCOL (disturbance-recolonization) experiment was conducted in the Peru Basin (7°5'S, 88°27'W) in order to simulate potential effects of deep-sea mining equipment and monitor the impact of these on benthic communities [65]. As part of the follow-up survey organized by the Joint Programming Initiative Healthy and Productive Seas and Oceans (JPI Oceans) in 2015, an experimental survey using a UHI mounted on the ROV Kiel 6000 was conducted in a manganese nodule field in 4200 m water depth and presented in Paper F and [6]. The dataset consists of 15 line transects with lengths of 2-20 m. The hyperspectral payload data was recorded at 20 fps, with each frame consisting of a line of 1600 pixels with 112 color bands covering the range of wavelengths from 380 nm to 800 nm. Navigation data and video data from one HD camera and two SD cameras were recorded for the full 2-hour duration of the experiment.

An analysis of the UHI data is presented in Paper F. As a part of the post-processing, the UHI data had to be geocorrected with high relative accuracy. The ROV's acoustic positioning system has an accuracy of 0.2% of the range, which at a water depth of 4200m amounts to  $\pm 10$ m. The position and orientation data of the ROV were recorded at 1Hz and were also affected by noise, thus making the navigation data unsuitable for geocorrecting the 20 Hz UHI data.

Geocorrection of the UHI data was therefore done using the approach described in Section 3.4, which involved generating improved 5 Hz navigation data from 1 Hz DVL-based Dead Reckoning data by combining it with the HD video data or, in cases where HD video was not available, SD video data. The framegrabs were color corrected using the GW approach (Section 3.2.3), as the video was captured at near constant altitude over a flat sea bottom. Fig. 3.12 displays how this approach cancels out both the vignetting effect and additional shadows in the image, which were caused by the ROV's manipulator arm and the UHI sensor.



(a)



(b)

Figure 3.12: HD-video frame showing manganese nodules (dark shapes, 10-15 cm diameter) in the Peru Basin. (a) Raw frame with shadows from illumination and ROV equipment. (b) GW-corrected frame where shadows from light sources and ROV infrastructure have been reduced. The GW algorithm is able to correct both for the effects of the water and the shadows caused by the ROV's manipulator arm and the UHI-sensor. Some faint outlines of the shadows can still be detected in (b). These are caused by oscillations in the pitch motion of the ROV, which induce slight variations in the depth map between images.

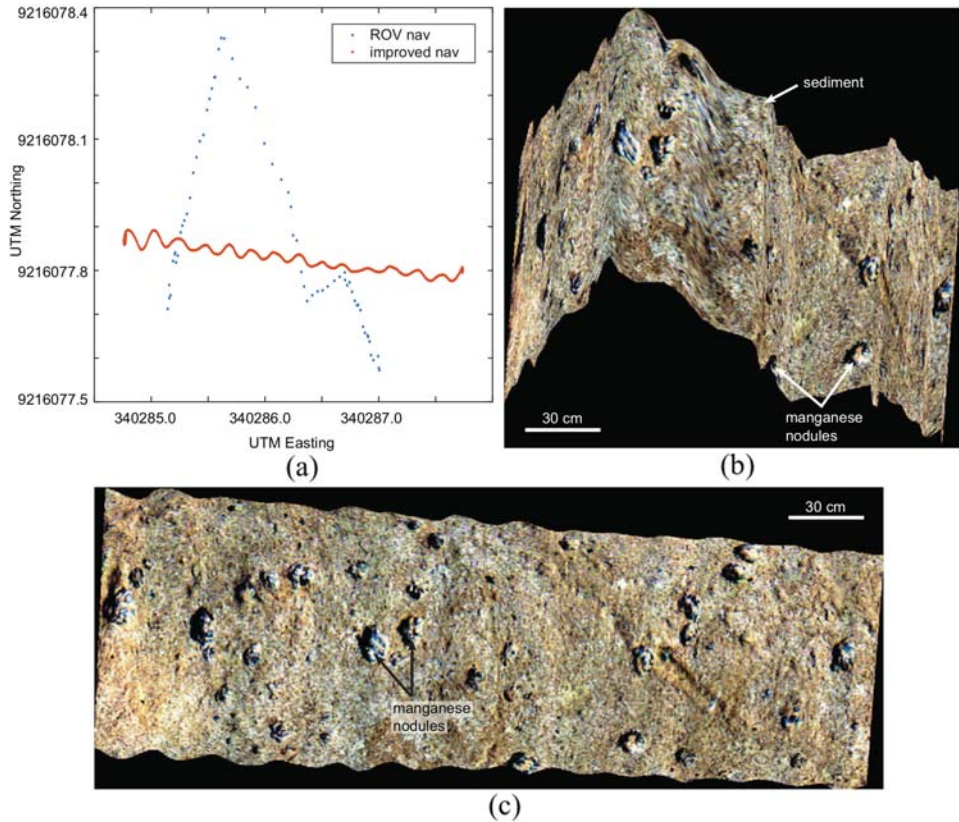


Figure 3.13: (a) Filtered 1 Hz ROV positioning data and improved positioning data using the photogrammetry approach for a 3.3 m long transect. (b) UHI mosaic in pseudo-RGB (R: 645 nm, G: 571 nm, B: 473 nm) for the same transect, geocorrected using the 1 Hz ROV positions in (a) and showing manganese nodules (dark objects) on deep-sea sediment. The image is distorted due to the insufficient positioning data. (c) UHI mosaic in pseudo-RGB, geocorrected based on the photogrammetry-derived localization.

Geocorrection of the UHI data using the photogrammetry-derived positioning data (361 data points) resulted in considerably improved image data than when the filtered ROV positioning data (66 data points) were used. The photogrammetry-derived positions showed relatively straight transects in general (Fig. 3.13a, c), whereas the ROV-based position data were characterized by frequent jumps of up to several meters (Fig. 3.13a). This resulted in distorted UHI images after geocorrection (Fig. 3.13b), making interpretations of the data difficult. In contrast, manganese nodules and other features were easy to identify in the images geocorrected using the photogrammetry-based navigation data (Fig. 3.13c).

### 3.6 Mapping, Monitoring and Management

Mapping the quantity and distribution of OOIs on the seafloor, including discrimination and classification, is an important part of scientific surveys in different fields of research. By relying on georeferenced maps and mosaics rather than raw video or still images, this analysis is simplified both for researchers manually examining the results, and also for automated computer vision algorithms. Fig. 3.11 shows an example analysis of the biodiversity of the rock wall at Stokkbergnset (Section 3.5.2). When compared to the 3D structure of the area (Fig. 3.10a), the mosaic clearly demonstrates that valleys and obstacles create patchy habitats with a higher biodiversity and biomass than the smooth surfaces. The benefit of the high resolution mosaic can be seen in the case of the small gorgonian type octocoral *Swiftia pallida* (Northern sea fan). This species is often overlooked due to its size, but is easily detected in the smooth bedrock areas of the mosaic (Fig. 3.11b). In contrast, this species may be hard to identify if living on reef building deep and cold water coral reefs dominated by *Lophelia pertusa* [20].

An underwater image color correction is needed to be able to separate OOIs based on color. For instance, the bubblegum coral in Fig. 3.6 may appear as different color morphs (red, pink, orange and white), and a proper color correction is needed to discriminate between color morphs of the same species and other color groups or species. The ability to run automated identification on color consistent imagery could increase the value of non-invasive visual data, and thus reduce the need for invasive physical sampling for ground verification.

Such automated analysis and identification have been predominantly concerned with 2D representations such as top view site plans and photo mosaics. However, there is an increasing demand for mapping of areas with more complex 3D structure. As mentioned, areas with complex 3D structure will tend to display higher biodiversity than areas with low structure complexity. Additionally, the UNESCO convention defines shipwrecks as underwater cultural heritage if they are at least 100 years old, and as a result, ships sunk as recently as the middle of WWI are now part of the cultural heritage that requires monitoring [66]. These relatively intact steel hulls standing proud of the seabed pose new challenges for heritage management that are not covered by existing methods and guidelines, which have focused on predominantly flat wreck sites [25]. The cases in Sections 3.5.1 and 3.5.2 demonstrate that computer vision photogrammetry can provide a viable solution to the problem of orthographic recording of complex 3D structures. According to [44], the method can even provide new insight into site formation processes, e.g. proving that a particular wreck's hull is collapsing outward instead of inward.

The method of UUV-based photogrammetry described in this chapter benefits from high input data quality, both with regards to imagery and navigation data. However, the method has also been demonstrated to perform well on datasets with limited image quality (Section 3.5.1) and limited navigation data quality (Section 3.5.3). The approach could therefore also be applied to older datasets, so called legacy datasets. References [27], [43] and [69] have shown how similar methods can be used to extract valuable information from legacy datasets. Older video recordings and numerous still photos can thus be of renewed value when reprocessed with modern computer technology. As described in Section 3.2, several algorithms

for color correction are available to extract information from images that at first sight seem to be of limited value.

The need for increased spatial coverage to map unexplored sites is undeniable, but the need for revisiting already explored sites to increase temporal coverage and facilitate monitoring over time is also apparent. For instance, an important part of cultural heritage management is monitoring of sites to better decide if preservative or mitigating actions should be considered. Many marine biological applications also require identification, mapping and monitoring of benthic organisms over large areas and over considerable time. This would generate knowledge regarding for instance biodiversity and patchiness in time and space, information that can be essential for environmental management and sound decision making. Coral reefs are dying at an alarming rate [29], and cultural heritage is disappearing [28], stressing a fundamental need for knowledge based management and well informed decision making to protect the health of our ocean ecosystems. Considering the NOAA estimation mentioned in the introduction to this paper, the discrepancy between actual and desired states of knowledge is apparent.

Due to the high resolution, comparison of 2D-mosaics or 3D-models from repeated photogrammetry surveys can be used to monitor the state of sites with high accuracy and still at a relatively low cost. This does, however, increase the requirements of the navigation accuracy, as the datasets need to be coregistered with high relative position accuracy to ensure valid change detection. Techniques such as SLaM, computer vision and feature recognition will be important in achieving the necessary relative accuracy. Algorithms that are able to convert legacy datasets to mosaics that can be compared to new data represent a particular value, since they provide instant increase in temporal coverage for the monitoring at no added survey cost.

In order to increase the amount of seafloor mapping to the desired level, a higher degree of vehicle autonomy and integrated autonomous underwater operations will be required [41]. Reducing human interaction could reduce costs and open up new areas for exploration that have previously been considered inaccessible. By applying computer vision for quality control, automated identification and adaptive replanning, the system would be able to ensure both data quality and area coverage. Additionally, this would allow for more selective mapping based on information density, and also revisiting sites during a single dive for increased temporal coverage. Due to the increase in information obtained from the non-intrusive visual data, this could also reduce the need for intrusive ground verification (physical sampling).



## Chapter 4

# Towards Autonomy

This chapter presents a brief introduction to the field of autonomy for sensor platforms, focusing on the application of robotic intervention, planning and replanning that is covered in the Papers.

### 4.1 Levels of Autonomy

Reliance on human interaction can become a significant obstacle for operations that are in distant areas where communication and infrastructure is limited or non-existent. A higher level of autonomy can increase safety, efficiency and data quality while also reducing costs and open up new areas that were earlier deemed inaccessible for research.

The border between automation and autonomy can be difficult to distinguish, but automation of fixed, preplanned tasks are often seen as the lowest level of autonomy. Higher-level autonomy then refers to intelligent systems able to manage unexpected events and unstructured and uncertain environments [64]. A common way to define the levels of autonomy is based on the amount of human interaction [14, 41, 67]:

1. **Automatic operation (remote control)** means that even though the system operates automatically. The human operator directs and controls all high-level mission-planning functions, often preprogrammed (**human-in-the-loop/human operated**).
2. **Management by consent (teleoperation)** means that the system automatically makes recommendations for mission actions related to specific functions, and the system prompts the human operator at important points in time for information or decisions. At this level, the system may have limited communication bandwidth including time delay, due to i.e. distance. The system can perform many functions independently of human control when delegated to do so (**human-delegated**).
3. **Semi-autonomous or management by exception** means that the system automatically executes mission-related functions when response times are too short for human intervention. The human may override or change parameters

and cancel or redirect actions within defined time lines. The operator’s attention is only brought to exceptions for certain decisions (**human-supervisory control**).

4. **Highly autonomous**, which means that the system automatically executes mission-related functions in an unstructured environment with ability to plan and re-plan the mission. The human may be informed about the progress. The system is independent and “intelligent” (**human-out-of-the loop**).

Most systems today operate at levels 1 and 2, and some systems such as the Hugin AUV are approaching level 3. In this project we have adopted a bottom-up approach to autonomy, as in [41]. The mapping and navigation systems developed in this project will be part of the foundation building towards a fully autonomous system.

## 4.2 Planning and Replanning

An important part of a system with a higher level of autonomy is the ability to generate and execute a plan based on information gathered by the payload sensors. As new information becomes available, the system must be able to replan accordingly, in order to select the best course of action without human intervention.

### 4.2.1 Method Concept

Building on the frameworks established in Paper G and [48], Fig. 4.1 presents a concept for autonomous planning/replanning of a marine archaeological survey developed in collaboration with [50]. To map an area efficiently, the system first covers the area using long range acoustic mapping e.g. HISAS. Even disintegrated shipwrecks have been demonstrated to be perceivable in SAS-imagery [51], and a list of anomalies/targets can be generated from the SAS-data [71]. Depending on the capabilities of the imagery analysis, the targets may also be classified as different types of targets (e.g. ‘Shipwreck’, ‘Man-made object’, etc.).

Selecting the optimal path between all targets is similar to the Traveling Salesman Problem, which cannot be solved in polynomial time [36]. A more realistic approach to the problem could be to use a greedy algorithm approach to select targets based on

$$W = \arg \max_{W_i \in \mathbb{W}} V_1(W_i) \quad (4.1)$$

where  $\mathbb{W}$  is the set of detected anomalies in the HISAS dataset,  $V_1(W_i)$  is the perceived value of the potential target  $W_i$ , and  $W$  is the selected target. The perceived value can be defined as

$$V_1(W_i) = P_1(W_i)V_0(W_i) - C(W_i) \quad (4.2)$$

where  $P_1(W_i)$  is a probability score indicating the likelihood that the target is an interesting wreck,  $V_0(W_i)$  is the base value score of recording a wreck of the type classified by the SAS-analysis, and the cost  $C(W_i)$  represents the energy, time and data storage required to travel to and map the target. The site is visited if the

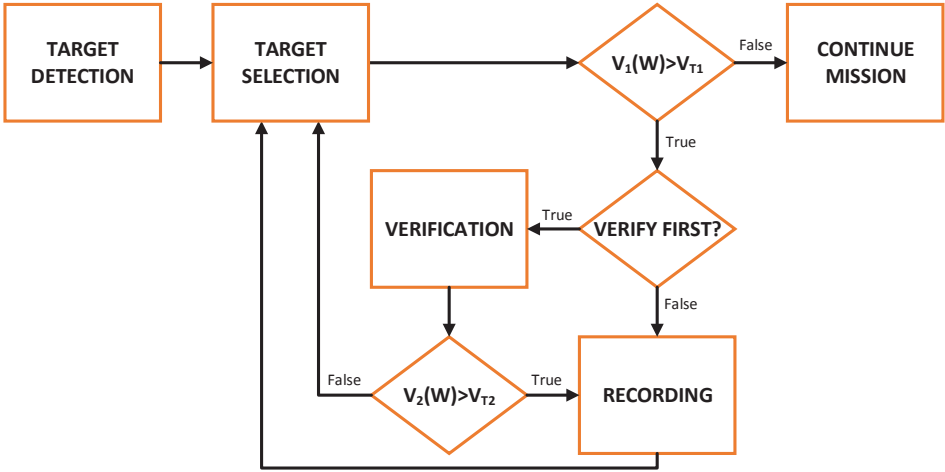


Figure 4.1: Concept flowchart for autonomous planning/replanning in a marine archaeological survey.  $W$ : Current target,  $V_1$ : Wreck perceived value,  $V_2$ : Accumulated perceived value  $VT_1, VT_2$ : Value thresholds

perceived value exceeds a given threshold  $V_{T1}$ , otherwise the system will proceed to the next stage in the mission.

When approaching a site, the system can immediately run a full site recording with e.g. photogrammetry, or decide to run a preliminary site verification with e.g. UHI. The decision may be made according to

$$C_{ver}(W) + P_1(W)C_{rec} < C_{rec}(W) \quad (4.3)$$

where  $C_{ver}$  is the cost of a site verification, and  $C_{rec}$  is the cost of a full site recording. After a site verification, an accumulated perceived value is calculated similarly to (4.2) with the updated probability score  $P_2(W)$  and used to determine whether to run a full site recording, or continue to the next target.

#### 4.2.2 Example of Application

A good example of a mapping operation that could have benefited from an autonomous system capable of replanning its mission can be found in Section IIIB of Paper D:

A post World War II dumping field outside Agdenes was mapped using two AUV dives and one ROV dive, spread over two separate surveys. The first AUV dive mapped a 2.2 km<sup>2</sup> area using HISAS (Section 3.1.5). The SAS-data was analyzed by scientists, before the AUV was deployed for a second dive to revisit identified shipwrecks and unidentified anomalies and record optical imagery. Based on inspection of the resulting optical data, the anomalies were determined to be shaped like bombs and grenades. Finally, a follow-up survey with ROV 30K (Section 2.1.2) was conducted to acquire detailed photogrammetry data and physical samples.

The Hugin AUV (Section 2.1.3) is normally equipped with both HISAS and optical cameras at the same time. If the system had been configured for online analysis of the SAS data, the platform could have replanned a new trajectory for optical inspection of any potential targets recognized in the dataset. This would have made a second AUV deployment superfluous.

In principle, an advanced autonomous system might also be able to perform the detailed visual inspection and physical sampling previously performed by the ROV, and thus further reduce the number of necessary deployments. However, as mentioned in Section 2.1, a single platform that covers all of the desired mapping and monitoring needs is unrealistic. A more realistic approach could be a multi-platform system divided into fast exploration platforms like the Hugin AUV, and inspection platforms with hovering capabilities like the Girona 500 [54]. The exploration platforms would cover large areas efficiently and through image analysis provide the inspection platforms with the most relevant targets for detailed inspection and physical sampling.

### 4.3 Robotic Intervention

A marine robotic platform with the ability to actively interact with its environment through e.g. manipulator arms are an important part of offshore industry, but also for physical sampling purposes in the marine sciences. Manually piloted ROVs remain the primary platform for such operations as inspection, intervention, maintenance and repair, mainly due to the power demands of the manipulators combined with the need for real-time human interaction.

Conducting robotic intervention autonomously is a complex task, but represents a large potential for streamlining, increase in operation efficiency and cost reductions [55]. Relevant candidates for early introduction of autonomous intervention include periodic inspection, autonomous docking and valve turning, component maintenance and repair. References [13] and [2] introduced a strategy for automated underwater valve turning with a robotic arm based on imitation and machine learning. The GIRONA 500 AUV has been demonstrated the ability to perform both autonomous docking, target detection and object recovery [55]. Commercial platforms for autonomous intervention are also emerging: The NTNU based company Eelume have developed an intervention capable AUV snake robot, potentially covering the necessary inspection, maintenance and repair tasks on a subsea template as a resident AUV connected to a permanent docking station [19].

In 2016 NTNU AUR-Lab established a research group consisting of Master's and Ph.D students with the purpose of improving the autonomous capabilities of ROV 30K (Section 2.1.2). The resulting system is described in Paper H, [56] and Paper I. The project utilizes a hybrid agent structure with both deliberative and reactive behavior, allowing the system to handle both fast and slow moving behavior. Aiming to execute a complete, realistic inspection mission from surface deployment to inspection of the OOI, the project has been geared towards full-scale experiments. As of march 2018, the research group is working on adapting the system to a new light work class ROV and refining the acoustic and optic navigation and analysis.

## Chapter 5

# Conclusions and Recommendations for Further Work

This thesis worked towards autonomous marine robotic mapping systems. An automated relative motion control strategy for ROVs was proposed and demonstrated in full-scale experiments. A variety of marine robotic platforms were deployed on multiple scientific cruises for the mapping of both water column and seafloor. A control architecture for autonomous ROV inspection was proposed and demonstrated in full-scale experiments. The main research questions this thesis aimed to answer were:

1. How can the quality of data collected by marine robotic platforms be improved through increased focus on proper positioning of payload sensors in space and time?
2. How can the data interpretation, both manually and automatically, be streamlined by improved mosaicing and georeferencing of the collected data.
3. How can the mapping and monitoring efficiency of marine robotic platforms be increased by autonomy to combat the undersampling of the oceans?

### 5.1 Conclusions

Over the course of this thesis, autonomous marine robotic platforms were found to represent an important tool in increasing and improving the mapping and monitoring of the oceans.

Related to Question 1, Paper A introduced an automated relative motion control strategy for mapping steep underwater walls using an ROV. Using a DVL oriented towards the wall, the system was able to maintain a constant distance to the scene, ensuring high image quality. The strategy was further refined in Paper B to handle varying orientation of platform and sensor, enabling the orientation of the payload sensor to be adjusted to better match the terrain. Later, the quality and efficiency of the control strategy were demonstrated on a marine biology use case

in Section 3.5.2. The strategy achieved a mapping efficiency over 4 times higher than that of a recent comparable manual survey, thus also contributing towards Question 3.

While a variety of payload sensors were utilized over the course of the thesis, RGB imagery for the purpose of photogrammetry models was the primary mapping technique employed. Papers C and D both demonstrated how the advances in computing power and digital cameras have greatly reduced the required resources for photogrammetric surveys. Simultaneously, relating to both Questions 1 and 3, they highlighted potential for further increase in cost efficiency and data quality through the implementation of systems with a higher level of autonomy.

Related to Question 2, hyperspectral imaging was demonstrated to provide a promising tool for high-resolution seafloor exploration and characterization in Paper F. The addition of video aided improvement of navigation data described in Sections 3.4 and 3.5.3 enabled the mapping system to generate georeferenced mosaics well suited for automated classification and quantification of OOI's on the seafloor. Section 4.2 and Paper G outlined the importance of such georeferenced data in the decision making of an autonomous system.

Related to Question 3, The control architecture for autonomous ROV inspection proposed in Papers H and I demonstrated the autonomy potential for intervention missions and an ability to handle non-deterministic events.

A major benefit of unmanned sensor platforms is the ability to perform missions that are deemed too dull, dangerous or distant for manned vessels. The data presented in Paper E could not have been recorded from a manned vessel due to the crew's dependence on light for safe operation. Since the ASV was able to perform the mission in the dark removed from the manned vessel, the measurements were not affected by light pollution and therefore provided unbiased data and new insight into light dependent vertical migration of zooplankton in the arctic polar night. In relation to Question 3, the ability to gather data from areas and situations previously considered impossible to sample is an important step towards reducing the undersampling of the oceans.

## 5.2 Recommendations for Further Work

Marine robotic platforms with a higher level of autonomy show a great potential in combating the undersampling of the oceans. With lower reliance on costly crewed operations, both the quality and quantity of data collected for the marine sciences can be significantly increased. There are still challenges remaining before fully autonomous systems are available, however, the research is continually forming new building blocks building towards a greater whole.

Suggestions for further work related to marine robotic platforms:

- Improve redundancy in the distance observer from Paper B by including additional distance measurements. Potential sensors include
  - Acoustic Altimeter(s)
  - Stereo Cameras
  - Multi-Beam EchoSunder

– Scanning Sonar

- Additional distance measurements could also allow for a more complex seafloor approximation, replacing the linear seafloor function with a higher degree polynomial, making the system better equipped to handle variations in terrain.
- Include a preplanning stage for navigation on complex 3D structures, generating waypoints based on a priori information (e.g. long range Multi-Beam acoustics)

Suggestions for further work related to ocean mapping:

- Increase the adoption of SLaM and terrain-based navigation for UUVs to decrease the reliance on external acoustic positioning.
- Develop UHI into a near-real-time tool for differentiation between marine organisms, geological features and archaeological features based on their unique spectral reflectance signatures without human supervision.

Suggestions for further work related to autonomy:

- Explore the possibility of combining the planning/replanning concept from Section 4.2 with the control architecture from Paper H for a full-scale test of an autonomous marine archeological survey
- Include combined vehicle and manipulator control for research into autonomous intervention
- Increase the focus on cooperation between a fleet of diverse robotic platforms performing different subtasks.



# References

- [1] K. B. Ånonsen, O. K. Hagen, Ø. Hegrenæs, and P. E. Hagen. The hugin auv terrain navigation module. In *2013 OCEANS - San Diego*, pages 1–8, Sept 2013. doi: 10.23919/OCEANS.2013.6741128.
- [2] S. R. Ahmadzadeh, P. Kormushev, and D. G. Caldwell. Autonomous robotic valve turning: A hierarchical learning approach. In *2013 IEEE International Conference on Robotics and Automation*, pages 4629–4634, May 2013. doi: 10.1109/ICRA.2013.6631235.
- [3] Allied Vision Tehnologies. *GC1380/GC1380C Technical Manual*, 2010. URL [http://www.altavision.com.br/Arquivos/AVT/Manuals/GC1380\\_User\\_Manual.pdf](http://www.altavision.com.br/Arquivos/AVT/Manuals/GC1380_User_Manual.pdf).
- [4] ASV Global. *Products*, 2018. URL <https://www.asvglobal.com/products/>.
- [5] V. Berg. Development and commissioning of a dp system for rov sf 30k. Master’s thesis, Norwegian University of Science and Technology, Department of Marine Technology, 2012.
- [6] A. Boetius (ed.). *RV SONNE Fahrtbericht / Cruise Report SO242-2, JPI Oceans Ecological Aspects of Deep-Sea Mining, DISCOL Revisited, Guayaquil-Guayaquil (Ecuador), 28.08.-01.10.2015*. Geomar rep. no. 27, GEOMAR Helmholtz-Zentrum für Ozeanforschung, Kiel, Germany, Dec. 2015. URL <http://oceanrep.geomar.de/31076/>.
- [7] A. D. Bowen, D. R. Yoerger, C. Taylor, R. McCabe, J. Howland, D. Gomez-Ibanez, J. C. Kinsey, M. Heintz, G. McDonald, D. B. Peters, B. Fletcher, C. Young, J. Buescher, L. L. Whitcomb, S. C. Martin, S. E. Webster, and M. V. Jakuba. The Nereus hybrid underwater robotic vehicle. *Underwater Technol.: The Int. J. of the Soc. for Underwater Technol.*, 28(3):79–89, 2009.
- [8] M. Bryson, M. Johnson-Roberson, O. Pizarro, and S. B. Williams. Colour-consistent structure-from-motion models using underwater imagery. In N. Roy, P. Newman, and S. Srinivasa, editors, *Robotics: Science and Systems VIII*, pages 33–40. The MIT Press, 2013.
- [9] M. Bryson, M. Johnson-Roberson, O. Pizarro, and S. B. Williams. True color correction of autonomous underwater vehicle imagery. *Journal of Field Robotics*, 33(6):853–874, 2016. ISSN 1556-4967. doi: 10.1002/rob.21638. URL <http://dx.doi.org/10.1002/rob.21638>.

- [10] G. Buchsbaum. A spatial processor model for object colour perception. *J. of the Franklin Inst.*, 310(1):1 – 26, 1980. ISSN 0016-0032. doi: [http://dx.doi.org/10.1016/0016-0032\(80\)90058-7](http://dx.doi.org/10.1016/0016-0032(80)90058-7). URL <http://www.sciencedirect.com/science/article/pii/0016003280900587>.
- [11] M. Caccia, R. Bono, G. Bruzzone, and G. Veruggio. Bottom-following for remotely operated vehicles. *Control Engineering Practice*, 11(4):461 – 470, 2003. ISSN 0967-0661. doi: [http://dx.doi.org/10.1016/S0967-0661\(01\)00142-3](http://dx.doi.org/10.1016/S0967-0661(01)00142-3). URL <http://www.sciencedirect.com/science/article/pii/S0967066101001423>. {MCMC00}.
- [12] M. Candeloro, A. J. Sørensen, S. Longhi, and F. Dukan. Observers for dynamic positioning of rovs with experimental results. *IFAC Proceedings Volumes*, 45(27):85 – 90, 2012. ISSN 1474-6670. doi: <https://doi.org/10.3182/20120919-3-IT-2046.00015>. URL <http://www.sciencedirect.com/science/article/pii/S1474667016312095>. 9th IFAC Conference on Manoeuvring and Control of Marine Craft.
- [13] A. Carrera, R. Ahmadzadeh, A. Ajoudani, P. Kormushev, M. Carreras, and D. G Caldwell. Towards autonomous robotic valve turning. 12:17–26, 01 2012.
- [14] Committee on Autonomous Vehicles in Support of Naval Operations. *Autonomous Vehicles in Support of Naval Operations*. National Research Council, 2005. ISBN 9780309096768.
- [15] F. Dukan. *ROV Motion Control Systems*. PhD thesis, Dept. of Marine Technol., Norwegian Univ. of Sci. and Technol., Trondheim, Norway, 2014.
- [16] F. Dukan and A. J. Sørensen. Sea floor geometry approximation and altitude control of ROVs. *IFAC J. Control Eng. Practice (CEP)*, 29:135–146, 2014.
- [17] H. Durrant-Whyte and T. Bailey. Simultaneous localization and mapping: Part I & II. *IEEE Robot Autom Mag*, 13(2):99–117, 2006. URL <http://ieeexplore.ieee.org/stamp/stamp.jsp?arnumber=1638022>.
- [18] Dykkepedia. *Herkules*, 2011. URL <http://www.dykkepedia.com/wiki/Herkules>.
- [19] Eelume. *Reshaping underwater operations*, 2018. URL <https://eelume.com/>.
- [20] A. C. Elde, R. Pettersen, P. Bruheim, J. Järnegren, and G. Johnsen. Pigmentation and Spectral Absorbance Signatures in Deep-Water Corals from the Trondheimsfjord, Norway. *Marine Drugs*, 10(6):1400–1411, 2012. ISSN 1660-3397. doi: 10.3390/md10061400. URL <http://www.mdpi.com/1660-3397/10/6/1400>.
- [21] R. Eustice, O. Pizarro, H. Singh, and J. Howland. UWIT: Underwater image toolbox for optical image processing and mosaicking in Matlab. In *Proc. of the 2002 Int. Symp. on Underwater Technol.*, pages 141–145, Tokyo, Japan, April 2002.

- 
- [22] T. I. Fossen. *Handbook of Marine Craft Hydrodynamics and Motion Control*, chapter 11, pages 299–300. J. Wiley & Sons, 2011.
- [23] A. Francesconi. *BIMP*, 2017. URL <http://www.alessandrofrancesconi.it/projects/bimp/>.
- [24] GIMP. *White Balance*, 2015. URL <https://docs.gimp.org/en/gimp-layer-white-balance.html>.
- [25] J. Green. *Maritime Archaeology: A Technical Handbook*. Elsevier, 2004.
- [26] R. E. Hansen, T. O. Saebo, H. J. Callow, P. E. Hagen, and E. Hammerstad. Synthetic aperture sonar processing for the hugin auv. In *Europe Oceans 2005*, volume 2, pages 1090–1094 Vol. 2, June 2005. doi: 10.1109/OCEANSE.2005.1513210.
- [27] J. Hollick, S. Moncrieff, D. Belton, A. Woods, A. Hutchison, and P. Helmholz. Creation of 3d models from large unstructured image and video datasets. *Int. Archives of the Photogrammetry, Remote Sensing and Spatial Inform. Sci. - ISPRS Archives*, 40:133–137, May 2013.
- [28] O. Holmes, M. Ulmanu, and S. Roberts. *The world’s biggest grave robbery: Asia’s disappearing WWII shipwrecks*, 2017. URL <https://www.theguardian.com/world/ng-interactive/2017/nov/03/worlds-biggest-grave-robbery-asias-disappearing-ww2-shipwrecks>.
- [29] T. Hughes, J. Kerry, M. Álvarez Noriega, J. Álvarez Romero, K. Anderson, A. Baird, R. Babcock, M. Beger, D. Bellwood, R. Berkemans, T. Bridge, I. Butler, M. Byrne, N. Cantin, S. Comeau, S. Connolly, G. Cumming, S. Dalton, G. Diaz-Pulido, C. Eakin, W. Figueira, J. Gilmour, H. Harrison, S. Heron, A. Hoey, J. Hobbs, M. Hoogenboom, E. Kennedy, C. Kuo, J. Lough, R. Lowe, G. Liu, M. McCulloch, H. Malcolm, M. McWilliam, J. Pandolfi, R. Pears, M. Pratchett, V. Schoepf, T. Simpson, W. Skirving, B. Sommer, G. Torda, D. Wachenfeld, B. Willis, and S. Wilson. Global warming and recurrent mass bleaching of corals. *Nature*, 543(7645):373–377, Mar. 2017. ISSN 0028-0836. doi: 10.1038/nature21707.
- [30] V. A. I. Huvenne, A. Georgiopoulou, L. Chaumillon, C. Lo Iacono, and R. B. Wynn. *“Novel Method to Map the Morphology of Submarine Landslide Headwall Scarps Using Remotely Operated Vehicles”*, pages 135–144. Springer International Publishing, Cham, 2016. ISBN 978-3-319-20979-1. doi: 10.1007/978-3-319-20979-1\_13. URL [https://doi.org/10.1007/978-3-319-20979-1\\_13](https://doi.org/10.1007/978-3-319-20979-1_13).
- [31] B. Jalving, K. Gade, O. K. Hagen, and K. Vestgard. A toolbox of aiding techniques for the hugin auv integrated inertial navigation system. In *Oceans 2003. Celebrating the Past ... Teaming Toward the Future (IEEE Cat. No.03CH37492)*, volume 2, pages 1146–1153 Vol.2, Sept 2003. doi: 10.1109/OCEANS.2003.178505.

- [32] T. A. Johansen, A. Zolich, T. Hansen, and A. J. Sørensen. Unmanned aerial vehicle as communication relay for autonomous underwater vehicle - field tests. In *2014 IEEE Globecom Workshops (GC Wkshps)*, pages 1469–1474, Dec 2014. doi: 10.1109/GLOCOMW.2014.7063641.
- [33] M. Johnson-Roberson, O. Pizarro, S. B. Williams, and I. Mahon. Generation and visualization of large-scale three-dimensional reconstructions from underwater robotic surveys. *J. of Field Robotics*, 27(1):21–51, 2010.
- [34] J. W. Kaeli, H. Singh, C. Murphy, and C. Kunz. Improving color correction for underwater image surveys. In *OCEANS 2011 MTS/IEEE*, pages 1–6, Kona, USA, Sept 2011. doi: 10.23919/OCEANS.2011.6107143.
- [35] J. Kalwa, D. Tietjen, M. Carreiro-Silva, J. Fontes, L. Brignone, N. Gracias, P. Ridaio, M. Pflingsthor, A. Birk, T. Glotzbach, S. Eckstein, M. Caccia, J. Alves, T. Furfaro, J. Ribeiro, and A. Pascoal. The european project morph: Distributed uuv systems for multimodal, 3d underwater surveys. 50:26–41, 07 2016.
- [36] R. M. Karp. *Reducibility among Combinatorial Problems*, pages 85–103. Springer US, Boston, MA, 1972. ISBN 978-1-4684-2001-2. doi: 10.1007/978-1-4684-2001-2\_9. URL [https://doi.org/10.1007/978-1-4684-2001-2\\_9](https://doi.org/10.1007/978-1-4684-2001-2_9).
- [37] P. Kimball, J. Bailey, S. Das, R. Geyer, T. Harrison, C. Kunz, K. Manganini, K. Mankoff, K. Samuelson, T. Sayre-McCord, F. Straneo, P. Traykovski, and H. Singh. The WHOI Jetyak: An autonomous surface vehicle for oceanographic research in shallow or dangerous waters. In *2014 IEEE/OES Autonomous Underwater Vehicles (AUV)*, pages 1–7, Oct 2014. doi: 10.1109/AUV.2014.7054430.
- [38] M. Kirkeby. Comparison of controllers for dynamic positioning and tracking of rovs minerva. Master’s thesis, Norwegian University of Science and Technology, Department of Marine Technology, 2010.
- [39] Kongsberg Maritime. *HISAS 1030 High resolution interferometric synthetic aperture sonar*, 2017. URL [https://www.km.kongsberg.com/ks/web/nokbg0397.nsf/AllWeb/86E9FFB43569CDEEC12576B9006D75C7/\\$file/HISAS\\_1030\\_brochure\\_v1\\_lowres\\_v2.pdf?OpenElement](https://www.km.kongsberg.com/ks/web/nokbg0397.nsf/AllWeb/86E9FFB43569CDEEC12576B9006D75C7/$file/HISAS_1030_brochure_v1_lowres_v2.pdf?OpenElement).
- [40] Kystverket. *Åpner for test av autonome skip*, 2016. URL <http://www.kystverket.no/Nyheter/2016/september/apner-for-test-av-autonome-skip/>.
- [41] M. Ludvigsen and A. J. Sørensen. Towards integrated autonomous underwater operations for ocean mapping and monitoring. *Annu. Rev. in Control*, 42: 145 – 157, 2016. ISSN 1367-5788. doi: <http://dx.doi.org/10.1016/j.arcontrol.2016.09.013>. URL <http://www.sciencedirect.com/science/article/pii/S1367578816300256>.

- 
- [42] Maritime Robotics. *Our USV systems*, 2018. URL <https://maritimerobotics.com/usv/>.
- [43] J. Mertes, T. Thomsen, and J. Gulley. Evaluation of Structure from Motion Software to Create 3D Models of Late Nineteenth Century Great Lakes Shipwrecks Using Archived Diver-Acquired Video Surveys. *J. of Maritime Archaeology*, 9:173–189, Dec. 2014. doi: 10.1007/s11457-014-9132-x.
- [44] J. Mertes, C. N. Zant, J. D. Gulley, and T. M. Thomsen. Rapid, quantitative assessment of submerged cultural resource degradation using repeat video surveys and structure from motion. *J. of Maritime Archaeology*, pages 1–17, May 2017.
- [45] C. Mobley. *Ocean Optics Web Book*, 2017. URL <http://www.oceanopticsbook.info/>.
- [46] W. Munk. *THE U.S. COMMISSION ON OCEAN POLICY: Testimony in San Pedro, California*, 2002. URL [http://govinfo.library.unt.edu/oceancommission/meetings/apr18\\_19\\_02/munk\\_statement.pdf](http://govinfo.library.unt.edu/oceancommission/meetings/apr18_19_02/munk_statement.pdf).
- [47] National Oceanic and Atmospheric Administration. *How much of the ocean have we explored?*, 2017. URL <https://oceanservice.noaa.gov/facts/exploration.html>.
- [48] I. Nilssen, Ø. Ødegård, A. J. Sørensen, G. Johnsen, M. A. Moline, and J. Berge. Integrated environmental mapping and monitoring, a methodological approach to optimise knowledge gathering and sampling strategy. *Marine Pollution Bulletin*, 96(1):374 – 383, 2015. ISSN 0025-326X. doi: <https://doi.org/10.1016/j.marpolbul.2015.04.045>. URL <http://www.sciencedirect.com/science/article/pii/S0025326X15002477>.
- [49] P. Norgren, M. Ludvigsen, T. Ingebretsen, and V. E. Hovstein. Tracking and remote monitoring of an autonomous underwater vehicle using an unmanned surface vehicle in the Trondheim fjord. In *OCEANS 2015 MTS/IEEE*, pages 1–6, Washington, DC, USA, Oct 2015. doi: 10.23919/OCEANS.2015.7401975.
- [50] Ø. Ødegård. *Autonomous Operations and Systems in Marine Archaeology*. PhD thesis, Dept. of Marine Technol., Norwegian Univ. of Sci. and Technol., Trondheim, Norway, 2018.
- [51] Ø. Ødegård, R. E. Hansen, H. Singh, and T. J. Maarleveld. Archaeological use of synthetic aperture sonar on deepwater wreck sites in skagerrak. *Journal of Archaeological Science*, 89:1 – 13, 2018. ISSN 0305-4403. doi: <https://doi.org/10.1016/j.jas.2017.10.005>. URL <http://www.sciencedirect.com/science/article/pii/S0305440317301516>.
- [52] S. M. Pizer, E. P. Amburn, J. D. Austin, R. Cromartie, A. Geselowitz, T. Greer, B. Romeny, J. B. Zimmerman, and K. Zuiderveld. Adaptive Histogram Equalization and Its Variations. *Comput. Vision Graph. Image Process.*, 39(3):355–368, Sept. 1987. ISSN 0734-189X.

- doi: 10.1016/S0734-189X(87)80186-X. URL [http://dx.doi.org/10.1016/S0734-189X\(87\)80186-X](http://dx.doi.org/10.1016/S0734-189X(87)80186-X).
- [53] T. Pratchett and N. Gaiman. *Good Omens*. Gollancz, 1990. ISBN 0-575-04800-X.
- [54] D. Ribas, N. Palomeras, P. Ridao, M. Carreras, and A. Mallios. Girona 500 auv: From survey to intervention. *IEEE/ASME Transactions on Mechatronics*, 17(1):46–53, Feb 2012. ISSN 1083-4435. doi: 10.1109/TMECH.2011.2174065.
- [55] P. Ridao, M. Carreras, D. Ribas, P. J. Sanz, and G. Oliver. "intervention auvs: The next challenge". *Annual Reviews in Control*, 40:227 – 241, 2015. ISSN 1367-5788. doi: <https://doi.org/10.1016/j.arcontrol.2015.09.015>. URL <http://www.sciencedirect.com/science/article/pii/S1367578815000541>.
- [56] I. Rist-Christensen. Autonomous Robotic Intervention using ROV. Master's thesis, Norwegian University of Science and Technology, Department of Marine Technology, 2016.
- [57] K. Robert, V. A. I. Huvenne, A. Georgiopoulou, D. O. B. Jones, L. Marsh, G. D. O. Carter, and L. Chaumillon. New approaches to high-resolution mapping of marine vertical structures. *Scientific Reports*, 7(1):9005, 2017. ISSN 2045-2322. doi: 10.1038/s41598-017-09382-z. URL <https://doi.org/10.1038/s41598-017-09382-z>.
- [58] Safety4Sea. *China builds Asia's first autonomous ship test area*, 2018. URL <https://safety4sea.com/china-builds-asias-first-autonomous-ship-test-area/>.
- [59] P. C. Sames. *Unmanned ships on the horizon*, 2017. URL <https://www.dnvgl.com/article/unmanned-ships-on-the-horizon-94273>.
- [60] D. T. Sandwell, R. D. Müller, W. H. F. Smith, E. Garcia, and R. Francis. New global marine gravity model from CryoSat-2 and Jason-1 reveals buried tectonic structure. *Science*, 346(6205):65–67, 2014. ISSN 0036-8075. doi: 10.1126/science.1258213. URL <http://science.sciencemag.org/content/346/6205/65>.
- [61] R. T. Sayre-McCord, C. Murphy, J. Kaeli, C. Kunz, P. Kimball, and H. Singh. Advances in platforms and algorithms for high resolution mapping in the marine environment. In T. I. Fossen, K. Y. Pettersen, and H. Nijmeijer, editors, *Sensing and Control for Autonomous Vehicles: Applications to Land, Water and Air Vehicles*, pages 89–119. Springer Int. Publishing, 2017. ISBN 978-3-319-55372-6. doi: 10.1007/978-3-319-55372-6\_5. URL [https://doi.org/10.1007/978-3-319-55372-6\\_5](https://doi.org/10.1007/978-3-319-55372-6_5).
- [62] J. M. Soares, A. P. Aguiar, A. M. Pascoal, and A. Martinoli. Joint asv/auv range-based formation control: Theory and experimental results. In *2013 IEEE International Conference on Robotics and Automation*, pages 5579–5585, May 2013. doi: 10.1109/ICRA.2013.6631378.

- 
- [63] A. J. Sørensen, F. Dukan, M. Ludvigsen, D. A. Fernandez, and M. Candeloro. *Further Advances in Unmanned Marine Vehicles*, chapter 6: Development of Dynamic Positioning and Tracking System for the ROV Minerva, pages 113–128. IET, UK, 2012.
- [64] The Norwegian University of Science and Technology. Centre of Excellence Proposal to the Research Council of Norway, 2012.
- [65] H. Thiel and G. Schriever. Cruise Report DISCOL 1, SONNE – Cruise 61. *Berichte aus dem Zentrum für Meeres- und Klimaforschung der Universität Hamburg*, pages 1–75, 1989.
- [66] United Nations Educational, Scientific and Cultural Organization. *The UNESCO convention on the protection of the underwater cultural heritage*, 2001. URL [http://www.unesco.org/new/fileadmin/MULTIMEDIA/HQ/CLT/UNDERWATER/pdf/Info\\_kit/GB-2001CONVENTION-INFOKIT%2007-2009.pdf](http://www.unesco.org/new/fileadmin/MULTIMEDIA/HQ/CLT/UNDERWATER/pdf/Info_kit/GB-2001CONVENTION-INFOKIT%2007-2009.pdf).
- [67] I. B. Utne, A. J. Sørensen, and I. Schjølberg. Risk management of autonomous marine systems and operations, 2017. URL <http://dx.doi.org/10.1115/OMAE2017-61645>.
- [68] K. P. Valavanis and G. J. Vachtsevanos (Eds.). *Handbook of Unmanned Aerial Vehicles*. Springer Netherlands, Dordrecht, 2015. ISBN 978-90-481-9707-1.
- [69] T. Van Damme. Computer vision photogrammetry for underwater archaeological site recording in a low-visibility environment. *ISPRS - Int. Archives of the Photogrammetry, Remote Sensing and Spatial Inform. Sci.*, XL-5/W5: 231–238, Apr. 2015.
- [70] Z. Volent, G. Johnsen, and F. Sigernes. Microscopic hyperspectral imaging used as a bio-optical taxonomic tool for micro- and macroalgae. 48:4170–6, 08 2009.
- [71] D. P. Williams. Fast target detection in synthetic aperture sonar imagery: A new algorithm and large-scale performance analysis. *IEEE Journal of Oceanic Engineering*, 40(1):71–92, Jan 2015. ISSN 0364-9059. doi: 10.1109/JOE.2013.2294532.
- [72] K. Zuiderveld. Contrast limited adaptive histogram equalization. In P. S. Heckbert, editor, *Graphics Gems IV*, chapter 8, pages 474–485. Academic Press Professional, Inc., San Diego, CA, USA, 1994. ISBN 0-12-336155-9. URL <http://dl.acm.org/citation.cfm?id=180895.180940>.



# Appendix A

## ROV Specifications

### A.1 ROV Minerva

- Type: SUB-fighter 7500, electric “light workclass” ROV (Sperre AS)
- Operating Depth: 600m
- Dimensions (LWH): 1.44×0.8×0.8m
- Propulsion: 5 electric thrusters @ 2kW
- Weight: 440kg
- Payload: ~20kg
- Mass, added mass, linear and quadratic dampening as presented in [38]:

$$M = \begin{bmatrix} 460 & 0 & 0 & 0 & 0 & 0 \\ 0 & 460 & 0 & 0 & 0 & 0 \\ 0 & 0 & 460 & 0 & 0 & 0 \\ 0 & 0 & 0 & 105 & 0 & 0 \\ 0 & 0 & 0 & 0 & 104 & 0 \\ 0 & 0 & 0 & 0 & 0 & 50 \end{bmatrix} \quad (\text{A.1})$$

$$M_A = \begin{bmatrix} 293 & 0 & 0 & 0 & 0 & 0 \\ 0 & 302 & 0 & 0 & 0 & 0 \\ 0 & 0 & 326 & 0 & 0 & 0 \\ 0 & 0 & 0 & 52 & 0 & 0 \\ 0 & 0 & 0 & 0 & 52 & 0 \\ 0 & 0 & 0 & 0 & 0 & 57 \end{bmatrix} \quad (\text{A.2})$$

$$D = \begin{bmatrix} 29 & 0 & 0 & 0 & 0 & 0 \\ 0 & 41 & 0 & 0 & 0 & 0 \\ 0 & 0 & 254 & 0 & 0 & 0 \\ 0 & 0 & 0 & 34 & 0 & 0 \\ 0 & 0 & 0 & 0 & 59 & 0 \\ 0 & 0 & 0 & 0 & 0 & 45 \end{bmatrix} \quad (\text{A.3})$$

$$D_n = \begin{bmatrix} 292 & 0 & 0 & 0 & 0 & 0 \\ 0 & 584 & 0 & 0 & 0 & 0 \\ 0 & 0 & 635 & 0 & 0 & 0 \\ 0 & 0 & 0 & 84 & 0 & 0 \\ 0 & 0 & 0 & 0 & 148 & 0 \\ 0 & 0 & 0 & 0 & 0 & 100 \end{bmatrix} \quad (\text{A.4})$$

## A.2 ROV 30K

- Type: SUB-fighter 30K, electric “workclass” ROV (Sperre AS)
- Operating Depth: 1000m
- Dimensions (LWH): 2.6×1.5×1.6m
- Propulsion: 6 electric thrusters @ 3kW
- Weight: 1800kg
- Payload: ~60kg
- Mass, added mass, linear and quadratic dampening as presented in [5]:

$$M = \begin{bmatrix} 1862.9 & 0 & 0 & 0 & 0 & 0 \\ 0 & 1862.9 & 0 & 0 & 0 & 0 \\ 0 & 0 & 1862.9 & 0 & 0 & 0 \\ 0 & 0 & 0 & 525.4 & 1.4 & 33.4 \\ 0 & 0 & 0 & 1.4 & 794.2 & 2.6 \\ 0 & 0 & 0 & 33.4 & 2.6 & 691.2 \end{bmatrix} \quad (\text{A.5})$$

$$M_A = \begin{bmatrix} 779.8 & -6.9 & -103.3 & 8.5 & -165.5 & -7.8 \\ -6.9 & 1222 & 51.3 & 409.4 & -5.8 & 62.7 \\ -103.3 & 51.3 & 3659.9 & 6.1 & -386.4 & 10.8 \\ 8.5 & 409.4 & 6.1 & 534.9 & -10.0 & 21.0 \\ -165.5 & -5.8 & -386.4 & -10.0 & 842.7 & -1.1 \\ -7.8 & 62.7 & 10.8 & 21.0 & -1.1 & 224.3 \end{bmatrix} \quad (\text{A.6})$$

$$D = \begin{bmatrix} 74.82 & 0 & 0 & 0 & 0 & 0 \\ 0 & 69.48 & 0 & 0 & 0 & 0 \\ 0 & 0 & 728.40 & 0 & 0 & 0 \\ 0 & 0 & 0 & 268.80 & 0 & 0 \\ 0 & 0 & 0 & 0 & 309.77 & 0 \\ 0 & 0 & 0 & 0 & 0 & 105 \end{bmatrix} \quad (\text{A.7})$$

$$D_n = \begin{bmatrix} 748.22 & 0 & 0 & 0 & 0 & 0 \\ 0 & 992.53 & 0 & 0 & 0 & 0 \\ 0 & 0 & 1821.01 & 0 & 0 & 0 \\ 0 & 0 & 0 & 672 & 0 & 0 \\ 0 & 0 & 0 & 0 & 774.44 & 0 \\ 0 & 0 & 0 & 0 & 0 & 523.27 \end{bmatrix} \quad (\text{A.8})$$

### A.3 ROV Kiel 6000

- Type: QUEST 7, electric “workclass” ROV (Schilling Robotics)
- Operating Depth: 6000m
- Dimensions (LWH): 3.5×1.9×2.4m
- Propulsion: 7 electric thrusters SPE-380 @ 15kW
- Weight: 3500kg
- Payload: 100kg
- Drag forces of ROV: 530kgf (fw/bw), 340kgf (lat), 300/380kgf (vert)

For further details, see <http://www.geomar.de/en/centre/central-facilities/tlz/rovkiel6000/specifications-logistics/>



## Appendix B

# Python Scripts

### B.1 Photoscan Distance Export

Run the script on a meshed Photoscan model through “Tools\Run Script”(Ctrl+R), with an input argument that is the path of an empty folder for the output.

```
1 import sys, PhotoScan
2
3 folder = str(sys.argv[1])
4 chunk = PhotoScan.app.document.chunk
5 scale = chunk.transform.scale
6 for camera in chunk.cameras:
7     if bool(camera.transform):
8         depth = chunk.model.renderDepth(camera.transform, camera.sensor
9             .calibration)
10        depth_scaled = PhotoScan.Image(depth.width, depth.height, "_",
11            "F32")
12        for y in range(depth.height):
13            for x in range(depth.width):
14                depth_scaled[x,y] = (depth[x,y][0] * scale, )
15        savepath = folder+"\\\"+camera.label[:-3]+ ".tif"
16        depth_scaled.save(savepath)
```

## B.2 Blender Navigation Data Import

Create a simple cube object that will represent the movement of your vehicle. Your vehicle model and/or camera object can then be set as the child of this (invisible) cube object. With the cube as the selected object, copy the script below into the python console of Blender with the path to a csv-file of your navigation data with the format 'time,northing,easting,depth,roll,pitch,yaw'.

```
1 import csv, itertools, numpy
2
3 state_file_name=r"<yourpath>.txt"
4
5 starttime=[12,00,00] #[hr, min, sec]
6 start_sec=starttime[0]*3600+starttime[1]*60+starttime[2]
7 east=[]
8 north=[]
9 down=[]
10 roll=[]
11 pitch=[]
12 yaw=[]
13 frame=[]
14 fps=30 #fps of video to be made
15
16 with open(state_file_name) as state_file:
17     statereader=csv.reader(state_file, delimiter='\\t')
18     for row in itertools.islice(statereader, 1, None):
19         time=row[0].split(':')
20         frame.append((int(time[0])*3600+int(time[1])*60+float(
21             time[2])-start_sec)*fps)
22         north.append(float(row[1]))
23         east.append(float(row[2]))
24         down.append(float(row[3]))
25         roll.append(float(row[4]))
26         pitch.append(float(row[5]))
27         yaw.append(float(row[6]))
28
29 pos_off=[0,0,0] #ENU offset between agisoft and blender
30 obj = bpy.context.object
31 for i in range(0, len(row_east)):
32     obj.location=(east[i]-pos_off[0], north[i]-pos_off[1], -down[i]-
33         pos_off[2])
34     obj.rotation_euler=(roll[i], 0-pitch[i], pi/2-yaw[i])
35     obj.keyframe_insert(data_path="location", frame=frame[i])
36     obj.keyframe_insert(data_path="rotation_euler", frame=frame[i])
```

**Part II**  
**Articles**



# Article A

## Automatic Relative Motion Control and Photogrammetry Mapping on Steep Underwater Walls using ROV

---

Stein M. Nornes, Martin Ludvigsen and Asgeir J. Sørensen

ARTICLE A

---

This article is published in the proceedings of  
*MTS/IEEE OCEANS 2016*. Monterey, CA, USA, 19-22 September 2016.  
doi: 10.1109/OCEANS.2016.7761252

Is not included due to copyright



# Article B

## Motion Control of ROVs for Mapping of Steep Underwater Walls

---

Stein M. Nornes, Asgeir J. Sørensen and Martin Ludvigsen

ARTICLE B

This article is a book chapter of T.I. Fossen, K.Y. Pettersen, H. Nijmeijer (Eds.)  
*Sensing and Control for Autonomous Vehicles*, Chapter 1.3, pages 51–69,  
Lecture Notes in Control and Information Sciences 474,  
Springer International Publishing AG, 2017.  
doi: 10.1007/978-3-319-55372-6\_3

Is not included due to copyright





# Article C

## Underwater Photogrammetric Mapping of an Intact Standing Steel Wreck with ROV

---

Stein M. Nornes, Martin Ludvigsen, Øyvind Ødegård and Asgeir J. Sørensen

ARTICLE C

---

This article is published in the proceedings of the  
*4th IFAC Workshop on Navigation, Guidance and Control  
of Underwater Vehicles (NGCUV)*. IFAC-PapersOnLine,  
Volume 48 (2), pages 206-211. Girona, Spain, 28-30 April 2015.  
doi: 10.1016/j.ifacol.2015.06.034



# Underwater Photogrammetric Mapping of an Intact Standing Steel Wreck with ROV

Stein M. Nornes<sup>\*,\*</sup> Martin Ludvigsen<sup>\*</sup> Øyvind Ødegård<sup>\*,\*\*</sup>  
Asgeir J. Sørensen<sup>\*</sup>

<sup>\*</sup> Centre for Autonomous Marine Operations and Systems (AMOS),  
Department of Marine Technology, Norwegian University of Science  
and Technology, NTNU, NO-7491 Trondheim, Norway

<sup>\*\*</sup> Department of Archaeology and Cultural History, University  
Museum, Norwegian University of Science and Technology, NTNU,  
NO-7491 Trondheim, Norway

---

**Abstract:** This paper presents the results of an underwater photogrammetric survey of an intact standing steel wreck with high vertical profiles from the seabed at 60 meters depth. The survey was conducted in Trondheim Harbour in August 2014 using a Remotely Operated Vehicle (ROV) equipped with a stereo camera rig. The paper demonstrates how the emergence of commercially available photogrammetric software has reduced the required resources for creating high-resolution 3D-models of archaeological sites from photographs. At the same time, the resources and ROV-pilot skills required for the survey itself still represent an obstacle for the end users. The results and experiences of this survey are therefore used as the basis for a discussion on the possible benefits, challenges and strategies for conducting such a survey autonomously.

*Keywords:* Unmanned Underwater Vehicles (UUV), Marine archaeology, Mapping, UUV vision systems, Photogrammetry

---

## 1. INTRODUCTION

Only a fraction of our cultural heritage deposited on the seabed has been located and investigated, with UNESCO (2015) estimating over 3 million undiscovered shipwrecks spread across the planets oceans. Submerged prehistoric landscapes and shipwrecks deposited on the seabed are non-renewable sources to understanding and knowledge of our past, and the scientific community and antiquarian authorities around the world are working against the clock to secure as much of this heritage as possible for posterity. Climate change and increased commercial activities in the marine environments put this cultural heritage under pressure, and accentuates the need for new and efficient methods for recording and managing underwater cultural heritage.

Recent years have seen advances within underwater robotics that can remedy this situation by reducing the dependency on divers. Simultaneously, developments in sensor technologies and data processing have lead to relatively inexpensive commercially available off-the-shelf digital underwater cameras and photogrammetry software that can be run on a powerful but ordinary PC.

The inherent optical properties of the water (light reflectance, scattering and attenuation) means algorithms intended for underwater computer vision generally need to be more robust than algorithms intended for use in air. While the Scale Invariant Feature Transform (SIFT) is one of the most efficient feature detectors in many applications,

Meline et al. (2012) demonstrated how suspended particles causes the performance of SIFT to deteriorate severely relative to other approaches. Similarly, Campos et al. (2014) demonstrated how surface reconstruction methods with insufficient levels of noise tolerance can give wildly varying results for underwater datasets.

McCarthy and Benjamin (2014) have shown how a diver-based photogrammetric approach can significantly improve the efficiency of the process of recording underwater cultural heritage. Taking the diver out of the equation by using a Remotely Operated Vehicle (ROV) as a platform for data capture removes two very limiting operational constraints (depth and bottom time). Removing the pilot as well by having an Autonomous Underwater Vehicle (AUV) perform this task autonomously would represent a significant breakthrough for marine archaeological recording. Some photogrammetric AUV surveys have been conducted, but are restricted to wrecks and seafloor that provide a relatively flat and benign environment for AUV robotic operations (Foley et al., 2009; Johnson-Roberson et al., 2010; Gracias et al., 2013; Demesticha et al., 2014).

Drap et al. (2013) demonstrated an ROV based photogrammetric survey of parts of a more three-dimensional wreck, relying on a combination of high resolution images and sonar data to construct a georeferenced 3D-model. The reliance on sonar data increases the number of dives required to collect the necessary data.

In this paper we will present the process and results from an ROV based photogrammetric recording of a shipwreck

---

\* email: stein.nornes@ntnu.no

### 3. METHOD

with a high vertical profile. This recording demonstrates how accurate 3D-models can be produced relying only on lower resolution (1.4 megapixel) cameras and ROV navigation data for georeferencing, thus increasing the efficiency of a survey. The main contribution is in the analysis identifying the challenges and potential strategies for automating such a survey.

Section 2 presents the wreck and the motivation for its selection. Section 3 describes the method, hardware and software used for the data acquisition and processing. The experimental results are presented in section 4. The results and experiences from this recording is then analyzed in section 5, focusing on strategies for automating the process and exploring the potential benefits for marine archaeology and other marine sciences. Finally, a conclusion is given in section 6.

## 2. M/S HERKULES

The tugboat M/S Herkules sank just outside Trondheim Harbour on the 16th of September 1957 (Dykkepedia, 2015). While Herkules was towing the 9000 tonne M/S Lars Mehling, the cable ended up being pulled across the vessel. This caused the vessel to lean heavily towards port and rapidly take in water. No lives were lost.

Today the wreck rests on its keel at 60 meters depth with the top of the mast reaching 10 meters above the sea floor. The bow rises over the sea floor while the stern is buried in the sand, and the total length of the visible wreck is 20-25 meters.

### 2.1 Relevance of the wreck

This wreck was not chosen for any kind of archaeological significance. It is a well-known wreck frequently visited by technical divers. Rather, it was chosen for its close proximity to Trondheim, ease of access and limited size. Choosing such a new wreck in good structural condition also meant the risk of doing irreparable damage to an important archaeological find was essentially eliminated.

At the same time, this wreck demonstrates several of the challenges that will need to be resolved for a future autonomous survey approach.

The wreck has got a complex 3D-structure with both horizontal and vertical faces, and even some overhang for the lower part of the bow. Covering parts of the wreck are numerous ropes and wires, both part of the original construction and fishing equipment having caught on the wreck. This poses a risk for entangling the ROV and restricts how close the ROV is able to get to the steel parts of the wreck. The ropes and wires also pose a challenge for the modelling, being rather thin and complex compared to the solid steel plates.

Like any object with a high vertical profile on an otherwise flat seabed, manmade or natural, the wreck attracts biology like fish and crustaceans. For photogrammetry software assuming a stationary scene, these moving creatures can give false matches and erroneous camera positions. Generally, this means they need to be masked out of the images in the preprocessing, which can be time consuming.

The survey of M/S Herkules was conducted on the 25th and 26th of August 2014.

### 3.1 Minerva ROV

Minerva is a SUB-fighter 7500 ROV made by Sperre AS in 2003 for NTNU. It is a medium sized ROV (144x82x81 cm, 485 kg), and is a frequently used test platform for navigation and control research. Usually deployed from the NTNU research vessel (RV) Gunnerus, it is powered from and communicates with the surface vessel through a 600 m umbilical. All systems needed for operation such as power supply, navigation computers and monitors are fitted inside a 15 foot container.

For this survey, the ROV was also equipped with a stereo camera rig. This features two Allied Vision GC1380C cameras mounted in parallel on a horizontal bar, 42cm apart at a 45° forward facing angle. The cameras have a resolution of 1360x1024 pixels and are capable of recording at 20 frames per second. Their high light sensitivity and signal to noise ratio makes them suitable for underwater operation. The reduced resolution, combined with keeping the recording at 0.5 fps to reduce the number of redundant images, keeps the amount of data at a manageable level for the postprocessing stage. The orientation of the camera rig was chosen both for ease of assembly and to be able to capture images of both vertical and horizontal faces with the same setting.

Operating at depths from 50 to 60 meters in the Trondheimsfjord means there is basically no ambient light. The lighting for operation was provided by two HMI lamps and two halogen lamps mounted on the horizontal top bar on the front of the ROV.

The ROV can be piloted manually using a joystick console, or automated using a Dynamic Positioning system (DP) developed and continuously expanded at NTNU. For more details on Minerva and the DP system, the reader is referred to Dukan et al. (2011) and Sørensen et al. (2012).

### 3.2 Image capture strategy

To minimize the risk of cable entanglement and account for the limited ROV-time available, the survey was split in two: The starboard side of the wreck was mapped the first day with Gunnerus stationed north (the wrecks starboard) of the wreck, and the port side was mapped the second day with Gunnerus stationed south of the wreck.

While Minerva has got automated altitude control, no automated feature based navigation system for keeping horizontal distance to an unmapped object is currently implemented. As a result, the survey was conducted using manual control and a simple rotating sonar providing distance to the wreck. An archaeologist also continuously evaluated the captured images during the survey, giving feedback on image quality. A distance of 2-3 meters to the wreck was deemed to yield the desired lighting and image quality, while not being to risky (with regard to entanglement) or difficult for the pilot to maintain.

The main survey pattern was chosen as a vertical lawn-mower pattern with transects along constant depths (see

figure 1). By choosing constant-depth transects, the automatic depth control could be used, reducing the complexity for the pilot. This also reduced the risk of current related drift producing random gaps between transect lines.

The depth difference between the transects was approximately 1 meter the first day. This was reduced to approximately 0.8 meters on the second day, based on initial overnight processing of the data indicating insufficient vertical overlap. In addition to these vertical lawnmower patterns, some additional images of the flatter top of the wreck were collected because the coverage of this area was deemed insufficient.

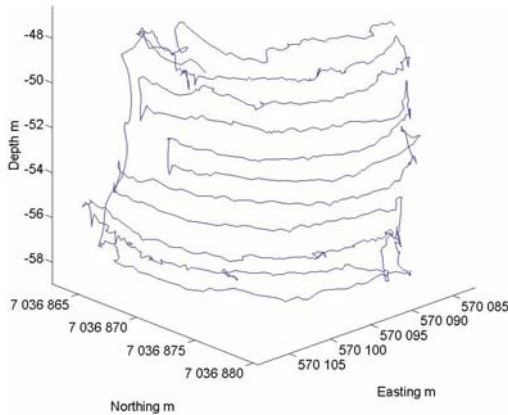


Fig. 1. ROV track for day 1 survey (starboard side of wreck)

### 3.3 Data processing

An overview of the processing pipeline is given in figure 2. Online data from the ROV is collected using LabVIEW (NI, 2015).

Due to the lack of automatic target distance control, quite a few images became underexposed while some became overexposed. In order to compensate for this, the images were colour corrected using the Automatic White Balance function in the open source image manipulation program GIMP 2.8 (GIMP, 2015). This command automatically adjusts the colours of the image by stretching the red green and blue channels separately. While this solution is not ideal, figure 3 demonstrates it offers a significant improvement. More importantly, the process is fast and can be run on the entire image set using the Batch Image Manipulation Plugin. With a dataset of several thousand images, efficient processing is obviously essential.

Agisoft Photoscan 1.1 (Agisoft LLC, 2015) is a commercially available program for producing photogrammetry models from regular 2D-images. While it does not specifically support underwater imagery, version 1.1 does have fisheye-camera support implemented. A fisheye lens in air displays some of the same warping behaviour as a regular lens in water, and thus improves the result when the software is applied to underwater images. The intrinsic parameters of the cameras were initially unknown and were estimated by the software as part of the aligning process. The aligning process produces a sparse point

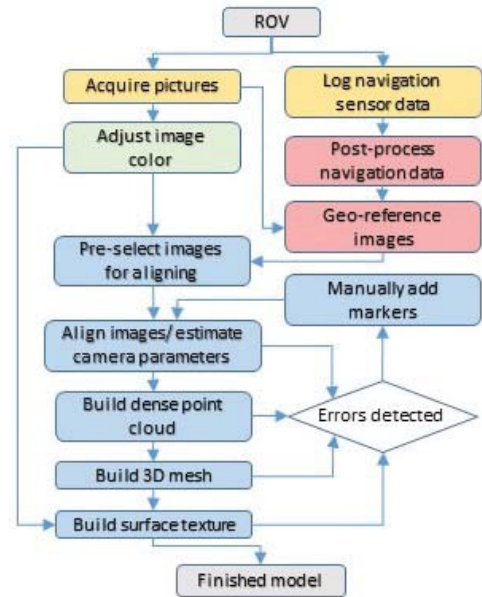


Fig. 2. Processing pipeline. Task color describes the software used: Yellow=LabVIEW (online), green=GIMP, red=MATLAB, blue=Agisoft Photoscan.



Fig. 3. Image from the bow of M/S Herkules, original on the left, colour adjusted on the right

cloud (figure 5), and further processing yields a dense point cloud (figure 6) and a 3D-mesh (figure 7). Finally, a mosaic of the original images are projected onto the 3D mesh, creating the final model seen in figures 8-11.

Poor image quality and lack of discernable features can lead to images being improperly aligned, or not aligned at all. Large, obvious errors in camera orientation or position can be reset directly. More subtle errors can also give a large impact if they accumulate over sequential images, but may remain hidden until later in the processing. To counteract these, markers can be added manually to multiple images indicating a shared feature. The complete model is then realigned with the added information of the marker(s).

	East	North	Altitude	Total
Error (full set)	1.35m	1.40m	0.14m	1.95m
Error (wild point excl.)	0.80m	1.10m	0.14m	1.37m
	Yaw	Pitch	Roll	Total
Error	31.5°	3.9°	5.7°	32.2°

Table 1. Camera accuracies (RMS) estimated by Agisoft

Using the timestamps of the recorded images and the navigation data, the camera positions can be calculated using MATLAB (MathWorks, 2015). Agisoft does calculate its own camera positions, but the navigation data provides geolocalization and scaling of the model. The navigation data also speeds up the aligning process, since the software can skip comparing images that are too far from each other to cover the same scene.

#### 4. RESULTS

Both survey days consisted of approximately 40 minutes of effective ROV-time on the wreck, resulting in a total of 4715 images.

Table 4 displays the root mean square (RMS) difference between the positions provided by the DP-system and the ones calculated by Agisoft. A jump in the absolute position measurement from Gunnerus caused 28 sequential images to receive an obvious error exceeding 10 meters, separate values excluding these images are therefore included. The quality of the navigation data was poor compared to similar cruises with the same system. The wreck may have reflected/blocked the acoustic position measurements. Furthermore, the steel wreck may have influenced the magnetic heading measurements, which in turn causes the error induced by the offset between cameras and acoustic transponder to become significant.

For the Herkules images, 4423 out of the original 4715 images were successfully aligned (figure 4) using 34 manually placed markers. The finished model is comprised of 1,450,000 vertices and 2,900,000 faces.

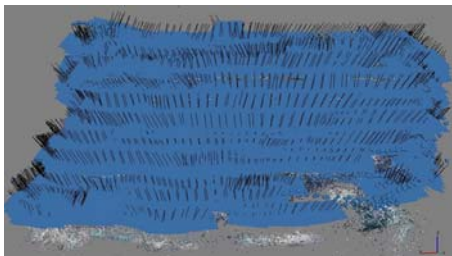


Fig. 4. Aligned cameras seen from starboard

The only quality measurement of the finished model presently available is the high level of consistency. Early results from a separate study on a nearby flat wreck using the same equipment indicates errors in length measurements below 1%, but with significantly better navigation accuracy. Assuming length accuracy is linearly dependant on navigation accuracy, errors in length measurements approaching 3% could be expected for the Herkules model.

A dive using technical scuba divers is planned to be conducted during spring/summer of 2015 to recover various length measurements to be compared to the digital model.



Fig. 5. Sparse point cloud model seen from starboard



Fig. 6. Dense point cloud model seen from starboard

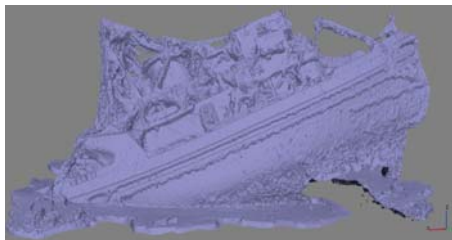


Fig. 7. Mesh model seen from starboard

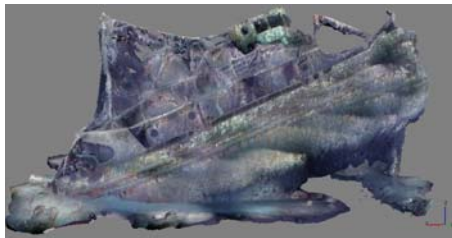


Fig. 8. Finished model seen from starboard

#### 5. DISCUSSION

This section describes the experiences that can be drawn from the Herkules survey, identifying issues that need to be handled and suggesting potential improvements.

The quality of a finished 3D-model will always depend on the quality of the captured images, which in turn depends on the image capture strategy. When comparing the model sides based on images from day 1 (figure 8) and day 2 (figure 10), there is an obvious increase in quality: Figure 8 features highly visible boundary lines between the images captured at different depths, while layer transitions in figure 10 are smooth. This improvement can be attributed to three main causes: Reduced depth intervals leading to increased vertical overlap, increased attention to distance



Fig. 9. Finished model seen from the bow



Fig. 10. Finished model seen from port

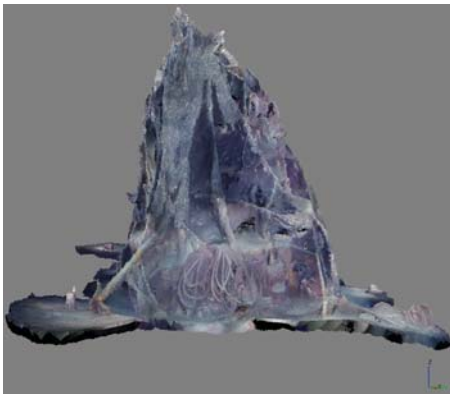


Fig. 11. Finished model seen from the stern

between ROV and wreck giving better image exposure, and a more beneficial positioning of RV Gunnerus leading to higher quality acoustic position measurements.

In our case, having the cameras mounted side by side while having horizontal runlines gave excessive horizontal overlap while vertical overlap at times was too low. To achieve better overlap, the camera rig should be mounted perpendicular to the runlines. Keeping the runlines horizontal and flipping the camera rig might be the simplest solution seen from a navigational standpoint, while opting

to keep the rig horizontal and using vertical runlines may give better ROV stability.

The camera rig with fixed orientation and reduced resolution has been demonstrated to be able to capture a model giving a better overview of the wreck than regular video or scuba diving. This does come with some limitations when it comes to studying smaller objects which may have too low resolution or not enough coverage. Having a mobile high resolution camera, for instance mounted on a robotic arm would allow closer inspection of specific objects of interest, resulting in local high resolution models.

Because light is rapidly attenuated in water, both the distance between the cameras and the target and the distance between the light sources and the target has a high impact on the image quality. As demonstrated in figure 3, even simple post-processing of images can improve the quality, and more advanced post-processing techniques will likely offer further improvements. Any such techniques should be automatic, since the amount of images effectively excludes manual adjustment. However, the end result will always be limited by the raw data, so improving the raw footage through better distance and lighting control should be a high priority. By integrating the stereocameras with the control system, similar to Negahdaripour and Firoozfam (2006), a distance feedback of the overlapping field of vision would be achieved. A more complex single-camera-approach like the Direct camera Pose Registration Structure From Motion (DPR-SFM) of Nicosevici et al. (2009) could also be used, but since the system is already equipped with stereocameras, not utilizing the available stereovision would be counterintuitive.

For a sufficiently large ROV, one could also envision a distributed lighting rig system automatically adjusting an array of lights to ensure even scene exposure. Through the distance feedback of the stereocameras, the round-trip distance of the light (source-scene-camera) from each source could be estimated and the light intensity adjusted accordingly.

Being able to handle mobile biology such as fish, both as part of the online algorithm and during post-processing, will be important when mapping such 3D-structures. Structures rising high above an otherwise flat sea bed tends to attract a lot of biology, and if the creatures move between images, false matches are likely to be produced. Even slow moving biology like starfish might cause issues if the survey is carried out over a prolonged period of time. While Agisoft does contain functionality to mask out unwanted objects, this is very time consuming for a large image set, so some form of automation would be helpful.

The complete dataset, both raw and processed, will provide a useful testbed for implementations of the suggested improvements. The finished 3D-model could be used to generate outputs for cameras of simulated vehicles in any position or orientation. Adding the option of adjusting visibility and lighting conditions would allow assessment of the robustness of an experimental autonomous approach.

ROVs and AUVs can give marine scientists access to areas beyond the traditional limits for diving (e.g. deep or covered waters). With HD cameras and appropriate lights the field of view is not reduced, so visually there should

be no cession of perceptive qualities. Comprehensive interpretation and understanding of features or objects on the seabed with dimensions that far exceeds the field of view can be difficult, and an accurate overview of e.g. a complex wreck site with pronounced 3D-structures is not easy to obtain. ROV-based photogrammetric recording can help marine scientists to overcome such difficulties.

For management of underwater cultural heritage this method will be particularly useful, since the number of relatively large steel wrecks older than one hundred years (UNESCO definition of UCH) will increase significantly in the coming years with all the wrecks from WWI. While many of these ships may have maintained a high degree of structural integrity, disintegration is only a question of time. A precise 3D model combined with full coverage photos will be very useful for interpreting and understanding such wreck sites, and also for determining their state of preservation. It will moreover enable archaeologists to do repeated, precise measurements of the exact same locations when revisiting the site, thus provide relevant data for monitoring purposes or for supporting management strategies and decisions. High resolution photo-rendered 3D-models are of course also very well suited for public dissemination and outreach (Chapman et al., 2006).

## 6. CONCLUSION

We have presented the results of an ROV-based photogrammetric survey of an intact standing steel wreck with a complex structure and high vertical profiles. The resulting 3D-model was reconstructed using available free-ware and commercial software. The results highlight the potential improvements that can be achieved by reducing the reliance on a pilot, both in terms of data quality, but also in reducing the required resources for a survey even further. Further research into increasing the level of autonomy for such a survey is needed, and this dataset will become a useful testbed for new algorithms.

## ACKNOWLEDGEMENTS

This work has been carried out at the Centre for Autonomous Marine Operations and Systems (AMOS). The Norwegian Research Council is acknowledged as the main sponsor of AMOS. This work was partly supported by the Research Council of Norway through the Centres of Excellence funding scheme, Project number 223254 - AMOS.

## REFERENCES

- Agisoft LLC (2015). <http://www.agisoft.com>. Retrieved 9. March.
- Campos, R., Garcia, R., Alliez, P., and Yvinec, M. (2014). A surface reconstruction method for in-detail underwater 3D optical mapping. *The International Journal of Robotics Research*.
- Chapman, P., Conte, G., Drap, P., Gambogi, P., Gauch, F., Hanke, K., Long, L., Loureiro, V., Papini, O., Pascoal, A., Richards, J., and Roussel, D. (2006). VENUS, Virtual Exploration of Underwater Sites. In *The 7th International Symposium on Virtual Reality, Archaeology and Cultural Heritage, VAST*.
- Demesticha, S., Skarlatos, D., and Neophytou, A. (2014). The 4th-century B.C. shipwreck at Mazotos, Cyprus: New techniques and methodologies in the 3D mapping of shipwreck excavations. *Journal of Field Archaeology*, 39, 134–150.
- Drap, P., Merad, D., Mahiddine, A., Seinturier, J., Peloso, D., Boi, J.M., Chemisky, B., and Long, L. (2013). Underwater Photogrammetry for Archaeology. What Will Be the Next Step? *International Journal of Heritage in the Digital Era*, 2, 375–394.
- Dukan, F., Ludvigsen, M., and Sørensen, A.J. (2011). Dynamic positioning system for a small size ROV with experimental results. In *OCEANS 2011 IEEE - Spain*.
- Dykkepedia (2015). <http://www.dykkepedia.com/wiki/Herkules>. Retrieved 9. March.
- Foley, B.P., Dellaporta, K., Sakellariou, D., Bingham, B.S., Camilli, R., Eustice, R.M., Evagelistis, D., Ferrini, V.L., Katsaros, K., Kourkoumelis, D., Mallios, A., Micha, P., Mindell, D.A., Roman, C., Singh, H., Switzer, D.S., and Theodoulou, T. (2009). The 2005 Chios Ancient Shipwreck Survey: New Methods for Underwater Archaeology. *Hesperia: The Journal of the American School of Classical Studies at Athens*, 78(2), 269–305.
- GIMP (2015). <http://www.gimp.org/>. Retrieved 9. March.
- Gracias, N., Ridao, P., Garcia, R., Escartin, J., L'Hour, M., Cibecchini, F., Campos, R., Carreras, M., Ribas, D., Palomeras, N., Magi, L., Palomer, A., Nicosevici, T., Prados, R., Hegedus, R., Neumann, L., de Filippo, F., and Mallios, A. (2013). Mapping the Moon: Using a lightweight AUV to survey the site of the 17th century ship 'La Lune'. In *OCEANS - Bergen, 2013 MTS/IEEE*, 1–8.
- Johnson-Roberson, M., Pizarro, O., Williams, S.B., and Mahon, I. (2010). Generation and visualization of large-scale three-dimensional reconstructions from underwater robotic surveys. *Journal of Field Robotics*, 27(1), 21–51.
- MathWorks (2015). <http://se.mathworks.com/products/matlab/>. Retrieved 9. March.
- McCarthy, J. and Benjamin, J. (2014). Multi-image Photogrammetry for Underwater Archaeological Site Recording: An Accessible, Diver-Based Approach. *Journal of Maritime Archaeology*, 9(1), 95–114.
- Meline, A., Triboulet, J., and Jouvenel, B. (2012). Comparative study of two 3D reconstruction methods for underwater archaeology. In *Intelligent Robots and Systems (IROS), 2012 IEEE/RSJ International Conference on*, 740–745.
- Negahdaripour, S. and Firoozfam, P. (2006). An ROV Stereovision System for Ship-Hull Inspection. *Oceanic Engineering, IEEE Journal of*, 31(3), 551–564.
- NI (2015). <http://www.ni.com/labview/>. Retrieved 9. March.
- Nicosevici, T., Gracias, N., Negahdaripour, S., and Garcia, R. (2009). Efficient Three-dimensional Scene Modeling and Mosaicing. *J. Field Robot.*, 26(10), 759–788.
- Sørensen, A.J., Dukan, F., Ludvigsen, M., Fernandez, D.A., and Candeloro, M. (2012). *Further Advances in Unmanned Marine Vehicles*, chapter 6: Development of Dynamic Positioning and Tracking System for the ROV Minerva, 113–128. IET, UK.
- UNESCO (2015). The UNESCO convention on the protection of the underwater cultural heritage. [http://www.unesco.org/new/fileadmin/MULTIMEDIA/HQ/CLT/UNDERWATER/pdf/Info\\_kit/GB-2001CONVENTION-INFOKIT%2007-2009.pdf](http://www.unesco.org/new/fileadmin/MULTIMEDIA/HQ/CLT/UNDERWATER/pdf/Info_kit/GB-2001CONVENTION-INFOKIT%2007-2009.pdf), Retrieved 9. March.

# Article D

## Underwater vehicles for environmental management in coastal areas

---

Martin Ludvigsen, Terje Thorsnes, Roy E. Hansen, Asgeir J. Sørensen,  
Geir Johnsen, Petter A. Lågstad, Øyvind Ødegård, Mauro Candeloro,  
**Stein M. Nornes**, and Christian Malmquist

ARTICLE D

---

This article is published in the proceedings of  
*MTS/IEEE OCEANS 2015*. Genova, Italy, 18-21 May 2015.  
doi: 10.1109/OCEANS-Genova.2015.7271728

Is not included due to copyright



# Article E

## Use of an Autonomous Surface Vehicle reveals small-scale diel vertical migrations of zooplankton and susceptibility to light pollution under low solar irradiance

---

Martin Ludvigsen, Jørgen Berge, Maxime Geoffroy, Jonathan H. Cohen, Pedro R. de la Torre, **Stein M. Nornes**, Hanumant Singh, Asgeir J. Sørensen, Malin Daase and Geir Johnsen

ARTICLE E

This article is published in *Science Advances*, vol. 4 (1), eaap9887, 2018.  
doi: 10.1126/sciadv.aap9887



## ENVIRONMENTAL STUDIES

## Use of an Autonomous Surface Vehicle reveals small-scale diel vertical migrations of zooplankton and susceptibility to light pollution under low solar irradiance

Martin Ludvigsen,<sup>1,2\*</sup> Jørgen Berge,<sup>2,3,4,\*†</sup> Maxime Geoffroy,<sup>4,5\*</sup> Jonathan H. Cohen,<sup>6\*</sup> Pedro R. De La Torre,<sup>1</sup> Stein M. Nornes,<sup>1</sup> Hanumant Singh,<sup>7</sup> Asgeir J. Sørensen,<sup>1</sup> Malin Daase,<sup>2</sup> Geir Johnsen<sup>2,3\*</sup>

Light is a major cue for nearly all life on Earth. However, most of our knowledge concerning the importance of light is based on organisms' response to light during daytime, including the dusk and dawn phase. When it is dark, light is most often considered as pollution, with increasing appreciation of its negative ecological effects. Using an Autonomous Surface Vehicle fitted with a hyperspectral irradiance sensor and an acoustic profiler, we detected and quantified the behavior of zooplankton in an unpolluted light environment in the high Arctic polar night and compared the results with that from a light-polluted environment close to our research vessels. First, in environments free of light pollution, the zooplankton community is intimately connected to the ambient light regime and performs synchronized diel vertical migrations in the upper 30 m despite the sun never rising above the horizon. Second, the vast majority of the pelagic community exhibits a strong light-escape response in the presence of artificial light, observed down to 100 m. We conclude that artificial light from traditional sampling platforms affects the zooplankton community to a degree where it is impossible to examine its abundance and natural rhythms within the upper 100 m. This study underscores the need to adjust sampling platforms, particularly in dim-light conditions, to capture relevant physical and biological data for ecological studies. It also highlights a previously uncharted susceptibility to light pollution in a region destined to see significant changes in light climate due to a reduced ice cover and an increased anthropogenic activity.

## INTRODUCTION

At any given moment in time, half Earth's surface is in the dark. Although darkness prevails, processes induced by solar illumination are considered to be inactive. When it is dark, light is often considered as pollution that potentially affects light-controlled rhythms and behavior. However, darkness is a relative state, and even small natural changes in ambient solar and lunar light may have an effect on marine organisms (1, 2). Light-induced responses on animal behavior during dark or dim conditions have been documented for a variety of environments and organisms. For instance, lunar illumination affects zooplankton and micronekton, as well as their predators in tropical, subtropical, and Arctic waters (1, 3–6). In addition, changes in ambient light can affect the vertical distribution of deep scattering layers down to 1000 m in deep-sea environments (7). Despite an increased awareness that small changes in natural light affect the behavior of marine organisms in naturally dim environments, we are only starting to understand how and why organisms respond to changes in light that occur on scales below what most commercial sensors can detect (1, 2, 8, 9).

Artificial light pollution is widespread in the marine environment, with increased shipping and light fishing that introduce a substantial

source of disturbance in an otherwise dim environment (8). However, the effects and behavioral responses to this light pollution are still poorly understood (8), not the least in the marine Arctic characterized by constant daylight during summer and prevailing darkness during the polar night. Toward the poles, the period of total winter darkness (and summer midnight sun) increases gradually (Fig. 1) (1, 2). At its extreme, the entire year is simply one long day and one long night—each 6 months in duration at the North Pole. However, although illumination at summer solstice does not change radically with latitude, the polar night not only becomes longer but also crucially darker along a latitudinal gradient (Fig. 1). At the same time, and because of the fact that sea ice reduces light penetration into the underlying water by up to 99%, the region destined to see the greatest relative change in its light climate following both a retreat of the ice cover and increased human activities is the central Arctic Ocean during the polar night (Fig. 1). In this marine environment, increased shipping and anthropogenic presence may introduce a substantial source of disturbance in an otherwise dim environment. Because biological responses to small variations in both solar and lunar illumination have been documented (1, 9, 10), we hypothesize that the susceptibility to light pollution is at its extreme in this region.

Among biological responses are diel vertical migrations (DVMs) or cyclic patterns of vertical movement synchronized with variations in irradiance that are commonly observed in zooplankton (11, 12) and fish (13, 14) across all aquatic habitats. DVM is triggered by light (15) but ultimately driven by predator-prey interactions (16) and the need to avoid depths with light intensities sufficient for visual predators. On acoustic echograms, a DVM pattern is seen as one or more sound scattering layers (SSLs) migrating vertically according to a diel cycle in illumination (16). At high latitudes, DVMs have been considered to be less prominent (17, 18), because the absence of day/night cycles

<sup>1</sup>Centre of Autonomous Marine Operations and Systems (AMOS), Department of Marine Technology, Norwegian University of Technology and Science (NTNU), Trondheim, Norway. <sup>2</sup>Departments of Arctic Biology and Technology, University Centre in Svalbard, Longyearbyen, Norway. <sup>3</sup>Centre for Autonomous Operations and Systems, Department of Biology, NTNU, Trondheim, Norway. <sup>4</sup>Department Arctic and Marine Biology, Faculty for Bioscience, Fisheries and Economy, UiT The Arctic University of Norway, Tromsø, Norway. <sup>5</sup>Centre for Fisheries Ecosystems Research, Memorial University of Newfoundland, St. John's A1C 5R3, Canada. <sup>6</sup>School of Marine Science and Policy, University of Delaware, Lewes, DE 19958, USA. <sup>7</sup>Department of Electrical and Computer Engineering, Northeastern University, Boston, MA 02115, USA.

\*These authors contributed equally to this work.

†Corresponding author. Email: jorgen.berge@uit.no

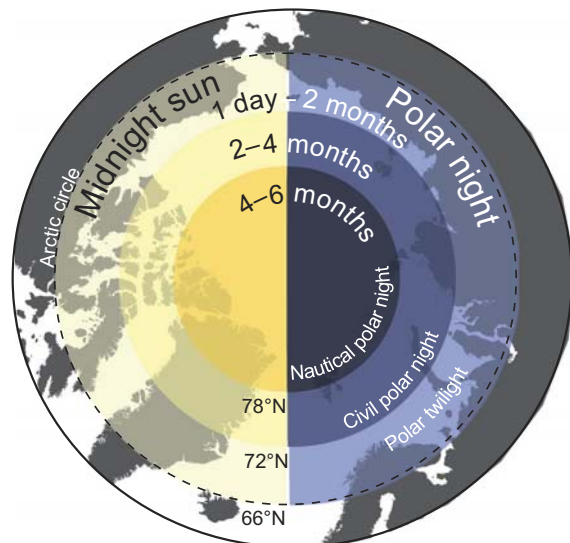


**Fig. 1. The light-climate regions of the Arctic.** Circles of yellow (left) indicate duration of the midnight sun period (3). Circles of blue (right) indicate duration of the polar night period with illumination at winter solstice defined as polar twilight (outer), civil polar night (middle), and nautical polar night (inner).

during extended periods of either midnight sun or polar night leaves organisms without temporal refuge. However, recent studies have documented that zooplankton, particularly krill, carry out DVM during the polar night and in particular during periods of civil twilight (solar altitude not exceeding  $0^\circ$  to  $-6^\circ$ ) (19, 20). Although preliminary studies also reported DVM during nautical polar night (solar altitude not exceeding  $-6^\circ$  to  $-12^\circ$ ) (19), and in response to lunar light (1), no study has unequivocally described DVM in response to the diel solar irradiance cycle during nautical polar night. We hypothesize that this is partly due to research vessels introducing an artificial light field, biasing measurements of both natural ambient light and light-dependent ecological processes (10, 21–25). If present, then DVM during the darkest period of the polar night is likely restricted to surface layers and temporally centered on the very short period of elevated light intensity at solar noon due to small variations in ambient light that can only be detected by organisms near the surface (9). Other sampling issues apart from light pollution may bias DVM detections under low solar irradiance conditions. Towed zooplankton nets generally have a coarse vertical sampling resolution ( $>10$  m), whereas bottom-moored and hull-mounted echo sounders generally fail to provide data from the upper 5 to 15 m of the water column due to the conical shape of the acoustic beam, strong reflection at the water-air interface, and/or to the ship's draft that adds to the near-field region (26). Thus, using these traditional sampling methods during dark periods, such as the Arctic polar night, we potentially miss crucial processes occurring in the upper water column.

Autonomous Surface Vehicles (ASVs) provide new opportunities for marine studies (27). These vehicles do not require facilities to provide an operator or helmsman with working light, safety, and comfort, which results in smaller and more efficient platforms without artificial light, particularly beneficial in the Arctic where heavy logistics is necessary for human presence and security. The automated behavior of these systems not only provides increased accuracy and repeatability of

maneuvering during data collection over larger temporal and spatial scales (28) but also offers a unique opportunity to autonomously sample in an undisturbed environment without introducing artificial light (29), an aspect critical to this study.

Here, we test the use of the Jetyak, a purpose-built ASV fitted with a multifrequency echo sounder and a spectroradiometer to study the distribution and potential DVM of zooplankton during the polar night in Kongsfjorden, a high Arctic fjord on Svalbard (fig. S1). By comparing the data provided from the ASV with those from manned research vessels, we also investigate the impact of artificial light on the pelagic community and the ability of traditional sampling platforms to provide data that represent the natural state of the ecosystem in the upper 50 to 100 m of the water column during dark periods.

## RESULTS

### Variations in diffuse skylight irradiance

During the Jetyak deployments over three consecutive days (21 to 23 January 2016), the sun remained below the horizon with inclination angles at solar noon of  $-8.9^\circ$ ,  $-8.7^\circ$ , and  $-8.4^\circ$ , respectively. The waxing moon (full on 24 January) was above the horizon all day at inclination angles of  $6^\circ$  to  $10^\circ$  during the times of deployment. During the 21 January deployment, scattered clouds resulted in diffuse skylight irradiance ( $E_d$ ) at the water's surface initially decreasing early in the deployment (minimum at  $\sim 0.012 \mu\text{W m}^{-2}$  or  $5.5 \times 10^{-9} \mu\text{mol photons m}^{-2} \text{s}^{-1}$ ) before increasing around the time of solar noon (1123 GMT) (maximum at  $\sim 0.017 \mu\text{W m}^{-2}$  or  $8.0 \times 10^{-9} \mu\text{mol photons m}^{-2} \text{s}^{-1}$ ) followed by decreasing irradiance at the end of the deployment (fig. S2). Longer deployments on 22 and 23 January provided a more complete measurement of the solar cycle with increasing and decreasing  $E_d$  about solar noon (1124 GMT) (Fig. 2A and fig. S2). Minimum irradiances for deployments on 22 and 23 January were 0.0031 and 0.0017  $\mu\text{W m}^{-2}$  ( $1.6 \times 10^{-8}$  and  $8.8 \times 10^{-9} \mu\text{mol photons m}^{-2} \text{s}^{-1}$ ), respectively. Maximum irradiances were 0.0091 and 0.0084  $\mu\text{W m}^{-2}$  ( $4.9 \times 10^{-8}$  and  $4.6 \times 10^{-8} \mu\text{mol photons m}^{-2} \text{s}^{-1}$ ).

### SSLs and DVMs

An SSL was present in the top 50 m during all three deployments (fig. S2). The SSL was slightly deeper in shallow than in deep areas, which explains the bottom-related oscillation within the echograms, as the Jetyak was cruising back and forth from deep to shallow areas (fig. S2). The median depth of the SSL significantly increased with irradiance (Spearman's rank correlation;  $P \leq 0.001$ ; Fig. 2A and fig. S2). This correlation indicates the occurrence of a small-scale (6 to 8 m) light-triggered DVM within the top 50 m during the polar night. The acoustic backscatter was stronger at 455 kHz than at 200 and 125 kHz for 58% of the echo integration cells within this SSL on 21 January, 60% on 22 January, and 67% on 23 January, indicating that copepods dominated the assemblage (30). Copepods, mainly *Calanus* spp., *Pseudocalanus* spp., and *Oithona similis*, also dominated the zooplankton assemblage from two multinet (180- $\mu\text{m}$  mesh size) deployments in Kongsfjorden during the survey, particularly in the 20- to 0-m strata (fig. S4). The speeds of ascent and descent measured at 455 kHz (that is, the frequency that better detects copepods) varied from 0.06 to 0.72  $\text{cm s}^{-1}$  and from 0.07 to 1.33  $\text{cm s}^{-1}$ , respectively (table S1).

### Depth limit of *Calanus* light detection

To independently assess whether the DVM of 6- to 8-m amplitude observed in the acoustics could be in response to changes in the ambient

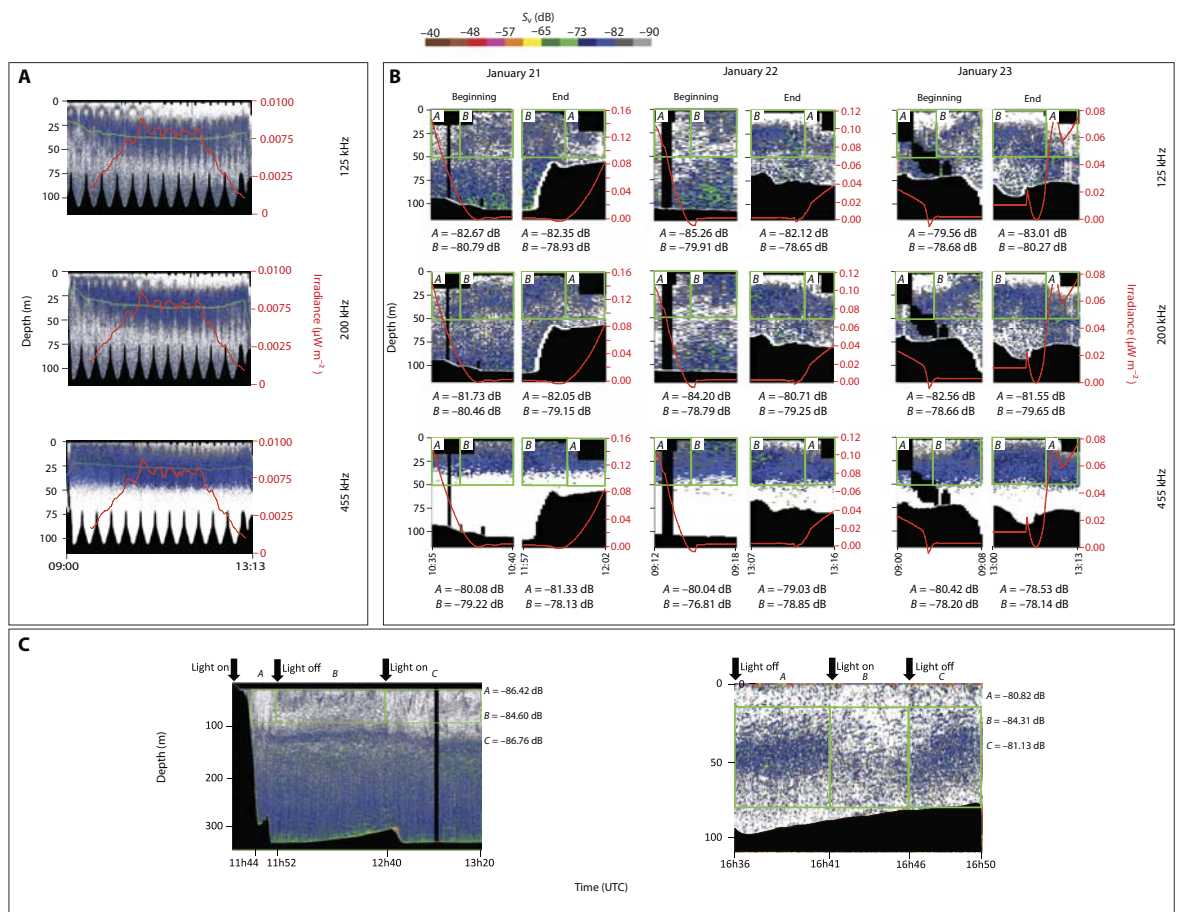


**Fig. 2. Volume backscattering ( $S_v$ ) echograms.** (A) Acoustic Zooplankton Fish Profiler (AZFP; ASL Environmental Science Inc.) echograms at 125 (dominated by euphausiids), 200 (dominated by chaetognaths), and 455 kHz (dominated by copepods) on 23 January. The red line (and second y axis) indicates the irradiance ( $\mu\text{W m}^{-2}$ ) when away from the ship. The green line indicates the median depth of the SSL at each frequency. Note that a time-varied threshold of  $-122$  dB was applied at 455 kHz. (B) AZFP echograms at 125, 200, and 455 kHz at the beginning and at the end of each survey. The red line indicates the irradiance, and the green boxes indicate acoustic backscatter data collected in the top 50 m (A) close to the ship and (B) away from the ship. Mean  $S_v$  within each box is indicated below the echograms. (C) Responses of zooplankton to ambient versus artificial light. The RV *Helmer Hanssen* EK60 echogram was recorded at 120 kHz in Kongsfjorden on 9 January 2017 (left) and the AZFP echogram at 125 kHz was recorded from a small boat in Kongsfjorden on 21 January 2017 (right). Black arrows indicate when the lights were turned off and on, and the SSL responds accordingly with avoidance during the “Light on” period. In all echograms, black areas mask the near-field region, noise, and areas below the seafloor.

light field at depth, we modeled how diffuse skylight irradiance measured from the Jetyak propagated through the water column. The resulting quantity of light [scalar irradiance,  $E_0(\lambda)$ ] was calculated over time at 1-m depth intervals on 23 January.  $E_0(\lambda)$  represents light in all directions and is therefore ecologically relevant to visual systems capable of detecting light from a broad range of angles, as is the case for copepods (31). Furthermore, we weighted  $E_0(\lambda)$  by the light capture capabilities of *Calanus* spp. copepods, which dominated the assemblage, yielding a measure of light in terms of “*Calanus*-utilized light” that most closely represents the light available to copepods. Spectral irradiance calculated this way was maximal at 500 nm throughout the measurement period and across depth. According to Båtnes *et al.* (32), an

isolume of  $5 \times 10^{-8}$   $\mu\text{mol photons m}^{-2} \text{ s}^{-1}$  (as *Calanus*-utilized light) represents a photo-behavioral irradiance threshold for *Calanus* spp. On 23 January, we calculated this isolume to be located at 51.5-m depth at 9:30, descending to a maximum of 60-m depth at 12:00, and then shoaling to 53-m depth at 13:00 (Fig. 3). Thus, on the basis of the underwater light field and *Calanus* spp. sensitivity to light, we predict DVM of  $\sim 8$  m for these copepods during the Jetyak deployments.

#### Artificial light affecting the zooplankton community

Diffuse skylight irradiance increased by 15 times when the Jetyak departed or returned to the research vessel (that is, at the beginning

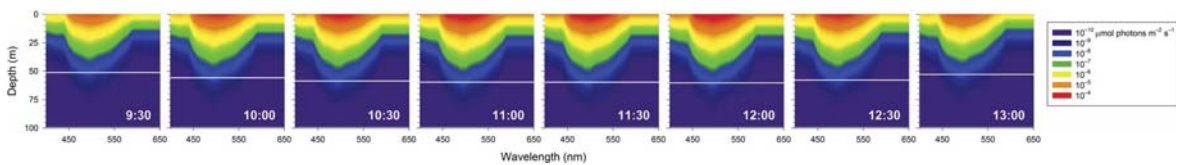


**Fig. 3. Modeled depth of a constant light level (isolume) set to be the depth limit of copepod light-mediated behavior in Kongsfjorden.** Underwater spectral scalar irradiance [ $E_0(\lambda)$ ,  $\mu\text{mol photons m}^{-2} \text{s}^{-1}$ ] was weighted by the spectral response of *C. finmarchicus* to yield a photometric quantity of *Calanus*-utilized light that is shown in colored contours as a function of depth at 30-min intervals on the 23 January Jetyak deployment. White horizontal lines show the depth of an isolume at  $5 \times 10^{-8} \mu\text{mol photons m}^{-2} \text{s}^{-1}$  of *Calanus*-utilized light. UTC, coordinated universal time.

and end of all deployments) (Fig. 2B). Irradiance increased from  $<0.01 \mu\text{W m}^{-2}$  ( $\sim 5 \times 10^{-9} \mu\text{mol photons m}^{-2} \text{s}^{-1}$ ) away from the RV *Helmer Hanssen* to over  $0.15 \mu\text{W m}^{-2}$  ( $\sim 7 \times 10^{-7} \mu\text{mol photons m}^{-2} \text{s}^{-1}$ ) in its vicinity. The mean volume acoustic backscattering strength ( $S_v$ , calculated in the linear form before being transformed in dB re  $1 \text{ m}^{-1}$ ) in the top 50 m was consistently lower close to the ship compared to areas not affected by artificial light sources (Fig. 2B). This impact had a horizontal footprint varying from 22 to 188 m from the boat, depending on the deployment. The ship draft ( $\sim 7$  m) and the near field of the EK60 echo sounder (3.3 m at 120 kHz) resulted in a 10.3-m blind zone below the RV *Helmer Hanssen*, which prevented the detection of vertical migrations just below the surface (fig. S3). In comparison, the blind zone of the Jetyak-mounted AZFP was  $\sim 2$  m.

In January 2017, further testing in Kongsfjorden with the RV *Helmer Hanssen* (Fig. 2C, left) and an 8-m-long Polarcirkel boat (Fig. 2C, right) confirmed that zooplankton in the SSL avoided artificial light and that the effect can reach depths of  $>80$  m. Zooplankters rapidly came back to their normal distribution once the lights were turned off (Fig. 2C).

## DISCUSSION

The DVM of zooplankton is the most widespread and synchronized movement of biomass on the planet (33) and thus is one of the most important factors to consider for understanding marine food-web interactions and ecosystem structures (16). In the high Arctic, this behavior has been frequently observed during autumn and spring when the day/night cycle is pronounced [(2, 34) and references therein], whereas a number of studies have failed to find any coordinated vertical migration during periods of continuous light or darkness (18, 35). Despite this, Berge *et al.* (19) detected a synchronized DVM of zooplankton from two fjords in Svalbard ( $78^\circ$  and  $80^\circ\text{N}$ ), even during the darkest period of the polar night, using moored acoustic instruments. These behaviors have biogeochemical significance. Vertical transport to depth of millions of tons of organic carbon through zooplankton DVM contributes to ocean uptake and sequestration of  $\text{CO}_2$  and represents an important process for the mitigation of the planetary greenhouse effect causing climate change (30, 36). However, this process is poorly quantified at high latitudes, partly due to a lack of quantitative measurements of polar night DVM (20). Our results are the first to unequivocally show that short-ranged DVMs, with an amplitude of only 8 m, occur under natural light conditions. This DVM is restricted to the upper 20 m of the water column (Fig. 4). Furthermore, our results suggest that artificial light from both a large research vessel and headlamps on a small open vessel introduce light pollution that induce an avoidance response in the pelagic community down to more than 80-m depth. Consequently, any attempt to quantify DVMs and their biogeochemical impact in the

upper water column during polar night or any other low solar irradiance condition will be insufficient if traditional sampling methods are used.

Avoidance of artificial light from ships at night by marine organisms has been previously documented for euphausiids down to 60 m on the Nova Scotia continental shelf (37). Furthermore, artificial light is known to affect the distribution of fish by either attracting or repulsing them (38, 39). In addition, a recent study using data sets from across the Arctic, including Kongsfjorden, documented moonlight effects on the vertical distribution of zooplankton down to around 50 m (1). Here, we demonstrated that most of the zooplankton community avoided artificial light from research vessels during the polar night, biasing measurements of abundance, vertical distribution, and DVM. Copepods dominated the zooplankton assemblage and the acoustic signal, and they were most likely performing DVM under ambient conditions and avoiding artificial light. However, the difference in  $S_v$  in the proximity and away from the ship was generally greater at 125 than at 455 kHz (Fig. 2B), indicating that zooplankton larger than copepods also avoided artificial light.

Each time the Jetyak approached the RV *Helmer Hanssen*, the acoustic signal showed that zooplankton reacted by avoiding the artificial light field of the vessel (that is, the acoustic backscatter decreased) rather than slowly descending as when ambient irradiance was changing gradually. This effect could be seen up to  $\sim 190$  m away from the ship. Change in light intensity is a well-known cue for initiating zooplankton DVM and other predator-avoidance behavior (15). However, and although our data do not allow for a quantification of swimming speed, the observed response appeared immediate and faster than any previously reported average swimming speeds. The reported swimming speed for euphausiids (for example, *Thysanoessa* spp.) is in the range of 10 to 45  $\text{mm s}^{-1}$  (40, 41) and 2 to 30  $\text{mm s}^{-1}$  with an escape speed of up to 120 to 400  $\text{mm s}^{-1}$  for *Calanus* spp. (42, 43). With an acoustic beam angle of  $7^\circ$ , the maximum distance to exit the beam is 1.2 m at 20-m depth, 3.1 m at 50-m depth, and 6.1 m at 100-m depth. Applying a combination of the fastest swimming speeds and escape speeds reported, the escape time for these organisms would range in the order of 0.5 to 2 min, depending on depth. In addition, a synchronized change in orientation relative to the light and acoustic beam could explain part of the reduction in observed  $S_v$  values. Further surveys should focus on identifying the main functional groups reacting to artificial light; however, we conclude that the observed and sudden reduction in  $S_v$  values following the introduction of artificial light (Fig. 2) could plausibly be explained by the reported swimming and escape speeds of *Calanus* spp. and *Thysanoessa* spp. We also suggest that the sudden and sustained increase in irradiance in an otherwise dim environment caused by the bright artificial illumination of the ship, as well as the seemingly insignificant illumination caused by researcher headlamps on an open

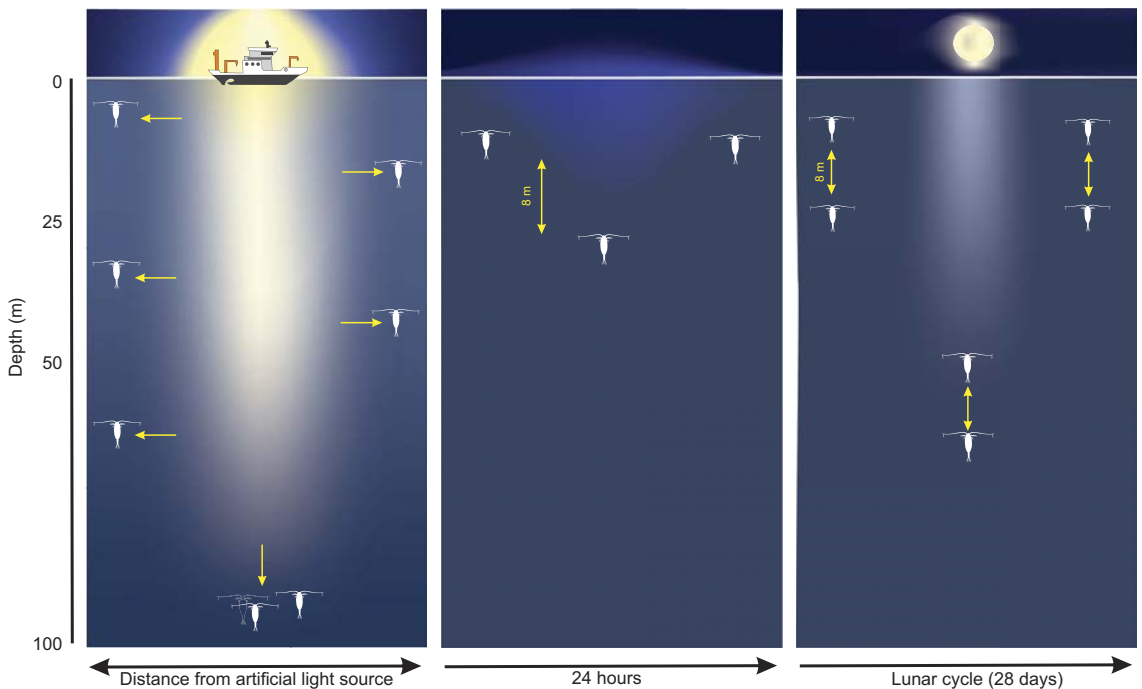


**Fig. 4. Conceptual model of the behavioral response of zooplankton to natural solar light, light pollution, and lunar light.** (A) Light escape response (vertical and horizontal arrows) from light pollution from a ship detected down to 100 m and up to 180 m on each side of the ship. (B) DVM of zooplankton in response to natural ambient light during the polar night. Centered around noon, organisms perform a DVM with an amplitude of 8 m within the upper 20 m of the water column. (C) In response to lunar light, zooplankton and fish perform DVM but at different depths depending on the moon phase.

boat (Fig. 2C), resulted in zooplankters rapidly moving down and/or laterally to return to their ambient illumination conditions (Fig. 4A).

Using an ASV capable of both measuring ambient light in a natural environment and taking acoustic profiles of zooplankton in the water column, we provide evidence of DVM synchronized with background illumination of the sun even during the polar night, when the sun remains over  $8^\circ$  below the horizon. The low-amplitude (6 to 8 m) DVM behavior included a slow but significant descent centered around solar noon within the upper 30 m of the water column (Fig. 4B). This is in line with the results presented by Last *et al.* (1) who reported a mass escape from the upper 50 m of the water column during periods of full moon during the polar night (Fig. 4C). The vertical distribution of biomass follows the change in ambient irradiance and is hence indicative of the proximate role of light as a cue for vertical movement of zooplankton in the SSL in the middle of the polar night. In particular, the observed magnitude of SSL migration matches the  $\sim 8$ -m shift in the depth of the modeled isolume over the 23 January deployment (Fig. 3). Although the lower SSL limit is near the isolume depth, the discrepancy between median SSL depth at 455 kHz (15 to 33 m) and isolume depth (51.5 to 60 m) is likely due in part to the choice of ambient irradiance that we tracked ( $5 \times 10^{-8} \mu\text{mol photons m}^{-2} \text{s}^{-1}$  of *Calanus*-utilized light). This value approximates the absolute photo-behavioral threshold of *Calanus* spp. (32), and it is probable that the median photosensitivity for copepods in SSLs is not that low. Although copepods dominated the assemblage within the SSL, a slight difference ( $<10$  m) between the median depth of the SSL at 125, 200, and 455 kHz (Fig. 2A and fig. S2)

suggests that other functional groups also conducted DVM, which could partly explain the discrepancy between median SSL depth and isolume depth. Polar night DVMs have previously been reported on the basis of moored acoustic instruments (19, 30); however, it has never been possible to quantitatively sample nor detect this behavior using traditional nets or ship-borne acoustics (20). In light of the data presented herein, this is likely due to the avoidance of zooplankton in the upper 100 m of the water column when exposed to artificial light from research vessels (Fig. 4A). The short vertical extent of the DVM behavior also provides an explanation as to why polar night DVM has often remained undetected by moored acoustic surveys (34), and on the basis of the reported observations herein, we postulate that the vertical bin size used in previous acoustic analyses (generally 4 m) has usually been too deep to detect such a pattern.

Recognition of artificial light effects on DVM is not new (44); however, our work highlights a particular vulnerability for zooplankton in the Arctic during the polar night period, which extends up to 6 months. Artificial light is poised to increase in this region with sea ice loss facilitating new shipping routes and opportunities for oil and gas exploration and production, activities that lead to light pollution and cascading ecological consequences (23, 45). Light transmits well in the optically clear water before the spring bloom (9, 46), with the potential to affect organisms far deeper than in more turbid water. This combination of high susceptibility to light pollution and the predicted increased anthropogenic activity in high Arctic seas has the potential to severely affect natural rhythms and processes at a local scale.

Our results suggest that ship-based acoustic measurements or net sampling conducted under dim-light conditions result in abundance estimates lower than reality. Thus, studies of light-dependent behaviors in organisms during polar night or at night in optically clear water need to be devoid of any artificial light to ensure ecologically sound measurements. Together, these findings suggest that certain aspects of the polar marine ecosystems are extremely sensitive to potential light pollution and that traditional sampling techniques are insufficient to study them. Although this study was carried out in the high Arctic and during the polar night, similar effects are to be expected for nighttime processes in other parts of the globe. ASVs, such as the Jetyak, could represent better instrument-carrying platforms than research vessels and small manned boats for detecting vertical migrations of zooplankton and nekton near the surface under dim-light conditions due to (i) a smaller acoustic blind zone and (ii) the absence of artificial light that results in ship avoidance of the animals. If larger vessels are used, then artificial light sources from the ship need to be turned off when sampling zooplankton at night. In any case, biological sampling during the polar night needs to be reshaped around small-scale migrations and strong light avoidance behavior.

## MATERIALS AND METHODS

### The ASV Jetyak

The Jetyak ASV was first developed by the Woods Hole Oceanographic Institution based on a commercially available polyethylene single-person kayak (47). The vessel's shape was similar to that of a river kayak, but it was fitted with a petrol engine driving a water jet unit at the aft. The vehicle was 3 m long and 0.9 m wide, weighed 160 kg, and had an operational range of 8 hours at a speed of 7 to 11 knots. The onboard control system allowed the vehicle to follow preprogrammed transect lines or to operate in a remotely controlled mode. Batteries provided power for the control systems as well as navigation and scientific instruments. A radio frequency modem provided low-bandwidth communication for the Jetyak at ranges up to 20 km.

### Study area and design

The Jetyak was deployed three consecutive days in Kongsfjorden in 2016, on the west coast of the Svalbard archipelago, and a total of 54.7 km of transects was ran (Table 1). Kongsfjorden is 26 km long, and the inlet was approximately 10 km wide, with the deepest point at approximately 370 m depth (fig. S1). Ice floes and growlers from the glaciers Kronebreen and Kongsbreen were encountered during the survey. The Jetyak was deployed from the RV *Helmer Hanssen*

and programmed to patrol a predefined transect while continuously measuring diffuse atmospheric light intensities and acoustic backscatter from zooplankton before and after solar noon. Manual remote control was used during the launch and recovery. On the basis of the results obtained in 2016, acoustic measurements with and without light were conducted from RV *Helmer Hanssen* and from an 8-m-long Polarcirkel boat in Kongsfjorden in January 2017 to test the potential light avoidance by the zooplankton community.

### Sampling and processing of hydroacoustic data

A downward-looking AZFP was mounted in the sea chest of the Jetyak and recorded hydroacoustic data at 125, 200, 455, and 769 kHz during transects. Because the range of the 769-kHz transducer is limited to a few meters below the instrument, only data from the three lower frequencies were considered in this study. Vertical spatial resolution was 1 m, pulse duration was 300  $\mu$ s, source level was 210 dB (reference 1  $\mu$ Pa at 1 m), and ping rate was 1 ping 2  $s^{-1}$  (0.5 Hz). The AZFP was calibrated by the manufacturer ( $\pm 1$  dB) before deployment. In parallel, acoustic data were continuously recorded from a ship-based multifrequency (18, 38, and 120 kHz) Simrad EK60 echo sounder calibrated before departure and located approximately 1 to 2 km from the Jetyak throughout its missions.

Acoustic data were processed with EchoView 6.1. Noise and the near-field region (48) were excluded from the analysis. Conductivity-temperature-depth (CTD) profiles provided the average sound speed and coefficient of absorptions. A time-varied threshold ranging from  $-118$  to  $-122$  dB at 1 m was added to the 455-kHz echogram to offset noise amplification at depth by the time varied gain (49). The echograms were divided into 1-m-vertical by 1-min-horizontal echo-integration cells, and the mean volume acoustic backscattering strength ( $S_v$  in decibel reference 1  $m^{-1}$ ) within each cell was exported at each frequency. For each cell, the mean  $S_v$  at each frequency was compared to determine the dominant scattering zooplankton group. Following the model described in Darnis *et al.* (30) for Kongsfjorden, cells with  $S_{v125kHz} > S_{v200kHz} < S_{v455kHz}$  were assumed to be dominated by euphausiids, cells with  $S_{v125kHz} < S_{v200kHz} < S_{v455kHz}$  by copepods, and cells with  $S_{v125kHz} < S_{v200kHz} > S_{v455kHz}$  by chaetognaths. To eliminate the effects of bathymetry on the depth of the SSL, the echograms were divided into deep (that is, in the middle of transects) and shallow (that is, at the end of transects) echograms (fig. S2). For each of these echograms, the depths of the top and bottom edges of the SSL at each frequency were identified by the  $-82$  dB backscatter contour, and the median depth of the SSL was exported. The median SSL depths from the deep and shallow echograms were then averaged to obtain the

**Table 1. Details of the ASV deployments.** Time is local time (GMT + 1 hour).

Date	Number of transects	Duration	Start time	End time	Platform	Distance (km)
21 January 2016	2	00:47	10:42	11:29	ASV Jetyak	4.5
22 January 2016	21	03:30	09:22	12:52	ASV Jetyak	23.9
23 January 2016	23	03:45	09:10	12:55	ASV Jetyak	26.2
09 January 2017	1	01:36	12:44	14:20	<i>Helmer Hanssen</i>	0
21 January 2017	1	00:14	17:36	17:50	Polarcirkel	0
<b>Sum</b>		<b>09:50</b>				<b>54.7</b>

median depth of the whole SSL. To verify the potential effects of artificial light from the ship on the abundance of acoustic scatterers during each deployment, the mean  $S_v$  within the SSL when the Jetyak was near the ship was compared to the mean  $S_v$  away from the vessel, that is, the zone with ambient polar night light conditions not affected by light pollution from human activity.

### Sampling and processing of zooplankton net samples

Zooplankton was sampled by vertical hauls (towing speed,  $0.5 \text{ m s}^{-1}$ ) from close to the seafloor to the surface using a multiple opening/closing net (Multinet, Hydrobios; mouth opening,  $0.25 \text{ m}^2$ ; mesh size,  $180 \mu\text{m}$ ). Five depth strata (320, 200, 100, 50, 20, and 0 m) were sampled in mid-fjord ( $78^\circ 57' \text{N}$ ,  $11^\circ 57' \text{E}$ ; bottom depth, 340 m) in January 2016 and January 2017, and three depth strata (60, 50, 20, and 0 m) were sampled in the inner fjord in January 2016 ( $78^\circ 53' \text{N}$ ,  $12^\circ 26' \text{E}$ ; bottom depth, 80 m). Samples were preserved in a 4% formaldehyde-in-seawater solution and later analyzed under a Leica stereomicroscope. Samples were examined by subsampling with aliquots obtained with 5-ml automatic pipette, with the pipette tip cut at a diameter of 5-mm to allow free collection of mesozooplankton. Large (total length,  $>5 \text{ mm}$ ) organisms were removed before taking subsamples and identified and counted. The number of subsamples analyzed was chosen so that at least 100 individual of *Calanus* and 300 other copepods were counted. Samples with low abundance were examined in their entirety.

### Sampling and processing of irradiance data

Diffuse sky spectral irradiance,  $E_\lambda$  at  $0.4 \text{ nm}$  spectral resolution, was measured from the Jetyak synchronously with hydroacoustics. Spectral irradiance was captured by a QE Pro fiber optic spectrometer (Ocean Optics) calibrated for absolute irradiance measurement with a  $200\text{-}\mu\text{m}$  entrance slit and  $1000\text{-}\mu\text{m}$  optical fiber (9). The spectrometer was held within the hull compartment of the Jetyak in a watertight insulated box, with its internal charge-coupled device array detector thermoelectrically cooled by Peltier element to reduce noise (dark current). A spectrally neutral (350 to  $730 \text{ nm}$ ) Spectralon reflectance standard plate (SRT-99-050, Labsphere) was mounted to a mast on the Jetyak and faced upward collecting light, which was sampled by the optical fiber attached to spectrometer. In this way, the plate collected and reflected 99% of diffuse skylight at each wavelength. The spectrometer's optical fiber was positioned on an articulating arm clamped to the mast and pointed downward at  $\sim 45^\circ$  such that the fiber's field of view contained only reflected skylight from plate. Spectra from  $350$  to  $730 \text{ nm}$  were captured at  $10\text{-s}$  intervals, corresponding to the integration time of the instrument. In this configuration, the acceptable detection limit for the spectrometer was  $\sim 1 \times 10^{-7} \mu\text{W m}^{-2} \text{ nm}^{-1}$  across the calibrated wavelength range ( $\sim 4 \times 10^{-10} \mu\text{mol photons m}^{-2} \text{ s}^{-1}$  as  $E_{\text{PAR}}$ ). For irradiance time series to compare to hydroacoustic data, spectral irradiance at each time point ( $\mu\text{W m}^{-2} \text{ nm}^{-1}$ ) was integrated ( $350$  to  $730 \text{ nm}$ ;  $\mu\text{W m}^{-2}$ ) and smoothed with a 5-min Savitzky-Golay filter in Matlab.

### Light modeling

To determine whether the movement of SSLs captured by the AZFP was consistent with changes in isolume depths that would be expected if light were serving as a cue for migrating zooplankton (15), we used the radiative transfer model HydroLight 5.2 (41) to characterize the underwater light field for one of our transects (23 January from 9:30 to 13:00) with model runs at 30-min intervals. Light input to the model was diffuse downwelling atmospheric spectral irradiance measured from the Jetyak, with additional inclusion of Raman scattering, chloro-

phyll a fluorescence (emitted light) at  $0.06 \mu\text{g liter}^{-1}$  over the whole water column, and spectral coefficients for absorption, scattering, and beam attenuation (50) collected near that location in Kongsfjorden in January 2015 [additional parameter and model details are described in the study of Cohen *et al.* (9)]. Because the genus *Calanus* spp. is among the most abundant copepods in Kongsfjorden in January and contributes to the SSL [(20); this study], we weighted the underwater spectral scalar irradiance generated from the model [ $E_0$  ( $\lambda$ );  $360$  to  $720 \text{ nm}$  at  $10\text{-nm}$  resolution;  $\mu\text{mol photons m}^{-2} \text{ s}^{-1} \text{ nm}^{-1}$ ] by the spectral response of *Calanus finmarchicus* photo-behavior (51). Thus, model runs yielded a photometric quantity of *Calanus*-utilized light; that is, only the spectral bandwidth that *Calanus* was capable of detecting (blue-green part of the visible spectrum). Model results were in  $1\text{-m}$ -depth bins from just below the surface to  $99\text{-m}$  depth, at intervals of  $30 \text{ min}$  for a 4-hour duration centered on solar noon.

### SUPPLEMENTARY MATERIALS

Supplementary material for this article is available at <http://advances.sciencemag.org/cgi/content/full/4/1/eaap9887/DC1>  
 fig. S1. Map of the study area in Kongsfjorden.  
 fig. S2. AZFP echograms from ASV.  
 fig. S3. EK60 echograms from RV Helmer Hansen.  
 fig. S4. Vertical distribution of zooplankton.  
 table S1. Ascent and descent rates of the SSL at  $455 \text{ kHz}$  in January 2016.

### REFERENCES AND NOTES

1. K. S. Last, L. Hobbs, J. Berge, A. S. Brierley, F. Cottier, Moonlight drives ocean-scale mass vertical migration of zooplankton during the Arctic winter. *Curr. Biol.* **26**, 244–251 (2016).
2. J. Berge, P. E. Renaud, G. Darnis, F. Cottier, K. Last, T. M. Gabrielsen, G. Johnsen, L. Seuthe, J. M. Weslawski, E. Leuc, M. Moline, J. Nahrang, J. E. Søreide, Ø. Varpe, O. J. Lønne, M. Daase, S. Falk-Petersen, In the dark: A review of ecosystem processes during the Arctic polar night. *Prog. Oceanogr.* **139**, 258–271 (2015).
3. S. Hernández-León, C. Almeida, L. Yebra, J. Aristegui, Lunar cycle of zooplankton biomass in subtropical waters: Biogeochemical implications. *J. Plankton Res.* **24**, 935–939 (2002).
4. K. J. Benoit-Bird, W. W. L. Au, D. W. Wisdom, Nocturnal light and lunar cycle effects on diel migration of micronekton. *Limnol. Oceanogr.* **54**, 1789–1800 (2009).
5. J. C. Drazen, L. G. De Forest, R. Domokos, Micronekton abundance and biomass in Hawaiian waters as influenced by seamounts, eddies, and the moon. *Deep Sea Res. Part I Oceanogr. Res. Pap.* **58**, 557–566 (2011).
6. D. Rubolini, I. Maggini, R. Ambrosini, S. Imperio, V. H. Paiva, G. Gaibani, N. Saino, J. G. Cecere, The effect of moonlight on Scopoli's shearwater *Calonectris diomedea* colony attendance patterns and nocturnal foraging: A test of the foraging efficiency hypothesis. *Ethology* **121**, 284–299 (2015).
7. D. L. Aksnes, A. Rostad, S. Kaartvedt, U. Martinez, C. M. Duarte, X. Irigoien, Light penetration structures the deep acoustic scattering layers in the global ocean. *Sci. Adv.* **3**, e1602468 (2017).
8. T. W. Davies, J. P. Duffy, J. Bennie, K. J. Gaston, The nature, extent, and ecological implications of marine light pollution. *Front. Ecol. Environ.* **12**, 347–355 (2014).
9. J. H. Cohen, J. Berge, M. A. Moline, A. J. Sørensen, K. Last, S. Falk-Petersen, P. E. Renaud, E. S. Leu, J. Grenvald, F. Cottier, H. Cronin, S. Menze, P. Norgren, Ø. Varpe, M. Daase, G. Darnis, G. Johnsen, Is ambient light during the high Arctic polar night sufficient to act as a visual cue for zooplankton? *PLOS ONE* **10**, e0126247 (2015).
10. H. A. Cronin, J. H. Cohen, J. Berge, G. Johnsen, M. A. Moline, Bioluminescence as an ecological factor during high Arctic polar night. *Sci. Rep.* **6**, 36374 (2016).
11. D. H. Cushing, The vertical migration of planktonic crustacea. *Biol. Rev. Camb. Philos. Soc.* **26**, 158–192 (1951).
12. J. Ringelberg, E. Van Gool, On the combined analysis of proximate and ultimate aspects in diel vertical migration (DVM) research. *Hydrobiologia* **491**, 85–90 (2003).
13. C. W. Clark, D. A. Levy, Diel vertical migrations by juvenile sockeye salmon and the antipredation window. *Am. Nat.* **131**, 271–290 (1988).
14. D. Benoit, Y. Simard, J. Gagné, M. Geoffroy, L. Fortier, From polar night to midnight sun: Photoperiod, seal predation, and the diel vertical migrations of polar cod (*Boreogadus saida*) under landfast ice in the Arctic Ocean. *Polar Biol.* **33**, 1505–1520 (2010).

15. J. H. Cohen, R. B. Forward, Zooplankton diel vertical migration—A review of proximate control, in *Oceanography and Marine Biology: An Annual Review*, Vol 47, R. N. Gibson, R. J. A. Atkinson, J. D. M. Gordon, Eds. (CRC Press, 2009), vol. 47, pp. 77–109.
16. G. C. Hays, A review of the adaptive significance and ecosystem consequences of zooplankton diel vertical migrations. *Hydrobiologia* **503**, 163–170 (2003).
17. A. Longhurst, D. Sameoto, A. Herman, Vertical distribution of Arctic zooplankton in summer: Eastern Canadian Archipelago. *J. Plankton Res.* **6**, 137–168 (1984).
18. K. Blachowiak-Samolyk, S. Kwasniewski, K. Richardson, K. Dmoch, E. Hansen, H. Hop, S. Falk-Petersen, L. T. Mouritsen, Arctic zooplankton do not perform diel vertical migration (DVM) during periods of midnight sun. *Mar. Ecol. Prog. Ser.* **308**, 101–116 (2006).
19. J. Berge, F. Cottier, K. S. Last, Ø. Varpe, E. Leu, J. Søreide, K. Eiane, S. Falk-Petersen, K. Willis, H. Nygård, D. Vogedes, C. Griffiths, G. Johnsen, D. Lorentzen, A. S. Brierley, Diel vertical migration of Arctic zooplankton during the polar night. *Biol. Lett.* **5**, 69–72 (2009).
20. J. C. Grenvald, T. A. Callesen, M. Daase, L. Hobbs, G. Darnis, P. E. Renaud, F. Cottier, T. G. Nielsen, J. Berge, Plankton community composition and vertical migration during polar night in Kongsfjorden. *Polar Biol.* **39**, 1879–1895 (2016).
21. T. Longcore, C. Rich, Ecological light pollution. *Front. Ecol. Environ.* **2**, 191–198 (2004).
22. M. H. Depledge, C. A. J. Godard-Coddling, R. E. Bowen, Light pollution in the sea. *Mar. Pollut. Bull.* **60**, 1383–1385 (2010).
23. T. W. Davies, M. Coleman, K. M. Griffith, S. R. Jenkins, Night-time lighting alters the composition of marine epifaunal communities. *Biol. Lett.* **11**, 20150080 (2015).
24. K. J. Gaston, M. E. Visser, F. Höflker, The biological impacts of artificial light at night: The research challenge. *Philos. Trans. R. Soc. B Biol. Sci.* **370**, 20140133 (2015).
25. R. Tamir, A. Lerner, C. Haspel, Z. Dubinsky, D. Iluz, The spectral and spatial distribution of light pollution in the waters of the northern Gulf of Aqaba (Eilat). *Sci. Rep.* **7**, 42329 (2017).
26. C. Scalabrin, C. Marfia, J. Boucher, How much fish is hidden in the surface and bottom acoustic blind zones? *ICES J. Mar. Sci.* **66**, 1355–1363 (2009).
27. O. Schofield, H. W. Ducklow, D. G. Martinson, M. P. Meredith, M. A. Moline, W. R. Fraser, How do polar marine ecosystems respond to rapid climate change? *Science* **328**, 1520–1523 (2010).
28. I. Nilssen, Ø. Ødegaard, A. J. Sørensen, G. Johnsen, M. A. Moline, J. Berge, Integrated environmental mapping and monitoring, a methodological approach to optimise knowledge gathering and sampling strategy. *Mar. Pollut. Bull.* **96**, 374–383 (2015).
29. M. Ludvigsen, A. J. Sørensen, Towards integrated autonomous underwater operations for ocean mapping and monitoring. *Annu. Rev. Control* **42**, 145–157 (2016).
30. G. Darnis, L. Hobbs, M. Geoffroy, J. C. Grenvald, P. E. Renaud, J. Berge, F. Cottier, S. Kristiansen, M. Daase, J. E. Søreide, A. Wold, N. Morata, T. Gabrielsen, From polar night to midnight sun: Diel vertical migration, metabolism and biogeochemical role of zooplankton in a high Arctic fjord (Kongsfjorden, Svalbard). *Limnol. Oceanogr.* **62**, 1586–1605 (2017).
31. R. Elofsson, The frontal eyes of crustaceans. *Arthropod Struct. Dev.* **35**, 275–291 (2006).
32. A. S. Båtnes, C. Miljeteig, J. Berge, M. Greenacre, G. Johnsen, Quantifying the light sensitivity of *Calanus* spp. during the polar night: Potential for orchestrated migrations conducted by ambient light from the sun, moon, or aurora borealis? *Polar Biol.* **38**, 51–65 (2015).
33. G. A. Tarling, M. L. Johnson, Satiation gives krill that sinking feeling. *Curr. Biol.* **16**, R83–R84 (2006).
34. M. I. Wallace, F. R. Cottier, J. Berge, G. A. Tarling, C. Griffiths, A. S. Brierley, Comparison of zooplankton vertical migration in an ice-free and a seasonally ice-covered Arctic fjord: An insight into the influence of sea ice cover on zooplankton behavior. *Limnol. Oceanogr.* **55**, 831–845 (2010).
35. J. Fischer, M. Visbeck, Seasonal variation of the daily zooplankton migration in the Greenland Sea. *Deep Sea Res. Part I Oceanogr. Res. Pap.* **40**, 1547–1557 (1993).
36. H. W. Ducklow, D. K. Steinberg, K. O. Buesseler, Upper ocean carbon export and the biological pump. *Oceanography* **14**, 50–58 (2001).
37. D. Sameoto, N. A. Cochrane, A. W. Herman, Response of biological acoustic backscattering to ships' lights. *Can. J. Fish. Aquat. Sci.* **42**, 1535–1543 (1985).
38. M. Marchesan, M. Spoto, L. Verginella, E. A. Ferrero, Behavioural effects of artificial light on fish species of commercial interest. *Fish. Res.* **73**, 171–185 (2005).
39. B. Nightingale, T. Longcore, C. A. Simenstad, Artificial night lighting and fishes, in *Ecological Consequences of Artificial Night Lighting*, C. Rich, T. Longcore, Eds. (Island Press, 2006), pp. 257–276.
40. H. J. Price, Swimming behavior of krill in response to algal patches: A mesocosm study. *Limnol. Oceanogr.* **34**, 649–659 (1989).
41. A. De Robertis, C. Schell, J. S. Jaffe, Acoustic observations of the swimming behavior of the euphausiid *Euphausia pacifica* Hansen. *ICES J. Mar. Sci.* **60**, 885–898 (2003).
42. J. Mauchline, *Advances Marine Biology: The Biology of Calanoid Copepods* (Academic Press, 1998), vol. 33, pp. 1–710.
43. D. M. Fields, S. D. Shema, H. I. Browman, T. Q. Browne, A. B. Skiftesvik, Light primes the escape response of the calanoid copepod, *Calanus finmarchicus*. *PLOS ONE* **7**, e39594 (2012).
44. M. V. Moore, S. M. Pierce, H. M. Walsh, S. K. Kvalvik, J. D. Lim, Urban light pollution alters the diel vertical migration of *Daphnia*, in *Proceedings of the International Association of Theoretical and Applied Limnology*, W. D. Williams, Ed. (2001), vol. 27, pp. 779–782.
45. E. E. Cordes, D. O. B. Jones, T. A. Schlacher, D. J. Amon, A. F. Bernardino, S. Brooke, R. Carney, D. M. DeLeo, K. M. Dunlop, E. G. Escobar-Briones, A. R. Gates, L. Génio, J. Gobin, L.-A. Henry, S. Herrera, S. Hoyt, M. Joye, S. Kark, N. C. Mestre, A. Metaxas, S. Pfeifer, K. Sink, A. K. Sweetnam, U. Witte, Environmental impacts of the deep-water oil and gas industry: A review to guide management strategies. *Front. Environ. Sci.* **4**, 58 (2016).
46. Z. Volent, G. Johnsen, F. Sigernes, Kelp forest mapping by use of airborne hyperspectral imager. *J. Appl. Remote Sens.* **1**, 011503 (2007).
47. P. Kimball, J. Bailey, S. Das, R. Geyer, T. Harrison, C. Kunz, K. Manganini, K. Mankoff, K. Samuelson, T. Sayre-McCord, F. Straneo, P. Traykovski, H. Singh, The WHOI Jettyak: An autonomous surface vehicle for oceanographic research in shallow or dangerous waters, in *2014 IEEE/OES Autonomous Underwater Vehicles (AUV)* (IEEE, 2014), pp. 1–7.
48. J. Simmonds, D. N. MacLennan, *Fisheries Acoustics: Theory and Practice* (Blackwell Science Ltd., ed. 2, 2008).
49. M. Geoffroy, F. R. Cottier, J. Berge, M. E. Inall, AUV-based acoustic observations of the distribution and patchiness of pelagic scattering layers during midnight sun. *ICES J. Mar. Sci.* **74**, 2342–2353 (2016).
50. M. S. Twardowski, J. M. Sullivan, P. L. Donaghay, J. R. V. Zaneveld, Microscale quantification of the absorption by dissolved and particulate material in coastal waters with an ac-9. *J. Atmos. Oceanic Tech.* **16**, 691–707 (1999).
51. E. J. Buskey, E. Swift, Behavioral responses of oceanic zooplankton to simulated bioluminescence. *Biol. Bull.* **168**, 263–275 (1985).

**Acknowledgments:** We thank the students on the University Centre on Svalbard course AB334 “Underwater robotics and polar night biology” for help and efforts during the field campaign, and the crew onboard RV *Helmer Hanssen*. We also thank the employees of Kings Bay AS for hospitality and help during the campaigns. **Funding:** The work was co-funded by The Norwegian Research Council through project numbers 195160, 223254, 226417, and 244319. **Author contributions:** M.L., J.B., M.G., J.H.C., A.J.S., and G.J. planned and executed the work; M.L., J.B., M.G., J.H.C., A.J.S., M.D., and G.J. analyzed the data and wrote the text; P.R.D.L.T., S.M.N., and H.S. provided expertise using the autonomous platform and sensors. **Competing interest:** The authors declare that they have no competing interests. **Data and materials availability:** All data needed to evaluate the conclusions in the paper are present in the paper and/or the Supplementary Materials. Additional data related to this paper may be requested from the authors.

Submitted 19 September 2017  
Accepted 6 December 2017  
Published 10 January 2018  
10.1126/sciadv.aap9887

**Citation:** M. Ludvigsen, J. Berge, M. Geoffroy, J. H. Cohen, P. R. De La Torre, S. M. Nornes, H. Singh, A. J. Sørensen, M. Daase, G. Johnsen, Use of an Autonomous Surface Vehicle reveals small-scale diel vertical migrations of zooplankton and susceptibility to light pollution under low solar irradiance. *Sci. Adv.* **4**, eaap9887 (2018).

# Article F

## First hyperspectral imaging survey of the deep seafloor: high-resolution mapping of manganese nodules

---

Ines Dumke, **Stein M. Nornes**, Autun Purser, Yann Marcon, Martin Ludvigsen,  
Steinar L. Ellefmo, Geir Johnsen and Fredrik Søreide

ARTICLE F

---

This article is published in *Remote Sensing of Environment*,  
Volume 209, pages 19-30, 2018.  
doi: 10.1016/j.rse.2018.02.024





Contents lists available at ScienceDirect

## Remote Sensing of Environment

journal homepage: [www.elsevier.com/locate/rse](http://www.elsevier.com/locate/rse)

# First hyperspectral imaging survey of the deep seafloor: High-resolution mapping of manganese nodules



Ines Dumke<sup>a,\*</sup>, Stein M. Nornes<sup>a</sup>, Autun Purser<sup>b</sup>, Yann Marcon<sup>b,c</sup>, Martin Ludvigsen<sup>a</sup>, Steinar L. Ellefmo<sup>d</sup>, Geir Johnsen<sup>e</sup>, Fredrik Sørdeide<sup>a</sup>

<sup>a</sup> Department of Marine Technology, Norwegian University of Science and Technology (NTNU), Otto Nielsens vei 10, 7491 Trondheim, Norway

<sup>b</sup> Alfred Wegener Institute, Helmholtz Centre for Polar and Marine Research, Am Handelshafen 12, 27570 Bremerhaven, Germany

<sup>c</sup> MARUM, Center for Marine Environmental Sciences, Leobener Str. 2, 28359 Bremen, Germany

<sup>d</sup> Department of Geoscience and Petroleum, Norwegian University of Science and Technology (NTNU), Sem Sælands vei 1, 7491 Trondheim, Norway

<sup>e</sup> Centre for Autonomous Marine Operations and Systems, Department of Biology, Norwegian University of Science and Technology (NTNU), 7491 Trondheim, Norway

## ARTICLE INFO

### Keywords:

Hyperspectral imaging  
Underwater Hyperspectral Imager (UHI)  
Manganese nodules  
DISCOL  
Supervised classification  
Support Vector Machine  
Spectral Angle Mapper

## ABSTRACT

Hyperspectral seafloor surveys using airborne or spaceborne sensors are generally limited to shallow coastal areas, due to the requirement for target illumination by sunlight. Deeper marine environments devoid of sunlight cannot be imaged by conventional hyperspectral imagers. Instead, a close-range, sunlight-independent hyperspectral survey approach is required. In this study, we present the first hyperspectral image data from the deep seafloor. The data were acquired in approximately 4200 m water depth using a new Underwater Hyperspectral Imager (UHI) mounted on a remotely operated vehicle (ROV). UHI data were recorded for 112 spectral bands between 378 nm and 805 nm, with a high spectral (4 nm) and spatial resolution (1 mm per image pixel). The study area was located in a manganese nodule field in the Peru Basin (SE Pacific), close to the DISCOL (DISturbance and reCOLonization) experimental area. To test whether underwater hyperspectral imaging can be used for detection and mapping of mineral deposits in potential deep-sea mining areas, we compared two supervised classification methods, the Support Vector Machine (SVM) and the Spectral Angle Mapper (SAM). The results show that SVM is superior to SAM and is able to accurately detect nodule surfaces. The UHI therefore represents a promising tool for high-resolution seafloor exploration and characterisation prior to resource exploitation.

## 1. Introduction

Hyperspectral imaging is defined as the acquisition of images in hundreds of contiguous spectral bands so that a full spectrum is recorded for each image pixel (Goetz et al., 1985; Goetz, 2009). Each pixel spectrum contains different spectral components arising not only from the surface material or vegetation, but also from water, atmosphere, the illumination source (typically the sun), and the hyperspectral sensor itself.

Calibrations are required to correct for any external influences and obtain a reflectance spectrum specific for the objects of interest (OOI) and representing the percentage of light reflected by the OOI for each wavelength. Different OOI differ in their reflectance spectra, providing so-called “optical fingerprints”. By comparing each pixel’s reflectance spectrum to reference spectra obtained from, e.g. a spectral library or field samples, reflectance spectra can be used to classify OOI and produce coverage maps based on spectral signatures.

Hyperspectral data are typically acquired by passive hyperspectral imagers that use the sun as light source and record reflected solar radiation (and other spectral components associated with external influences) over a wavelength range of 400–2500 nm (e.g. Resmini et al., 1997; Kruse et al., 2003; Dickey et al., 2006), thus covering the visible range (400–700 nm) and part of the infrared portions (> 700 nm) of the solar spectrum. Most passive imagers are either airborne or spaceborne. In addition, passive hyperspectral imagers or spectroradiometers for underwater use have been developed over the past two decades to measure in-situ optical properties of the ocean, e.g. operated at mooring stations or by divers (Mazel, 1997; Hochberg and Atkinson, 2000; Pons et al., 2007; Ramírez-Pérez et al., 2015).

Hyperspectral imaging has been used mostly in terrestrial settings, but has also been applied in the marine environment. Terrestrial applications include mapping of vegetation (Underwood et al., 2003; Adam et al., 2010; Landmann et al., 2015), infrastructure (Roessner et al., 2001; Dell’Acqua et al., 2004; Herold et al., 2004), and surface

\* Corresponding author at: GEOMAR Helmholtz Centre for Ocean Research Kiel, Wischhofstr. 1-3, 24148 Kiel, Germany.

E-mail address: [idumke@geomar.de](mailto:idumke@geomar.de) (I. Dumke).

<https://doi.org/10.1016/j.rse.2018.02.024>

Received 17 June 2017; Received in revised form 21 December 2017; Accepted 16 February 2018

0034-4257/© 2018 The Authors. Published by Elsevier Inc. This is an open access article under the CC BY-NC-ND license (<http://creativecommons.org/licenses/by-nc-nd/4.0/>).

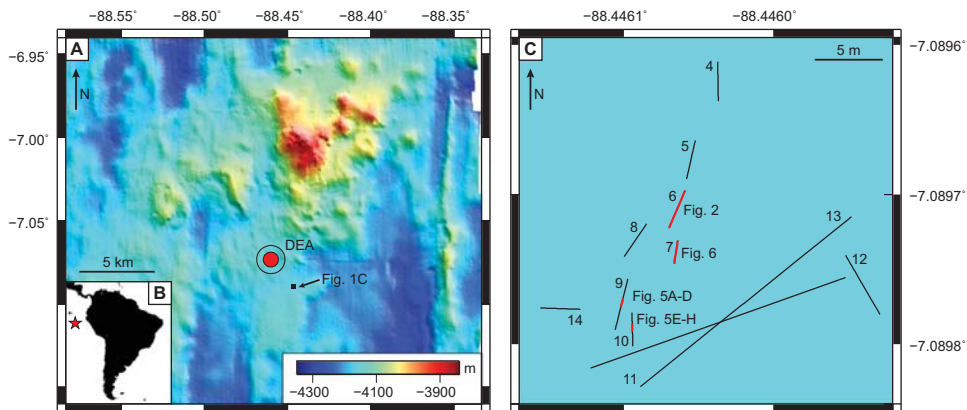


**Fig. 1.** (a) Bathymetric map (50 m resolution, courtesy of GEOMAR) showing the location of the study area in (c) and the DISCOL experimental area (DEA) in the Peru Basin. The filled red circle represents the central DISCOL area (1 km radius), the black circle marks the outer extent of the disturbance experiment (1.877 km radius). (b) Overview map indicating the location of the DEA offshore Peru (red star). (c) Locations of the main 11 survey tracks (tracks 4–14) to which supervised classification was applied. Bathymetry colour scale is the same as in (a); the water depth in the study area is about 4195 m. (For interpretation of the references to colour in this figure legend, the reader is referred to the web version of this article.)

minerals (e.g. Resmini et al., 1997; Bierwirth et al., 1999; Sabins, 1999; Kruse et al., 2003). The main motivation for hyperspectral mapping of mineral distribution is the detection of ore deposits for mineral exploration purposes (Bierwirth et al., 1999; Sabins, 1999; van der Meer et al., 2012). In marine settings, hyperspectral methods have been used mainly in oceanographic and biological studies (Chang et al., 2004; Dickey et al., 2006), including mapping of ocean colour (Dickey et al., 2006; Dierssen and Randolph, 2013) and seafloor habitats (Klonowski et al., 2007; Fearnas et al., 2011) such as reefs (Hochberg and Atkinson, 2000, 2003; Kutser et al., 2006; Petit et al., 2017), seagrass ecosystems (Dierssen, 2013; Dierssen et al., 2015), and kelp forests (Volent et al., 2007). Given that the majority of sunlight penetrates no deeper than 50 m into water, the application of passive hyperspectral sensors in marine settings is limited to coastal areas and shallow water depths (e.g. Klonowski et al., 2007; Volent et al., 2007; Fearnas et al., 2011).

More recently, active hyperspectral imagers for underwater applications have been developed (Chennu et al., 2013; Johnsen et al., 2013; Tegdan et al., 2015). Active hyperspectral sensors use their own external light sources for target illumination, thus allowing seafloor studies in water depths with no natural light penetration. Due to the strong in-water attenuation of wavelengths in the near-infrared and infrared part of the spectrum, these underwater hyperspectral sensors are limited to the visible range of wavelengths.

The first active underwater hyperspectral imagers were mounted on mechanical sledges or carts operated on the seafloor in shallow water depths (< 6 m), with illumination provided by two halogen lamps (Chennu et al., 2013; Johnsen et al., 2013; Pettersen et al., 2014). Since then, scientific Underwater Hyperspectral Imagers (UHIs) developed by Ecotone AS (Trondheim, Norway) have been deployed on remotely operated vehicles (ROVs) in water depths of up to 600 m. The UHIs have a spectral range of 378–805 nm, with a spectral resolution of up to 0.5 nm (Johnsen et al., 2013, 2016; Tegdan et al., 2015), and have been used to study e.g. cold-water corals and kelp forests in the Trondheimsfjord (Tegdan et al., 2015; Johnsen et al., 2016), a vertical rock wall at Haugberneset (Tegdan et al., 2015), benthic organisms in Kongsfjorden, Svalbard (Johnsen et al., 2016), and a wreck site at Trygghamna, Svalbard (Daase, 2016). In addition to ROVs, autonomous underwater vehicles (AUVs) can also serve as UHI mounting platforms (Johnsen et al., 2013). A first AUV-based UHI survey was recently conducted successfully at the Arctic Mid-Ocean Ridge as part of the MarMine project (Ludvigsen et al., 2016; Sture et al., 2017).

The majority of these underwater hyperspectral studies focused on biological OOIs, but Johnsen et al. (2013) demonstrated that UHIs can

also be used for mapping of seafloor minerals. As with terrestrial mineral deposits, seafloor mineral deposits may be detected and characterized based on their spectral signatures. Provided a sufficient sensor depth-rating, underwater hyperspectral imaging may therefore be of interest for exploration in potential deep-sea mining areas. Although not yet an active industry, deep-sea mining is predicted to start within the next decade in areas of prospective seafloor mineral deposits such as manganese nodules and massive sulphide deposits (Glasby, 2002; Rona, 2003; Gwyther, 2008; Hoagland et al., 2010). A detailed seafloor mapping and characterisation of mineral deposits, as well as fauna distribution and understanding of ecosystem functioning in these remote seafloor areas is required prior to exploitation.

Manganese nodules are seafloor mineral deposits that grow concentrically around a nucleus, usually at the sediment-water interface. In addition to Mn and Fe, the nodules typically contain Ni, Cu, Co, and Zn, which are supplied either by the underlying sediments (diagenetic deposits) or by seawater (hydrogenous deposits) (e.g. Glasby, 2000). Nodule compositions can vary on regional as well as local scales (e.g. Cronan and Tooms, 1969; Glasby, 1972, 2000), and it is this mixed composition which has rendered manganese nodules an important potential resource for exploitation. Dimensions are generally between < 3 cm and > 10 cm, and growth rates are hypothesised to be 2–100 mm Myr<sup>-1</sup> (e.g. Glasby, 2000). Manganese nodules are found in deep-sea basins (> 4000 m water depth) characterized by low sedimentation rates (< 5 mm kyr<sup>-1</sup>), with major nodule regions including the Clarion-Clipperton Zone in the equatorial North Pacific, the Central Pacific Basin, and the Peru Basin.

Here, we present the first hyperspectral image data of the seafloor in water depths > 600 m. The data were acquired by a new deep-sea UHI in a manganese nodule field in the Peru Basin (SE Pacific) in 4195 m water depth. We compare two supervised classification methods and estimate nodule coverage for the surveyed area from the classification results. We also evaluate the potential of underwater hyperspectral imaging as an exploration method in prospective deep-sea mining areas.

## 2. Study area

The study area was located in a manganese nodule field in the Peru Basin (SE Pacific Ocean) in about 4195 m water depth (Fig. 1a). It was situated about 700 m southeast of the DISCOL (DISturbance and re-COLONization) experimental area (DEA), which comprises a generally flat, circular area of 10.8 km<sup>2</sup> in 4140–4200 m water depth (Thiel and

Schriever, 1989; Foell et al., 1990; Borowski, 2001). Surface sediments consist of 7–10 cm of dark brown silicate oozes overlaying lighter-coloured clays enriched in biogenic carbonate (Borowski, 2001). Manganese nodules in the area have diameters of up to 15 cm, with a nodule density estimated to be 5–10 kg m<sup>-2</sup>, prior to the DISCOL experiment (Thiel and Schriever, 1989).

The DISCOL experiment was conducted in 1989 in order to simulate potential effects of deep-sea mining equipment and monitor the impact of these on benthic communities (Thiel and Schriever, 1989; Foell et al., 1990). Within the DEA, the seafloor was disturbed by a “plough-harrow” device towed along 78 straight tracks that crossed the centre of the DEA (Thiel and Schriever, 1989; Foell et al., 1990; Borowski and Thiel, 1998). Besides the direct disturbance of the seabed, the experimental plough harrow buried the manganese nodules within the ploughtracks into the sediments, and produced a sediment plume that later settled out across both ploughed and unploughed areas (Foell et al., 1990; Schriever, 1995).

Since 1989, the DEA has been revisited several times to monitor the recolonization process via video surveys and physical sampling. After a strong reduction in abundance of all faunal taxa immediately after the experiment, recolonization started rapidly but had not reached pre-impact conditions even seven years after the experiment (Schriever, 1995; Borowski and Thiel, 1998; Borowski, 2001). In 2015, 26 years after the experiment, the area was revisited by the RV SONNE cruises SO242/1 and SO242/2. Detailed mapping and sampling campaigns, including ROV and AUV surveys, revealed that the disturbance tracks were still visible after 26 years, manganese nodules within and near the DEA were either partly covered by sediment or completely buried, and from preliminary results currently being analysed, faunal communities remain distinct from those present within the DEA prior to the disturbance (Greinert, 2015; Boetius, 2015).

### 3. Methods

#### 3.1. Data acquisition

Hyperspectral data were acquired in 2015 during the RV SONNE cruise SO242/2 with a new UHI (UHI #4) developed by Ecotone AS (Trondheim, Norway). The UHI is depth-rated to 6000 m and was tested in this study for the first time. It is a push-broom scanner with beam-widths of 60° (transverse) and 0.4° (longitudinal) and is mounted looking vertically downwards to record lines of 1600 pixels perpendicular to the track direction. Intensities of reflected light can be measured for up to 896 spectral bands between 378 and 805 nm, with recording frequencies of up to 100 Hz. In this study, data were recorded at 20 Hz with spectral binning of 8, resulting in 112 spectral bands with a spectral resolution of 4 nm.

The KIEL6000 ROV (GEOMAR) was used as the sensor platform for the UHI. For data acquisition, the UHI was mounted on the fully outstretched manipulator arm of the ROV. With this setup, it was not possible to accommodate UHI-dedicated light sources on either side of the sensor, as is normally preferred (Johnsen et al., 2013, 2016; Tegdan et al., 2015). Seafloor illumination was instead provided by the ten ROV light sources, which included an LED, seven halogen lamps (five Deep Multi-SeaLite lamps and two Sea Arc 5000 lamps), and two HMI lamps (SeaArc2). This illumination from behind and above the UHI was not optimal, and resulted in two kinds of shadows in the recorded data: a constant dark shading across half of the swath, due to the manipulator arm blocking part of the light, and shadows on nodule sides facing away from the ROV, caused by the illumination source positioned behind the UHI.

A total of 15 tracks with constant speed (0.05 m s<sup>-1</sup>) and heading were acquired within a 20 × 40 m<sup>2</sup> area containing manganese nodules and different benthic fauna (ROV dive SO242/2\_191-1; Boetius, 2015). Track length ranged between 1.7 m and 4.9 m except for two tracks with lengths of 20 m (Fig. 1c). ROV altitude was approximately

1–1.2 m, resulting in a track width of 1–1.2 m and an across-track resolution of about 1 mm per pixel.

ROV navigation was provided by POSIDONIA ultra-short baseline (USBL) positioning with an accuracy of about 0.02% of the water depth. Position data were recorded at < 0.25 Hz and ROV attitude data (velocity and orientation) were logged at 1 Hz. In addition to the UHI data, SD and HD video data were acquired on all tracks. The video data were used to identify larger seabed fauna (Dumke et al., in prep.), and frame grabs from the HD and SD video data served as a basis for upsampling of the navigation data (see Section 3.2.3 and Normes et al. (in prep.)).

#### 3.2. Data processing

Processing of the hyperspectral images consisted of three steps: (1) calibration of the raw data (digital counts) to radiance data (in W m<sup>-2</sup> sr<sup>-1</sup> nm<sup>-1</sup>) by correcting for sensor-specific influences, (2) conversion of radiance to reflectance by correcting for external influences from illumination sources and the inherent optical properties of the water column, and (3) geocorrection. The desired output is reflectance data that only depends on the seafloor material and OOI.

##### 3.2.1. Radiance processing

Calibration of raw data to radiance data was done through radiometric correction using the Hypermap software tool (Ecotone). The radiance data were then loaded into MATLAB (MathWorks Inc.) and formatted as a 3-dimensional array  $A(m,n,i)$  of  $m$  lines (number of lines along the track),  $n$  samples (number of pixels of the UHI slit, or across the track), and  $i$  spectral bands. As the outer bands (< 400 nm and > 710 nm) were rather noisy, spectral subsetting was done to reduce the data to the 83 bands between 400 nm and 710 nm. In addition, spatial subsetting was performed to remove redundant lines at the track ends caused by the time lag between the end of the ROV track and the end of UHI data recording.

##### 3.2.2. (Pseudo-) reflectance processing

Following radiance processing, the next step was the correction for external influences on the spectral characteristics of the reflected light. The main external influence was the illumination, which was relatively consistent along the track but varied laterally due to the setup-induced shadow. As the combined spectral characteristics of the ten ROV lamps could not be determined, the illumination influence was approximated by a reference spectrum calculated from the data collected during each track. For each sample  $n$  along the UHI slit, a reference spectrum  $s_{ref}(n)$  was calculated as the median spectrum of all radiance spectra  $s_{rad}(m,n)$  recorded for sample  $n$  over all lines  $m$  along a particular survey track. For each image pixel  $(m,n)$ , the radiance spectrum was then divided by its respective reference spectrum:

$$s_{corr}(m,n) = \frac{s_{rad}(m,n)}{s_{ref}(n)} \quad (1)$$

where  $s_{corr}(m,n)$  is the corrected spectrum for the image pixel  $(m,n)$ . The spectra were then smoothed by a moving average filter with a window of 11 bands.

While this method worked well in general and removed effects that were constant in along-track direction, it did not take into account altitude variations, which change the light field occasionally along the track. However, most tracks were run at a relatively constant altitude of 1 m, and altitude effects were therefore considered to be negligible.

Correction by median spectra also takes into account the inherent optical properties of the water column, which were unknown for the area but were assumed to be constant during the period of study. Based on the high water depth and the video data, which showed that the sediment remained undisturbed during the survey period, we assumed optically clear waters with a likely negligible influence on the recorded spectral intensities.

### 3.2.3. Geocorrection via photomosaic-based navigation data

Due to the small scale of the imaged areas, some of which covered only 2 m<sup>2</sup>, georeferencing of the UHI data required very high-resolution navigation data. The ROV's POSIDONIA USBL navigation had an accuracy of approximately 0.02% of the water depth, which thus amounted to  $\pm 10$  m in the study area. As the ROV navigation data contained frequent jumps of several metres and the recording frequencies (1 Hz for ROV velocity and orientation, < 0.25 Hz for position data) were generally too low for combination with the 20 Hz UHI data, the ROV navigation data did not provide satisfactory geocorrection of the UHI data.

In order to acquire navigation data of sufficient quality, the velocity and orientation data of the ROV were integrated to create a smooth relative position trajectory for each track, a process known as Dead Reckoning (DR; Fossen, 2011). The average USBL position recorded during the track was used to globally position the DR-derived track line. Using the photogrammetry and photomosaic software Agisoft PhotoScan, the DR-derived navigation was then combined with frame grabs from the HD and SD videos to produce upsampled and refined 5 Hz navigation data. This procedure is further detailed in Nornes et al. (in prep.).

The photomosaic-based navigation was corrected for a time shift between the navigation and the UHI data. Time shifts varied between 0 s (no shift) and  $-0.9$  s. As the navigation data contained a few outliers, probably arising from noise introduced during image processing in Agisoft PhotoScan, a moving average filter with a window of 5 data points was applied to smooth the navigation data. Georeferencing, including correction for vehicle attitude influences, was done using the Hypermap software and the corrected data were output with a pixel size of 1 mm.

The correction by median spectra and subsequent geocorrection were able to remove most of the undesired external influences, including the setup-induced dark shading across the track. However, some residual influences, mostly from illumination, likely remain. The corrected data are therefore not true reflectance data, and are referred to as pseudo-reflectance data in the following.

### 3.3. Spectral classification

Based on the processing results, 11 of the tracks (Fig. 1c) were selected for spectral classification and further analyses. Classification was done using the ENVI software (v. 5.3; Exelis VIS) and two supervised classification methods, the Support Vector Machine (SVM) and the Spectral Angle Mapper (SAM), were applied. Both methods required training data as input for the classification. In the absence of an existing spectral library applicable to our study setting, training data were derived from the UHI data through user-defined regions of interest (ROIs). ROIs were defined manually for each track based on visual identification in the UHI “pseudo”-RGB data, which was composed of the three bands 645 nm (R), 571 nm (G), and 473 nm (B). In addition, visual comparisons of pixel spectra as well as the ROV video data were used to define ROIs.

The output of the spectral classification is a classification image showing the distribution of the different spectral classes on a pixel basis. In the following, we use the term “category” rather than “class” in order to differentiate it from the taxonomic rank “class” used in biological classification of organisms.

#### 3.3.1. Support Vector Machine (SVM)

SVM is widely used in supervised classification and is based on statistical learning theory. Categories are separated by decision surfaces (hyperplanes) maximizing the margin between categories, with support vectors from the training data defining the points closest to the hyperplanes (Camps-Valls et al., 2004; Melgani and Bruzzone, 2004; Mountrakis et al., 2011, and references therein). SVM is often superior to other supervised classification methods (Melgani and Bruzzone,

2004; Bioucas-Dias et al., 2013) and also works well for noisy and complex data (Camps-Valls et al., 2004).

SVM classification was applied to the 11 tracks shown in Fig. 1c. The SVM results were compared to the UHI pseudo-RGB images for accuracy, as an alternative ground-truthing image did not exist. If necessary, SVM was rerun with improved ROIs. The SVM result was then smoothed using ENVI's classification aggregation tool to integrate smaller pixel clusters into the surrounding category. A pixel cluster threshold of 25–35 pixels was found to give the best balance between removing potential noise and loss of information.

#### 3.3.2. Spectral Angle Mapper (SAM)

SAM is also a standard supervised classification method and is simpler and faster than SVM. Pixel spectra and endmember spectra from training data are treated as vectors in n-D space, where n corresponds to the number of spectral bands. Spectral similarity between a pixel spectrum and an endmember spectrum is determined from the angle between the two spectra and categories are assigned based on a defined maximum angle threshold (Kruse et al., 1993; Sohn and Rebello, 2002).

SAM was applied to only four tracks, as visual comparisons distinctly showed that the results were inferior to those of SVM. The same ROIs as for SVM were used. Initially, the maximum angle was set to the default value of 0.1 rad for all categories, but angles were adjusted after the first SAM run in order to improve the classification result. The default angle of 0.1 rad worked well for the background sediment. For the other categories, angles were either increased to up to 0.15 rad to increase classification sensitivity (e.g. for nodules, shadows, and most of the fauna), or decreased to 0.05 rad to reduce sensitivity and the number of false positives. The SAM results were smoothed via classification aggregation with a pixel cluster threshold of 25–30 pixels.

#### 3.3.3. Relative classification accuracy

To determine the accuracy of a classification result, the classification image is normally compared to a ground-truthing image. However, no ground-truthing information, aside from the video data, was available. Therefore, this approach was used to compare the SAM results against the SVM results to determine the classification accuracy of SAM relative to SVM. The comparison was performed using ENVI's confusion matrix tool, which conducts a pixel-by-pixel comparison of a classification image (here: the SAM result) against a ground-truthing image (here: the SVM result). For each pixel in the SVM image, the location and category were compared to the corresponding location and category in the SAM image. The confusion matrix then output an overall accuracy, i.e., the number of pixels classified in the same way by both methods divided by the total number of pixels, as well as percentages of correctly classified pixels for each category.

### 3.4. Estimation of areal nodule density

The areal nodule density, or number of nodules per m<sup>2</sup>, was determined from the amount of nodules identified in the UHI pseudo-RGB images of the nine shorter tracks (up to 5 m length) and verified by the video data. Manual nodule counting was not done for the two 20 m long tracks due to their length and associated high number of nodules, and because nodule distribution appeared to be similar to that of the shorter tracks.

In addition, we also tested if the areal nodule density can be estimated from quantitative analysis of the SVM classification images through automatic counting of nodule category areas. However, as shown below, the nodules appeared as very fragmented patches in the classification image, rather than one connected area per nodule. Automatic counting of nodule objects in the SVM image would consequently interpret each fragment as a separate nodule object and thus strongly overestimate the areal nodule density.

To obtain a better estimation, therefore, the classification image was

first smoothed by a classification aggregation of 300 pixels to remove the influence from very small pixel clusters. We then used ENVI's clump tool to grow and merge category areas belonging to the same nodule, as indicated by the UHI pseudo-RGB data. The clump tool clumps adjacent areas of the same category together by applying a dilate operation followed by an erode operation, both of which are controlled by a kernel of a user-defined size. Kernel sizes were 17–38 pixels for the dilate operation and 3–9 pixels for the erode operation. The clumping process was done in two ways. In case 1, clumping was applied only to the nodule category, while all other categories were merged into one background category. In case 2, clumping was done for both the nodule and the shadow category. The reason for case 2 was that some nodules were more conspicuous by their shadow than by nodule category pixels.

The resulting clump images were loaded into MATLAB and nodule objects were counted using a method by Reddy (2010) based on a foreground-background separation. The areal nodule density, which was calculated from the count results and imaged areas, was then compared to the reference density determined from the UHI pseudo-RGB images and video data.

#### 4. Results

##### 4.1. Quality of pseudo-reflectance data

The UHI pseudo-reflectance data are of generally good quality. For all tracks, the division by along-track median spectra completely removed the dark shading (Fig. 2a) caused by the influence of the ROV's manipulator arm on illumination, as shown by the example in Fig. 2b. Both manganese nodules and larger megafauna, e.g. the stalked sponge in Fig. 2b, are easy to distinguish from the relatively uniform background sediment. The data also show that most nodule surfaces are not fully exposed, but are partly or almost completely covered by sediment.

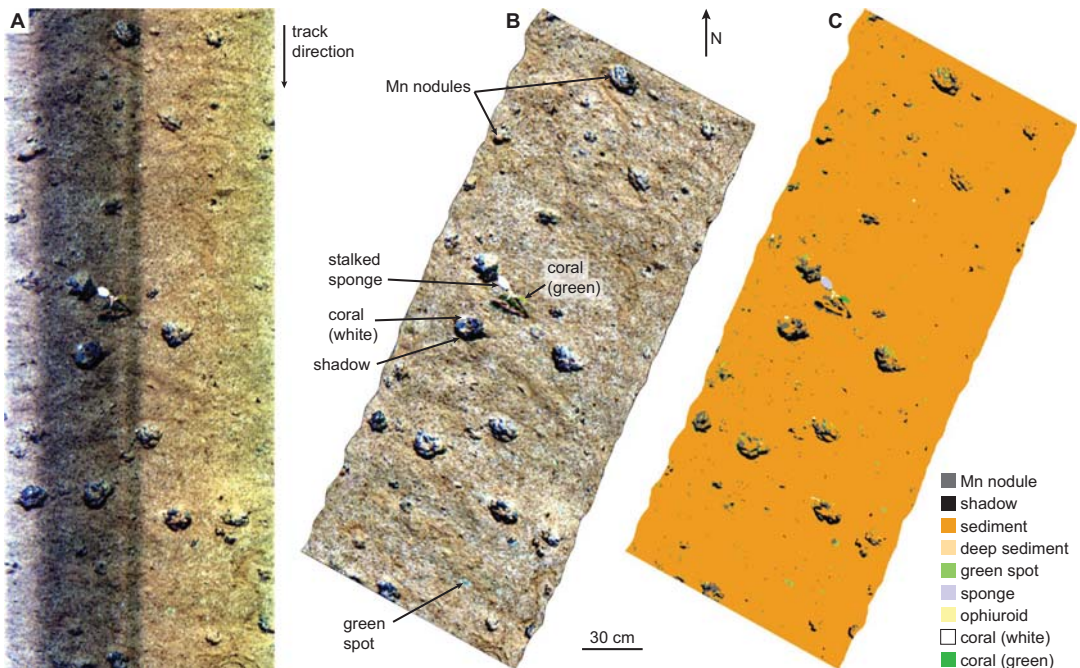


Fig. 2. (a) UHI radiance data in pseudo-RGB (R: 645 nm, G: 571 nm, B: 473 nm), showing manganese nodules and a stalked sponge (*Hexactinellida*) with an ophiuroid (brittle star, *Echinodermata ophiuroidea*) wrapped around the stalk. Note the dark shading caused by the ROV's manipulator arm blocking the light. (b) Geocorrected pseudo-reflectance data in pseudo-RGB. Division of each pixel spectrum by its corresponding along-track median spectrum completely removed the dark shadow. (c) SVM classification image based on the data in (b) and user-defined ROIs. Track location is shown in Fig. 1c.

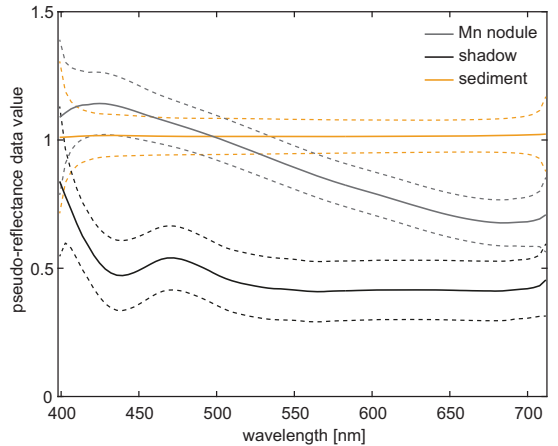


Fig. 3. Spectral responses for the three categories common to all tracks: manganese nodule, shadow (mostly behind nodules), and background sediment. Solid lines represent the mean spectrum based on ROIs of tracks 4–14, dashed lines mark the standard deviation.

Most nodules exhibit prominent shadows on the side facing away from the ROV lamps (Fig. 2a, b).

##### 4.2. Supervised classification results

The same ROIs were used for the SVM and SAM classifications. In total, 20 categories were defined, three of which were common to all

tracks: nodule, sediment, and shadow. Mean spectra for these three categories are shown in Fig. 3. Although the shadows represented an illumination effect rather than seafloor material or fauna, it was necessary to include them as ROIs to avoid misclassification of the shadow areas. The sediment category represented the background sediment, i.e., the brown silicate oozes that typically constituted the surface sediment (Borowski, 2001). In addition, brighter sediment patches associated with light-coloured clays exposed from beneath the surface layer (Borowski, 2001) occurred on some tracks and were assigned to a separate category termed “deeper sediment”.

Based on taxa identification in the video data and the spectral characteristics, 16 spectral categories were defined for the megafauna, including sponges, corals, crustaceans, ophiuroids and dead salps. Further information is given in Dumke et al. (in prep.). Not all of these categories were present on each track; the number of fauna categories per track varied between one and six, with an average of 3.5.

In addition, one category was defined for distinct green spots in the UHI image. The associated spectra showed a minimum around 675 nm (Dumke et al., in prep.), which is characteristic for in vivo absorption of chlorophyll-a (e.g. Hakvoort et al., 1997). These spots may potentially represent increased concentrations of chlorophyll-a or degraded products associated with biomass that sank down to the seafloor from shallow waters (Dumke et al., in prep.).

#### 4.2.1. SVM results

Comparison with the UHI pseudo-RGB images showed that the SVM classification results were relatively accurate. The exposed nodule surfaces were generally well classified, as were the larger types of megafauna (Figs. 2c, 4b, f). The nodules were commonly characterized by a combination of the nodule category and the shadow category, but they did not appear as connected nodule-shadow objects. Instead, they consisted of several small patches that belong to the nodule or shadow category and are surrounded by the background sediment category (Figs. 2c, 4b, f). In between the larger nodules, many small nodule and also shadow category patches were apparent even after classification aggregation of 25–35 pixels.

With a coverage of 94.7–97.5%, the background sediment category was by far the most dominant material category in the study area. Only 0.9–3.4% of the imaged surface areas were associated with nodules, while shadow areas constituted 1.0–2.6% (Fig. 5a). Combining the 16 fauna categories detailed in Dumke et al. (in prep.) resulted in a fauna coverage of < 0.5% of the seafloor. Both the green spots and deeper exposed sediment category had a maximum coverage of about 0.2% (Fig. 5a), with the deeper, light coloured sediment exposed on only five of the 11 tracks.

#### 4.2.2. SAM results

The SAM results were generally inferior to those produced using the SVM method. While SAM was able to distinguish the larger nodules from the background sediment category, they were not always classified well, and many non-sediment pixels remained unclassified (Fig. 4c, g). Also, small megafauna and green spots were often not classified correctly. For example, in the lower left of Fig. 4g, SAM classified pixels as green spots whereas SVM classified these pixels as nodule or sediment (Fig. 4f), which appears to be supported by the pseudo-reflectance data (Fig. 4e). Larger megafauna such as the coral in Fig. 4g were generally classified well by SAM.

Due to the differences between the SVM and SAM classifications, the areal coverage estimations also varied by category. For the four tracks classified by SAM, the mean coverages for the nodule category (0.5–1.6%) and the shadow category (0.3–0.7%) were lower estimations than those determined by the SVM results (Fig. 5a). In contrast, coverage for the combined 16 fauna categories and the green spot category was estimated to be higher via the SAM method than the SVM method. Roughly 1% of the image pixels remained unclassified by SAM (Fig. 5a).

#### 4.2.3. Accuracy of SAM relative to SVM

Based on the pseudo-reflectance images (Fig. 4a, e), SVM yielded a good classification of the nodule and shadow areas, as well as of most megafauna such as the crustacean and isopod in Fig. 4b and the coral in Fig. 4f. SAM also distinguished these areas from the background

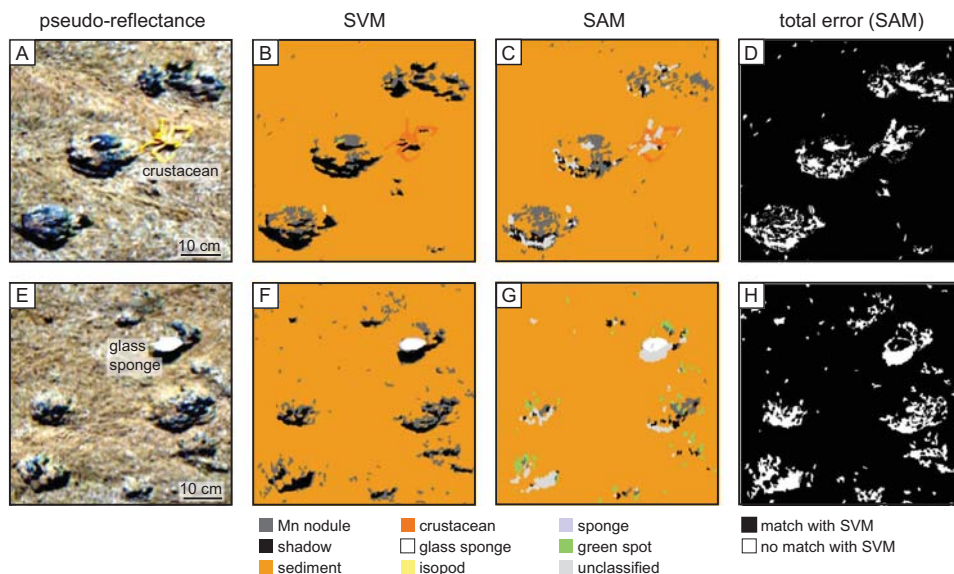


Fig. 4. Comparison of the SVM and SAM classification results for two examples (locations are shown in Fig. 1c). (a) and (e): pseudo-reflectance data (in pseudo-RGB with R: 645 nm, G: 571 nm, B: 473 nm), showing manganese nodules with a crustacean (Decapoda, Parapaguridae, *Probebebi mirabilis*) and an isopod (Isopoda, Munnopsidae) in (a) and manganese nodules with a glass sponge in (e). (b) and (f): SVM classification result after classification aggregation of 35 in (b) and 30 in (f). (c) and (g): SAM classification result after classification aggregation of 25 in (c) and 30 in (g). (d) and (h): total error of SAM relative to the SVM classification result.

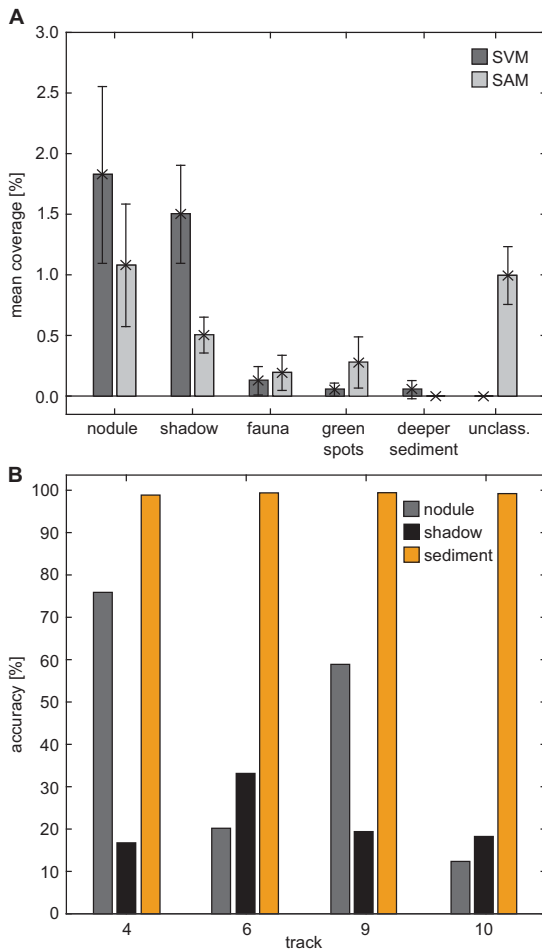


Fig. 5. (a) Mean coverage of each category for the SVM and SAM classifications, shown in percentage of the total number of pixels per track and excluding the background sediment category. The fauna category comprises 16 different megafauna detailed in Dumke et al. (in prep.). (b) Classification accuracy of SAM relative to SVM for the nodule, shadow, and background sediment categories on the four tracks classified by both methods (locations are shown in Fig. 1c). While the relative accuracy is high (> 98%) for the sediment category, it is much lower and more variable for the nodule and shadow categories.

sediment, and the coral, crustacean and parts of the nodule areas were classified in agreement with SVM (Fig. 4c, g). However, other non-sediment areas were assigned a different category, and many pixels, e.g. shadow pixels, were not classified at all.

The overall accuracy of SAM relative to SVM varied between 94.7% and 97.2%, as determined from direct comparison of the classification images via ENVI's confusion matrix tool. However, these high values were mostly due to the high accuracy for the background sediment category (98.8–99.4%; Fig. 5b), which constituted > 94% of the image pixels. For the other categories, the relative accuracy was much lower, with 12.3–75.9% for the nodule category and 16.7–33.1% for the shadow category (Fig. 5b). This discrepancy is further illustrated by the total error of the SAM classification as inferred from the confusion matrix (Fig. 4d, h). The pixels for which the SAM classification agreed with the SVM result mostly belonged to the background sediment category, whereas pixels of categories different from those assigned by SVM generally belonged to the non-sediment categories. Hence, while

the SAM method was able to distinguish these non-sediment pixels from the background sediment, it was often not able to classify them in the same way as SVM.

#### 4.3. Areal nodule density

On all tracks, case 1 resulted in less nodule objects being identified than the true number of nodules (Table 1). In contrast, the amount of nodules suggested by case 2 was overestimations of the numbers actually present on the seafloor. Therefore, using only the nodule category for the clumping method underestimated the number of nodules, while also taking into account the shadow category overestimated the amount.

Comparison with the UHI pseudo-RGB images showed that not all of the clumped objects were confirmed nodules. For case 1, on average 86.9% of the clumped objects were confirmed nodules, while for case 2, 76.0% of all objects represented nodules (Table 1). The remaining objects were false positive identifications, i.e., other anomalies not associated with nodules. For example, larger megafauna also caused shadows that were included in the case 2 objects.

In addition, some confirmed nodules were not included in the clumped objects and thus represented false negatives. Only 62.1% of the confirmed nodules corresponded to the clumped objects of case 1, whereas 86.5% were detected in case 2 (Table 1). Case 2 therefore included less false negatives but more false positives than case 1. Some tracks also exhibited double counts, i.e., two separate objects belonging to the same nodule, which further influenced the nodule count.

The different success rates of the nodule counts based on the two clumping methods are indicated in Fig. 6. The manual nodule count in the pseudo-reflectance data (Fig. 6a) and the video data revealed 17 nodules, which are generally also apparent in the SVM classification image (Fig. 6b). Case 1 detected 11 of these, with the remaining six representing false negatives (Fig. 6c, Table 1). In case 2 (Fig. 6d), the number of counted objects equals that of the manual count (17), but only 14 of these are confirmed nodules. The other three are two false positives and one double count where a nodule object and a shadow object belonging to the same nodule are not connected (Fig. 6d, Table 1). Three confirmed nodules were not detected by case 2 (false negatives). Note that in case 2, three nodules were detected that were not recognized by case 1.

Based on the number of confirmed nodules and the dimensions of the imaged areas, the reference nodule density varied between 6.9 and 11 nodules per  $m^2$ , with an average of  $9.4 m^{-2}$ . The areal nodule density inferred from case 1 was generally lower ( $3.4$ – $10.3 m^{-2}$ , average  $7.0 m^{-2}$ ); for case 2, it was higher ( $8.4$ – $12.4 m^{-2}$ , average  $10.7 m^{-2}$ ). For the example in Fig. 6, the true areal nodule density is  $8.4 m^{-2}$ , but the nodule count of case 1 resulted in a lower nodule density of  $5.4 m^{-2}$ . Case 2 arrived at the correct density of  $8.4 m^{-2}$ , though this is a result of the false positives numerically equalling the false negatives.

## 5. Discussion

In this study, we presented hyperspectral image data acquired in 4195 m water depth, using a UHI on an ROV. As it was the first time a hyperspectral imaging study of this kind was conducted in the deep sea, we first evaluate the acquisition setup used, before discussing the results of the supervised classifications as well as their implications.

#### 5.1. Evaluation of the acquisition setup and suggestions for improvement

Acquisition of UHI data can be challenging, because several requirements have to be fulfilled by the underwater vehicle used as the mounting platform for the UHI. These requirements include the maintenance of constant velocity, heading and altitude, as well as high-resolution (about 5 kHz) navigation and vehicle attitude data (Johnsen

**Table 1**

Overview of the true number of nodules (manual count) and the nodule amount determined from the clumping results (clump count) for case 1 (nodule category only) and case 2 (nodule and shadow category). Track locations are shown in Fig. 1c.

Track	Manual count	Clump count	No. of correct nodules	Correct nodules: % of manual count	Correct nodules: % of growth count	Double count	False positive	False negative
Case 1								
4	32	12	12	37.50	100.00	0	0	20
5	38	38	30	78.95	78.95	0	8	8
6	25	24	18	72.00	75.00	1	5	7
7	17	11	11	64.71	100.00	0	0	6
8	36	34	29	80.56	85.29	0	5	7
9	34	17	17	50.00	100.00	0	0	17
10	28	27	21	75.00	77.78	0	6	7
12	58	38	32	55.17	84.21	5	1	26
14	29	16	13	81.25	81.25	2	1	16
Case 2								
4	32	43	26	81.25	60.47	4	13	6
5	38	43	33	86.84	76.74	1	9	5
6	25	32	22	88.00	68.75	0	10	3
7	17	17	14	82.35	82.35	1	2	3
8	36	42	32	88.89	76.19	0	10	4
9	34	47	34	100.00	72.34	0	13	0
10	28	31	25	89.29	80.65	0	6	3
12	58	50	38	65.52	76.00	3	9	20
14	29	31	28	96.55	90.32	0	3	1

et al., 2013, 2016; Tegdan et al., 2015). In addition, sufficiently even illumination is necessary. While the ROV used in this study met most of these requirements, the USBL navigation data was of too low accuracy, due to the great water depth, so the use of video-based navigation data (Nornes et al. (in prep.)) for geocorrection of the UHI data was a required additional processing step.

Issues with seafloor illumination were also encountered. As demonstrated by the radiance data (Fig. 2a), the acquisition setup was not optimal in terms of illumination. As a result, a prominent shadow caused by the manipulator arm holding the UHI was present in the data, which could not be avoided, as the UHI could not be mounted on the ROV in any more appropriate configuration. Smaller shadows occurring behind nodules and other elevated features were due to the positioning of the illumination source above and behind the UHI. If it had been possible to mount dedicated lamps on either side of the UHI, as has been done for shallow-water UHI surveys using ROVs (Johnsen et al., 2013, 2016; Tegdan et al., 2015), illumination would have been directly from above, which would have reduced the occurrence of shadows behind nodules. Moreover, the manipulator arm would not have influenced illumination. Fortunately, it was possible to remove the setup-induced shadow completely during post-processing, but we recommend that such a setup should be avoided in the future.

Due to the lack of dedicated lighting with a known spectrum, as well as lack of knowledge of the inherent optical properties of the water column, it was not possible to obtain an optimal illumination reference for reflectance processing. The applied reference spectra derived from the median-spectra approach resulted in generally good processing results, but they could not correct for all external influences and therefore resulted in pseudo-reflectance data rather than true reflectance data. Obtaining true reflectance data would have required more extensive processing, e.g. involving radiative transfer modelling to determine an accurate illumination reference for the light field of the combined ROV lamps, which was outside the scope of this study.

To provide a spectral classification of OOI, which was the aim of this study, true reflectance data were not necessarily required. However, for comparison of spectral signatures with spectra from existing spectral databases, as well as with spectral responses acquired in other areas or on different platforms, obtaining true reflectance data would be essential. Moreover, with true reflectance data a spectral database for endmember spectra could be set up. Such a database would facilitate supervised classification of potential future hyperspectral image data

from the study area, as manual definition of ROIs to obtain endmember spectra would no longer be required if an OOI's reflectance spectrum is already contained in the database.

## 5.2. Relative accuracy of the classification methods

Our results show that the SVM method provided a more accurate classification than the SAM method. While the SVM results are interpreted as a good approximation of ground-truthing images, the SAM results contain unclassified pixels, and additionally, non-sediment pixels were often classified differently than by SVM. Visual comparison with the pseudo-reflectance data suggests that the SVM results appear generally correct, while the SAM results are likely erroneous when they differ from the SVM results. The discrepancies in estimations of seafloor coverage by the different categories between the two methods (Fig. 5a) are therefore thought to be largely due to misclassifications by the SAM method.

Although the SVM method is more accurate than SAM, it did not perform perfectly, as misclassification of pixels did occur. However, in the absence of suitable ground-truthing data, the true accuracy of the SVM method cannot be determined. Generally, visual comparison with the UHI pseudo-RGB images suggested that most of the exposed nodule surfaces, larger megafauna and shadows were classified accurately. However, very small patches classified as nodule or shadow often remained in between the larger features after classification aggregation (25–35 pixels) was applied. It is unclear whether these small pixels clusters were classified correctly. They could represent classification noise where the classification did not work well, but the UHI pseudo-RGB data are not conclusive in this regard, and potential features would be too small to be clearly resolved in the video data. Alternatively, at least the larger of these patches could represent small outcrops of nodules that have been almost completely buried, e.g. by re-sedimentation of the sediment plume produced by the 78 plough trawls comprising the DISCOL experiment. Another explanation could be small-scale terrain roughness causing shadows on the side facing away from the ROV lamps, but without micro-scale bathymetry, this can neither be confirmed nor excluded.

In the absence of ground-truthing images, absolute classification accuracies of the two classification methods used here could not be determined. Therefore, only estimates of relative accuracies were possible. Based on the very good classification results of the SVM method,

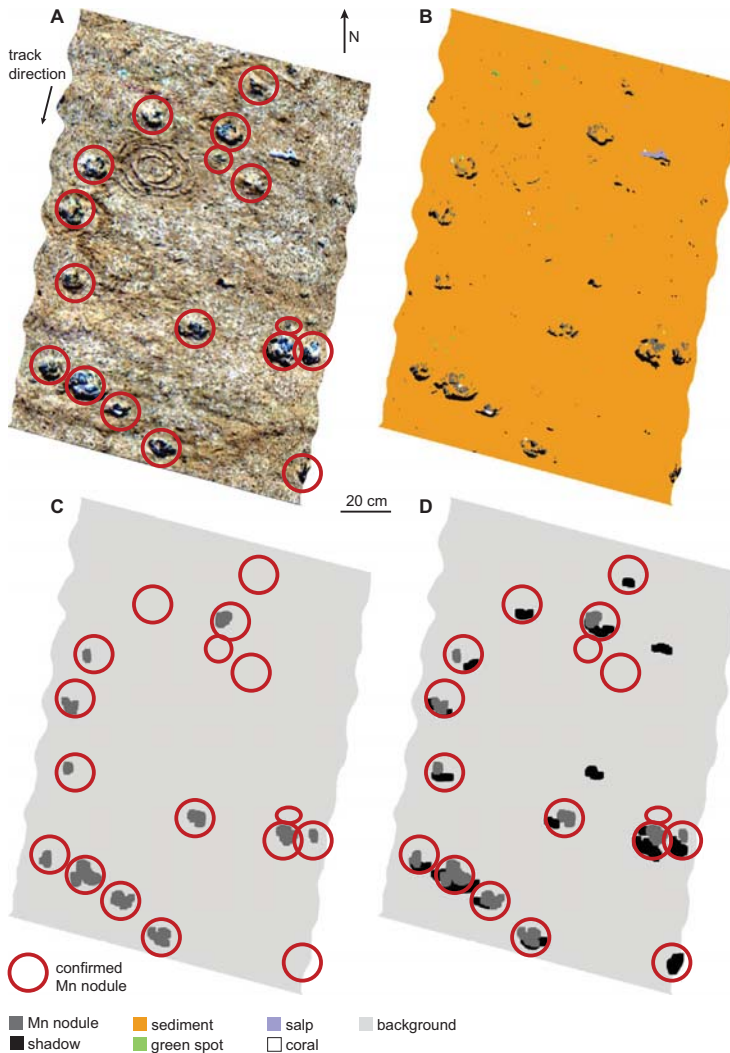


Fig. 6. (a) UHI pseudo-reflectance data (in pseudo-RGB) showing 17 manganese nodules highlighted by red circles, as well as a dead salp and a coral. (b) SVM classification image that served as a basis for the clumping of category areas. (c) Clump image for case 1 (nodule category only) based on the SVM classification image in (b). A total of 11 nodule objects were detected, with six false negatives marked by empty circles. (d) Clump image for case 2 (nodule category and shadow category combined) based on (b). Although 17 potential nodule objects were detected, they include two false positives and one double count, while three nodules were not detected (false negatives). (For interpretation of the references to colour in this figure legend, the reader is referred to the web version of this article.)

we estimate a classification accuracy of > 90% for the non-sediment categories and about 99% for the background sediment category. For SAM, the classification accuracy was considerably lower than for SVM and was estimated to about 40% for the non-sediment categories and > 90% for the background sediment category.

### 5.3. Detection of seafloor manganese nodules

Supervised classification using the SVM method is able to detect manganese nodules imaged in UHI data. This is shown by the clumping results and comparison of the potential nodule objects with the true nodule presence. Although it should be noted that the shape and size of the clumped objects do not necessarily represent the true nodule dimensions, the clumped objects indicate where nodules are suggested to be present based on the classification results.

When only the nodule category was used in the clumping procedure (case 1), in most cases not all nodules present were detected, which resulted in false negatives. Nevertheless, this approach is preferred over case 2, which generally overestimated the amount of nodules by

introducing more false positives. The number of false negatives in the case 1 results could potentially be reduced by decreasing the degree of classification aggregation before the clumping process, thus allowing nodules marked by only small pixel clusters to be taken into account. However, this would also increase the number of false positives, as more non-nodule areas (misclassifications) would also be included.

In addition to nodule detection, the classification images also allowed estimating nodule coverage, which was about 1–4% in the SVM classification images. However, this amount only represents the minimum nodule coverage, given that most nodules were partly covered by sediment. As a nodule half covered by sediment will only have half of its surface area classified as nodule, the resulting category coverage is lower than the true nodule coverage. Therefore, coverage estimates derived from the clumped objects (1–6% for case 1 and 4–9% for case 2) are probably more realistic, even though they also include false positives and false negatives. Nodule coverages of up to 9% are in agreement with nodule coverages determined in other areas such as in the Clarion-Clipperton Zone (2–20%; Le Bas and North, 2016) and the Central Indian Ocean Basin (2–15%; Sharma et al., 2010).

Current methods for determining nodule coverage are largely based on conventional RGB photo imagery from which nodule coverage is derived through unsupervised or supervised classification (Sharma et al., 2010; Schoening et al., 2012, 2014), image segmentation methods (Schoening et al., 2016; Kuhn and Rathke, 2017), object-based image analysis (Le Bas and North, 2016), or kriging methods (Kuhn et al., 2016). High-resolution photo imagery has also been correlated with acoustic backscatter data to extrapolate nodule coverage over larger areas based on backscatter values (Chakraborty and Kodagali, 2004; Le Bas and North, 2016). In addition, image data can be combined with results from box corer samples to determine resource estimates in  $\text{kg m}^{-2}$  (Kuhn et al., 2016; Kuhn and Rathke, 2017).

Hyperspectral image data provide an alternative to the conventional RGB imagery used by these approaches. Although it was beyond the scope of this study to directly compare the hyperspectral classification results to classification of RGB imagery, it is expected that the higher spectral resolution of hyperspectral data yield more accurate classification results than RGB imagery (Johnsen et al., 2013). Comparisons between hyperspectral and multispectral classifications (e.g. Hochberg and Atkinson, 2003) showed that hyperspectral classifications were generally superior to those based on fewer spectral bands. Hyperspectral imaging may thus provide a better basis for determining seafloor nodule coverage.

#### 5.4. Potential for hyperspectral mapping of seafloor mineral resources

Our results show that underwater hyperspectral image data can be used similarly to conventional hyperspectral data to detect and evaluate mineral resources of interest for mining purposes. The main differences between the conventional approach applied in terrestrial mineral exploration and our underwater approach are the spectral band range and the areal coverage.

Conventional hyperspectral imaging for mineral exploration usually does not focus on the visible range. Instead, the near-infrared and infrared parts of the solar spectrum are used in preference (Resmini et al., 1997; Bierwirth et al., 1999; Sabins, 1999; Kruse et al., 2003), as these contain characteristic absorption minima in mineral spectra (Clark et al., 1990). However, our data indicate that mineral deposits such as manganese nodules are well imaged and spectrally distinct in the visible range. Based on these observations, we suggest that the necessary omission of near-infrared and infrared wavelengths in underwater hyperspectral imaging does not affect the detection of seafloor mineral resources.

Due to the requirement to maintain a low altitude of 1–2 m, resulting in a swath width of 1–2 m, UHI surveys have a much lower areal coverage than conventional hyperspectral surveys. UHIs are therefore only suitable for mapping small areas of up to a few 1000  $\text{m}^2$ . Coverage could be increased by increasing the altitude to up to 7 m (approximately 7 m swath width), provided the illumination sources are strong enough to ensure sufficient seafloor illumination (S. Ekehaug, pers. comm.). Alternatively, an AUV could be used as UHI platform, which would allow increased coverage due to higher survey altitudes of 6–9 m and the autonomous operation mode (Sture et al., 2017). However, in both cases, the image resolution and hence feature detectability would suffer. For low-altitude (1–2 m) ROV-based studies, the spatial resolution is considerably higher and allows more detailed mapping of deposits, including mapping of individual manganese nodules, as shown in this study.

With the growing interest in commercial deep-sea mining, the need for high-resolution seafloor exploration is also increasing (Van Dover, 2011; Boschen et al., 2013, 2016; Collins et al., 2013). While a UHI would not be suitable to map an entire mining claim, UHI surveys could be used for detailed investigations of target sites that were identified in larger-scale seabed data, e.g. acquired by acoustic methods.

As with terrestrial hyperspectral image data, seafloor hyperspectral images also have the potential to allow different types of mineral

deposits to be distinguished (Johnsen et al., 2013). In the case of manganese nodules, compositions can vary over larger spatial scales, e.g. nodules from the Peru Basin differ in composition from those in the Clarion-Clipperton Zone (Glasby, 2000). These variations are, however, unlikely to be directly reflected by the nodule surfaces imaged by UHI surveys, and our data show that in the study area, spectral variations within the nodule category are low (Fig. 3). The potential for spectrally distinguishing different types of deposits is expected to be higher for hydrothermal deposits in massive sulphide areas, which are also a current target for potential future resource exploitation (Glasby, 2002; Rona, 2003; Hoagland et al., 2010; Boschen et al., 2013). First results (Dumke and Ellefmo, 2017) indicate that differences in the surface material composition of such deposits are apparent in UHI data.

## 6. Conclusions

In this study, we presented the first hyperspectral image data from the deep seafloor. Manganese nodules and seabed fauna may be well imaged at high spectral and spatial resolutions. Comparison of two supervised classification methods showed that the SVM method is superior to the SAM method in classifying manganese nodules as well as fauna and sediment anomalies. Nodule coverages within the surveyed region of the nodule field investigated were inferred from the SVM classification images and varied between 1 and 9% of the seafloor. Most nodule surfaces are not fully exposed due to sediment partially covering the top surfaces of nodules, which resulted in these sections of nodules being classified as sediment rather than nodule.

Our results show that underwater hyperspectral imaging allows extending seafloor hyperspectral surveys from shallow coastal waters to the deep sea, and therefore represents a promising new method for high-resolution mapping and classification of seafloor composition in terms of mineral deposit quantification. Moreover, the approach has a high potential for habitat mapping and environmental monitoring, e.g. in terms of fauna characterisation and distribution (Tegdan et al., 2015; Johnsen et al., 2016; Dumke et al., in prep.), which are also of high importance for environmental management in future mining areas (International Seabed Authority, 2012; Boschen et al., 2013, 2016; Durden et al., 2016; Vanreusel et al., 2016). Provided a broader exploration technique is applied first to identify areas of interest for high-resolution surveys, the UHI may become a promising tool for high-resolution seafloor exploration and monitoring in potential deep-sea mining areas.

## Acknowledgements

This study received funding by the Norwegian Research Council (grant no. 250228) under the framework of JPI Oceans “MiningImpact”. Additional funding was provided by the European Union’s Seventh Framework Programme for research, technological development and demonstration under the Blue Mining project (grant no. 604500) and by the Norwegian Research Council through the NTNU AMOS Centre of Excellence (grant no. 223254). Funding for the JPIO SONNE expedition SO242/2 and associated research was made available by the German Federal Ministry of Education and Research (BMBF; grant no. 03F0707A-G). Particular thanks are directed to chief scientist Antje Boetius, GEOMAR’s KIEL6000 ROV team, as well as Captain Oliver Meyer and the crew of RV SONNE for their excellent support. Lars Martin Sandvik Aas and Stefan Ekehaug (both Ecotone AS) are thanked for advice on data processing. We also thank the associate editor and two anonymous reviewers for their constructive comments, which helped to improve the manuscript. The UHI data of cruise SO242/2 are available at <https://doi.pangaea.de/10.1594/PANGAEA.874408>.

## References

- Adam, E., Mutanga, O., Rugege, D., 2010. Multispectral and hyperspectral remote sensing for identification and mapping of wetland vegetation: a review. *Wetl. Ecol. Manag.* 18, 281–296. <http://dx.doi.org/10.1007/s11273-009-9169-z>.
- Bierwirth, P., Blewett, R., Huston, D., 1999. Finding new mineral prospects with HYMAP: early results from a hyperspectral remote-sensing case study in the west Pilbara. *AGSO Res. Newsl.* 31, 29–31.
- Bioucas-Dias, J.M., Plaza, A., Camps-Valls, G., Scheunders, P., Nasrabadi, N.M., Chanussot, J., 2013. Hyperspectral remote sensing data analysis and future challenges. *IEEE Geosci. Remote Sens. Mag.* 1, 6–36. <http://dx.doi.org/10.1109/MGRS.2013.2244672>.
- Boettius, A. (Ed.), 2015. *RV SONNE Fahrtbericht/Cruise Report SO242-2*, JPI Oceans Ecological Aspects of Deep-sea Mining, DISCOL Revisited, Guayaquil-Guayaquil (Ecuador), 28.08.-01.10.2015. GEOMAR Report No. 27. GEOMAR Helmholtz Centre for Ocean Research, Kiel, Germany (552 pp.).
- Borowski, C., 2001. Physically disturbed deep-sea macrofauna in the Peru Basin, south-east Pacific, revisited 7 years after the experimental impact. *Deep-Sea Res. II* 48, 3809–3839. [http://dx.doi.org/10.1016/S0967-0645\(01\)00069-8](http://dx.doi.org/10.1016/S0967-0645(01)00069-8).
- Borowski, C., Thiel, H., 1998. Deep-sea macrofaunal impacts of a large-scale physical disturbance experiment in the Southeast Pacific. *Deep-Sea Res. II* 45, 55–81.
- Boschen, R.E., Rowden, A.A., Clark, M.R., Gardner, J.P.A., 2013. Mining of deep-sea seafloor massive sulfides: a review of the deposits, their benthic communities, impacts from mining, regulatory frameworks and management strategies. *Ocean Coast. Manag.* 84, 54–67. <http://dx.doi.org/10.1016/j.ocecoaman.2013.07.005>.
- Boschen, R.E., Rowden, A.A., Clark, M.R., Pallentin, A., Gardner, J.P.A., 2016. Seafloor massive sulfide deposits support unique megafaunal assemblages: implications for seabed mining and conservation. *Mar. Environ. Res.* 115, 78–88. <http://dx.doi.org/10.1016/j.marenvres.2016.02.005>.
- Camps-Valls, G., Gómez-Chova, L., Calpe-Maravilla, J., Martín-Guerrero, J.D., Soriano-Olivas, E., Alonso-Chordá, L., Moreno, J., 2004. Robust support vector method for hyperspectral data classification and knowledge discovery. *IEEE Trans. Geosci. Remote Sens.* 42, 1530–1542. <http://dx.doi.org/10.1109/TGRS.2004.827262>.
- Chakraborty, B., Kodagali, V., 2004. Characterizing Indian Ocean manganese nodule-bearing seafloor using multi-beam angular backscatter. *Geo-Mar. Lett.* 24, 8–13. <http://dx.doi.org/10.1007/s00367-003-0153-y>.
- Chang, G., Mahoney, K., Briggs-Whitmore, A., Kohler, D.D.R., Mobley, C.D., Lewis, M., Moline, M.A., Boss, E., Kim, M., Philpot, W., Dickey, T.D., 2004. The new age of hyperspectral oceanography. *Oceanography* 17, 16–23. <http://dx.doi.org/10.5670/oceanog.2004.43>.
- Chennu, A., Färber, P., Volkenborn, N., Al-Najjar, M.A.A., Janssen, F., de Beer, D., Polerecky, L., 2013. Hyperspectral imaging of the microscale distribution and dynamics of microphytobenthos in intertidal sediments. *Limnol. Oceanogr. Methods* 11, 511–528. <http://dx.doi.org/10.4319/lom.2013.11.511>.
- Clark, R.N., King, T.V.V., Klejwa, M., Swayze, G.A., 1990. High spectral resolution reflectance spectroscopy of minerals. *J. Geophys. Res.* 95, 12653–12680. <http://dx.doi.org/10.1029/JB095iB08p12653>.
- Collins, P.C., Croot, P., Carlsson, J., Colaço, A., Grehan, A., Hyeong, K., Kennedy, R., Mohn, C., Smith, S., Yamamoto, H., Rowden, A., 2013. A primer for the environmental impact assessment of mining at seafloor massive sulfide deposits. *Mar. Policy* 42, 198–209. <http://dx.doi.org/10.1016/j.marpol.2013.01.020>.
- Cronan, D.S., Tooms, J.S., 1969. The geochemistry of manganese nodules and associated pelagic deposits from the Pacific and Indian Oceans. *Deep-Sea Res.* 16, 335–359. [http://dx.doi.org/10.1016/0011-7471\(69\)90003-5](http://dx.doi.org/10.1016/0011-7471(69)90003-5).
- Daase, M. (Ed.), 2016. *Cruise Report – Polar Night Cruise 2016*. University of Tromsø (39 pp.).
- Dell'Acqua, F., Gamba, P., Ferrari, A., Palmason, J.A., Benediktsson, J.A., Arnason, K., 2004. Exploiting spectral and spatial information in hyperspectral urban data with high resolution. *IEEE Geosci. Remote Sens. Lett.* 1, 322–326. <http://dx.doi.org/10.1109/LGRS.2004.837009>.
- Dickey, T., Lewis, M., Chang, G., 2006. Optical oceanography: recent advances and future directions using global remote sensing and in situ observations. *Rev. Geophys.* 44, RG1001. <http://dx.doi.org/10.1029/2003RG000148>.
- Dierrsen, H.M., 2013. Overview of hyperspectral remote sensing for mapping marine benthic habitats from airborne and underwater sensors. *Imaging Spectrometry XVIII*. Proc. SPIE 1–7. <http://dx.doi.org/10.1117/12.2026529>.
- Dierrsen, H.M., Randolph, K., 2013. Remote sensing of ocean color. In: *Encyclopedia of Sustainable Science and Technology*. Springer. [http://dx.doi.org/10.1007/978-1-4614-5684-1\\_18](http://dx.doi.org/10.1007/978-1-4614-5684-1_18).
- Dierrsen, H.M., Chlus, A., Russell, B., 2015. Hyperspectral discrimination of floating mats of seagrass wrack and the macroalgae *Sargassum* in coastal waters of Greater Florida Bay using airborne remote sensing. *Remote Sens. Environ.* 167, 247–258. <http://dx.doi.org/10.1016/j.rse.2015.01.027>.
- Dumke, I., Ellefmo, S.L., 2017. Report on visual data acquisition in the field and interpretation for SMS. In: *Blue Mining Deliverable D1.31*, Blue Mining Project, European Commission Seventh Framework Programme, (33 pp.).
- Dumke, I., Purser, A., Marcon, Y., Nornes, S.M., Johnsen, G., Ludvigsen, M., Søreide, F., 2018. Underwater hyperspectral imaging as an in-situ taxonomic tool for deep-sea megafauna (unpublished).
- Durden, J.M., Billett, D.S.M., Brown, A., Dale, A.C., Goulding, L., Gollner, S., Murphy, K., Pape, E., Purser, A., Rolin, J.-F., Smith, A.J., Stewart, I., Turner, P.J., de Wachter, T., Weaver, P.P.E., van Dover, C.L., Verlaan, P., Jones, D.O.B., 2016. Report on the Managing Impacts of Deep-sea Resource Exploitation (MIDAS) workshop on environmental management of deep-sea mining. *Res. Ideas Outcomes* 2, e10292. <http://dx.doi.org/10.3897/rio.2.e10292>.
- Fearn, P.R.C., Klonowski, W., Babcock, R.C., England, P., Phillips, J., 2011. Shallow water substrate mapping using hyperspectral remote sensing. *Cont. Shelf Res.* 31, 1249–1259. <http://dx.doi.org/10.1016/j.csr.2011.04.005>.
- Foell, E.J., Thiel, H., Schriever, G., 1990. DISCOL: A Long-term, Large-scale, Disturbance-recolonization Experiment in the Abyssal Eastern Tropical South Pacific Ocean. *Offshore Technology Conference 1990*, Houston, Texas, pp. 497–503. <http://dx.doi.org/10.4043/6328-MS>.
- Fossen, T.L., 2011. *Handbook of Marine Craft Hydrodynamics and Motion Control*. John Wiley and Sons, UK.
- Glasby, G.P., 1972. The mineralogy of manganese nodules from a range of marine environments. *Mar. Geol.* 13, 57–72. [http://dx.doi.org/10.1016/0025-3227\(72\)90071-0](http://dx.doi.org/10.1016/0025-3227(72)90071-0).
- Glasby, G.P., 2000. Manganese: predominant role of nodules and crusts. In: Schulz, H.D., Zable, M. (Eds.), *Marine Geochemistry*. Springer, Berlin, pp. 335–372.
- Glasby, G.P., 2002. Deep seabed mining: past failures and future prospects. *Mar. Georesour. Geotechnol.* 20, 161–176. <http://dx.doi.org/10.1080/0368860290051859>.
- Goetz, A.F.H., 2009. Three decades of hyperspectral remote sensing of the Earth: a personal view. *Remote Sens. Environ.* 113, S5–S16. <http://dx.doi.org/10.1016/j.rse.2007.12.014>.
- Goetz, A.F.H., Vane, G., Solomon, J.E., Rock, B.N., 1985. Imaging spectrometry for Earth remote sensing. *Science* 228, 1147–1153. <http://dx.doi.org/10.1126/science.228.4704.1147>.
- Greiner, J. (Ed.), 2015. *RV SONNE Fahrtbericht/Cruise Report SO242-1*, JPI Oceans Ecological Aspects of Deep-Sea Mining, DISCOL Revisited, Guayaquil-Guayaquil (Ecuador), 28.07.-25.08.2015. GEOMAR Report No. 26. GEOMAR Helmholtz Centre for Ocean Research, Kiel, Germany (290 pp.).
- Gwyther, D., 2008. *Environmental Impact Statement, Solwara 1 Project*. Nautilus Minerals Niugini Limited, Main Report. Coffey Natural Systems, Brisbane.
- Hakvoort, H., Heymann, K., Stein, C., Murphy, D., 1997. In-situ optical measurements of sediment type and phytochemicals of tidal flats: a basis for imaging remote sensing spectroscopy. In: *Deutsche Hydrographische Zeitschrift*. 49. <http://dx.doi.org/10.1007/BF02764045>. (367–272).
- Herold, M., Roberts, D., Smadi, O., Noronha, V., 2004. Road Condition Mapping Using Hyperspectral Remote Sensing. 2004 AVIRIS Workshop, Pasadena, California. (15 pp.).
- Hoagland, P., Beaulieu, S., Tivey, M.A., Eggert, R.G., German, C., Glowka, L., Lin, J., 2010. Deep-sea mining of seafloor massive sulfides. *Mar. Policy* 34, 728–732. <http://dx.doi.org/10.1016/j.marpol.2009.12.001>.
- Hochberg, E.J., Atkinson, M.J., 2000. Spectral discrimination of coral reef benthic communities. *Coral Reefs* 19, 164–171. <http://dx.doi.org/10.1007/s003380000087>.
- Hochberg, E.J., Atkinson, M.J., 2003. Capabilities of remote sensors to classify coral, algae, and sand as pure and mixed spectra. *Remote Sens. Environ.* 85, 174–189. [http://dx.doi.org/10.1016/S0034-4257\(02\)00202-X](http://dx.doi.org/10.1016/S0034-4257(02)00202-X).
- International Seabed Authority, 2012. *Environmental management needs for exploration and exploitation of deep sea minerals*. ISA Technical Study Series 10. International Seabed Authority, Kingston, Jamaica.
- Johnsen, G., Volent, Z., Dierrsen, H., Pettersen, R., Van Ardelan, M., Søreide, F., Fearn, P., Ludvigsen, M., Moline, M., 2013. Underwater hyperspectral imagery to create biogeochemical maps of seafloor properties. In: Watson, J., Zielinski, O. (Eds.), *Subsea Optics and Imaging*. Woodhead Publishing Ltd., Cambridge, pp. 508–535.
- Johnsen, G., Ludvigsen, M., Sørensen, A., Sandvik Aas, L.M., 2016. The use of underwater hyperspectral imaging deployed on remotely operated vehicles – methods and applications. *IFAC-PapersOnLine* 49 (23), 476–481. <http://dx.doi.org/10.1016/j.ifacol.2016.10.541>.
- Klonowski, W.M., Fearn, P.R.C.S., Lynch, M.J., 2007. Retrieving key benthic cover types and bathymetry from hyperspectral imagery. *J. Appl. Remote Sens.* 1, 011505. <http://dx.doi.org/10.1117/1.2816113>.
- Kruse, F.A., Lefkoff, A.B., Boardman, J.W., Heidebrecht, K.B., Shapiro, A.T., Barloon, P.J., Goetz, A.F.H., 1993. The Spectral Image Processing System (SIPS) – interactive visualization and analysis of imaging spectrometer data. *Remote Sens. Environ.* 44, 145–163. [http://dx.doi.org/10.1016/0034-4257\(93\)90013-N](http://dx.doi.org/10.1016/0034-4257(93)90013-N).
- Kruse, F.A., Boardman, J.W., Huntington, J.F., 2003. Comparison of airborne hyperspectral data and EO-1 Hyperion for mineral mapping. *IEEE Trans. Geosci. Remote Sens.* 41, 1388–1400. <http://dx.doi.org/10.1109/TGRS.2003.812908>.
- Kuhn, T., Rathke, M., 2017. Report on Visual Data Acquisition in the Field and Interpretation for SMn. *Blue Mining Deliverable D1.31*, Blue Mining project, European Commission Seventh Framework Programme. (34 pp.).
- Kuhn, T., Rühlemann, C., Knobloch, A., 2016. Classification of manganese nodule estimates: can we reach the “measured resource” level? In: Hong, S., Morgen, C.L. (Eds.), *Resource and Environmental Assessments for Seafloor Mining Development*. Underwater Mining Conference 2016, Incheon, Korea, (6 pp.).
- Kutser, T., Miller, I., Jupp, D.L.B., 2006. Mapping coral reef benthic substrates using hyperspectral space-borne images and spectral libraries. *Estuar. Coast. Shelf Sci.* 70, 449–460. <http://dx.doi.org/10.1016/j.ecss.2006.06.026>.
- Landmann, T., Piironen, R., Makori, D.M., Abdel-Rahman, E.M., Makau, S., Pellikka, P., Raina, S.K., 2015. Application of hyperspectral remote sensing for flower mapping in African savannas. *Remote Sens. Environ.* 166, 50–60. <http://dx.doi.org/10.1016/j.rse.2015.06.006>.
- Le Bas, T., North, L., 2016. *Acoustic Model for Seafloor FeMn Nodules*. Blue Mining Deliverable D2.51, Blue Mining Project, European Commission Seventh Framework Programme. (62 pp.).
- Ludvigsen, M., Aasly, K., Ellefmo, S., Hilario, A., Ramirez-Llodra, E., Søreide, F., Falcon-Suarez, I., Juliani, C., Kieswetter, A., Lim, A., Malmquist, C., Nornes, S.M., Paulsen, E., Reimers, H., Sture, Ø., 2016. *Marine Cruise Report*. NTNU Cruise Reports 2016 No. 1. (108 pp.).

- Mazel, C.H., 1997. Diver-operated instrument for in situ measurement of spectral fluorescence and reflectance of benthic marine organisms and substrates. *Opt. Eng.* 36. <http://dx.doi.org/10.1117/1.601486>.
- Melgani, F., Bruzzone, L., 2004. Classification of hyperspectral remote sensing images with support vector machines. *IEEE Trans. Geosci. Remote Sens.* 42, 1778–1790. <http://dx.doi.org/10.1109/TGRS.2004.831865>.
- Mountrakis, G., Im, J., Ogole, C., 2011. Support vector machines in remote sensing: a review. *ISPRS J. Photogramm. Remote Sens.* 66, 247–259. <http://dx.doi.org/10.1016/j.isprsjprs.2010.11.001>.
- Nornes, S.M., Ødegård, Ø., Dumke, I., Ludvigsen, M., Johnsen, G., Sørensen, A.J., 2018. Unmanned underwater vehicle-based photogrammetry for marine benthic mapping. (unpublished).
- Petit, T., Bajjouk, T., Mouquet, P., Rochette, S., Vozel, B., Delacourt, C., 2017. Hyperspectral remote sensing of coral reefs by semi-analytical model inversion – comparison of different inversion setups. *Remote Sens. Environ.* 190, 348–365. <http://dx.doi.org/10.1016/j.rse.2017.01.004>.
- Pettersen, R., Johnsen, G., Bruheim, P., Andreassen, T., 2014. Development of hyperspectral imaging as a bio-optical taxonomic tool for pigmented marine organisms. *Org. Divers. Evol.* 14, 237–246. <http://dx.doi.org/10.1007/s13127-013-0163-1>.
- Pons, S., Aymerich, I.F., Torrecilla, E., Piera, J., 2007. Monolithic spectrometer for environmental monitoring applications. In: Proceedings of IEEE/OEE Oceans Conference and Exhibition, OCEANS'07 Europe, Aberdeen, <http://dx.doi.org/10.1109/OCEANSE.2007.4302402>. (3 pp.).
- Ramírez-Pérez, M., Röttgers, R., Torrecilla, E., Piera, J., 2015. Cost-effective hyperspectral transmissometers for oceanographic applications: performance analysis. *Sensors* 15, 20967–20989. <http://dx.doi.org/10.3390/s150920967>.
- Reddy, A., 2010. Image processing and counting using MATLAB. <http://www.instructables.com/id/Image-Processing-and-Counting-using-MATLAB/>, Accessed date: 19 April 2017.
- Resmini, R.G., Kappus, M.E., Aldrich, W.S., Harsanyi, J.C., Anderson, M., 1997. Mineral mapping with Hyperspectral Digital Imagery Collection Experiment (HYDICE) sensor data at Cuprite, Nevada, U.S.A. *Int. J. Remote Sens.* 18, 1553–1570. <http://dx.doi.org/10.1080/014311697218278>.
- Roessner, S., Segl, K., Heiden, U., Kaufmann, H., 2001. Automated differentiation of urban surfaces based on airborne hyperspectral imagery. *IEEE Trans. Geosci. Remote Sens.* 39, 1525–1532. <http://dx.doi.org/10.1109/36.934082>.
- Rona, P.A., 2003. Resources of the sea floor. *Science* 299, 673–674. <http://dx.doi.org/10.1126/science.1080679>.
- Sabins, F.F., 1999. Remote sensing for mineral exploration. *Ore Geol. Rev.* 14, 157–183. [http://dx.doi.org/10.1016/S0169-1368\(99\)00007-4](http://dx.doi.org/10.1016/S0169-1368(99)00007-4).
- Schoening, T., Kuhn, T., Nattkemper, T.W., 2012. Estimation of poly-metallic nodule coverage in benthic images. In: Proceedings of the 41st Conference of the Underwater Mining Institute. UMI.
- Schoening, T., Kuhn, T., Nattkemper, T.W., 2014. Seabed classification using a bag-of-prototypes feature representation. In: 2014 ICPR Workshop on Computer Vision for Analysis of Underwater Imagery (CVAUI). IEEE, pp. 17–24. <http://dx.doi.org/10.1109/CVAUI.2014.9>.
- Schoening, T., Kuhn, T., Jones, D.O.B., Simon-Lledo, E., Nattkemper, T.W., 2016. Fully automated image segmentation for benthic resource assessment of poly-metallic nodules. *Methods Oceanogr.* 15–16, 78–89. <http://dx.doi.org/10.1016/j.mio.2016.04.002>.
- Schriever, G., 1995. DISCOL – disturbance and recolonization experiment of a manganese nodule area of the Southeastern Pacific. In: Proceedings of the ISOPE – Ocean Mining Symposium 1995, Tsukuba, Japan, pp. 163–166.
- Sharma, R., Sankar, S.J., Samanta, S., Sardar, A.A., Gracius, D., 2010. Image analysis of seafloor photographs for estimation of deep-sea minerals. *Geo-Mar. Lett.* 30, 617–626. <http://dx.doi.org/10.1007/s00367-010-0205-z>.
- Sohn, Y., Rebello, N.S., 2002. Supervised and unsupervised spectral angle classifiers. *Photogramm. Eng. Remote Sens.* 68, 1271–1280.
- Sture, Ø., Ludvigsen, M., Søreide, F., Sandvik Aas, L.M., 2017. Autonomous Underwater Vehicles as a Platform for Underwater Hyperspectral Imaging. OCEANS 2017 MTS/IEEE, Aberdeen, UK. <http://dx.doi.org/10.1109/OCEANSE.2017.8084995>.
- Tegdan, J., Ekehaug, S., Myrnes Hansen, I., Sandvik Aas, L.M., Steen, K.J., Pettersen, R., Beuchel, F., Camus, L., 2015. Underwater hyperspectral imaging for environmental mapping and monitoring of seabed habitats. OCEANS 2015, Genova. <http://dx.doi.org/10.1109/OCEANS-Genova.2015.7271703>. (6 pp.).
- Thiel, H., Schriever, G., 1989. Cruise Report DISCOL 1, SONNE – Cruise 61. *Berichte aus dem Zentrum für Meeres- und Klimaforschung der Universität Hamburg.* 3 (75 pp.).
- Underwood, E., Ustin, S., DiPietro, D., 2003. Mapping nonnative plants using hyperspectral imagery. *Remote Sens. Environ.* 86, 150–161. [http://dx.doi.org/10.1016/S0034-4257\(03\)00096-8](http://dx.doi.org/10.1016/S0034-4257(03)00096-8).
- van der Meer, F.D., van der Werff, H.M.A., van Ruitenbeek, F.J.A., Hecker, C.A., Bakker, W.H., Noomen, M.F., van der Meijde, M., Carranza, E.J.M., de Smeth, J.B., Woldai, T., 2012. Multi- and hyperspectral geologic remote sensing: a review. *Int. J. Appl. Earth Obs. Geoinf.* 14, 112–128. <http://dx.doi.org/10.1016/j.jag.2011.08.002>.
- Van Dover, C.L., 2011. Mining seafloor massive sulphides and biodiversity: what is at risk? *ICES J. Mar. Sci.* 68, 341–348. <http://dx.doi.org/10.1093/icesjms/fsq086>.
- Vanreusel, A., Hilario, A., Ribeiro, P., Menot, L., Martínez Arbizu, P., 2016. Threatened by mining, polymetallic nodules are required to preserve abyssal epifauna. *Sci. Rep.* 6 (26808). <http://dx.doi.org/10.1038/srep26808>.
- Volent, Z., Johnsen, G., Sigernes, F., 2007. Kelp forest mapping by use of airborne hyperspectral imager. *J. Appl. Remote Sens.* 1, 011503. <http://dx.doi.org/10.1117/1.2822611>.

# Article G

## Autonomy in Marine Archaeology

---

Øyvind Ødegård, **Stein M. Nornes**, Martin Ludvigsen,  
Thijs J. Maarleveld and Asgeir J. Sørensen

ARTICLE G

This article is published in S. Campana, R. Scopigno, G. Carpenterio, M. Cirillo (Eds.) *CAA2015 Keep The Revolution Going: Proceedings of the 43rd Annual Conference on Computer Applications and Quantitative Methods in Archaeology*, pages 857-865, Archaeopress, Oxford, 2016.



# Autonomy in Marine Archaeology

Øyvind Ødegård<sup>(1, 2)</sup>

oyvind.odegard@ntnu.no

Stein M. Nornes<sup>(1)</sup>

stein.nornes@ntnu.no

Martin Ludvigsen<sup>(1)</sup>

martin.ludvigsen@ntnu.no

Thijs J. Maarleveld<sup>(3)</sup>

t.maarleveld@sdu.dk

Asgeir J. Sørensen<sup>(1)</sup>

asgeir.sorensen@ntnu.no

<sup>1</sup> Centre for Autonomous Marine Operations and Systems (AMOS) Department of Marine Technology, Norwegian University of Science and Technology, Norway

<sup>2</sup> Department of Archaeology and Cultural History, University Museum, Norwegian University of Science and Technology, Norway

<sup>3</sup> Department of History, Maritime Archaeology Programme, University of Southern Denmark

*Abstract: After what oceanographers have called ‘a century of undersampling’, the marine sciences are now benefiting from tremendous technological advances in sensors and sensor platforms. Efficient exploration of the deep or remote marine environments depends on the use of underwater robotics, particularly untethered Autonomous Underwater Vehicles (AUVs) that can be sent out on missions covering large areas and return with data from multiple sensors. As technological developments allow AUVs to be deployed on long duration missions (months), the need for robust autonomous guidance, navigation and control systems become evident. For long duration missions in areas that prohibit human involvement (e.g. ultra-deep or under ice), it will be of interest for marine archaeologists to have an AUV that can find as many wrecks or other traces of cultural heritage on the seabed as possible. A hypothetical long duration AUV survey implementing archaeological mission objectives is described and discussed.*

*\*This work has been carried out at the Centre for Autonomous Marine Operations and Systems (AMOS). The Norwegian Research Council is acknowledged as the main sponsor of AMOS. This work was supported by the Research Council of Norway through the Centres of Excellence funding scheme, Project number 223254 - AMOS.*

*Keywords: Marine archaeology, Underwater robotics, Autonomy, Cybernetics, AUV*

## Introduction

Climate change and enabling technologies are driving forces for an increased attention to mapping and expanding our understanding of the oceans. Industry and management have common needs for knowledge and data to better exploit marine resources both economically and environmentally. This is also true for management of underwater cultural heritage. The lack of data from the underwater environment has become a major problem for the discipline. True: exemplary research can usefully focus on those sites for which evidence exists. However, the quantitative lack of data affects the way research issues can be resolved and is particularly dramatic in relation to present management schemes. This is the more urgent since management, including cultural heritage management and the management of research funding have become addicted to quantitative control (Anthony and Govindarajan 2007). After a century of undersampling, new technologies show promising potential for mapping larger areas with high temporal and spatial coverage and resolution helping scientists to acquire

data relevant and appropriate for questions that previously were difficult nor even impossible to answer (Nilssen *et al.* 2015). The new technologies are sensors such as Synthetic Aperture Sonar (SAS) (Hansen 2011) and Underwater Hyperspectral Imaging (UHI) (Johnsen 2013), advanced sensor platforms, increased processing abilities and progress in research on control methods for autonomy. This development seen in light of the holistic principles behind emerging Ecosystem Based Management models (de la Mare 2005) should enable large scale data gathering operations in the ocean space to integrate archaeological aspects without much ado.

On land, in relation to occupation sites, and in relation to sites of a monumental character a quantitative body of observations has consistently been built up by populations that run in the tens of millions. Subsequently, over more than 200 years, these observations have been systematized by antiquarians and archaeologists who had relatively easy access, and who could make sure that observations were reliably corroborated. Under water and in relation with marine sites this is far less the

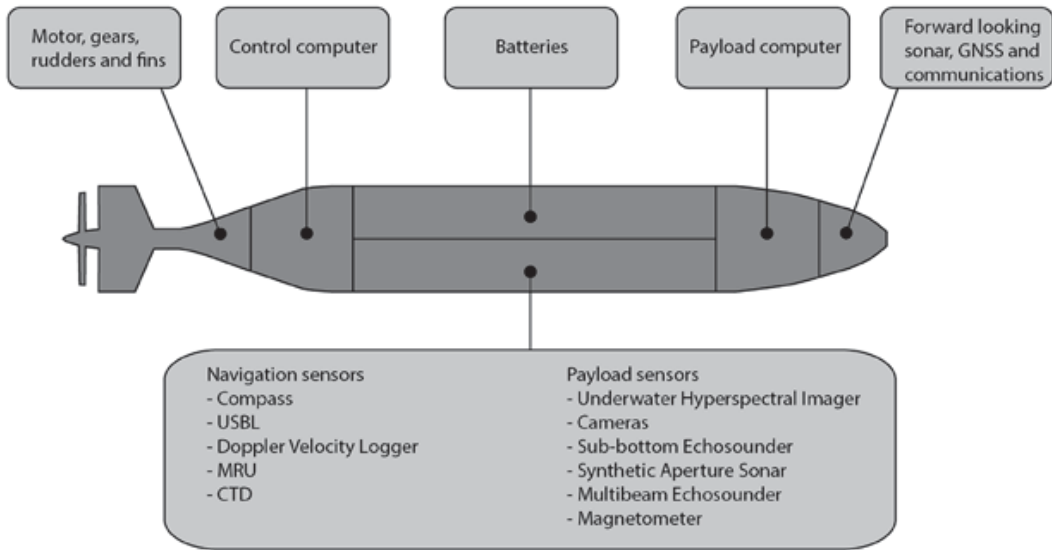


FIG. 1. OUTLINE OF AUV ANATOMY.

case. Even though the last 70 years have seen the discipline of marine archaeology develop, the intensity of observations lags far behind. Apart from systematic survey – and even there – observations are limited to where people go, which stands in no relation to the sheer extent of the underwater landscape. For various reasons many observations never enter the archaeological record (Maarleveld 2010). Moreover, many underwater observations are uncorroborated, as corroboration is relatively impracticable in the underwater environment. However, it begs the question whether vague data is data at all.

While there are considerable advances made in control systems, navigation system and manipulators for remotely operated vehicles (ROVs) that will also benefit ocean space mapping (Sorensen *et al.* 2012) this paper will focus on untethered autonomous underwater vehicles (AUVs). Because of the exponentially growing amount of data new sensors can provide, an important challenge is to reduce the amount of data describing ‘uninteresting observations’, and on the other hand get as much as possible from ‘interesting observations’. This is of course due to storage capacity, processing time and energy budget. Having robots that stop, turn on additional sensors, lights, and do detailed surveying only when they have found something worth investigating, will save energy to do longer missions and cover larger areas.

In this paper we will be discussing future missions to explore the ocean space that are based on certain assumptions. For long duration surveys in deeper waters, the costs of revisiting areas are very high. We will therefore be assuming that these are ‘one shot’ operations with only one chance to get it right, and revisiting or inspecting objects of interest (OOI) later is not considered an option. Another assumption is that purely archaeological missions are not likely to happen. There probably will be interdisciplinary cruises/surveys with multiple stakeholders involved including archaeology as one of them. As limited available energy is the main constraint for AUV

operations, we assume that resources allocated to archaeology must be negotiated, and that a high number of false positives, is a negative argument regarding archaeology.

As technological developments allow AUVs to be deployed on long duration missions (months), the need for robust autonomous guidance, navigation and control systems become evident. Intelligent control command and task execution with obstacle avoidance, fault-detection and diagnosis as a basis for reconfigurable control and re-planning of path and missions will be necessary in order to improve capabilities to operate in an unstructured environment with little or no *a priori* knowledge. In the years to come the field of artificial intelligence and learning systems as driven forward in the field of software science will strengthen the interactions between top-down and bottom-up approaches towards improved autonomy and more intelligent systems and operations. Adaptive planning and strategical and tactical decision making are methods that have already been used successfully by marine sciences and for navy purposes. This paper will present some examples of these methods in a discussion of *if* and *how* they can be adapted to archaeological applications. The paper aims to identify and define some challenges regarding autonomy in marine archaeology, and to demonstrate the importance of debating them.

## 1 AUV

Autonomous Underwater Vehicles (AUVs) are untethered robots that can operate independent of human operators at different levels of autonomy. AUVs come in many different shapes and sizes. For long duration missions covering large areas, slender bodied torpedo shaped vehicles with one propeller are commonly used (Hobson *et al.* 2012). An AUV typically consists of battery or energy cell for power, a propulsion unit, communication unit, navigation and payload sensors and computers (Fig. 1). Typical navigational sensors

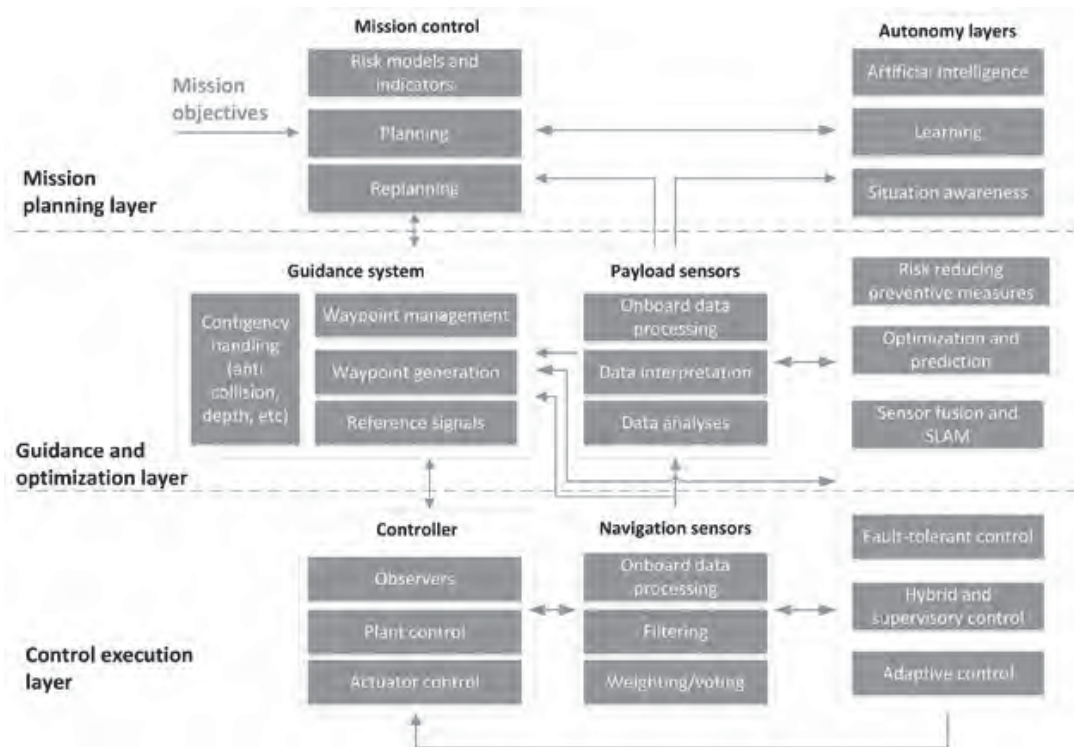


FIG. 2. AUV CONTROL ARCHITECTURE.

are Doppler Velocity Logger (DVL), Current Temperature and Depth (CTD), Compass and Motion Reference Unit (MRU). Typical payload sensors are long range sonar systems like Side Scan Sonar (SSS), Synthetic Aperture Sonar (SAS) and Multi Beam Echo sounders (MBE). Sub Bottom Profilers (SBP), magnetometers, different types of cameras and other instruments are deployed for measuring bio-geo-chemical properties. For a description of typical payload and navigation sensors in the autonomy architecture, it should be mentioned that data from several sensors can be used for multiple mission objectives, and are not exclusive for one particular purpose.

### 1.1 Control system

In addition to hardware an AUV is completely dependent on a control system to operate. The control system is the ‘brain’ of the robot, and commands and coordinates every single part of the AUV to make it behave in accordance with a mission plan. Complex mission plans may require many parallel or sequential tasks to be performed interdependently, often with conditional choices for the next action. If an AUV is to operate in an environment with many unknowns and uncertainties, which typically characterizes the marine environment, an intelligent control system will increase the chances for success in performing its mission. Since the late 1980s there have been great advances in the research field of intelligent control. The challenges of introducing Artificial Intelligence (AI)

and autonomy into the predominantly mathematical field of conventional control theory was recognized early (Meystel, 1989), and the necessity for multi- or interdisciplinary work efforts were acknowledged (Antsaklis *et al.* 1989; Zeigler 1990). The three layered hybrid architecture emerged as a successful framework for autonomy, and became a standard approach to autonomy for mobile robots (Gat, 1998). Many of the most successful systems today have evolved from these early models, and have similar divisions. The three layers all have important roles to play with regards to autonomy. The following AUV autonomy framework (Fig. 2) is based on the autonomy architecture presented in Sørensen and Ludvigsen (2015). At the top is the mission planning layer where the mission objective is defined and the mission is planned with tasks to fulfil the mission goal(s). Subject to contingency handling, any input from payload sensor data analysis and any other input from the autonomy layer, the mission may be re-planned. This layer also manages and maintains a world model by continuous updating from sensor data. The guidance and optimization layer translates these tasks into sequences of behaviours that are carried out by distributing commands to actuators and sensors in the control execution level.

### 1.2 Autonomy

Discussing autonomy from an end-user perspective can bring untraditional problems into an established discourse, as concepts can represent different meanings in different disciplines (Bal 2009). The need for precise taxonomy to avoid

misunderstandings is important. The terms Autonomy and Level of Autonomy (LOA) are used to describe the relationship between human and machine, and are often expressed along a scale with increasing machine control and less human interference. Different models are used since robot/human relationships can be very diverse and take on quite different forms. Some models are very simplistic with few levels, and short descriptions of each level, while other are more intricate with several dimensions necessary for describing complex relationships, e.g. involving contextual factors like environment and data processing. A good overview of autonomy taxonomy can be found in Vagia *et al.* (in press).

Hagen *et al.* (2009) links levels of autonomy for AUVs to their performance in energy autonomy, navigation autonomy and decision autonomy. To see autonomy in relation to tasks, and not just as a relationship between human and machine, we need to investigate how high level archaeological goals can be formulated in an autonomy layer, but also how marine archaeological practice can be translated into meaningful actions and behaviours for the robot.

For short term missions in relatively known environments, uncertainties can be handled by e.g. simple IF-THEN-ELSE rules (Gat, 1998). The programmer can predict possible events, and have the robot to act based on rules encompassing these events. This can involve multiple conditions, creating a more solid basis for decisions. However, as the number of conditions grows the conditional variations grow exponentially, and the purely logical decision model becomes exceedingly complex very fast. The robot now needs to deliberate combinations of events, both in its environment and regarding its own state, that are beyond practical predictability. This problem is especially relevant for longer missions in unknown environments.

### 1.3 SLAM

Simultaneous Localization and Mapping (SLAM) addresses the problem of constructing a spatial map of the environment around a mobile robot while simultaneously utilizing this map to calculate the position of the robot relative to this map (Siciliano and Khatib 2008).

Efficient method for SLAM is generally regarded as one of the most important problems to solve in the pursuit of building truly autonomous mobile robots capable of operating unassisted in unknown environments for a prolonged period of time with limited access to external navigation systems such as acoustics or surface based satellite systems. With global position updates such as GPS being unavailable underwater one would often rely on dead-reckoning methods for navigation. In such systems small measurement errors from navigation sensors will accumulate over time causing the estimated position of the vehicle to drift. With SLAM, a vehicle revisiting an area mapped earlier in the mission can use the new position calculated from the map to counteract this time related drift. This is often referred as ‘closing the loop’ and bound the error drift.

An autonomous vehicle will also be limited by both power consumption and data storage. To map large areas efficiently, it is often beneficial to do an initial coarse resolution mapping and return to smaller areas with features and objects of interest (OOI) for a higher resolution mapping. Doing this on a single dive is known as adaptive replanning (Wiig *et al.* 2012).

Obviously, the map built using SLAM will be highly beneficial for relocating the features and OOI for re-examining.

SLAM methods have now reached a state of considerable maturity (Durrant-Whyte and Bailey 2006; Bailey and Durrant-Whyte 2006). Several successful implementations have been demonstrated, ranging from structured man-made environments (Ribas *et al.* 2008) to drowned coral reefs (Williams *et al.* 2009) to visual mapping of the RMS Titanic (Eustice *et al.* 2005). Newer research (Kim and Eustice 2014) is also moving from passive SLAM where the vehicle follows a predetermined path, to active SLAM where the path is modified to improve both map building and localization performance.

The main obstacle for SLAM has traditionally been computational complexity. With continuous improvements in computational power and research into new algorithms, the field has grown considerably the last decade, and is likely to continue improving.

## 2 Archaeological survey

For long duration missions in areas that prohibit human involvement (e.g. ultra-deep or under ice), it will be of interest for marine archaeologists to have an AUV that can find as many wrecks or other traces of cultural heritage on the seabed as possible. The AUV should return with good data from each site that can serve as a foundation for decision making regarding management issues, or as material for research and knowledge production in case the site will not be revisited again. This is a comprehensive mission objective, and one must expect to make many compromises both in terms of what can be done, and how it can be done. Since an exhaustive high resolution multi sensor mapping of every inch of the seabed is not feasible with current technologies, we must introduce elements of deliberation and choices into the mission plan that will reduce the amount of work to be done, and have the robot only spend time and resources on sites that are likely to be of interest. A high level formulation of this mission objective can be divided into three missions: Mission 1 – Detect; Mission 2 – Verify and Mission 3 – Record (Fig. 3). The missions are sequentially dependent, mission 2 will only be performed if mission 1 produces waypoints, likewise mission 3 will only be performed if mission 2 result in any Objects of interest (OOI).

To see how these missions can best be implemented into the control architecture of an AUV, we must decompose/deconstruct each mission into tasks that better matches the behaviours AUVs typically can perform. This requires the archaeologist to see marine archaeological praxis independent of the methodological and cognitive constraints typical for the tools commonly available today, and instead adopt and investigate the possibilities offered by the perceptive and operational abilities and constraints of the AUV.

Consider the following as an outline of a hypothetical AUV survey to illustrate how the mission objectives described above could be resolved.

### 2.1 Mission 1 Detect

The AUV will explore an area of the seabed (Fig. 4 a) of which it has limited if any a priori knowledge. It will keep a constant altitude above the seabed optimal for maximum areal

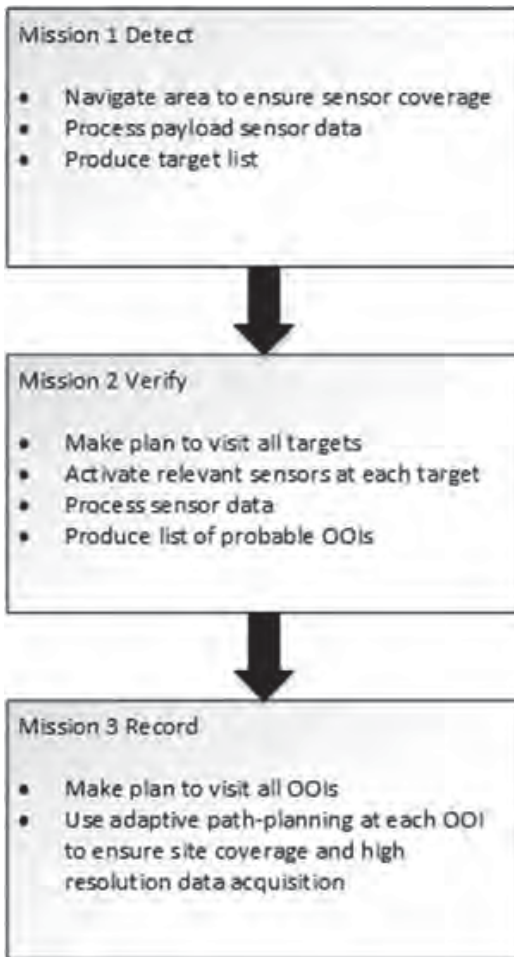


FIG. 3. TRIPARTITE MISSION PLAN FOR AN ARCHAEOLOGICAL SURVEY.

coverage, using one or several long range acoustic sensors (e.g. SAS and MBES) while navigating in a lawnmower pattern (Fig. 4 b). The SAS/MBES data is processed in real time producing both imagery and bathymetric data that is used both for safely navigating the environment (SLaM), and for feature detection (segmentation using e.g. computer vision algorithms). Interferometric SAS data can also be analyzed to find the maximum range for a predefined data quality threshold, and thus adjust line spacing to ensure that the whole area is covered (Krogstad and Wiig 2014). Detecting features that could possibly be OOIs (Fig. 4 c), the AUV creates a list of waypoints to be used as input in re-planning as shown in Fig. 3.

### 2.2 Mission 2 Verify

The AUV re-plans its mission to navigate along a route to visit all the waypoints. To save energy the path planning will involve use of Traveling Salesman Planning (TSP) algorithms to have the new path as short as possible (Krogstad and Wiig 2014; Tsiogkas *et al.* 2014). At every target it activates

relevant sensors (UHI, magnetometer, O2-optode etc.) for measuring and sampling (Fig. 4 d). This data is then processed to determine if the targets should be regarded as possible OOIs. The autonomy layer then decides if it should reject the targets and continue with its original mission, or revisit again for full data acquisition (Fig. 4 e).

### 2.3 Mission 3 Record

Targets determined to be OOIs are revisited and recorded with all relevant sensors to secure optimal data sets (Fig. 4 f). The AUV will plan survey lines with spacing and altitude appropriate for the sensors that are activated (e.g. ensure at least 60 percent image overlap for photogrammetry). In addition the AUV must apply computer vision and machine learning algorithms to sensor data in real time to ensure that the area of interest has been covered completely, and to decide when the operation is finished (Giguere *et al.* 2009).

## 3 Autonomous detection and recognition of wrecks

Detecting and classifying features in imagery are nontrivial and complex problems. Image segmentation using computer vision and machine learning is a research field given much attention in the last decades, and is currently seeing many breakthroughs – especially within deep learning and artificial neural networking. However, as time and computing power are limited resources for AUVs, simpler algorithms would be preferable for on-board calculations. Imagery produced by acoustic sensors is monochrome, and in principle shows the intensity of echoes for each pixel that represents a specific location on the seabed. In archaeological applications, to recognize features in such imagery as potential OOIs would entail comparison of morphological qualities of the features with an on-board knowledge representation (library) of shapes likely to be found on wreck sites. This approach using learned classifiers for feature or object recognition has been successfully pursued by using Automated Target Recognition algorithms in research on Mine Counter Measures (Petillot *et al.* 2010; Groen *et al.* 2010). While this method could probably successfully detect and classify some features as wrecks, a problem would be that the method is inherently biased towards what is already known and therefore less likely to recognize sites that are disintegrated, decomposed or otherwise scattered in an unprecedented (un-modelled) pattern. Wreck site formation processes are very complex, chiefly determined by the characteristics of the ship, the events causing its deposition on the seabed (how it wrecked), the environment of the wreck site and the time it has spent on the seabed (assuming it has remained undisturbed). Muckelroy's (1978) classic model treats the site formation process almost like a cybernetic system with the ship as input, and loss of integrity and materials as conditional outputs depending on a number of 'extracting filters' and 'scrambling devices'. While this model may seem a bit positivistic today, it nevertheless accounts for the factors influencing a site formation process and describes the variations from structurally intact wrecks like the *Vasa*, to examples like the *Kennemerland* where disintegration and deposition of materials on the seabed happened over a relatively long time and the traces left on the seabed were spread over several hundreds of meters. It can be argued that in deeper waters, wreck site formation processes are more coherent, as a wreck once it is deposited on the seabed is less likely to be mechanically disturbed (Church 2014). However, even

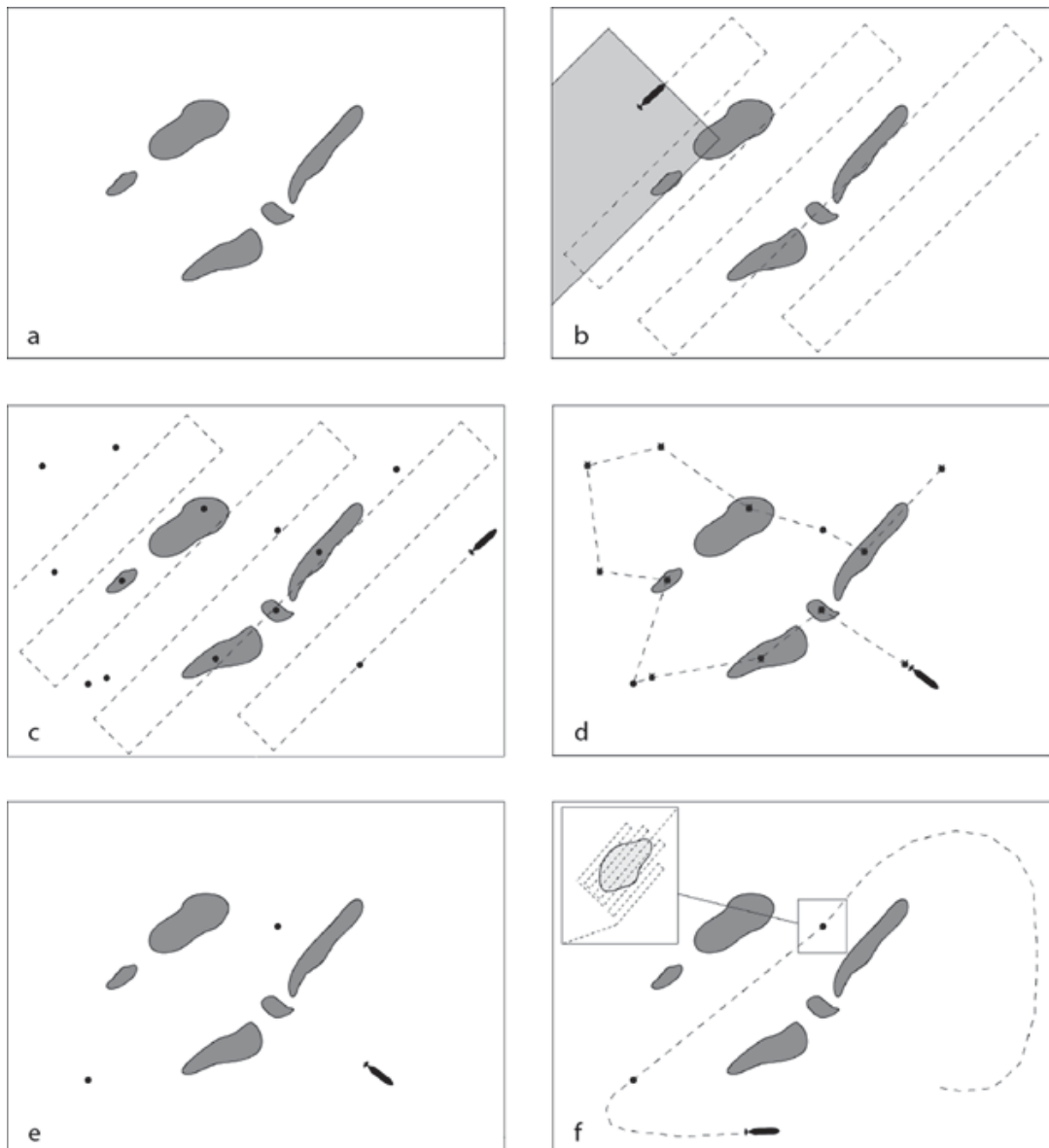


FIG. 4. AUV SURVEY: A) AREA TO SURVEY; B) LAWNMOWER PATTERN TO COVER AREA; C) DETECT TARGETS; D) VISIT AND INSPECT TARGETS; E) LIST OF OOI; F) REVISIT AND RECORD OOI.

though intact hull structures could presumably be modelled as variations of some shared qualities regarding shape and size, any typical morphological characteristics would eventually be broken down by biology, chemistry, gravity and time (Björðal *et al.* 2011). The recognition of wreck sites as they appear in sonar imagery is therefore often a heuristic undertaking where the archaeologist will perceive features in the imagery based on his understanding of the technology (Quinn *et al.* 2005), and in the context of knowledge of the sea bed terrain (e.g. aided by additional sensors as described by Sakellariou *et al.* (2007)), empirical experience of probable or possible wrecking processes (Muckelroy 1978), and of course the prevailing

currents and other known or assumed environmental conditions in the area.

An alternative approach could be to look for what stands out as different or unusual on the seabed (Girdhar and Dudek 2014). By simply stating that a feature is different from what has been perceived so far, and therefore interesting, this approach sheds the problems of morphological ambiguity discussed above. There would be no need for archaeological knowledge representation and wreck site modeling in mission 1 (the analysis of acoustic data), as the AUV would generate a target list based on its experiences made in the local environment.

This way of shifting the allocation of a problem from the deliberate high-level end of the control architecture towards the more reactive, low-level end could also probably make it easier to adjust and fine tune algorithms as less abstractions and semantic representations are involved.

While this approach will reduce the number of false negatives, it is very likely to include many false positives. Recording will be a very energy and time consuming part of such missions, and to avoid wasting resources on what we can expect to be a high number of uninteresting features, we introduce a mission 2 for verification of targets. While the initial target list in mission 1 was selected to encompass every possible OOI, the purpose of mission 2 is to reduce the final number of false positives. This is done by navigating over all targets found in mission 1 for an inspection with multiple sensors activated. While the morphological variations of wreck sites are almost unlimited, the material composition of the remains of shipwrecks would be easier to delimit. Iron anchors, cannons, and chains are some typical objects that can be found on many wreck sites. An AUV equipped with a magnetometer (e.g. Hugin HUS has a Honeywell HMR 2300 magnetometer) could register magnetic signals near a shipwreck with such objects present. Underwater Hyperspectral Imagers are optical sensors that can record the spectral signature of the seabed with centimeter resolution (Johnsen 2013). The UHI detects light in the spectral range 380-800 nm, with a resolution of 1 nm (Ludvigsen *et al.* 2014). If the AUV carries a library describing the spectral signatures of materials typically present at wreck sites, it could look for matches or close similarities in the sensor data. Methods in sensor fusion can be used to calculate probabilities with many uncertainties involved - see for instance Wu (2002). This means that signals from sensors that acting alone would give very unreliable indications of e.g. a potential wreck site, in combination with each other could yield estimations with higher degrees of confidence. For instance, a magnetometer could register a magnetic anomaly that together with UHI detection of pigments typical for bricks, would indicate a probable wreck site. Targets found in mission 1 that remain unsupported by sensor data from mission 2 will not be considered possible OOIs. By reducing the number of targets to be fully documented in mission 3, a considerable amount of time and energy is saved.

Marine archaeology, as most marine sciences, have used robotics and utilized the technological development both in sensors and platforms to gain access to areas normally not accessible by diving methods. However, the potential for interdisciplinary benefits in the application of robotics has so far largely remained unexplored as a methodologically significant choice by archaeologists as end users. Rather, robots and sensors have been seen as extensions or replacements/proxies for human presence and observation (for some notable exceptions see Bingham and Foley *et al.* 2010 and Allotta *et al.* 2015). When archaeologists inspect a wreck site with an ROV, common for surveys beyond diving range, focus will predominantly be on the visual data acquired by cameras, what the archaeologist sitting next to the ROV-pilot can see, and what can be recognized and classified. This is no wonder, as state-of-the-art HD-cameras now can produce fantastic imagery exceeding the perceptible constraints of the human eye. It seems that the *primacy of vision*, as described by Jonathan Adams (2013), has been transferred to these new methods, and while the diver is no longer situated at the site – with all the cognitive processes

that follows – the operation could be seen as an adaptation of traditional marine archaeological diver based practice.

On land the implementation of computer vision and machine learning in archaeological knowledge production has met resistance (Bennett *et al.* 2014). It is different under water. The operational constraints of ultra-deep or ice covered waters make autonomous operations the only way to access certain areas. Even if some will argue that the methods deployed are ill-suited or inappropriate, the alternative would be nothing at all. This doesn't mean that the critiques of these methods are irrelevant, but the outcome of such a discourse would have less practical consequences. The abilities to consider and fruitfully deliberate archaeology will only be developed if archaeologists engage with the inner workings of robotic autonomy. It requires an understanding of how intelligent autonomy frameworks function, and it of course requires an understanding of archaeological praxis – both critical to current methods, and aware of trade-offs in transferring a traditionally humanistic praxis to machines.

#### 4 Conclusion and future work

This paper has proposed a strategy to implement archaeological mission objectives as input to the design of autonomous control systems for AUVs. By dividing the missions into tasks that the AUV can perform with behaviours within given parameters, the abstract goals are moved from the higher deliberative layer to the middle coordination layer and finally can be executed in the lowest control layer with commands and direct reactions to sensor data determining actions.

It has been demonstrated that SAS in terms of resolution and coverage allows detection of relatively indistinct wreck sites at considerable distances (Ødegård *et al.* 2013). Future work at the Centre for Autonomous Marine Operations and Systems (AMOS) will look at how on-board SAS image analysis can best be applied to detect wrecks with a focus on avoiding false negatives. UHI-technology is still a novel tool with a huge potential for the marine sciences, but has already been used to investigate wreck sites with good results (Ludvigsen *et al.* 2014). Ongoing work at AMOS will build a library of spectral signatures for typical materials found at wreck sites. UHI data from wreck sites will be used together with this library to develop methods for aided detection and classification.

#### Bibliography

- Adams, J. 2013. Experiencing Shipwrecks and the Primacy of Vision. In J. Adams and J. Rönby (eds.), *Interpreting Shipwrecks: Maritime Archaeological Approaches*: 85-96. Southampton, Highfield Press.
- Allotta, B., Costanzi, R., Ridol, A., Colombo, C., Bellavia, F., Fanfani, M., Pazzaglia, F., Salvetti, O., Moroni, D., Pascali, M. A., Reggiannini, M., Kruusmaa, M., Salumäe, T., Frost, G., Tsiogkas, N., Lane, D. M., Cocco, M., Gualdesi, L., Roig, D., Gündogdu, H. T., Tekdemir, E. I., Dede, M. I. C., Baines, S., Agneto, F., Selvaggio, P., Tusa, S., Zangara, S., Dresen, U., Lätti, P., Saar, T., Daviddi, W. (in press). The ARROWS project: adapting and developing robotics technologies for underwater archaeology. *IFAC Workshop on Navigation Guidance and Control of Underwater Vehicles (NGCUV 2015)*, 2015 Girona, Spain.

- Anthony, R. N. and Govindarajan, V. 2007. *Management control systems*. McGraw-Hill Irwin, Chicago.
- Antsaklis, P. J., Passino, K. M., Wang, S. 1989. Towards intelligent autonomous control systems: Architecture and fundamental issues. *Journal of Intelligent and Robotic Systems* 1: 315-42.
- Bailey, T., Durrant-Whyte, H. 2006. Simultaneous localization and mapping (SLAM): Part II. *IEEE Robotics & Automation Magazine* 13: 108-17.
- Bal, M. 2009. Working with concepts. *European Journal of English Studies* 13: 13-23.
- Bennett, R., Cowley, D., De Laet, V. 2014. The data explosion: tackling the taboo of automatic feature recognition in airborne survey data. *Antiquity* 88: 896-905.
- Bingham, B., Foley, B., Singh, H., Camilli, R., Delaporta, K., Eustice, R., Mallios, A., Mindell, D., Roman, C., Sakellariou, D. 2010. Robotic tools for deep water archaeology: Surveying an ancient shipwreck with an autonomous underwater vehicle. *Journal of Field Robotics* 27: 702-17.
- Björdal, C. G., Gregory, D., Trakadas, A. 2011. *WreckProtect: decay and protection of archaeological wooden shipwrecks*. Oxford, Archaeopress.
- Church, R. A. 2014. Deep-Water Shipwreck Initial Site Formation: The Equation of Site Distribution. *Journal of Maritime Archaeology* 9: 27-40.
- De La Mare, W. K. 2005. Marine ecosystem-based management as a hierarchical control system. *Marine Policy* 29: 57-68.
- Durrant-Whyte, H., Bailey, T. 2006. Simultaneous localization and mapping: part I. *Robotics & Automation Magazine, IEEE* 13: 99-110.
- Eustice, R., Singh, H., Leonard, J. J., Walter, M., Ballard, R. 2005. Visually Navigating the RMS Titanic with SLAM Information Filters. *Robotics: Science and Systems* 2005: 57-64.
- Adams, J. 2013. Experiencing Shipwrecks and the Primacy of Vision. In J. Adams and J. Rönby
- Giguere, P., Dudek, G., Prahacs, C., Plamondon, N., Turgeon, K. 2009. Unsupervised learning of terrain appearance for automated coral reef exploration. *Canadian Conference on Computer and Robot Vision, CRV'09. IEEE*: 268-75.
- Girdhar, Y., Dudek, G. 2014. Exploring Underwater Environments with Curiosity. *Canadian Conference on Computer and Robot Vision (CRV)*. IEEE: 104-10.
- Groen, J., Coiras, E., Williams, D. 2010. False-alarm reduction in mine classification using multiple looks from a synthetic aperture sonar. *OCEANS 2010 IEEE-Sydney, IEEE*: 1-8.
- Hagen, P. E., Hegrenæs, Ø., Jalving, B., Midtgaard, Ø., Wiig, M., Hagen, O. K. 2009. Making AUVs Truly Autonomous. In A. V. Inzartsev (ed.), *Underwater Vehicles*. InTech.
- Hansen, R. E. 2011. Introduction to Synthetic Aperture Sonar. In N. Kolev, *Sonar Systems*, InTech, Croatia. doi: 10.5772/23122. Available at: <http://www.intechopen.com/books/sonar-systems/introduction-to-synthetic-aperture-sonar>.
- Hobson, B. W., Bellingham, J. G., Kieft, B., Mcewen, R., Godin, M., Zhang, Y. 2012. Tethys-class long range AUVs-extending the endurance of propeller-driven cruising AUVs from days to weeks. *Proceedings of the Autonomous Underwater Vehicles (AUV)*. IEEE: 1-8.
- Johnsen, G., Volent, Z., Dierssen, H., Pettersen, R., Van Ardelan, M., Søreide, F., Fearn, P., Ludvigsen, M., Moline, M. 2013. Underwater hyperspectral imagery to create biogeochemical maps of seafloor properties. *Subsea optics and imaging*. Woodhead Publishing Limited.
- Kim, A., Eustice, R. M. 2014. Active visual SLAM for robotic area coverage: Theory and experiment. *The International Journal of Robotics Research*. [Online] Available at: doi: 10.1177/0278364914547893.
- Krogstad, T. R. and Wiig, M. S. 2014. Autonomous Survey and Identification Planning for AUV MCM Operations. *UDT 2014*.
- Ludvigsen, M., Johnsen, G., Sørensen, A. J., Lågstad, P. A., Ødegård, Ø. 2014. Scientific Operations Combining ROV and AUV in the Trondheim Fjord. *Marine Technology Society Journal* 48: 59-71.
- Maarleveld, T. J. 2010. 10. Fish and «Chips of Knowledge»: Some Thoughts on the Biases of the Archaeological Record. In T. Bekker-Nielsen and D. Bernal Casasola (eds.), *Ancient Nets and Fishing Gear: Proceedings of the International workshop on Nets and Fishing Gear in Classical Antiquity: a First Approach, Cadiz, 15-17 November 2007*: 257-71. Universidad de Cadiz and Aarhus University Press.
- Meystel, A. 1989. Intelligent control: A sketch of the theory. *Journal of Intelligent & Robotic Systems* 2: 97-107.
- Muckelroy, K. 1978. *Maritime archaeology*. Cambridge, Cambridge University Press.
- Nilssen, I., Ødegård, Ø., Sørensen, A. J., Johnsen, G., Moline, M. A., Berge, J. 2015. Integrated environmental mapping and monitoring, a methodological approach to optimise knowledge gathering and sampling strategy. *Marine Pollution Bulletin* 96: 374-83.
- Petillot, Y., Pailhas, Y., Sawas, J., Valeyrie, N., Bell, J. 2010. Target recognition in synthetic aperture and high resolution side-scan sonar using auvs. In *Proceedings of the International Conference: Synthetic Aperture Sonar and Synthetic Aperture Radar, Institute of Acoustics, Lerici, Italy, September* 2010.
- Quinn, R., Dean, M., Lawrence, M., Liscoe, S., Boland, D. 2005. Backscatter responses and resolution considerations in archaeological side-scan sonar surveys: a control experiment. *Journal of archaeological science* 32:1252-64.
- Ribas, D., Ridaou, P., Tardós, J. D., Neira, J. 2008. Underwater SLAM in man-made structured environments. *Journal of Field Robotics* 25: 898-921.
- Sakellariou, D., Georgiou, P., Mallios, A., Kapsimalis, V., Kourkoumelis, D., Micha, P., Theodoulou, T., Dellaporta, K. 2007. Searching for Ancient Shipwrecks in the Aegean Sea: the Discovery of Chios and Kythnos Hellenistic Wrecks with the Use of Marine Geological-Geophysical Methods. *International Journal of Nautical Archaeology* 36: 365-81.
- Siciliano, B. and Khatib, O. 2008. *Springer handbook of robotics*. Springer Science & Business Media.
- Sørensen, A. J., Dukan, F., Ludvigsen, M., Fernandes, D. A., Candeloro, M. 2012. Development of dynamic positioning tracking system for the ROV Minerva. In G. Roberts and B. Sutton (eds.), *Further Advances in Unmanned Marine Vehicles*. The Institution of engineering and Technology.
- Sørensen, J. A. and Ludvigsen, M. (in press). Towards Integrated Autonomous Underwater Operations. *IFAC Workshop on Navigation Guidance and Control of Underwater Vehicles, Girona, Spain 2015*.
- Tsiogkas, N., Papadimitriou, G., Saigol, Z., Lane, D. 2014. Efficient multi-AUV cooperation using semantic knowledge representation for underwater archaeology missions. In *Oceans-St. John's 2014, 14-19 september 2014, IEEE*: 1-6. [Online] doi: 10.1109/OCEANS.2014.7003085.

- Vagia, M., Transeth, A. A., Fjerdings, S. A. (in press). A survey on levels of autonomy during the years. What are the different taxonomies that have been proposed? *Applied Ergonomics*.
- Wiig, M. S., Krogstad, T. R., Midtgaard, O. 2012. Autonomous identification planning for mine countermeasures. *Autonomous Underwater Vehicles (AUV), 2012. IEEE*: 1-8.
- Williams, S. B., Pizarro, O., Mahon, I., Johnson-Roberson, M. 2009. Simultaneous localisation and mapping and dense stereoscopic seafloor reconstruction using an AUV. *Experimental robotics 2009*: 407-16. Springer.
- Wu, H., Siegel, M., Stiefelhagen, R., Jie, Y. 2002. Sensor fusion using Dempster-Shafer theory [for context-aware HCI]. In *Proceedings of the 19th IEEE Instrumentation and Measurement Technology Conference, IMTC/2002, 21-23 May 2002*: 7-12.
- Zeigler, B. P. 1990. High autonomy systems: concepts and models. In *Proceedings of AI, Simulation and Planning in High Autonomy Systems: 2-7*. IEEE Computer Society Press, Tucson, AZ.
- Ødegård, Ø., Ludvigsen, M., Lågstad, P. A. 2013. Using synthetic aperture sonar in marine archaeological surveys- Some first experiences. In *OCEANS-Bergen, MTS/IEEE, 2013*: 1-7.



# Article H

## Autonomous Robotic Intervention using ROV: An Experimental Approach

---

Trygve O. Fossum, Martin Ludvigsen, **Stein M. Nornes**,  
Ida Rist-Christensen and Lars Brusletto

ARTICLE H

This article is published in the proceedings of  
*MTS/IEEE OCEANS 2016*. Monterey, CA, USA, 19-22 September 2016.  
doi: 10.1109/OCEANS.2016.7761178

Is not included due to copyright



# Article I

## Vision based obstacle avoidance and motion tracking for autonomous behaviors in underwater vehicles

---

Marco Leonardi, Annette Stahl, Michele Gazzea, Martin Ludvigsen,  
Ida Rist-Christensen and **Stein M. Nornes**

This article is published in the proceedings of  
*MTS/IEEE OCEANS 2017*. Aberdeen, UK, 19-22 June 2017.  
doi: 10.1109/OCEANSE.2017.8084619

ARTICLE I

---

Is not included due to copyright



Previous PhD theses published at  
the Departement of Marine  
Technology



**Previous PhD theses published at the Departement of Marine Technology  
(earlier: Faculty of Marine Technology)  
NORWEGIAN UNIVERSITY OF SCIENCE AND TECHNOLOGY**

<b>Report No.</b>	<b>Author</b>	<b>Title</b>
	Kavlie, Dag	Optimization of Plane Elastic Grillages, 1967
	Hansen, Hans R.	Man-Machine Communication and Data-Storage Methods in Ship Structural Design, 1971
	Gisvold, Kaare M.	A Method for non-linear mixed -integer programming and its Application to Design Problems, 1971
	Lund, Sverre	Tanker Frame Optimalization by means of SUMT-Transformation and Behaviour Models, 1971
	Vinje, Tor	On Vibration of Spherical Shells Interacting with Fluid, 1972
	Lorentz, Jan D.	Tank Arrangement for Crude Oil Carriers in Accordance with the new Anti-Pollution Regulations, 1975
	Carlsen, Carl A.	Computer-Aided Design of Tanker Structures, 1975
	Larsen, Carl M.	Static and Dynamic Analysis of Offshore Pipelines during Installation, 1976
UR-79-01	Brigt Hatlestad, MK	The finite element method used in a fatigue evaluation of fixed offshore platforms. (Dr.Ing. Thesis)
UR-79-02	Erik Pettersen, MK	Analysis and design of cellular structures. (Dr.Ing. Thesis)
UR-79-03	Sverre Valsgård, MK	Finite difference and finite element methods applied to nonlinear analysis of plated structures. (Dr.Ing. Thesis)
UR-79-04	Nils T. Nordsve, MK	Finite element collapse analysis of structural members considering imperfections and stresses due to fabrication. (Dr.Ing. Thesis)
UR-79-05	Ivar J. Fylling, MK	Analysis of towline forces in ocean towing systems. (Dr.Ing. Thesis)
UR-80-06	Nils Sandsmark, MM	Analysis of Stationary and Transient Heat Conduction by the Use of the Finite Element Method. (Dr.Ing. Thesis)
UR-80-09	Sverre Haver, MK	Analysis of uncertainties related to the stochastic modeling of ocean waves. (Dr.Ing. Thesis)
UR-81-15	Odland, Jonas	On the Strength of welded Ring stiffened cylindrical Shells primarily subjected to axial Compression
UR-82-17	Engesvik, Knut	Analysis of Uncertainties in the fatigue Capacity of

## Welded Joints

UR-82-18	Rye, Henrik	Ocean wave groups
UR-83-30	Eide, Oddvar Inge	On Cumulative Fatigue Damage in Steel Welded Joints
UR-83-33	Mo, Olav	Stochastic Time Domain Analysis of Slender Offshore Structures
UR-83-34	Amdahl, Jørgen	Energy absorption in Ship-platform impacts
UR-84-37	Mørch, Morten	Motions and mooring forces of semi submersibles as determined by full-scale measurements and theoretical analysis
UR-84-38	Soares, C. Guedes	Probabilistic models for load effects in ship structures
UR-84-39	Aarsnes, Jan V.	Current forces on ships
UR-84-40	Czujko, Jerzy	Collapse Analysis of Plates subjected to Biaxial Compression and Lateral Load
UR-85-46	Alf G. Engseth, MK	Finite element collapse analysis of tubular steel offshore structures. (Dr.Ing. Thesis)
UR-86-47	Dengody Sheshappa, MP	A Computer Design Model for Optimizing Fishing Vessel Designs Based on Techno-Economic Analysis. (Dr.Ing. Thesis)
UR-86-48	Vidar Aanesland, MH	A Theoretical and Numerical Study of Ship Wave Resistance. (Dr.Ing. Thesis)
UR-86-49	Heinz-Joachim Wessel, MK	Fracture Mechanics Analysis of Crack Growth in Plate Girders. (Dr.Ing. Thesis)
UR-86-50	Jon Taby, MK	Ultimate and Post-ultimate Strength of Dented Tubular Members. (Dr.Ing. Thesis)
UR-86-51	Walter Lian, MH	A Numerical Study of Two-Dimensional Separated Flow Past Bluff Bodies at Moderate KC-Numbers. (Dr.Ing. Thesis)
UR-86-52	Bjørn Sortland, MH	Force Measurements in Oscillating Flow on Ship Sections and Circular Cylinders in a U-Tube Water Tank. (Dr.Ing. Thesis)
UR-86-53	Kurt Strand, MM	A System Dynamic Approach to One-dimensional Fluid Flow. (Dr.Ing. Thesis)
UR-86-54	Arne Edvin Løken, MH	Three Dimensional Second Order Hydrodynamic Effects on Ocean Structures in Waves. (Dr.Ing. Thesis)
UR-86-55	Sigurd Falch, MH	A Numerical Study of Slamming of Two-Dimensional Bodies. (Dr.Ing. Thesis)
UR-87-56	Arne Braathen, MH	Application of a Vortex Tracking Method to the Prediction of Roll Damping of a Two-Dimension Floating Body. (Dr.Ing. Thesis)

UR-87-57	Bernt Leira, MK	Gaussian Vector Processes for Reliability Analysis involving Wave-Induced Load Effects. (Dr.Ing. Thesis)
UR-87-58	Magnus Småvik, MM	Thermal Load and Process Characteristics in a Two-Stroke Diesel Engine with Thermal Barriers (in Norwegian). (Dr.Ing. Thesis)
MTA-88-59	Bernt Arild Bremdal, MP	An Investigation of Marine Installation Processes – A Knowledge - Based Planning Approach. (Dr.Ing. Thesis)
MTA-88-60	Xu Jun, MK	Non-linear Dynamic Analysis of Space-framed Offshore Structures. (Dr.Ing. Thesis)
MTA-89-61	Gang Miao, MH	Hydrodynamic Forces and Dynamic Responses of Circular Cylinders in Wave Zones. (Dr.Ing. Thesis)
MTA-89-62	Martin Greenhow, MH	Linear and Non-Linear Studies of Waves and Floating Bodies. Part I and Part II. (Dr.Techn. Thesis)
MTA-89-63	Chang Li, MH	Force Coefficients of Spheres and Cubes in Oscillatory Flow with and without Current. (Dr.Ing. Thesis)
MTA-89-64	Hu Ying, MP	A Study of Marketing and Design in Development of Marine Transport Systems. (Dr.Ing. Thesis)
MTA-89-65	Arild Jæger, MH	Seakeeping, Dynamic Stability and Performance of a Wedge Shaped Planing Hull. (Dr.Ing. Thesis)
MTA-89-66	Chan Siu Hung, MM	The dynamic characteristics of tilting-pad bearings
MTA-89-67	Kim Wikstrøm, MP	Analysis av projekteringen for ett offshore projekt. (Licenciat-avhandling)
MTA-89-68	Jiao Guoyang, MK	Reliability Analysis of Crack Growth under Random Loading, considering Model Updating. (Dr.Ing. Thesis)
MTA-89-69	Arnt Olufsen, MK	Uncertainty and Reliability Analysis of Fixed Offshore Structures. (Dr.Ing. Thesis)
MTA-89-70	Wu Yu-Lin, MR	System Reliability Analyses of Offshore Structures using improved Truss and Beam Models. (Dr.Ing. Thesis)
MTA-90-71	Jan Roger Hoff, MH	Three-dimensional Green function of a vessel with forward speed in waves. (Dr.Ing. Thesis)
MTA-90-72	Rong Zhao, MH	Slow-Drift Motions of a Moored Two-Dimensional Body in Irregular Waves. (Dr.Ing. Thesis)
MTA-90-73	Atle Minsaas, MP	Economical Risk Analysis. (Dr.Ing. Thesis)
MTA-90-74	Knut-Aril Farnes, MK	Long-term Statistics of Response in Non-linear Marine Structures. (Dr.Ing. Thesis)
MTA-90-75	Torbjørn Sotberg, MK	Application of Reliability Methods for Safety Assessment of Submarine Pipelines. (Dr.Ing. Thesis)

		Thesis)
MTA-90-76	Zeuthen, Steffen, MP	SEAMAID. A computational model of the design process in a constraint-based logic programming environment. An example from the offshore domain. (Dr.Ing. Thesis)
MTA-91-77	Haagensen, Sven, MM	Fuel Dependant Cyclic Variability in a Spark Ignition Engine - An Optical Approach. (Dr.Ing. Thesis)
MTA-91-78	Løland, Geir, MH	Current forces on and flow through fish farms. (Dr.Ing. Thesis)
MTA-91-79	Hoen, Christopher, MK	System Identification of Structures Excited by Stochastic Load Processes. (Dr.Ing. Thesis)
MTA-91-80	Haugen, Stein, MK	Probabilistic Evaluation of Frequency of Collision between Ships and Offshore Platforms. (Dr.Ing. Thesis)
MTA-91-81	Sødahl, Nils, MK	Methods for Design and Analysis of Flexible Risers. (Dr.Ing. Thesis)
MTA-91-82	Ormberg, Harald, MK	Non-linear Response Analysis of Floating Fish Farm Systems. (Dr.Ing. Thesis)
MTA-91-83	Marley, Mark J., MK	Time Variant Reliability under Fatigue Degradation. (Dr.Ing. Thesis)
MTA-91-84	Krokstad, Jørgen R., MH	Second-order Loads in Multidirectional Seas. (Dr.Ing. Thesis)
MTA-91-85	Molteberg, Gunnar A., MM	The Application of System Identification Techniques to Performance Monitoring of Four Stroke Turbocharged Diesel Engines. (Dr.Ing. Thesis)
MTA-92-86	Mørch, Hans Jørgen Bjelke, MH	Aspects of Hydrofoil Design: with Emphasis on Hydrofoil Interaction in Calm Water. (Dr.Ing. Thesis)
MTA-92-87	Chan Siu Hung, MM	Nonlinear Analysis of Rotordynamic Instabilities in Highspeed Turbomachinery. (Dr.Ing. Thesis)
MTA-92-88	Bessason, Bjarni, MK	Assessment of Earthquake Loading and Response of Seismically Isolated Bridges. (Dr.Ing. Thesis)
MTA-92-89	Langli, Geir, MP	Improving Operational Safety through exploitation of Design Knowledge - an investigation of offshore platform safety. (Dr.Ing. Thesis)
MTA-92-90	Sævik, Svein, MK	On Stresses and Fatigue in Flexible Pipes. (Dr.Ing. Thesis)
MTA-92-91	Ask, Tor Ø., MM	Ignition and Flame Growth in Lean Gas-Air Mixtures. An Experimental Study with a Schlieren System. (Dr.Ing. Thesis)
MTA-86-92	Hessen, Gunnar, MK	Fracture Mechanics Analysis of Stiffened Tubular Members. (Dr.Ing. Thesis)

MTA-93-93	Steinebach, Christian, MM	Knowledge Based Systems for Diagnosis of Rotating Machinery. (Dr.Ing. Thesis)
MTA-93-94	Dalane, Jan Inge, MK	System Reliability in Design and Maintenance of Fixed Offshore Structures. (Dr.Ing. Thesis)
MTA-93-95	Steen, Sverre, MH	Cobblestone Effect on SES. (Dr.Ing. Thesis)
MTA-93-96	Karunakaran, Daniel, MK	Nonlinear Dynamic Response and Reliability Analysis of Drag-dominated Offshore Platforms. (Dr.Ing. Thesis)
MTA-93-97	Hagen, Arnulf, MP	The Framework of a Design Process Language. (Dr.Ing. Thesis)
MTA-93-98	Nordrik, Rune, MM	Investigation of Spark Ignition and Autoignition in Methane and Air Using Computational Fluid Dynamics and Chemical Reaction Kinetics. A Numerical Study of Ignition Processes in Internal Combustion Engines. (Dr.Ing. Thesis)
MTA-94-99	Passano, Elizabeth, MK	Efficient Analysis of Nonlinear Slender Marine Structures. (Dr.Ing. Thesis)
MTA-94-100	Kvålsvold, Jan, MH	Hydroelastic Modelling of Wetdeck Slamming on Multihull Vessels. (Dr.Ing. Thesis)
MTA-94-102	Bech, Sidsel M., MK	Experimental and Numerical Determination of Stiffness and Strength of GRP/PVC Sandwich Structures. (Dr.Ing. Thesis)
MTA-95-103	Paulsen, Hallvard, MM	A Study of Transient Jet and Spray using a Schlieren Method and Digital Image Processing. (Dr.Ing. Thesis)
MTA-95-104	Hovde, Geir Olav, MK	Fatigue and Overload Reliability of Offshore Structural Systems, Considering the Effect of Inspection and Repair. (Dr.Ing. Thesis)
MTA-95-105	Wang, Xiaozhi, MK	Reliability Analysis of Production Ships with Emphasis on Load Combination and Ultimate Strength. (Dr.Ing. Thesis)
MTA-95-106	Ulstein, Tore, MH	Nonlinear Effects of a Flexible Stern Seal Bag on Cobblestone Oscillations of an SES. (Dr.Ing. Thesis)
MTA-95-107	Solaas, Frøydis, MH	Analytical and Numerical Studies of Sloshing in Tanks. (Dr.Ing. Thesis)
MTA-95-108	Hellan, Øyvind, MK	Nonlinear Pushover and Cyclic Analyses in Ultimate Limit State Design and Reassessment of Tubular Steel Offshore Structures. (Dr.Ing. Thesis)
MTA-95-109	Hermundstad, Ole A., MK	Theoretical and Experimental Hydroelastic Analysis of High Speed Vessels. (Dr.Ing. Thesis)
MTA-96-110	Bratland, Anne K., MH	Wave-Current Interaction Effects on Large-Volume Bodies in Water of Finite Depth. (Dr.Ing. Thesis)
MTA-96-111	Herfjord, Kjell, MH	A Study of Two-dimensional Separated Flow by a Combination of the Finite Element Method and

		Navier-Stokes Equations. (Dr.Ing. Thesis)
MTA-96-112	Æsøy, Vilmar, MM	Hot Surface Assisted Compression Ignition in a Direct Injection Natural Gas Engine. (Dr.Ing. Thesis)
MTA-96-113	Eknes, Monika L., MK	Escalation Scenarios Initiated by Gas Explosions on Offshore Installations. (Dr.Ing. Thesis)
MTA-96-114	Erikstad, Stein O., MP	A Decision Support Model for Preliminary Ship Design. (Dr.Ing. Thesis)
MTA-96-115	Pedersen, Egil, MH	A Nautical Study of Towed Marine Seismic Streamer Cable Configurations. (Dr.Ing. Thesis)
MTA-97-116	Moksnes, Paul O., MM	Modelling Two-Phase Thermo-Fluid Systems Using Bond Graphs. (Dr.Ing. Thesis)
MTA-97-117	Halse, Karl H., MK	On Vortex Shedding and Prediction of Vortex-Induced Vibrations of Circular Cylinders. (Dr.Ing. Thesis)
MTA-97-118	Igland, Ragnar T., MK	Reliability Analysis of Pipelines during Laying, considering Ultimate Strength under Combined Loads. (Dr.Ing. Thesis)
MTA-97-119	Pedersen, Hans-P., MP	Levendefiskteknologi for fiskefartøy. (Dr.Ing. Thesis)
MTA-98-120	Vikestad, Kyrre, MK	Multi-Frequency Response of a Cylinder Subjected to Vortex Shedding and Support Motions. (Dr.Ing. Thesis)
MTA-98-121	Azadi, Mohammad R. E., MK	Analysis of Static and Dynamic Pile-Soil-Jacket Behaviour. (Dr.Ing. Thesis)
MTA-98-122	Ulltang, Terje, MP	A Communication Model for Product Information. (Dr.Ing. Thesis)
MTA-98-123	Torbergsen, Erik, MM	Impeller/Diffuser Interaction Forces in Centrifugal Pumps. (Dr.Ing. Thesis)
MTA-98-124	Hansen, Edmond, MH	A Discrete Element Model to Study Marginal Ice Zone Dynamics and the Behaviour of Vessels Moored in Broken Ice. (Dr.Ing. Thesis)
MTA-98-125	Videiro, Paulo M., MK	Reliability Based Design of Marine Structures. (Dr.Ing. Thesis)
MTA-99-126	Mainçon, Philippe, MK	Fatigue Reliability of Long Welds Application to Titanium Risers. (Dr.Ing. Thesis)
MTA-99-127	Haugen, Elin M., MH	Hydroelastic Analysis of Slamming on Stiffened Plates with Application to Catamaran Wetdecks. (Dr.Ing. Thesis)
MTA-99-128	Langhelle, Nina K., MK	Experimental Validation and Calibration of Nonlinear Finite Element Models for Use in Design of Aluminium Structures Exposed to Fire. (Dr.Ing. Thesis)
MTA-99-	Berstad, Are J., MK	Calculation of Fatigue Damage in Ship Structures.

129		(Dr.Ing. Thesis)
MTA-99-130	Andersen, Trond M., MM	Short Term Maintenance Planning. (Dr.Ing. Thesis)
MTA-99-131	Tveiten, Bård Wathne, MK	Fatigue Assessment of Welded Aluminium Ship Details. (Dr.Ing. Thesis)
MTA-99-132	Søreide, Fredrik, MP	Applications of underwater technology in deep water archaeology. Principles and practice. (Dr.Ing. Thesis)
MTA-99-133	Tønnessen, Rune, MH	A Finite Element Method Applied to Unsteady Viscous Flow Around 2D Blunt Bodies With Sharp Corners. (Dr.Ing. Thesis)
MTA-99-134	Elvekrok, Dag R., MP	Engineering Integration in Field Development Projects in the Norwegian Oil and Gas Industry. The Supplier Management of Norne. (Dr.Ing. Thesis)
MTA-99-135	Fagerholt, Kjetil, MP	Optimeringsbaserte Metoder for Ruteplanlegging innen skipsfart. (Dr.Ing. Thesis)
MTA-99-136	Bysveen, Marie, MM	Visualization in Two Directions on a Dynamic Combustion Rig for Studies of Fuel Quality. (Dr.Ing. Thesis)
MTA-2000-137	Storteig, Eskild, MM	Dynamic characteristics and leakage performance of liquid annular seals in centrifugal pumps. (Dr.Ing. Thesis)
MTA-2000-138	Sagli, Gro, MK	Model uncertainty and simplified estimates of long term extremes of hull girder loads in ships. (Dr.Ing. Thesis)
MTA-2000-139	Tronstad, Harald, MK	Nonlinear analysis and design of cable net structures like fishing gear based on the finite element method. (Dr.Ing. Thesis)
MTA-2000-140	Kroneberg, André, MP	Innovation in shipping by using scenarios. (Dr.Ing. Thesis)
MTA-2000-141	Haslum, Herbjørn Alf, MH	Simplified methods applied to nonlinear motion of spar platforms. (Dr.Ing. Thesis)
MTA-2001-142	Samdal, Ole Johan, MM	Modelling of Degradation Mechanisms and Stressor Interaction on Static Mechanical Equipment Residual Lifetime. (Dr.Ing. Thesis)
MTA-2001-143	Baarholm, Rolf Jarle, MH	Theoretical and experimental studies of wave impact underneath decks of offshore platforms. (Dr.Ing. Thesis)
MTA-2001-144	Wang, Lihua, MK	Probabilistic Analysis of Nonlinear Wave-induced Loads on Ships. (Dr.Ing. Thesis)
MTA-2001-145	Kristensen, Odd H. Holt, MK	Ultimate Capacity of Aluminium Plates under Multiple Loads, Considering HAZ Properties. (Dr.Ing. Thesis)
MTA-2001-146	Greco, Marilena, MH	A Two-Dimensional Study of Green-Water

			Loading. (Dr.Ing. Thesis)
MTA-2001-147	Heggelund, Svein E., MK		Calculation of Global Design Loads and Load Effects in Large High Speed Catamarans. (Dr.Ing. Thesis)
MTA-2001-148	Babalola, Olusegun T., MK		Fatigue Strength of Titanium Risers – Defect Sensitivity. (Dr.Ing. Thesis)
MTA-2001-149	Mohammed, Abuu K., MK		Nonlinear Shell Finite Elements for Ultimate Strength and Collapse Analysis of Ship Structures. (Dr.Ing. Thesis)
MTA-2002-150	Holmedal, Lars E., MH		Wave-current interactions in the vicinity of the sea bed. (Dr.Ing. Thesis)
MTA-2002-151	Rognebakke, Olav F., MH		Sloshing in rectangular tanks and interaction with ship motions. (Dr.Ing. Thesis)
MTA-2002-152	Lader, Pål Furset, MH		Geometry and Kinematics of Breaking Waves. (Dr.Ing. Thesis)
MTA-2002-153	Yang, Qinzheng, MH		Wash and wave resistance of ships in finite water depth. (Dr.Ing. Thesis)
MTA-2002-154	Melhus, Øyvind, MM		Utilization of VOC in Diesel Engines. Ignition and combustion of VOC released by crude oil tankers. (Dr.Ing. Thesis)
MTA-2002-155	Ronæss, Marit, MH		Wave Induced Motions of Two Ships Advancing on Parallel Course. (Dr.Ing. Thesis)
MTA-2002-156	Økland, Ole D., MK		Numerical and experimental investigation of whipping in twin hull vessels exposed to severe wet deck slamming. (Dr.Ing. Thesis)
MTA-2002-157	Ge, Chunhua, MK		Global Hydroelastic Response of Catamarans due to Wet Deck Slamming. (Dr.Ing. Thesis)
MTA-2002-158	Byklum, Eirik, MK		Nonlinear Shell Finite Elements for Ultimate Strength and Collapse Analysis of Ship Structures. (Dr.Ing. Thesis)
IMT-2003-1	Chen, Haibo, MK		Probabilistic Evaluation of FPSO-Tanker Collision in Tandem Offloading Operation. (Dr.Ing. Thesis)
IMT-2003-2	Skaugset, Kjetil Bjørn, MK		On the Suppression of Vortex Induced Vibrations of Circular Cylinders by Radial Water Jets. (Dr.Ing. Thesis)
IMT-2003-3	Chezhan, Muthu		Three-Dimensional Analysis of Slamming. (Dr.Ing. Thesis)
IMT-2003-4	Buhaug, Øyvind		Deposit Formation on Cylinder Liner Surfaces in Medium Speed Engines. (Dr.Ing. Thesis)
IMT-2003-5	Tregde, Vidar		Aspects of Ship Design: Optimization of Aft Hull with Inverse Geometry Design. (Dr.Ing. Thesis)
IMT-	Wist, Hanne Therese		Statistical Properties of Successive Ocean Wave

2003-6		Parameters. (Dr.Ing. Thesis)
IMT-2004-7	Ransau, Samuel	Numerical Methods for Flows with Evolving Interfaces. (Dr.Ing. Thesis)
IMT-2004-8	Soma, Torkel	Blue-Chip or Sub-Standard. A data interrogation approach of identity safety characteristics of shipping organization. (Dr.Ing. Thesis)
IMT-2004-9	Ersdal, Svein	An experimental study of hydrodynamic forces on cylinders and cables in near axial flow. (Dr.Ing. Thesis)
IMT-2005-10	Brodtkorb, Per Andreas	The Probability of Occurrence of Dangerous Wave Situations at Sea. (Dr.Ing. Thesis)
IMT-2005-11	Yttervik, Rune	Ocean current variability in relation to offshore engineering. (Dr.Ing. Thesis)
IMT-2005-12	Fredheim, Arne	Current Forces on Net-Structures. (Dr.Ing. Thesis)
IMT-2005-13	Heggernes, Kjetil	Flow around marine structures. (Dr.Ing. Thesis)
IMT-2005-14	Fouques, Sebastien	Lagrangian Modelling of Ocean Surface Waves and Synthetic Aperture Radar Wave Measurements. (Dr.Ing. Thesis)
IMT-2006-15	Holm, Håvard	Numerical calculation of viscous free surface flow around marine structures. (Dr.Ing. Thesis)
IMT-2006-16	Bjørheim, Lars G.	Failure Assessment of Long Through Thickness Fatigue Cracks in Ship Hulls. (Dr.Ing. Thesis)
IMT-2006-17	Hansson, Lisbeth	Safety Management for Prevention of Occupational Accidents. (Dr.Ing. Thesis)
IMT-2006-18	Zhu, Xinying	Application of the CIP Method to Strongly Nonlinear Wave-Body Interaction Problems. (Dr.Ing. Thesis)
IMT-2006-19	Reite, Karl Johan	Modelling and Control of Trawl Systems. (Dr.Ing. Thesis)
IMT-2006-20	Smogeli, Øyvind Notland	Control of Marine Propellers. From Normal to Extreme Conditions. (Dr.Ing. Thesis)
IMT-2007-21	Storhaug, Gaute	Experimental Investigation of Wave Induced Vibrations and Their Effect on the Fatigue Loading of Ships. (Dr.Ing. Thesis)
IMT-2007-22	Sun, Hui	A Boundary Element Method Applied to Strongly Nonlinear Wave-Body Interaction Problems. (PhD Thesis, CeSOS)
IMT-2007-23	Rustad, Anne Marthine	Modelling and Control of Top Tensioned Risers. (PhD Thesis, CeSOS)
IMT-2007-24	Johansen, Vegar	Modelling flexible slender system for real-time simulations and control applications
IMT-2007-25	Wroldsen, Anders Sunde	Modelling and control of tensegrity structures.

(PhD Thesis, CeSOS)

IMT-2007-26	Aronsen, Kristoffer Høyve	An experimental investigation of in-line and combined inline and cross flow vortex induced vibrations. (Dr. avhandling, IMT)
IMT-2007-27	Gao, Zhen	Stochastic Response Analysis of Mooring Systems with Emphasis on Frequency-domain Analysis of Fatigue due to Wide-band Response Processes (PhD Thesis, CeSOS)
IMT-2007-28	Thorstensen, Tom Anders	Lifetime Profit Modelling of Ageing Systems Utilizing Information about Technical Condition. (Dr.ing. thesis, IMT)
IMT-2008-29	Refsnes, Jon Erling Gorset	Nonlinear Model-Based Control of Slender Body AUVs (PhD Thesis, IMT)
IMT-2008-30	Berntsen, Per Ivar B.	Structural Reliability Based Position Mooring. (PhD-Thesis, IMT)
IMT-2008-31	Ye, Naiquan	Fatigue Assessment of Aluminium Welded Box-stiffener Joints in Ships (Dr.ing. thesis, IMT)
IMT-2008-32	Radan, Damir	Integrated Control of Marine Electrical Power Systems. (PhD-Thesis, IMT)
IMT-2008-33	Thomassen, Paul	Methods for Dynamic Response Analysis and Fatigue Life Estimation of Floating Fish Cages. (Dr.ing. thesis, IMT)
IMT-2008-34	Pákozdi, Csaba	A Smoothed Particle Hydrodynamics Study of Two-dimensional Nonlinear Sloshing in Rectangular Tanks. (Dr.ing.thesis, IMT/ CeSOS)
IMT-2007-35	Grytøyr, Guttorm	A Higher-Order Boundary Element Method and Applications to Marine Hydrodynamics. (Dr.ing.thesis, IMT)
IMT-2008-36	Drummen, Ingo	Experimental and Numerical Investigation of Nonlinear Wave-Induced Load Effects in Containerships considering Hydroelasticity. (PhD thesis, CeSOS)
IMT-2008-37	Skejic, Renato	Maneuvering and Seakeeping of a Singel Ship and of Two Ships in Interaction. (PhD-Thesis, CeSOS)
IMT-2008-38	Harlem, Alf	An Age-Based Replacement Model for Repairable Systems with Attention to High-Speed Marine Diesel Engines. (PhD-Thesis, IMT)
IMT-2008-39	Alsos, Hagbart S.	Ship Grounding. Analysis of Ductile Fracture, Bottom Damage and Hull Girder Response. (PhD-thesis, IMT)
IMT-2008-40	Graczyk, Mateusz	Experimental Investigation of Sloshing Loading and Load Effects in Membrane LNG Tanks Subjected to Random Excitation. (PhD-thesis, CeSOS)
IMT-2008-41	Taghipour, Reza	Efficient Prediction of Dynamic Response for Flexible amd Multi-body Marine Structures. (PhD-

		thesis, CeSOS)
IMT-2008-42	Ruth, Eivind	Propulsion control and thrust allocation on marine vessels. (PhD thesis, CeSOS)
IMT-2008-43	Nystad, Bent Helge	Technical Condition Indexes and Remaining Useful Life of Aggregated Systems. PhD thesis, IMT
IMT-2008-44	Soni, Prashant Kumar	Hydrodynamic Coefficients for Vortex Induced Vibrations of Flexible Beams, PhD thesis, CeSOS
IMT-2009-45	Amlashi, Hadi K.K.	Ultimate Strength and Reliability-based Design of Ship Hulls with Emphasis on Combined Global and Local Loads. PhD Thesis, IMT
IMT-2009-46	Pedersen, Tom Arne	Bond Graph Modelling of Marine Power Systems. PhD Thesis, IMT
IMT-2009-47	Kristiansen, Trygve	Two-Dimensional Numerical and Experimental Studies of Piston-Mode Resonance. PhD-Thesis, CeSOS
IMT-2009-48	Ong, Muk Chen	Applications of a Standard High Reynolds Number Model and a Stochastic Scour Prediction Model for Marine Structures. PhD-thesis, IMT
IMT-2009-49	Hong, Lin	Simplified Analysis and Design of Ships subjected to Collision and Grounding. PhD-thesis, IMT
IMT-2009-50	Koushan, Kamran	Vortex Induced Vibrations of Free Span Pipelines, PhD thesis, IMT
IMT-2009-51	Korsvik, Jarl Eirik	Heuristic Methods for Ship Routing and Scheduling. PhD-thesis, IMT
IMT-2009-52	Lee, Jihoon	Experimental Investigation and Numerical in Analyzing the Ocean Current Displacement of Longlines. Ph.d.-Thesis, IMT.
IMT-2009-53	Vestbøstad, Tone Gran	A Numerical Study of Wave-in-Deck Impact using a Two-Dimensional Constrained Interpolation Profile Method, Ph.d.thesis, CeSOS.
IMT-2009-54	Bruun, Kristine	Bond Graph Modelling of Fuel Cells for Marine Power Plants. Ph.d.-thesis, IMT
IMT 2009-55	Holstad, Anders	Numerical Investigation of Turbulence in a Sekwed Three-Dimensional Channel Flow, Ph.d.-thesis, IMT.
IMT 2009-56	Ayala-Uraga, Efen	Reliability-Based Assessment of Deteriorating Ship-shaped Offshore Structures, Ph.d.-thesis, IMT
IMT 2009-57	Kong, Xiangjun	A Numerical Study of a Damaged Ship in Beam Sea Waves. Ph.d.-thesis, IMT/CeSOS.
IMT 2010-58	Kristiansen, David	Wave Induced Effects on Floaters of Aquaculture Plants, Ph.d.-thesis, CeSOS.

IMT 2010-59	Ludvigsen, Martin	An ROV-Toolbox for Optical and Acoustic Scientific Seabed Investigation. Ph.d.-thesis IMT.
IMT 2010-60	Hals, Jørgen	Modelling and Phase Control of Wave-Energy Converters. Ph.d.thesis, CeSOS.
IMT 2010- 61	Shu, Zhi	Uncertainty Assessment of Wave Loads and Ultimate Strength of Tankers and Bulk Carriers in a Reliability Framework. Ph.d. Thesis, IMT/ CeSOS
IMT 2010-62	Shao, Yanlin	Numerical Potential-Flow Studies on Weakly-Nonlinear Wave-Body Interactions with/without Small Forward Speed, Ph.d.thesis,CeSOS.
IMT 2010-63	Califano, Andrea	Dynamic Loads on Marine Propellers due to Intermittent Ventilation. Ph.d.thesis, IMT.
IMT 2010-64	El Khoury, George	Numerical Simulations of Massively Separated Turbulent Flows, Ph.d.-thesis, IMT
IMT 2010-65	Seim, Knut Sponheim	Mixing Process in Dense Overflows with Emphasis on the Faroe Bank Channel Overflow. Ph.d.thesis, IMT
IMT 2010-66	Jia, Huirong	Structural Analysis of Intact and Damaged Ships in a Collision Risk Analysis Perspective. Ph.d.thesis CeSoS.
IMT 2010-67	Jiao, Linlin	Wave-Induced Effects on a Pontoon-type Very Large Floating Structures (VLFS). Ph.D.-thesis, CeSOS.
IMT 2010-68	Abrahamsen, Bjørn Christian	Sloshing Induced Tank Roof with Entrapped Air Pocket. Ph.d.thesis, CeSOS.
IMT 2011-69	Karimirad, Madjid	Stochastic Dynamic Response Analysis of Spar-Type Wind Turbines with Catenary or Taut Mooring Systems. Ph.d.-thesis, CeSOS.
IMT - 2011-70	Erlend Meland	Condition Monitoring of Safety Critical Valves. Ph.d.-thesis, IMT.
IMT – 2011-71	Yang, Limin	Stochastic Dynamic System Analysis of Wave Energy Converter with Hydraulic Power Take-Off, with Particular Reference to Wear Damage Analysis, Ph.d. Thesis, CeSOS.
IMT – 2011-72	Visscher, Jan	Application of Particle Image Velocimetry on Turbulent Marine Flows, Ph.d.Thesis, IMT.
IMT – 2011-73	Su, Biao	Numerical Predictions of Global and Local Ice Loads on Ships. Ph.d.Thesis, CeSOS.
IMT – 2011-74	Liu, Zhenhui	Analytical and Numerical Analysis of Iceberg Collision with Ship Structures. Ph.d.Thesis, IMT.
IMT – 2011-75	Aarsæther, Karl Gunnar	Modeling and Analysis of Ship Traffic by Observation and Numerical Simulation. Ph.d.Thesis, IMT.

Imt – 2011-76	Wu, Jie	Hydrodynamic Force Identification from Stochastic Vortex Induced Vibration Experiments with Slender Beams. Ph.d.Thesis, IMT.
Imt – 2011-77	Amini, Hamid	Azimuth Propulsors in Off-design Conditions. Ph.d.Thesis, IMT.
IMT – 2011-78	Nguyen, Tan-Hoi	Toward a System of Real-Time Prediction and Monitoring of Bottom Damage Conditions During Ship Grounding. Ph.d.thesis, IMT.
IMT- 2011-79	Tavakoli, Mohammad T.	Assessment of Oil Spill in Ship Collision and Grounding, Ph.d.thesis, IMT.
IMT- 2011-80	Guo, Bingjie	Numerical and Experimental Investigation of Added Resistance in Waves. Ph.d.Thesis, IMT.
IMT- 2011-81	Chen, Qiaofeng	Ultimate Strength of Aluminium Panels, considering HAZ Effects, IMT
IMT- 2012-82	Kota, Ravikiran S.	Wave Loads on Decks of Offshore Structures in Random Seas, CeSOS.
IMT- 2012-83	Sten, Ronny	Dynamic Simulation of Deep Water Drilling Risers with Heave Compensating System, IMT.
IMT- 2012-84	Berle, Øyvind	Risk and resilience in global maritime supply chains, IMT.
IMT- 2012-85	Fang, Shaoji	Fault Tolerant Position Mooring Control Based on Structural Reliability, CeSOS.
IMT- 2012-86	You, Jikun	Numerical studies on wave forces and moored ship motions in intermediate and shallow water, CeSOS.
IMT- 2012-87	Xiang ,Xu	Maneuvering of two interacting ships in waves, CeSOS
IMT- 2012-88	Dong, Wenbin	Time-domain fatigue response and reliability analysis of offshore wind turbines with emphasis on welded tubular joints and gear components, CeSOS
IMT- 2012-89	Zhu, Suji	Investigation of Wave-Induced Nonlinear Load Effects in Open Ships considering Hull Girder Vibrations in Bending and Torsion, CeSOS
IMT- 2012-90	Zhou, Li	Numerical and Experimental Investigation of Station-keeping in Level Ice, CeSOS
IMT- 2012-91	Ushakov, Sergey	Particulate matter emission characteristics from diesel engines operating on conventional and alternative marine fuels, IMT
IMT- 2013-1	Yin, Decao	Experimental and Numerical Analysis of Combined In-line and Cross-flow Vortex Induced Vibrations, CeSOS

IMT-2013-2	Kurniawan, Adi	Modelling and geometry optimisation of wave energy converters, CeSOS
IMT-2013-3	Al Ryati, Nabil	Technical condition indexes doe auxiliary marine diesel engines, IMT
IMT-2013-4	Firoozkoohi, Reza	Experimental, numerical and analytical investigation of the effect of screens on sloshing, CeSOS
IMT-2013-5	Ommani, Babak	Potential-Flow Predictions of a Semi-Displacement Vessel Including Applications to Calm Water Broaching, CeSOS
IMT-2013-6	Xing, Yihan	Modelling and analysis of the gearbox in a floating spar-type wind turbine, CeSOS
IMT-7-2013	Balland, Océane	Optimization models for reducing air emissions from ships, IMT
IMT-8-2013	Yang, Dan	Transitional wake flow behind an inclined flat plate----Computation and analysis, IMT
IMT-9-2013	Abdillah, Suyuthi	Prediction of Extreme Loads and Fatigue Damage for a Ship Hull due to Ice Action, IMT
IMT-10-2013	Ramirez, Pedro Agustin Pérez	Ageing management and life extension of technical systems- Concepts and methods applied to oil and gas facilities, IMT
IMT-11-2013	Chuang, Zhenju	Experimental and Numerical Investigation of Speed Loss due to Seakeeping and Maneuvering. IMT
IMT-12-2013	Etemaddar, Mahmoud	Load and Response Analysis of Wind Turbines under Atmospheric Icing and Controller System Faults with Emphasis on Spar Type Floating Wind Turbines, IMT
IMT-13-2013	Lindstad, Haakon	Strategies and measures for reducing maritime CO2 emissons, IMT
IMT-14-2013	Haris, Sabril	Damage interaction analysis of ship collisions, IMT
IMT-15-2013	Shainee, Mohamed	Conceptual Design, Numerical and Experimental Investigation of a SPM Cage Concept for Offshore Mariculture, IMT
IMT-16-2013	Gansel, Lars	Flow past porous cylinders and effects of biofouling and fish behavior on the flow in and around Atlantic salmon net cages, IMT
IMT-17-2013	Gaspar, Henrique	Handling Aspects of Complexity in Conceptual Ship Design, IMT
IMT-18-2013	Thys, Maxime	Theoretical and Experimental Investigation of a Free Running Fishing Vessel at Small Frequency of Encounter, CeSOS
IMT-19-2013	Aglen, Ida	VIV in Free Spanning Pipelines, CeSOS

IMT-1-2014	Song, An	Theoretical and experimental studies of wave diffraction and radiation loads on a horizontally submerged perforated plate, CeSOS
IMT-2-2014	Rogne, Øyvind Ygre	Numerical and Experimental Investigation of a Hinged 5-body Wave Energy Converter, CeSOS
IMT-3-2014	Dai, Lijuan	Safe and efficient operation and maintenance of offshore wind farms ,IMT
IMT-4-2014	Bachynski, Erin Elizabeth	Design and Dynamic Analysis of Tension Leg Platform Wind Turbines, CeSOS
IMT-5-2014	Wang, Jingbo	Water Entry of Freefall Wedged – Wedge motions and Cavity Dynamics, CeSOS
IMT-6-2014	Kim, Ekaterina	Experimental and numerical studies related to the coupled behavior of ice mass and steel structures during accidental collisions, IMT
IMT-7-2014	Tan, Xiang	Numerical investigation of ship's continuous- mode icebreaking in level ice, CeSOS
IMT-8-2014	Muliawan, Made Jaya	Design and Analysis of Combined Floating Wave and Wind Power Facilities, with Emphasis on Extreme Load Effects of the Mooring System, CeSOS
IMT-9-2014	Jiang, Zhiyu	Long-term response analysis of wind turbines with an emphasis on fault and shutdown conditions, IMT
IMT-10-2014	Dukan, Fredrik	ROV Motion Control Systems, IMT
IMT-11-2014	Grimsmo, Nils I.	Dynamic simulations of hydraulic cylinder for heave compensation of deep water drilling risers, IMT
IMT-12-2014	Kvittem, Marit I.	Modelling and response analysis for fatigue design of a semisubmersible wind turbine, CeSOS
IMT-13-2014	Akhtar, Juned	The Effects of Human Fatigue on Risk at Sea, IMT
IMT-14-2014	Syahroni, Nur	Fatigue Assessment of Welded Joints Taking into Account Effects of Residual Stress, IMT
IMT-1-2015	Böckmann, Eirik	Wave Propulsion of ships, IMT
IMT-2-2015	Wang, Kai	Modelling and dynamic analysis of a semi-submersible floating vertical axis wind turbine, CeSOS
IMT-3-2015	Fredriksen, Arnt Gunvald	A numerical and experimental study of a two-dimensional body with moonpool in waves and current, CeSOS
IMT-4-2015	Jose Patricio Gallardo Canabes	Numerical studies of viscous flow around bluff bodies, IMT

IMT-5-2015	Vegard Longva	Formulation and application of finite element techniques for slender marine structures subjected to contact interactions, IMT
IMT-6-2015	Jacobus De Vaal	Aerodynamic modelling of floating wind turbines, CeSOS
IMT-7-2015	Fachri Nasution	Fatigue Performance of Copper Power Conductors, IMT
IMT-8-2015	Oleh I Karpa	Development of bivariate extreme value distributions for applications in marine technology, CeSOS
IMT-9-2015	Daniel de Almeida Fernandes	An output feedback motion control system for ROVs, AMOS
IMT-10-2015	Bo Zhao	Particle Filter for Fault Diagnosis: Application to Dynamic Positioning Vessel and Underwater Robotics, CeSOS
IMT-11-2015	Wenting Zhu	Impact of emission allocation in maritime transportation, IMT
IMT-12-2015	Amir Rasekhi Nejad	Dynamic Analysis and Design of Gearboxes in Offshore Wind Turbines in a Structural Reliability Perspective, CeSOS
IMT-13-2015	Arturo Jesús Ortega Malca	Dynamic Response of Flexibles Risers due to Unsteady Slug Flow, CeSOS
IMT-14-2015	Dagfinn Husjord	Guidance and decision-support system for safe navigation of ships operating in close proximity, IMT
IMT-15-2015	Anirban Bhattacharyya	Ducted Propellers: Behaviour in Waves and Scale Effects, IMT
IMT-16-2015	Qin Zhang	Image Processing for Ice Parameter Identification in Ice Management, IMT
IMT-1-2016	Vincentius Rumawas	Human Factors in Ship Design and Operation: An Experiential Learning, IMT
IMT-2-2016	Martin Storheim	Structural response in ship-platform and ship-ice collisions, IMT
IMT-3-2016	Mia Abrahamsen Prsic	Numerical Simulations of the Flow around single and Tandem Circular Cylinders Close to a Plane Wall, IMT
IMT-4-2016	Tufan Arslan	Large-eddy simulations of cross-flow around ship sections, IMT

IMT-5-2016	Pierre Yves-Henry	Parametrisation of aquatic vegetation in hydraulic and coastal research,IMT
IMT-6-2016	Lin Li	Dynamic Analysis of the Instalation of Monopiles for Offshore Wind Turbines, CeSOS
IMT-7-2016	Øivind Kåre Kjerstad	Dynamic Positioning of Marine Vessels in Ice, IMT
IMT-8-2016	Xiaopeng Wu	Numerical Analysis of Anchor Handling and Fish Trawling Operations in a Safety Perspective, CeSOS
IMT-9-2016	Zhengshun Cheng	Integrated Dynamic Analysis of Floating Vertical Axis Wind Turbines, CeSOS
IMT-10-2016	Ling Wan	Experimental and Numerical Study of a Combined Offshore Wind and Wave Energy Converter Concept
IMT-11-2016	Wei Chai	Stochastic dynamic analysis and reliability evaluation of the roll motion for ships in random seas, CeSOS
IMT-12-2016	Øyvind Selnes Patricksson	Decision support for conceptual ship design with focus on a changing life cycle and future uncertainty, IMT
IMT-13-2016	Mats Jørgen Thorsen	Time domain analysis of vortex-induced vibrations, IMT
IMT-14-2016	Edgar McGuinness	Safety in the Norwegian Fishing Fleet – Analysis and measures for improvement, IMT
IMT-15-2016	Sepideh Jafarzadeh	Energy efficiency and emission abatement in the fishing fleet, IMT
IMT-16-2016	Wilson Ivan Guachamin Acero	Assessment of marine operations for offshore wind turbine installation with emphasis on response-based operational limits, IMT
IMT-17-2016	Mauro Caneloro	Tools and Methods for Autonomous Operations on Seabed and Water Coumn using Underwater Vehicles, IMT
IMT-18-2016	Valentin Chabaud	Real-Time Hybrid Model Testing of Floating Wind Tubines, IMT
IMT-1-2017	Mohammad Saud Afzal	Three-dimensional streaming in a sea bed boundary layer
IMT-2-2017	Peng Li	A Theoretical and Experimental Study of Wave-induced Hydroelastic Response of a Circular Floating Collar
IMT-3-2017	Martin Bergström	A simulation-based design method for arctic maritime transport systems

IMT-4-2017	Bhushan Taskar	The effect of waves on marine propellers and propulsion
IMT-5-2017	Mohsen Bardestani	A two-dimensional numerical and experimental study of a floater with net and sinker tube in waves and current
IMT-6-2017	Fatemeh Hoseini Dadmarzi	Direct Numerical Simulation of turbulent wakes behind different plate configurations
IMT-7-2017	Michel R. Miyazaki	Modeling and control of hybrid marine power plants
IMT-8-2017	Giri Rajasekhar Gunnu	Safety and efficiency enhancement of anchor handling operations with particular emphasis on the stability of anchor handling vessels
IMT-9-2017	Kevin Koosup Yum	Transient Performance and Emissions of a Turbocharged Diesel Engine for Marine Power Plants
IMT-10-2017	Zhaolong Yu	Hydrodynamic and structural aspects of ship collisions
IMT-11-2017	Martin Hassel	Risk Analysis and Modelling of Allisions between Passing Vessels and Offshore Installations
IMT-12-2017	Astrid H. Brodtkorb	Hybrid Control of Marine Vessels – Dynamic Positioning in Varying Conditions
IMT-13-2017	Kjersti Bruserud	Simultaneous stochastic model of waves and current for prediction of structural design loads
IMT-14-2017	Finn-Idar Grøtta Giske	Long-Term Extreme Response Analysis of Marine Structures Using Inverse Reliability Methods
IMT-15-2017	Stian Skjong	Modeling and Simulation of Maritime Systems and Operations for Virtual Prototyping using co-Simulations
IMT-1-2018	Yingguang Chu	Virtual Prototyping for Marine Crane Design and Operations
IMT-2-2018	Sergey Gavrilin	Validation of ship manoeuvring simulation models
IMT-3-2018	Jeevith Hegde	Tools and methods to manage risk in autonomous subsea inspection, maintenance and repair operations
IMT-4-2018	Ida M. Strand	Sea Loads on Closed Flexible Fish Cages
IMT-5-2018	Erlend Kvinge Jørgensen	Navigation and Control of Underwater Robotic Vehicles

IMT-6-2018	Bård Stovner	Aided Inertial Navigation of Underwater Vehicles
IMT-7-2018	Erlend Liavåg Grotle	Thermodynamic Response Enhanced by Sloshing in Marine LNG Fuel Tanks
IMT-8-2018	Børge Rokseth	Safety and Verification of Advanced Maritime Vessels
IMT-9-2018	Jan Vidar Ulveseter	Advances in Semi-Empirical Time Domain Modelling of Vortex-Induced Vibrations
IMT-10-2018	Chenyu Luan	Design and analysis for a steel braceless semi-submersible hull for supporting a 5-MW horizontal axis wind turbine
IMT-11-2018	Carl Fredrik Rehn	Ship Design under Uncertainty
IMT-12-2018	Øyvind Ødegård	Towards Autonomous Operations and Systems in Marine Archaeology
IMT-13-2018	Stein Melvær Normes	Guidance and Control of Marine Robotics for Ocean Mapping and Monitoring